

***CHROMATIN INTERACTION DYNAMICS REVEALED BY LIQUID***

***CHROMATIN Hi-C***

A Dissertation Presented

By

**Houda Belaghzal**

Submitted to the Faculty of the

University of Massachusetts Graduate School of Biomedical Sciences, Worcester

in partial fulfillment of the requirements for the degree of

**DOCTOR OF PHILOSOPHY**

July 12th , 2019

# ***CHROMATIN INTERACTION DYNAMICS REVEALED BY LIQUID***

## ***CHROMATIN Hi-C***

A Dissertation Presented

By

**Houda Belaghzal**

This work was undertaken in the Graduate School of Biomedical Sciences

Interdisciplinary Graduate Program

Under the mentorship of

---

Job Dekker, PhD; Thesis Advisor

---

Jeanne Lawrence , PhD; Member of Committee

---

Craig Peterson, PhD; Member of Committee

---

Amir Mitchell, PhD; Member of Committee

---

Stavros Lomvardos, PhD; External Member of Committee

---

Paul Kaufman, PhD, Chair of Committee

Mary Ellen Lane, Ph.D.,

Dean of the Graduate School of Biomedical Sciences

July 12<sup>th</sup> , 2019

## **DEDICATION**

In memory of my uncle Aziz Rrhious- a father figure to me, who lost his battle with lung cancer in February of 2019. Uncle Aziz never missed an opportunity to show me how much he cared and supported me in the pursuit of my dreams, especially when it comes to my love and dedication to science. His encouragement and never ending generosity to all of those around him motivated me to keep going even in the most challenging moments.

To my courageous and precious mother, grandmother and sister: you have taught me the most valuable lessons that define me today as a person.

## ACKNOWLEDGEMENTS

This thesis would not have been possible without the continuous guidance from my advisor- Job Dekker, Ph.D. When I met Job, during one of my GSBS interviews, I instantly knew he will be the most profound mentor and role model any PhD student could ask for. I am honored to have had a chance to join his laboratory. What sets him apart from many others is not only his absolute command and knowledge of the field but most importantly his humbleness, patience and enthusiasm to teach others, and genuine effort he invests in others. Working with him hasn't only been an empowering and inspiring experience but also a mentorship that will be one of the guiding principles to live my life. I am immensely thankful for his patience, trust and support throughout the many challenges along this journey

I also would like to thank all of my collaborators, both past and present, especially Tyler Borrman for four years of collaboration, during which we developed new tools to analyze the data for our paper, "Liquid chromatin Hi-C", presented in the fourth chapter of this dissertation; we had a great collaboration. Also for the same project, "Liquid chromatin Hi-C", I thank John Marko and his postdoc Andrew D. Stephens for their collaboration, which entailed applying their cool micromanipulation techniques and for brainstorming about our results. Also, I thank Leonid A. Mirny and Edward J. Banigan for discussions about "Liquid chromatin Hi-C" presented in chapter IV

To my Committee Members: Paul Kaufman PhD, Jeannie Lawrence, PhD., and Craig Peterson, PhD, and Amir Mitchel, PhD- I am very thankful for your encouragement, constructive feedback and continuous support during this process.

During my time at the Dekker Lab, I had the privilege to work with a number of extremely talented scientists. Thank you to past members: Natalia Naumova. PhD, Amartya Sanyal, PhD, Jon-Matthew Belton, PhD, Emily Smith, PhD, Rachel Patton-McCord, PhD, Gaurav Jain, PhD, Noam Kaplan, PhD, Jennifer E. Phillips-Cremins, PhD, Filipe Tavares-Cadete, PhD, and Hakan Ozadam PhD. Special thank you to Bryan and Jon for their support, and kindness as colleagues and friends. And Jennifer E. Phillips-Cremins PhD for her tremendous support and help during my qualify exam. Thank you to my current lab team members: Ye Zhan, Anne-Laure Valton PhD , Marlies Oomen, Allana Schooley PhD, Nicki Fox PhD, Kristin Abramo, Betul Akgol Oksuz , Bastiaan Dekker , Denis L. Lafontaine, Johan Gibcus PhD, Liyan Yang, Ankita Nand, Sergey Venev PhD, Erica Hildebrand PhD, Yu Liu (Sunny) PhD, Ozgun Uyan, and of course, once again, our amazing mentor Job Dekker PhD. A heartfelt thank you goes to Allana Schooley and Anne-Laure Valton PhD for proofreading some content of this thesis.

To members of the Program in Systems Biology thank you for being a very inspiring and creative group during “Science On Tap” seminars and also

during our daily unscheduled interactions in the kitchen of our department. I thank Marian Walhout PhD for her support during some challenging times, and Amir Mitchell PhD for some insightful advice in the project I am presenting in the fourth chapter of this dissertation. Thanks to Ryan Richards PhD for his constructive edits for some content of this dissertation.

I will like to thank Allan S Jacobson PhD for believing in me, supporting me, and defended me fiercely. And Nadia Amrani for your enormous support and mentorship.

Thanks to all the administrative and technical support staff of the Systems Biology department, past and present; because of your hard work, we are able to work smoothly every day in the lab.

To all my amazing friends, especially Edina Skaljic you have been the most supportive friend; you believe in me and remind me of my strength during challenging times. Thank you for being very thoughtful and supportive. You are like a sister to me, and I feel so grateful and lucky to call you my best friend. To my superwoman, perfectionist, and very supportive friend Hasena Omanovic, I am very grateful for our friendship and your support. To Katharina Alshafie, thank you for being an amazing friend who makes time for me even after having two kids. Betul Akgol Oksuz, thank you for being such a great supportive friend, and for being there for me during hard days. To Anne-Laure thank you for your tremendous support continuous encouragement. To all of you, we have

supported each other through many struggles, I could not have done this without your support.

To my family, اركش. Finally the answer to your persistent question, when are you going to be done with your Ph.D.? Yes, I am almost done. Thank you in particular to the three most important women of my life, my Grandmother, my mother, and my only sister Naoual for supporting me and believing in me, and most importantly supporting my decision to leave the country to pursue my dream to be a scientist. Thanks for asking me to explain my research to you, even if you ask me the same question every year. Thank you for your continuous support and unconditional love. And the biggest thanks to my uncle Mohammed Bourdi, a scientist in National Institute of Health (NIH), for his tremendous support. He encouraged me and supported my decision to come to the US for an internship, then to get a PhD, and most importantly encouraged me to keep going throughout all the years of my PhD, Mohammed and Amina I would have never been able to get where I am today without your tremendous support.

## ABSTRACT

Development and application of genomic approaches based on 3C methods combined with increasingly powerful imaging approaches have enabled high-resolution genome-wide analysis of the spatial organization of chromosomes in genome function. In this thesis, I first describe an updated protocol for Hi-C (Hi-C 2.0), integrating recent improvements that significantly contribute to the efficient and high-resolution capture of chromatin interactions. Secondly, I present an assessment of the epigenetic landscape and chromosome conformation around the *MYC* gene in acute myeloid leukemia (AML) cells before and after small molecule, AI-10-49, treatment. *MYC* is up-regulated upon inhibition of the RUNX1 repressor by the fusion oncoprotein CBF $\beta$ -SMMHC. Treatment of AML cells with AI-10-49 blocks the RUNX1-CBF $\beta$ -SMMHC interaction, restoring RUNX1 at *MYC* regulatory elements. We demonstrate that the established loop is maintained and exchange between activating and repressive chromatin complexes at the regulatory elements, rather than altered chromatin topology, mediates disruption of target gene expression.

Finally, Hi-C interaction maps represent the population-averaged steady-states. To understand the forces that promote and maintain the association of loci with specific sub-nuclear structures genome-wide, we developed liquid chromatin Hi-C. Detection of intrinsic locus-locus interaction stabilities and chromatin mobility are enabled by fragmenting chromosomes prior to fixation and



Hi-C, thus removing strong polymeric constraints. Nuclear compartmentalization was found to be stable for average fragment lengths are 10-25 kb while fragmentation below 6kb led to a gradual loss of spatial genome organization. Dissolution kinetics of chromatin interactions vary widely for different domains and are analyzed in detail in the final chapter of this thesis., with lamin-associated domains being most stable, and speckle-associated loci most dynamic.

## TABLE OF CONTENTS

<b>CHAPTER I: Introduction.....</b>	<b>1</b>
<i>Introduction .....</i>	<i>1</i>
<i>Microscopy-based methods .....</i>	<i>1</i>
<i>3C-based methods.....</i>	<i>2</i>
<i>3D genome during interphase.....</i>	<i>4</i>
<i>Chromosomal territories.....</i>	<i>6</i>
<i>Interchromatin domain (ICD).....</i>	<i>7</i>
<i>Compartments.....</i>	<i>9</i>
<i>Compartmentalization model .....</i>	<i>14</i>
<i>Topologically associating domain (TAD).....</i>	<i>16</i>
TADs in single cells.....	17
TAD boundaries and gene regulation .....	18
Models for TAD formation .....	20
Depletion of TAD building elements.....	22
<i>The interplay between TADs and compartments.....</i>	<i>25</i>
<i>Promoter enhancer interactions.....</i>	<i>27</i>
Promoter enhancer interactions within TADs.....	27
Long-range promoter-enhancer interactions.....	29
Super-enhancers.....	29
Interchromosomal enhancer-promoter interactions .....	30
<i>Biophysical processes that form chromosome conformation .....</i>	<i>32</i>
<b>CHAPTER II: Hi-C 2.0: an optimized Hi-C procedure for high-resolution genome-wide mapping of chromosome conformation.....</b>	<b>36</b>
<i>PREFACE .....</i>	<i>36</i>
<i>Abstract .....</i>	<i>36</i>
<i>INTRODUCTION.....</i>	<i>37</i>
<i>MATERIALS AND METHODS .....</i>	<i>40</i>
Hi-C 2.0 .....	40
Crosslinking.....	40
Cells lysis: .....	41
Digestion .....	41

Biotin Fill-in:.....	42
Ligation:.....	42
Reverse Crosslinking .....	42
DNA purification: .....	43
Removal of Biotin from unligated ends: .....	44
Sonication: .....	44
Size fractionation using AMPure XP: .....	44
End Repair .....	46
Biotin pull-down .....	46
A-tailing: .....	47
Illumina adapter ligation and paired-end PCR .....	47
Illumina Truseq Kit for PCR:.....	48
<b>RESULTS.....</b>	<b>48</b>
CELL CULTURE & CROSSLINKING CELLS USING FORMALDEHYDE.....	48
Marking of DNA ends with biotin.....	53
In situ Ligation of proximal ends .....	54
Reversal of crosslinking and DNA purification .....	55
Quality Control of Hi-C ligation products.....	55
Removal of Biotin from un-ligated ends .....	56
Sonication .....	58
Size selection .....	58
End repair.....	59
Biotin pulldown .....	59
A-tailing and adaptor ligation .....	60
PCR titration and production .....	61
Sequencing .....	63
MAPPING AND BINNING PIPELINE .....	63
Bias in inward read orientation.....	66
Analysis of valid interaction pairs .....	67
Compartments.....	72
Topologically associated domains (TADs).....	72
Point to point interactions (loops).....	73
<b>CONCLUSION .....</b>	<b>75</b>
<b>CHAPTER III: CBF<math>\beta</math>-SMMHC Inhibition Triggers Apoptosis by .....</b>	<b>76</b>
<b>Disrupting MYC Chromatin Dynamics in Acute.....</b>	<b>76</b>
<b>Myeloid Leukemia .....</b>	<b>76</b>
PREFACE .....	76
SUMMARY.....	76
INTRODUCTION.....	77
MYC expression is critical for the survival of leukemia cells.....	78
The inhibitory role of CBF $\beta$ -SMMHC oncoprotein .....	80

AI-10-49 restores RUNX1 binding .....	81
The inhibitor AI-10-49 is a selective inhibitor of CBF $\beta$ -SMMHC which disrupts its binding to RUNX1 and induces apoptosis of inv(16) AML cells (Xue et al., 2015). Analysis of chromatin-immunoprecipitation (ChIP) experiments shows that treatment of ME-1 cells revealed that AI-10-49 restores RUNX1 transcriptional activity by increased RUNX1 binding to its target promoters (Fig. 3.1B) (Xue et al., 2015). .....	81
<b>MATERIALS AND METHODS</b> .....	82
Cell growth .....	82
Assay for Transposase-Accessible Chromatin with sequencing (ATAC-seq) .....	82
ATAC-qPCR .....	84
CRISPR/Cas9 – mediated deletion of the enhancer regions.....	84
5C experimental design .....	85
Primer settings .....	87
Generation of 5C libraries .....	87
5C read mapping.....	88
5C filtering and analysis.....	88
4C-style plots .....	90
<b>RESULTS</b> .....	90
Inhibition of CBF $\beta$ -SMMHC Activity by AI-10-49 Represses <i>MYC</i> Expression .....	90
AI-10-49 enhances genome-wide RUNX1 DNA binding .....	91
RUNX1 represses <i>MYC</i> expression through binding at downstream enhancers .....	93
ME1, ME2, and E3 enhancers physically interact with the <i>MYC</i> promoter .....	96
<i>MYC</i> expression and viability of inv(16) AML cells depend on ME1, ME2, and E3 enhancers .....	100
AI-10-49 induces a switch of SWI/SNF active to PRC-repressive complexes at the AML-associated <i>MYC</i> enhancers .....	102
<b>CONCLUSION</b> .....	105
Transcription factor function can determine leukemia maintenance .....	105
The direct role of RUNX1 in <i>MYC</i> repression .....	105
Enhancers can modulate the expression of their targets gene in a pair-wise manner .....	106
<b>CHAPTER IV: Compartment-dependent chromatin interaction dynamics revealed by liquid chromatin Hi-C</b> .....	108
<b>SUMMARY</b> .....	108
<b>INTRODUCTION</b> .....	109
<b>MATERIALS AND METHODS</b> .....	112
Digestion, cross-linking and copolymer architecture and hetero/euchromatin phase separation .....	112
K562 nuclei purification .....	116
3C (Chromosome Conformation Capture).....	117
BAC library for 3C-PCR .....	121
Chromosome Conformation Capture Carbon Copy (5C).....	121
Pre-digestion of nuclei (liquify chromatin) .....	125

Hi-C 2.0 .....	126
DpnII-Seq .....	127
Lamin A Immunofluorescence and DAPI .....	134
Chromatin fractionation assay .....	135
Micromanipulation force measurement and treatments of an isolated nuclei.....	137
3C-PCR .....	138
5C data processing .....	139
Hi-C data processing.....	140
A/B compartments.....	141
LOS and half-life calculation .....	141
DpnII-seq data analysis.....	144
Subcompartments .....	145
Sub-nuclear structures .....	146
Gene Expression.....	148
Compartmentalization saddle plots .....	149
Homotypic interaction saddle plots .....	149
Scaling plot.....	150
Mean z-score heatmap .....	150
Code availability .....	150
<b>RESULTS.....</b>	<b>151</b>
Measuring the stability of chromatin interactions that maintain nuclear .....	151
compartmentalization .....	151
Chromosome conformation in isolated nuclei.....	153
Extensive chromatin fragmentation leads to the formation of liquid chromatin .....	156
Liquid chromatin Hi-C analysis reveals that compartmental segregation requires chromatin .....	160
fragments larger than 6 kb .....	160
Quantification of chromosome conformation dissolution upon chromatin fragmentation ....	162
Independent contributions of compartment status and fragmentation level to chromatin .....	164
dissolution .....	164
Dissociation kinetics of chromatin interactions and compartments .....	171
Quantification of the half-life of chromosome conformation across the genome.....	173
Independent contributions of compartment status and fragmentation level to the half-life of .....	181
chromatin interactions .....	181
Compartment size and boundaries influence chromatin interaction stability .....	185
Chromatin loops dissociate upon chromatin fragmentation.....	196
<b>DISCUSSION.....</b>	<b>199</b>
<b>CHAPTER V: Discussion.....</b>	<b>200</b>
<i>3C-based technologies</i> .....	200
<i>Promoter-enhancer interactions</i> .....	202
<i>liquid chromatin Hi-C</i> .....	207
<b>BIBLIOGRAPHY.....</b>	<b>219</b>

## LIST OF FIGURES

Figure 1.1: Schematic of the different levels of genome organization in 3D .....	6
Figure 1.2 : A simple schematic of loop extrusion.....	22
Figure 1.3: Block copolymer folds into spatially segregated domains.....	35
Figure 2.1 : Overview of the Hi-C method .....	51
Figure 2.2: Quality Control of Hi-C ligation products.....	62
Figure 2.3: Possible products generated by Hi-C .....	65
Figure 2.4: Dangling end removal and to increase valid pair reads .....	70
Figure 2.5: Topological structures observed with Hi-C .....	74
Figure 3.1: Schematic of inv(16)(p13;q22), which fuse CBF $\beta$ and MYH11 genes. .....	81
Figure 3.2: Double alternating design for 5C probes. ....	86
Figure 3.3: MYC transcript level in response to AI-10-49 treatment. ....	91
Figure 3.4: RUNX1 binding in response to AI-10-49 treatment. ....	93
Figure 3.5: RUNX1 binding to MYC downstream enhancers.....	95
Figure 3.6: Three enhancers downstream of MYC interact directly with MYC promoter. ....	98
Figure 3.7: Deletion of Three RUNX1-Associated MYC Enhancer Elements Impairs MYC Expression and Viability of inv(16) AML.....	101
Figure 3.8: AI-10-49 Induces a Switch of Activation for Repressive Marks at RUNX1-Associated MYC Enhancers.....	104
Figure 4.1: Approach for measuring chromatin interaction stability .....	152
Figure 4.2: Chromosome conformation in isolated nuclei.....	154
Figure 4.3: Extensive fragmentation of chromatin leads to liquefied chromatin	159
Figure 4.5: Hi-C analysis reveals chromosome disassembly upon chromatin liquefaction.....	168
Figure 4.7: Kinetics of chromatin fragmentation and chromatin dissolution .....	177
Figure 4.8: Liquid chromatin-Hi-C protocol and quantification of loss of structure after chromatin pre-digestion .....	179
Figure 4.9: Variations in Half-life and LOS are not explained by DpnII digestion kinetics. ....	183
Figure 4.10: Associations between sub-nuclear structures, compartment characteristics and chromatin interaction stability.....	192
Figure 4.11: Dissociation kinetics of chromatin interactions at different sub- nuclear structures .....	194

Figure 4.12: Chromatin loop dissociation upon fragmentation.....	198
Figure 5.1: Illustration of chromatin interaction dynamics in the nucleus and model for cohesin loss after chromatin digestion.....	217

## COPYRIGHT MATERIAL

Some content or figures have been previously published as described below. According to the publisher's copyright policies, as an author of these articles, I retain the right to publish these contents in a thesis dissertation. Specific attributions are listed in the Preface section accompanying each chapter.

**Houda Belaghzal**<sup>1</sup>, Job Dekker<sup>1, 2\*</sup>, Johan H. Gibcus<sup>1</sup>. Methods. 2017 Jul 1;123:56-65. doi: 10.1016/j.ymeth.2017.04.004. Epub 2017 Apr 18.

John Anto Pulikkan,<sup>1</sup> Mahesh Hegde,<sup>1</sup> Hafiz Mohd Ahmad,<sup>1</sup> **Houda Belaghzal**,<sup>2</sup> Anuradha Illendula,<sup>3</sup> Jun Yu,<sup>1</sup> Kelsey O'Hagan,<sup>1</sup> Jianhong Ou,<sup>1</sup> Carsten Muller-Tidow,<sup>4</sup> Scot A. Wolfe,<sup>1</sup> Lihua Julie Zhu,<sup>1</sup> Job Dekker,<sup>2</sup> John Hackett Bushweller,<sup>3</sup> and Lucio Hernán Castilla<sup>1</sup>. Cell 174, 172–186, June 28, 2018

The content of chapter IV is a manuscript under revisions

**Houda Belaghzal**<sup>1\*</sup>, Tyler Borrman<sup>2\*</sup>, Andrew D. Stephens<sup>3</sup>, Denis L. Lafontaine<sup>1</sup>, Sergey Venev<sup>1</sup>, Zhiping Weng<sup>2</sup>, John F. Marko<sup>3,4</sup>, Job Dekker<sup>1</sup>

## **CHAPTER I: Introduction**

### **Introduction**

Sequencing the human genome was a revolutionary step toward understanding normal genome function and dysfunction in DNA related diseases. However, genome function is dependent on the folded state of DNA inside the cell nucleus. In humans, ~2 meters of DNA is intricately folded inside a small nucleus of ~10 micrometers in diameter. Consequently, a major challenge of genome folding is maintaining appropriate accessibility for regulatory elements across cell divisions. The genomic community has developed various technologies to help reveal the three-dimensional (3D) structure of the genome. Such advancements have shed light upon the 3D structure of the genome as it relates to its function, nuclear processes, and importantly some of the molecular mechanisms that build the 3D genome structure itself.

### **Microscopy-based methods**

Over the last decade, improvements in imaging approaches and 3C-based technologies led to the untangling of many complex questions pertaining to how the genome folds. In traditional Fluorescence In Situ Hybridization (FISH) experiments, a limited number of loci are targeted to investigate their interactions and their location inside the nucleus. More recently, high-throughput FISH experiments were developed, capable of investigating hundreds of chromatin interactions in single cells (Finn et al., 2019). Utilizing super-



resolution imaging, Boettiger and coworkers modified a previously reported oligopaint approach to produce tens of thousands of unique oligonucleotide probes, in order to label and visualize kilobase to megabase long genomic regions using massively parallel oligonucleotide synthesis (Boettiger et al., 2016). Finally, Genome Architecture Mapping (GAM) enables the measurement of chromatin contacts and other features of three-dimensional chromatin topology based on sequencing DNA from a large collection of thin nuclear sections (Beagrie et al., 2017).

### **3C-based methods**

Numerous biochemical approaches are capable of mapping physical genome interactions with the aid of DNA sequencing. Chromosome conformation capture (3C) based technologies (3C, 4C, 5C, capture-C, and Hi-C) (Job Dekker, Rippe, Dekker, & Kleckner, 2002) (Dryden et al., 2014) (Dostie et al., 2006) (Lieberman-aiden et al., 2009) use formaldehyde to capture DNA interactions that are in close proximity in 3-dimensional space. After formaldehyde crosslinking, DNA is fragmented followed by ligation of proximal fragments and sequencing of ligated products. Combinations of these 3C-based methods with next-generation sequencing technology have enabled the mapping of DNA interactions at high resolution. Building on these techniques, ChIA-PET (Fullwood et al., 2010) incorporates an immunoprecipitation step to 3C to enrich for pair-wise interactions bounds by a specific protein. Promoter Capture Hi-C “PCHi-C” enables enrichment of interactions between promoters and distal

regions in order to assign regulatory elements to their target genes (Schoenfelder et al., 2015). The power of all of these 3C-based techniques is that no prior knowledge of specific targets is needed, which allows for the detection of new interactions in the genome. On the other side, a caveat of 3C-based methods is that they are population-based and thus results reflect the average signal in the analyzed cell population.

The invention of many 3C-based techniques led to the challenging question: which 3C-based technique is best suited to answer a specific biological problem? The following differences between 3C-based methods should be taken into consideration when determining which method is most favorable. First, genomic coverage varies amongst all 3C-based techniques (~ 200 kb using 3C-PCR, up to ~5Mb using 5C or capture-C, and genome-wide coverage using Hi-C, 4C, and ChIA-PET). Second, 3C-PCR investigates the interactions between two genomic loci (one-vs-one), 4C reveals the interactions between one specific DNA anchor of interest and all other loci genome-wide (one-vs-all), 5C and Capture-C explore the interactions between all loci within the targeted region (many-vs-many) , and Hi-C reveals pair-wise interactions genome-wide (all-vs-all). However, in mammalian cells, sequencing depths on the order of  $10^8 - 10^9$  valid reads are required to produce a high-resolution Hi-C interaction map. One downside of ChIA-PET and PCHi-C techniques is the higher rate of false negative peak calls due to the techniques' enrichment for specific interactions. These false negative peaks would not get called in high-resolution Hi-C because they are not enriched

compared to their neighboring interactions. Further data normalization is necessary to decrease such false negative peaks. Recently, another 3C-based method, “split-pool recognition of interactions by tag extension” (SPRITE), was developed to overcome the limitations of pair-wise interactions in Hi-C (Quinodoz et al., 2018), this technique enriches for longer range and cluster of DNA interactions. Like all other 3C-based methods, SPRITE relies on crosslinking of proximal loci and DNA fragmentation. DNA, RNA, and proteins are crosslinked in cells, nuclei are isolated, chromatin is fragmented and interacting molecules within an individual complex are barcoded using a split-pool strategy. Finally, DNA interactions are identified by sequencing and matching all reads that contain identical barcodes, which enables genome-wide detection of multiple DNA interactions that occur simultaneously within the nucleus (Quinodoz et al., 2018).

### **3D genome during interphase**

The fractal globule is an attractive model for the 3D genome as it lacks knots and can facilitate polymer unfolding and refolding analogous to the unfolding and refolding of chromatin segments that are known to occur during gene activation, gene repression, or during the cell cycle. In a fractal globule, contiguous regions of the genome tend to form spatial sectors whose size corresponds to the length of the region and reflect the scaling of distance versus interactions seen in the interphase nucleus by Hi-C (Lieberman-aiden et al., 2009). The combination of microscopy and 3C-based methods was very

powerful in elucidating the different levels of genome organization, including chromosome territories (CT) and active (euchromatin) and inactive (heterochromatin) chromatin domains within CTs that tend to create separate compartments with an average size of 3Mb. Within compartments, insulated domains termed topologically associated domains (TADs) with an average size of 400kb further segregate the linear genome. Each TAD is a cluster of many genes and their regulatory elements (**Fig. 1.1**). Furthermore, 165 base pairs of DNA is wrapped around a nucleosome, and the first level of nucleosome packing is believed to produce a fiber of about 30 nanometers (nm) wide (Wu, Bassett, & Travers, 2007). However, a 3D model of chromosome III in yeast that was derived from 3C data, estimated a packing ratio of 11.1 nm/kb which allows chromatin flexibility (J Dekker, Rippe, Dekker, & Kleckner, 2002)

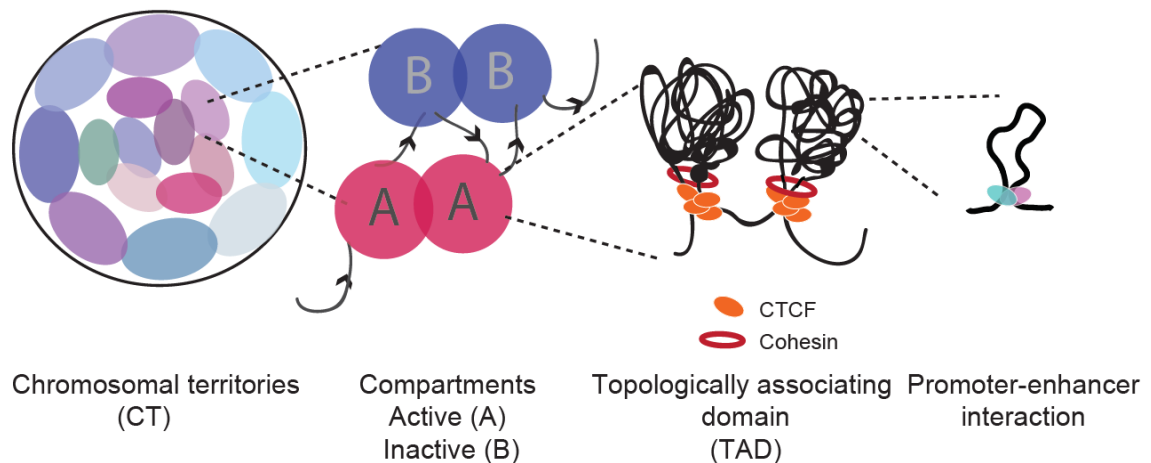


**Figure 1.1 Schematic of the different levels of genome organization in 3D**

### Chromosomal territories

Inside the nucleus, the spatial positioning of chromatin is not random. Chromatin is organized into chromosome territories that reflect the physical space each chromosome occupies during interphase (Cremer et al., 1982). Employing chromosome painting coupled with FISH, it was observed that chromosomes do not readily mix with other chromosomes. Each chromosome occupies a distinct volume, or territory, in the nucleus (Dekker & Misteli, 2015). Chromosome territories were also detected in genome-wide Hi-C interaction matrices (Lieberman-aiden et al., 2009). Moreover, the radial arrangement of the chromosomes inside the nucleus is tissue and cell type specific, which suggests

that appropriate positioning of chromosomes within the nucleus, is important for proper genes expression. Large and gene-poor chromosomes tend to localize toward the nuclear periphery, while small and gene-rich chromosomes preferentially localize near the center of the nucleus. For example, the positioning of chromosome 18 ( gene-poor) near the periphery and chromosome 19 (gene-rich) near the nuclear center has been observed in human lymphocytes (Thomas Cremer & Cremer, 2010). Similar preferential location patterns have been documented for all chromosomes in the human genome. Human chromosomes 13, 14, 15, 21, and 22, which are rich in ribosomal RNA genes, localize around nucleolus. Finally, X chromosomes localize more peripherally in liver cells compared to kidney cells (Parada, Mcqueen, & Misteli, 2004). Radial chromosome position often differs in diseased cells. For instance, in pancreatic cancer, chromosome 8 shifts to a more peripheral location. Similarly, chromosomes 18 and 19 were shown to change nuclear location in various cancers types, including cervical and colon cancer (Thomas Cremer & Cremer, 2010).

### **Interchromatin domain (ICD)**

Chromatin painting of all chromosomes using FISH revealed that CTs are insulated neighborhoods inside the nucleus. However, due to the limited local resolution of chromatin painting, interchromatin domains (ICDs) between different CTs were not detected. Higher-resolution cryo-FISH experiments revealed a greater level of intermingling between neighboring chromosomes than was

previously assumed (Branco & Pombo, 2006). Loci located at the surface of CTs interact with each other in a clustering manner once they are sufficiently close in 3D (Branco & Pombo, 2006). Interactions between loci from different chromosomes were also observed in Hi-C. Large chromosomes tend to intermingle with other large chromosomes, whereas the smaller and gene-dense chromosomes also preferentially interact (Lieberman-aiden et al., 2009). These preferential interminglings are consistent with the observations that large chromosomes are more peripherally localized, smaller gene-dense chromosomes tend to be more internally positioned in the nucleus, and intermingling of chromosomes can occur for neighboring CTs (T Cremer & Cremer, 2001). Furthermore, the ICD is not distributed randomly throughout the entire surface of a CT but is specific to loci that are anchored to transcriptions factories (PolII clusters) and splicing factories (Nuclear speckles) (Misteli, 2007). The degree of intermingling of chromatin from different CTs correlates highly with translocation frequency and is mediated by transcription (Branco & Pombo, 2006). For example, the clustering of chromosomes 12, 14, and 15, which associate with each other with high frequency in mouse lymphocytes are involved in chromosomal translocations in lymphoma (Parada, Mcqueen, Munson, & Misteli, 2002). Evidence for polymerase-mediated loops between genomic loci on different chromosomes exists in prokaryotes and eukaryotes ranging from yeast to humans (Cook, 2002). Furthermore, depletion of transcription results in less chromosome intermingling and rearrangements

(Branco & Pombo, 2006); indicating that transcription factories are stabilizing the intermingling of transcribed loci at the surface of different CTs. These loci are subject to high double-strand breaks which lead to a relatively high frequency of translocation.

The following section discusses another well-established compartmentalization of chromatin within the nucleus critical to the regulation of gene expression; the active (A) and inactive (B) compartments.

### **Compartments**

Based on simulations, a block copolymer consisting of alternating blocks of monomers of different types with different affinities for each other can form separate spatial compartments by microphase separation (Nuebler et al, 2018). In an analogous way, active (euchromatin) and inactive (heterochromatin) chromatin domains cluster to give rise to the A and B compartments, respectively, in the mammalian genome. Segregation of the two types of chromatin in the nucleus was first observed by electron microscopy and later detected by 4C and Hi-C. Alternating A (active) and B (inactive) compartments give rise to a nice checkboard pattern within each chromosome (Cis) and between chromosomes (Trans) readily visible in Hi-C contact maps (Lieberman-aiden et al., 2009).

It has been proposed that compartmentalization is driven by clustering of loci with similar epigenetic marks once they are in close proximity in 3D, similar



to the microphase separation phenomenon described in the block copolymer (Nuebler et al, 2018) (Lieberman-aiden et al., 2009) (Pieroo, Zhang, Lieberman, Wolynes, & Onuchic, 2016) (Falk et al., 2019) (Erdel & Rippe, 2018) (Jost et al., 2014) (Michieletto, Orlandini, & Marenduzzo, 2016) (Nuebler et al, 2018) (L. Liu, Shi, Thirumalai, & Changbong Hyeon, 2018)(Shin et al., 2018). Based on Hi-C data, the compartment pattern is cell-type specific, suggesting a role in genome function. However, population Hi-C can not entangle if the compartment patterns, emerge based on the average of population signal, or persist at the single-cell level. Recently a very sophisticated imaging method enabled the mapping of the spatial position of numerous genomic regions along individual chromosomes by using multiplexed FISH (Wang et al., 2016a). In this study, 3D tracking was performed for each 100kb loci in the middle of each TAD defined in Hi-C along chromosome 21. The resulting mean spatial distance matrix from 120 copies of chromosome 21 shows a high correlation with the inverse of contact frequency of Hi-C, with a Pearson correlation coefficient of 0.9. Further analysis shows the Hi-C contact frequency was inversely proportional to the fourth power of the mean spatial distance (Wang et al., 2016). Furthermore, the mean spatial distance matrix also recapitulates the A and B compartment signal seen in Hi-C population data. These results were able to answer a very important question about the direct relationship between interaction frequency detected by Hi-C and the spatial distance at the Mb scale. These data also affirm the existence of A and B compartments in single cells, indicating that compartments are functional

clusters that emerge in every single cell for a potent genomic function (Shin et al., 2018) (Wang et al., 2016).

Although initial Hi-C experiments (Lieberman-aiden et al., 2009) showed two types of compartments, the Hi-C checkboard pattern of high-resolution Hi-C reveals a subcompartmentalization of A to two distinct subcompartments and B into three subcompartments. These subcompartments correlate with different epigenetic marks (Rao et al., 2014) and were also validated in recent work by the Belmont group using TSA-seq, a new mapping method that estimates the mean chromosomal distance from a targeted protein (Chen et al., 2018). Belmont and colleagues were able to relate these sub-compartments directly to cytological structures observed by microscopy, such as speckles (mostly A1 domains) located in the nuclear interior and the peripherally located nuclear lamina (B2 and B3), with the remaining Hi-C sub-compartments (A2, B1) located in between (Chen et al., 2018).

Prior to Hi-C, many microscopy studies have shown compartmentalization of different genomic processes that are reflected by clustering of the protein factories necessary for each process throughout the nucleus. This clustering of protein factories suggests that subcompartments can be driven by specific colocalization of genomic loci based on their functional association with appropriate subnuclear structures. For example, active loci localize to transcription factories and splicing factories, while silenced chromatin interacts

with Lamin A and C (Misteli, 2007). Accordingly, transcription factories, also called hot spots of transcription, have been visualized throughout the genome as compartmentalized hubs anchoring transcription factories and polymerase. On average, each transcription hub contains 65,000 copies of the polymerase protein and 10,000 genes (Cook, 2002). One hypothesis for the function of these hubs is that the regulation of multiple constituent genes in each cluster is coordinated by their shared particular transcription factor composition. Surprisingly, *in vivo* imaging has demonstrated that the transcription factories are very dynamic (Gorski & Misteli, 2005), with an average residence time on chromatin in the order of a few seconds (Phair et al., 2004). Another example of clustering that was revealed by microscopy is DNA repair factories. Upon DNA double-strand breakage, a very fast requirement of repair factors leads to the formation of repair foci; which appear as clusters in the nucleus that are even less homogeneously distributed throughout the nucleus compared to transcription clusters (Misteli, 2007). These repair factors remain bound to chromatin until they complete their task at the specific foci (Politi et al., 2005). This principle of compartmentalization can thus provide the right environment for efficient processing of many loci simultaneously and may stabilize the chromatin fiber by anchoring them to the cluster.

Compartmentalization is also observed for other nuclear structures that share clustering of highly dynamic proteins including nuclear bodies, Cajal bodies, PML bodies, and speckles (Gorski & Misteli, 2005). In another study

examining the 3D organization of chromatin in different epigenetic states using super-resolution imaging, the genome was partitioned into three groups. This study classified genomic domains in *Drosophila* cells as transcriptionally active, inactive, or Polycomb-repressed states. The chromatin in the three different chromatin states was found to display a noticeable difference in packing density. Furthermore, distinctly different from the self-similar organization displayed by transcriptionally active and inactive chromatin, the Polycomb-repressed domains are characterized by a high degree of chromatin intermixing within the domain, and spatially exclude neighboring active chromatin to a much stronger degree (Boettiger et al., 2016).

Finally, several recent studies have been conducted to understand how microphase separation plays a role in genome organization inside the nucleus. In one particularly elegant study, the authors demonstrate condensation and clustering of DNA upon Hp1 $\alpha$  binding *in vitro* (Larson et al., 2017). Staining of HP1 $\alpha$  in cells revealed largely clustered puncta for wildtype HP1 $\alpha$  regardless of phosphorylation status, but substantially more diffuse localization for an HP1 $\alpha$  mutant that is defective in dimerization and *in vitro* DNA-driven phase-separation (Larson et al., 2017).

In summary, using 3C-based technologies and different microscopy techniques, compartments have been found to result from preferential interactions between loci with similar chromatin features, which may be explained

by microphase separation. This model is further motivated by the observed partitioning of chromatin into a small number of types based on histone modifications, which may entail different affinities for each other, and affect the recruitment of HP1 $\alpha$  and other proteins (Nuebler et al., 2018).

### **Compartmentalization model**

A model that explains chromatin compartmentalization inside the cell nucleus was recently developed by Leonid Mirny's group (Falk et al., 2019). In this study, they take advantage of the dramatic chromatin reorganization that takes place during rod differentiation from thymocytes in which localization of heterochromatin switches from the periphery to nuclear interior. Immunostaining of SINEs and LINEs combined with FISH for pre-defined A and B loci revealed that in inverted rod nuclei, euchromatin (A) is located at the periphery while heterochromatin (B) is found more toward the center of the nucleus. However, in the Hi-C contact matrix, no clear difference was seen for interaction frequencies genome-wide in rod cells compared to thymocytes. This surprising observation contradicts a prevailing theory that Lamina is the most important driver of compartmentalization in the nucleus. Instead, this study suggests that the nucleus has a mechanism that can compartmentalize heterochromatin and euchromatin in a manner independent of the spatial nuclear location.

Leonid Mirny's group in this study conducted a simulation that satisfies phase separation theory (Flory-Huggins), and in which compartmentalization of

heterochromatin and euchromatin is independent of the spatial nuclear location. They developed an equilibrium polymer model that represents chromosomes as blocks copolymers, similar to other phase separation models of compartmentalization (Flory-Huggins) with three different types of monomers: euchromatin, heterochromatin, and pericentromeric constitutive heterochromatin (which is unmapped by Hi-C but can be traced in microscopy) by modeling eight different chromosomes. Pair-wise attraction parameters were set for all possible chromatin-type interactions (A-A, A-B, B-B, B-C, C-C and A-C) leading to 720 hypothetical permutations. The only permutations that could drive inverted and conventional genome structure in the simulations were heterochromatin interactions in order of strength:  $A-B < A-C < B-B < B-C < C-C$ . When A-A interactions were assigned to have stronger attractions, globules formed in the middle of the nucleus. When C-B heterochromatin interactions were strengthened in the model, mixing between B and C occurred and when B-C was set as very weak C-domains tended to be expelled from the center. Finally, by changing only B-B attraction and keeping the order of strength they indicated above, an optimum fit was found that satisfies all the criteria of the inverted nuclei (Falk et al., 2019). In this case, B-B interactions are similar to B-Lamina interactions because there was no change in the epigenetic marks of loci connected to Lamin in conventional nuclei compared to the centrally located B-B chromatin in the inverted nuclei. A time course of inversion was modeled based on all the criteria, reflecting a smooth inversion similar to what was seen by

microscopy. This study concluded that heterochromatin interactions is what drives all compartmentalization in the genome, while B and lamina attraction controls the global spatial morphology.

### **Topologically associating domain (TAD)**

At the level of subcompartments, the genome is organized in distinct insulated blocks of chromatin with enriched interactions and an average size of 400kb called topologically associating domains (TADs) (Nora et al., 2012) (Jesse R Dixon et al., 2012). Ninety percent of TADs are insulated from the neighboring region by CTCF-enrichment at their boundaries (Nora et al., 2012), which is thought to play a role as an insulator against interactions between loci located in different topological domains. TAD boundary positioning is conserved during differentiation and in different cell types, tissues, and species (Job Dekker & Heard, 2015) although the internal organization of a TAD for a given genomic region in mouse ESCs, NPCs, and primary MEFs revealed some differences (Nora et al., 2012), suggesting that not all aspects of TAD structure are tissue invariant. High-resolution Hi-C shows another feature of some TADs, namely an enrichment of interactions for 50% of TADs between convergent CTCFs at the boundaries that give rise to visible corner peaks (Rao et al., 2014). Because of the prevalence of TADs as robust chromatin domains that display favorable interactions between the loci within them and a strong depletion of interactions between loci located in different domains, numerous studies in recent years were aimed at answering the following questions: Are

TADs functional domains? Can CTCF act alone to insulate TADs at the boundaries? What mechanism is robust enough to build TADs throughout the whole genome after exiting mitosis? Are TADs static or dynamic blocks?

### **TADs in single cells**

In order for a TAD to be a functional unit, it should persist in every single cell. This question could not be answered by Hi-C, since Hi-C contact probability matrices are built from averaging the interactions across a population of cells. A single cell study using Hi-C confirmed that TAD domains exist at the single cell level (Takashi Nagano et al., 2013). Single cell Hi-C performed for 60 cells, revealed domain-like structures with a size range from 100 kb to 1 Mb. Using 1,403 TADs called in population Hi-C for the same cell line, a statistical analysis of the ratio of intra to inter-domain contact at the single-cell level shows a two-fold enrichment of interactions within the domains.

Another single cell study aimed at visualizing TADs used a super-resolution chromatin tracing method that enabled the identification of 3D locale for specific genomic coordinates, similar to the multiplexed FISH technique discussed in an earlier section of this thesis regarding compartments. In order to query TADs, each 1.2 to 2.5 Mb region of interest was partitioned into consecutive 30-kb segments with unique probes. Each probe was then labeled and imaged following a sequential hybridization protocol and spatial distances and overlap between loci were determined (Bintu et al., 2018). The resulting



ensemble matrix which averaged thousands of cells shows a high correlation between the mean spatial distance determined by super-resolution chromatin tracing and interaction frequencies determined by Hi-C, with a Pearson correlation of -0.92 and power-law scaling between Hi-C contact frequencies and spatial distance on the kb scale. This study observed TAD-like domain structure at single cell level, although some of the domain boundaries display cell-cell variation, which could be due to the short residency of CTCF on chromatin which may generate variability from cell-cell at any given moment (Bintu et al., 2018). Accordingly, more frequently observed boundaries correlated with stronger CTCF and cohesin peaks defined in population ChIP data.

The fact that TAD structure persists in single cells supports the proposition that TADs act as functional blocks of chromatin that regulate gene expression. In agreement with this function for TADs, it was shown that gene expression is preferentially correlated for genes within the same TAD versus genes located in neighboring TADs (Nora et al., 2012). Another study using transposable elements to insert reporter genes randomly throughout the genome (Symmons et al., 2014), found that when a series of these reporter genes ended up at the same continuous domain, correlating with TAD, they exhibit very similar tissue-specific expression.

### **TAD boundaries and gene regulation**

Another important question pertains to the role of TAD boundaries in the regulation of gene expression by coordinating the cell-type appropriate communication between genes and their regulatory elements. Enrichment of small deletions in the TAD boundaries at CTCF sites adjacent to the LMO2 proto-oncogene, was detected in T-cell lymphoblastic leukemia patients. Patient cells that harbored these small deletions were found to have a high level of LMO2 expression (Hnisz et al., 2016). To analyze whether loss of the CTCF sites specifically drives the increase in gene expression, a Cas9 mediated deletion at the same regions in the leukemia patients was performed at two different boundaries near LMO2 and TAL1 in nonmalignant cells. In both cases, deletion led to the disruption of insulation between the neighboring TADs, and an increase of 2- and 2.3-fold in the expression of the LMO2 and TAL1 genes, respectively (Hnisz et al., 2016). In another study by Lupianez and co-workers, CRISPR/CAS9 was used to induce deletions and inversions at the TAD boundaries that cover the key loci for limb development in mouse: WNT6, IHH, EPHA4, and PAX3. These CRISPR-dependent rearrangements induced rewiring of gene–enhancer interactions and disruption of insulation domains (TADs). Interestingly, an inversion around a TAD boundary was able to rearrange the proximal TADs and led to abnormal long-range interactions between key genes and enhancers and downstream limb malformation (Visel & Mundlos, 2015). Taken together these data suggest that TADs are functional blocks with

boundaries that control normal long-range interactions between genes and their regulatory elements and inhibit aberrant interactions.

### **Models for TAD formation**

Numerous models have been proposed to explain the physical and molecular mechanisms underlying TAD formation and insulation in the boundaries. One of these models entails TAD formation by preferential interactions between loci with similar epigenetic landscapes, which results in domains wherein all loci possess similar epigenetic marks (Barbieri et al., 2012) (Jost et al., 2014). This mechanism fails to explain TAD formation for two reasons: First, the preferential interaction of loci would lead to an alternating pattern in the Hi-C contact matrix analogous to what is seen for compartments and this is not the case (Job Dekker & Mirny, 2016). Secondly, a model based on preferentially associating loci cannot explain the spreading of interactions across two neighboring TADs after the deletion of a boundary, as described above. Another proposed mechanism for the observed insulation at boundaries is unconstrained supercoiling driving domain-like structures (Benedetti, Dorier, Burnier, & Stasiak, 2014). However, this model is not able to explain the enrichment of interactions between TAD boundaries (Fudenberg et al., 2015).

In order for a model to explain the TAD, it must satisfy several criteria (Job Dekker & Mirny, 2016): 1) efficient establishment of interactions that spread to 1Mb, 2) conserved in different cell lines, with minimal cell to cell variation which

means that boundaries are site-specific, 3) constant insulation at the boundaries by CTCF and other proteins, and 4) accounts for the spreading of interactions between TADs after boundary deletion. A loop extrusion model that satisfies all these principles was proposed by several groups (Alipour & Marko, 2012) (Fudenberg et al., 2015) (Sanborn, Rao, Huang, Durand, & Huntley, 2015) (Bouwman & Laat, 2015) (Nichols & Corces, 2015) and successfully reproduces quantitatively and qualitatively the TADs observed in high resolution *in situ* Hi-C data. Based on polymer simulations of chromatin fibers, a simple loop extrusion motor (cohesin) can form dynamic, growing and dissociating loops (**Fig. 1.2**) (Fudenberg et al., 2015). The key that allows the loop extrusion models to recapitulate the Hi-C TAD-like structure is that extrusion machinery recruited to the chromatin fiber enlarges the loop until it touches another extrusion machine or is halted at the boundary by proteins, such as CTCF or PolII at a TSS (Nuebler et al, 2018). Loop extrusion can only act in cis and for loci that are 120-400kb apart and can not extrude loci at larger 1D distances or on different chromosomes (Nuebler et al, 2018). This emerging model highlights CTCF and cohesin as the most important players for TAD formation, with two distinct roles; cohesin is the motor that extrudes and enlarges the loop to package DNA and CTCF defines the sites of boundaries. At its inception, this loop extrusion model was very hypothetical and was criticized due to the fact that according to cohesin residency time and ATP dependency to function as a motor, it cannot efficiently generate the rapid processivity required to make 100 kb to 1 Mb domains. In

order for this model to be validated (**Fig. 1.2**), it is thus invaluable to determine whether cohesin can indeed act as an efficient motor that satisfies the model. In the next section, I discuss the crucial experimental evidence that cohesin and CTCF are the main players in the formation of TADs by loop extrusion in interphase chromatin.

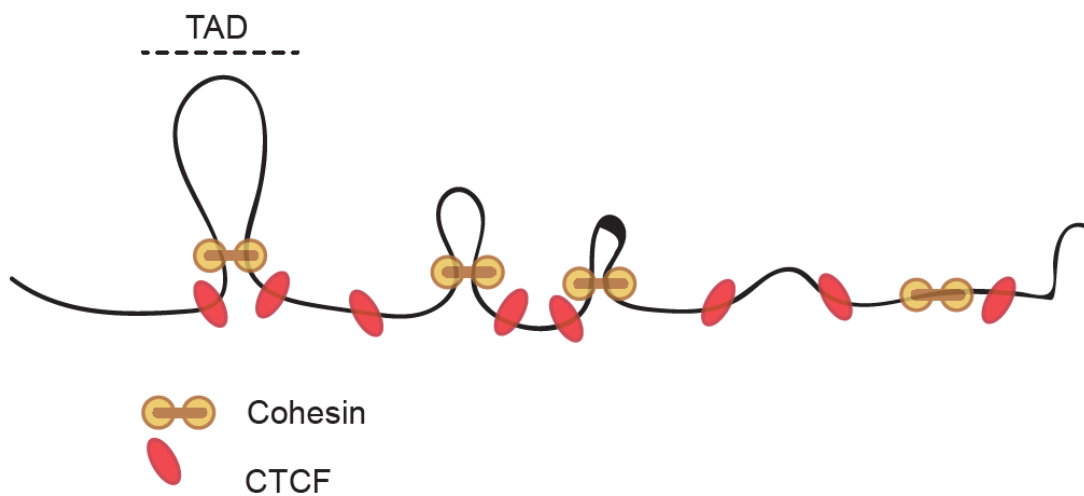


**Figure 1.2 : A simple schematic of loop extrusion**

### **Depletion of TAD building elements**

One of the first studies that depleted CTCF to study its effect on TAD structure used an auxin-inducible degron system in mouse embryonic stem cells. CTCF depletion led to the disappearance of TADs by the loss of insulation at TAD boundaries or a reduction of intra-TAD interactions compared to the level of inter-TAD interactions in Hi-C data. Recovery of CTCF levels could reestablish proper TAD structure on affected chromosomes (Nora et al., 2012). On the other

hand, intra-TAD FISH distances were unaffected by CTCF depletion, indicating that loss of CTCF does not trigger global chromatin reorganization. Finally, gene expression was altered upon CTCF depletion with upregulated genes typically located less than 200 kb from their enhancers across a TAD boundary (Nora et al., 2012). This study supports the notion that CTCF is a powerful and necessary element for insulating TAD boundaries promoting normal long-range interactions within a TAD and preventing undesired long-range interactions between genes and enhancers in neighboring TADs.

In order to deplete chromatin-associated cohesin, the cohesin-loading factor Nipbl was depleted in mouse liver, leading to global reorganization of chromosomal folding. In the Nipbl-depleted background, TADs and CTCF-CTCF peaks dissolve globally and independently of gene expression (Schwarzer et al., 2017). Both CTCF and cohesion depletion dissolve TADs; however, only the loss of chromatin-associated cohesin led to changes in DNA compaction at the level of intra-TAD (Nora et al., 2012)(Schwarzer et al., 2017). These observations suggest that TADs are cohesin-dependent and that CTCF and cohesin have essential and distinct roles in TAD formation. Cohesin is responsible for chromatin condensation, probably by loop extrusion, and CTCF dictates the TAD boundaries by halting cohesin at specific sites (Gassler et al., 2017) (Nuebler et al, 2018).

In contrast to Nipbl, WAPL limits the residence time of cohesin on chromatin by unloading it. Depletion of WAPL results in increased cohesin on chromatin and an increase in the strength and the number of CTCF-CTCF, and the loops accumulate in an axial structure called “vermicelli” (Wutz et al., 2017). In heatmaps of contact probability from Hi-C data, up to three regions of strong interaction frequency can be seen for each CTCF anchor (Haarhuis et al., 2017). Taken together, these results indicate that cohesin loading and unloading is very well balanced by NIPBL and WAPL under normal physiological conditions in order to generate and maintain proper genome structure (Nuebler et al, 2018).

Finally, inspiring work by Terakawa and co-workers examined the biophysical mechanism of condensin translocation along DNA *in vitro* using single-molecule imaging. The results show that condensin is a molecular motor capable of ATP hydrolysis-dependent translocation along double-stranded DNA in a very efficient manner (Terakawa, Bisht, Eeftens, Dekker, & Haering, 2017). Condensin’s translocation activity is rapid and highly processive, with individual complexes traveling an average distance of  $\geq 10$  kilobases at a velocity of  $\sim 60$  base pairs per second (Terakawa et al., 2017). Both condensin and cohesin have SMC proteins, and a distinguishing feature of SMC complexes is their large ring-like configuration that exists in both condensin and cohesin. This similarity suggests that cohesin may act as a motor with the capacity to translocate efficiently and provide an adequate driving force for loop extrusion during interphase.

## **The interplay between TADs and compartments**

The existence of different levels of genome folding, such as several TADs inside one compartment, could imply hierarchical folding of chromatin. Because TADs are the invariant building blocks of chromosomes and in a given cell type consecutive TADs of a similar epigenetic profile cluster in one compartment, it has also been proposed that the larger cell type-specific compartments are formed through a process of self-assembly of these smaller TADs (Job Dekker, 2014) (Gibcus & Dekker, 2013). However, as described in the previous section of this thesis regarding TADs, depletion of CTCF and chromatin-bound cohesin, decreased TAD structure without having a major effect on compartments, suggesting distinct mechanisms for TAD and compartment formation.

Compartments are remarkably resistant to CTCF depletion despite dramatic changes happening at the TAD level, indicating that compartments are established independently of CTCF (Nora et al., 2012). Compartments were not only resistant to chromatin-associated cohesin depletion, but small compartments emerged and the overall strength of compartments increased (Schwarzer et al., 2017). The opposite effect was achieved by increasing the residence time and the number of cohesin molecules on chromatin by deleting WAPL. In this case, TADs were sharper and CTCF-CTCF loops were stronger while compartmentalization weakened relative to the control (Extension et al., 2017). These results suggest that the molecular mechanisms that build TADs and compartments are independent. Furthermore, the cohesin motor is



responsible for attenuating compartmentalization in wildtype cells since CTCF removal did not have any effect in compartments while chromatin-bound cohesin depletion strengthened compartments. Therefore, TADs and compartments do not represent a hierarchy in the folding of mammalian chromosomes (Nuebler et al., 2018).

These depletion experiments offer a resource that can be further investigated by simulation modelling. In one such study by Johannes and colleagues, a polymer model that includes compartmentalization (by microphase separation) was integrated with loop extrusion in order to examine how an active loop extrusion mechanism affects compartmentalization and to determine whether the interplay between the two mechanisms can explain the biological data for cohesin and CTCF depletion. In order to address compartmentalization a copolymer composed of A (euchromatin) and B (heterochromatin) blocks was modelled such that the differential attraction between A and B versus the attraction within like compartments leads to phase separation and reproduces the compartmentalization observed in Hi-C datasets. If the conditions conducive to loop extrusion are removed from the model TADs disappear and compartments, particularly the smaller ones, become more pronounced, in perfect agreement with the cohesin depletion experiments (Schwarzer et al., 2017) (Wutz et al., 2017) (Nuebler et al., 2018). Furthermore, depletion of loop extrusion in this model enhanced compartments of 500 kb to 2 Mb in size but did not affect compartments greater than 2 Mb. The phenomenon of a length-dependent

transition is known from the physics of block copolymers. It occurs when the product of segment length and compartmental interaction parameter exceeds a critical value as described by the Flory-Huggins theory. In this copolymer simulation, adding loop extrusion shifts this phase transition to larger segments of  $\sim 1$  Mb. For example, 800-kb segments are segregated in the absence of loop extrusion but get mostly mixed in its presence. These results suggest that loop extrusion counteracts the innate phase separation of small compartments, and thus only larger-scale compartmentalization is visible in a wildtype mammalian cell (Nuebler et al., 2018). A further investigation using the same copolymer model that combines phase separation and loop extrusion demonstrates that dynamic loop extrusion reflects experimental Hi-C data in terms of the strength for both TADs and compartments compared to static loop with simulation of loop extrusion (loops remain static after their formation by loop extrusion, while the chromatin fiber is subject to thermal motion). These results also suggest that the motor-dependent dynamic loop extrusion mechanism is much faster than phase segregation, given that the chromatin fiber has less time to resegment by microphase separation for small compartments before the passage of cohesin. Finally, changing the volume occupied by the polymer in the simulation, increased compartmentalization but had no effect on TADs (Nuebler et al., 2018).

## **Promoter enhancer interactions**

### **Promoter enhancer interactions within TADs**

In the mammalian genome, only 22% of the active genes form looping interactions with the nearest regulatory element, indicating that genomic proximity is not a good predictor of promoter-enhancer interactions (Amartya Sanyal, Lajoie, Jain, & Dekker, 2012). The long distance separating genes from regulatory elements raised the need for detection of the specific physical pairwise interactions in order to understand the impact of long-range interactions on gene expression. Looping interactions are more common for active genes compared to silent ones (Misteli, 2007). Accordingly, loops detected by 5C in three different cell lines show enrichment for histones with modifications that are characteristic of active functional elements: H3K4me1, H3K4me2, and H3K4me3. Loops are also enriched for H3K9ac and H3K27ac, but significantly depleted for H3K27me3, a mark typically found at inactive or closed chromatin (Amartya Sanyal et al., 2012). Many of the promoters, for example in the case of the HoxD gene, interact with multiple regulatory elements, which results in a complex network of interactions (Andrey et al., 2013).

As we described earlier, TADs are highly conserved but intra-TAD interactions tend to be cell-type specific, possibly reflecting a role in regulated gene-expression (Nora et al., 2012). Direct contact between enhancers and promoters is controlled by the insulation in TAD boundaries such that the majority of promoter-enhancer interactions ( ~ 88%) occur within a TAD (Downen et al., 2014). One well-known example of enhancer-promoter loops is the locus control

region (LCR) regulatory elements and the  $\beta$ -globin gene which interact in erythroid cells (k562) but not in other cell types.

### **Long-range promoter-enhancer interactions**

On the other hand, some promoter-enhancer interactions resist the insulation at the TAD boundary to form giant loops greater than 1 Mb in size (Yashiro-ohtani et al., 2014) (Allahyar et al., 2018)(Dostie et al., 2006). These big loops can be explained by the positioning of promoters and enhancers that are engaged in very long looping interactions relatively near to their TAD boundary and their interaction with a CTCF hub. Interactions between multiple CTCF molecules at boundaries can lead to the formation of rosette-like structures that bring the promoters and enhancers from neighboring TADs in sufficiently close proximity to form a loop (Allahyar et al., 2018).

### **Super-enhancers**

Super-enhancer interaction networks invoke a large level of transcription of their associated genes. A recent study that probed super-enhancer and promoter interactions using ChIA-PET, found that the majority of super-enhancers possess a very unique chromatin feature. A super-enhancer and its associated genes are located within a loop connected by two interacting CTCF sites co-occupied by cohesin and enriched for mediator, which forms a super enhancer insulated domain within a TAD (Downen et al., 2014). This observation supports a previous study, showing that loops mediated by cohesin and CTCF

tend to be larger and more conserved across multiple cell types compared to promoter-enhancer loops associated with cohesin and Mediator (Phillips-cremins et al., 2013). These cell type-specific Mediator/cohesin loops bridge short-range enhancer-promoter interactions within and between larger subdomains in cells where they are expressed (Phillips-cremins et al., 2013). In contrast, the insulated subdomains that contain super-enhancer are persistent in cell types in which their target genes are silenced and enriched for polycomb proteins instead of mediators. The proper association of super-enhancers and their target genes in such “insulated neighborhoods” is of considerable importance, as the mistargeting of a single super-enhancer is sufficient to cause leukemia (Sanders et al., 2014).

### **Interchromosomal enhancer-promoter interactions**

There are many well-known instances of genes that are regulated by interchromosomal interactions. For example, in naive T cells, the  $\gamma$  locus on chromosome 10 and the Th2 interleukin locus on chromosome 11 form a cluster of interchromosomal interactions (Spilianakis, Lalioti, Town, Lee, & Flavell, 2005) (Noordermeer et al., 2011). Similarly, the interaction between super-enhancer LCR elements with the  $\beta$ -globin gene can occur in both cis and trans (Noordermeer et al., 2011), although the trans interactions happen in a very small fraction of cells in a population as chromosomes territories are not homogeneously distributed. In order for specific trans-chromosomal interactions to occur, the two chromosomes containing the promoter and enhancer have to

land near each other in the nucleus. In one example, extrachromosomal loops are induced upon activation of the mouse Hox cluster and the synchrony of this movement with the activation kinetics of the Hox cluster suggests a functional link (Chambeyron & Bickmore, 2004).

One of the most striking interchromosomal interactions between genes and their regulatory elements occurs in mouse olfactory receptors (OR) that are encoded by more than 1,000 olfactory receptor genes (Buck & Axel, 1991). The clustering of more than 1,000 OR genes from 18 chromosomes forms heterochromatin domains in both cis and trans, (Markenscoff-papadimitriou et al., 2014). Interestingly, in each mature olfactory sensory neuron only one single olfactory receptor gene is activated (Lomvardas et al., 2006). The activation of one specific OR occurs within the robust interchromosomal hub of 68 intergenic olfactory receptor enhancer ‘Greek islands’ which are enriched for the specific transcription factor LHX2 and LBD (Markenscoff-papadimitriou et al., 2014). Depletion of transcription factor LHX2 or LDB1 mediator results in a strong reduction of the cis and trans-Greek island interactions and widespread transcriptional downregulation (Alexander et al., 2019). These results indicate a direct role of the cooperative effort between the specific OR transcription factor LHX2 and LDB1 mediator in maintaining long-range interactions to bridge the active gene with its enhancers, and additionally, imply a vital role for long-range cis and trans interactions in regulated gene expression.

### **Biophysical processes that form chromosome conformation**

Major new questions revolve around the molecular and biophysical processes by which different aspects of chromosome conformation form. Significant progress has been made in developing and testing mechanistic models for TAD and loop formation. The model that currently has most experimental support proposes that TADs and CTCF-CTCF loops form via loop extrusion performed by the cohesin complex (Alipour & Marko, 2012)(Fudenberg et al., 2015) (Sanborn et al., 2015) (Bouwman & Laat, 2015) (Nichols & Corces, 2015)(Schwarzer et al., 2017). In this model, loop extrusion proceeds until the complex encounter a CTCF protein bound to a CTCF site in the convergent orientation. As a result, CTCF-CTCF loops form, and interactions between loci located between convergent CTCF sites are generally increased (TADs). The mechanisms of loop extrusion are not known in detail yet, but may involve the cohesin ring encircling strands of DNA at the bases of loops in a topological or pseudo-topological manner (Schwarzer et al., 2017) (Ivanov & Nasmyth, 2005)(Kagey et al., 2010)(Srinivasan et al., 2018).

Also much less in know about the processes that determine nuclear compartmentalization. Mechanisms of compartmentalization are distinct from the formation of TADs and loops, as mutations in CTCF or cohesin disrupt TADs but not compartmentalization per se (P. Nora et al., 2017) (Nuebler et al., 2018) (Haarhuis et al., 2017) (Extension et al., 2017) (Glenn, Hilaire, Casellas, Lander, & Aiden, 2017) (Schwarzer et al., 2017)(Wutz et al., 2017). Compartmentalization

has been proposed to be the result of polymer phase separation driven by attractions between chromatin domains of the same or similar status (Lieberman-aiden et al., 2009) (Pieroo et al., 2016) (Falk et al., 2019) (Erdel & Rippe, 2018) (Jost et al., 2014) (Michieletto et al., 2016) (Nuebler et al., 2018) (L. Liu et al., 2018)(Shin et al., 2018). Polymer models simulating such attractions can reproduce the plaid pattern characteristic of Hi-C interaction maps (Jost et al., 2014) (Michieletto et al., 2016) (Pieroo et al., 2016) (Falk et al., 2019). However, the molecular and biophysical basis of these attractions is unknown. Possibly these attractions result from co-association of domains with sub-nuclear bodies that themselves appear to form by a process of liquid-liquid phase separation (Feric et al., 2016) (Larson et al., 2017) (Marzahn et al., 2016) (Strom & Alexander, 2017). An example is the interactions between heterochromatic loci driven by multivalent interactions among HP1 proteins and between HP1 proteins and H3K9me3-modified chromatin domains (Larson et al., 2017) (Strom & Alexander, 2017).

The formation of spatially segregated heterochromatic and euchromatic domains can be viewed as microphase separation of a polymer composed of different types of monomers (loci). For instance, a “block copolymer” is a polymer that contains a series of alternating blocks (e.g., A-type and B-type, or blocks of euchromatin and heterochromatin), each composed of multiple monomers (A monomers and B monomers (**Fig. 1.3**). When As attract As and Bs attract Bs, such polymer can fold into spatially segregated domains of As and Bs (**Fig. 1.3**)



(Michael Rubinstein & Colby-standard, n.d.) (Leiblerf, 1980) (Matsen & Schick, 1994). A key point is that the A and B blocks of a copolymer cannot macroscopically phase separate because they are connected: copolymers undergo microphase separation, forming microdomains of sizes comparable to the polymer coil size of the individual blocks. Applied to chromatin *in vivo*, microphase separation may underlie the formation of chromatin interaction domains. However, the biophysical forces and interaction dynamics that determine chromosome compartmentalization in cells are not known.

Whether microphase separation of a block copolymer occurs depends on the interaction strengths between monomers as well as the lengths of the blocks of monomers of each type (**Fig. 1.3**). Flory-Huggins polymer theory predicts that spatial segregation will occur when the product of the length of the blocks ( $N$ , the number of monomers that make up blocks) and their effective preferential homotypic interaction strength ( $\chi$ , a parameter that represents the difference in the strength of homotypic interactions as compared to heterotypic (A-B) interactions) is larger than a critical value  $C$  (Leiblerf, 1980) (Matsen & Schick, 1994). Large blocks of a polymer can spatially segregate even when attractive interactions among monomers are weak, while short blocks will only phase separate when interactions are sufficiently strong. Given that in mammals, domains of heterochromatin and euchromatin are typically large (hundreds of kb up to several Mb), spatial segregation can occur even when attractive forces between monomers (loci) are weak. Thus, a wide range of interaction strengths

between loci within A and B compartments could lead to a spatially segregated genome. The corollary is that observation of spatially compartmentalized chromosomes per se, e.g., by Hi-C, does not provide quantitative information about the strength of the interactions that drive this organization. Should quantitative measurements of chromatin interaction strength or stability be available genome-wide, such data would allow deeper molecular understanding of the mechanisms leading to chromosome and nuclear compartmentalization, by relating these measurements to binding of specific factors, association with sub-nuclear structures, and the presence of chromatin modifications and processes such as transcription and replication. In Chapter V we will describe a strategy that allows quantitative measurements of chromatin interaction stability be available genome-wide, we call liquid chromatin Hi-C.

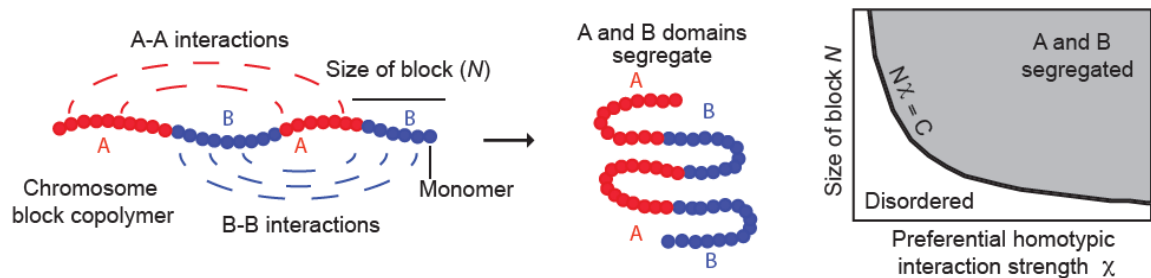


**Figure 1.3: Block copolymer folds into spatially segregated domains**

**A:** Block copolymer composed of a series of alternating A and B blocks, each composed of a number of monomers (left). The polymer can fold into spatially segregated domains of As and Bs (middle). Flory-Huggins polymer theory predicts that spatial segregation will occur when the product of the length of the blocks  $N$  (the number of monomers that make up blocks) and their effective preferential homotypic interaction strength  $\chi$  (difference in the strength of homotypic interactions as compared to heterotypic (A-B) interactions) is larger than a critical value  $C$ .

## **CHAPTER II: Hi-C 2.0: an optimized Hi-C procedure for high-resolution genome-wide mapping of chromosome conformation**

### **PREFACE**

The content of this chapter is a part of the following publication: **Houda Belaghzal**<sup>1</sup>, Job Dekker<sup>1, 2\*</sup>, Johan H. Gibcus<sup>1</sup>. *Methods*. 2017 Jul 1;123:56-65. doi: 10.1016/j.ymeth.2017.04.004. Epub 2017 Apr 18.

### **Abstract**

Chromosome conformation capture-based methods such as Hi-C have become mainstream techniques for the study of the 3D organization of genomes. These methods convert chromatin interactions reflecting topological chromatin structures into digital information (counts of pair-wise interactions). Here, we describe an updated protocol for Hi-C (Hi-C 2.0) that integrates recent improvements into a single protocol for efficient and high-resolution capture of chromatin interactions. This protocol combines chromatin digestion and frequently cutting enzymes to obtain kilobase (Kb) resolution. It also includes steps to reduce random ligation and the generation of uninformative molecules, such as unligated ends, to improve the amount of valid intra-chromosomal read pairs. This protocol allows for obtaining information on conformational structures such as compartment and topologically associating domains, as well as high-resolution conformational features such as DNA loops.

## INTRODUCTION

The spatial organization of chromatin has been a topic of study for many years since chromatin conformation, and long-range associations between genes and distal elements are thought to play important roles in gene expression regulation and other genomic activities. The concept that dense matrices of chromatin interactions could be used to determine the spatial organization of chromatin domains, chromosomes and ultimately entire genomes, was first introduced in the original publication that described the chromosome conformation capture (3C) method (Job Dekker et al., 2002). This concept was then tested by the development of the 3C technology, its application to yeast chromosomes, and analysis of interaction data using polymer models. This led to the first 3D model of a chromosome.

In 3C, chromatin is first fixed with formaldehyde to covalently link spatially proximal loci. This is essential for efficient detection of chromatin interactions, as leaving out cross-linking leads to the dramatic loss of detected contacts and, in our hands, inability to detect chromatin conformation beyond a few Kb. Chromatin is then fragmented with a nuclease and ends are re-ligated. This leads to unique ligation products between spatially proximal loci that can then be detected by PCR, ligation-mediated amplification, or direct sequencing.

The concept of using matrices of contact frequencies to infer chromatin folding, and its proof-of-principle in yeast (J Dekker et al., 2002) has led to many new studies and the development of a range of 3C-based assays with increased

throughput including 4C (Simonis et al., 2006; Z. Zhao et al., 2006), 5C (Ferrauiolo, Sanyal, Naumova, Dekker, & Dostie, 2012; Smith, Lajoie, Jain, & Dekker, 2016) and ChIA-PET (M J Fullwood, Han, Wei, Ruan, & Ruan, 2010). Hi-C was introduced in 2009 (Lieberman-Aiden et al., 2009) as a genome-wide version of 3C (J Dekker et al., 2002). The incorporation of biotinylated nucleotides at the digested DNA ends prior to ligation allowed for the specific capture of digested and subsequently ligated chimeric molecules using streptavidin-coated beads. These chimeric molecules are then directly sequenced, e.g. on an Illumina platform. Since its introduction, the technique has gone through several stages of optimization. We have previously presented a base protocol that used incorporation of biotinylated dCTP in an overhang generated by HindIII digestion (Belton et al., 2012).

Here we describe Hi-C 2.0, a further optimized Hi-C protocol that integrates several recent technical improvements in one single protocol. One adaptation to the base protocol is the removal of a SDS solubilization step after digestion to better preserve nuclear structure . This prevents random ligation between released chromatin fragments by ligation *in situ*, i.e. in intact nuclei (Takashi Nagano, Várnai, et al., 2015). This adaptation was first introduced for 4C (Splinter, de Wit, van de Werken, Klous, & de Laat, 2012) and has since been used for single cell Hi-C (T Nagano et al., 2013; Takashi Nagano, Lubling, et al., 2015) and more recently for Hi-C ( Rao et al., 2014). A second adaptation in recently developed protocols increases the resolution of Hi-C through the use of

restriction enzymes that digest more frequently, such as Mbol and DpnII, or nucleases such as DNaseI and Micrococcal nuclease (T.-H. S. Hsieh, Fudenberg, Goloborodko, & Rando, 2016; T. H. Hsieh et al., 2015; Ma et al., 2014; Rao et al., 2014). Thirdly, experimental steps can be included to reduce the number of uninformative sequences such as unligated (“dangling”) ends. This is important because even though many topological structures, including compartments and topologically associating domains (TADs) can effectively be resolved by binning 100 million valid pair reads at 100 kb and 40 kb resolution respectively (Bernardi, 2015; J R Dixon et al., 2012; Nora et al., 2012; Valton & Dekker, 2016), detection of point-to-point looping interactions, e.g. between promoters and enhancers or between pairs of CTCF sites typically require >1 billion valid pairs ( Rao et al., 2014). Therefore, steps to increase the fraction of informative intra-chromosomal reads will help reduce cost by increasing the relative quantity of valid pairs. Removing dangling ends is also important because a sub-population of dangling ends can appear as valid interactions between adjacent restriction fragments. As we describe below, this subgroup can be as large as ~10% of reads, and can represent a large fraction of interactions detected over short distances. This in turn can influence subsequent data analysis (section 3.1).

Alternative approaches to determine chromatin interactions for specific regions of interest in a more cost-effective way include targeted approaches such as 4C (Simonis et al., 2006; Z. Zhao et al., 2006), 5C (Ferraiuolo et al., 2012; Smith et

al., 2016), capture Hi-C (Mifsud, Tavares-Cadete, et al., 2015) and Capture C (M J Fullwood et al., 2009; Hughes et al., 2014).

Here we describe Hi-C 2.0 which uses the DpnII restriction enzyme, *in situ* ligation, and efficient unligated ends removal. A detailed step-by-step protocol is provided In method section.

## **MATERIALS AND METHODS**

### **Hi-C 2.0**

Hi-C was performed as described {Belaghzal, 2017 #1369} with some modifications in the crosslinking and lysis step as described below.

**Crosslinking:** isolated, undigested, and pre-digested (with liquified chromatin) nuclei were not pelleted after the pre-digestion step above but were crosslinked immediately as follows: for each sample 1,250  $\mu$ L volume of nuclei in the digestion buffer was transferred to a 21.875 mL mix [625  $\mu$ L of 37% formaldehyde + 21.25 mL of HBSS]. For intact cells: 5 million K562 cells or nuclei were washed twice with 15 mL of HBSS and pelleted at 300 g for 10 min, then resuspended in 2.5 mL of HBSS. The sample was transferred to 20.625 mL crosslinking mix [625  $\mu$ L of 37% formaldehyde + 20 mL of HBSS]. All samples were incubated at RT for 10 min on a rocking platform. Next, to stop cross-linking 1.25 mL of 2.5 M glycine was added to each sample and the mix was incubated

at RT for 5 min on a rocking platform. To pellet the crosslinked cells/nuclei, the sample was centrifuged at 1,000 g for 10 min at 4°C. The supernatant was discarded and the pellet was washed twice with HBSS before going to the next step or storing samples at -80°C.

**Cells lysis:** This step is not needed for isolated, undigested, and pre-digested (with liquified chromatin) nuclei. For Hi-C with intact cells: the 5 million crosslinked cells were lysed by adding 1 mL cold lysis buffer [10 mM Tris-HCl (pH=8.0), 10 mM NaCl, 0.2% Igepal CA-630 (NP40)] and 10 µL of 100X Protease inhibitors. The sample was incubated on ice for 15 min to let the cells swell. The cells were lysed on ice using a dounce homogenizer with pestle A (KIMBLE Kontes 885300-0002) by moving the pestle slowly up and down 30 times and incubating on ice for 1 min followed by another 30 strokes. The sample was transferred to a new 1.5 mL microcentrifuge tube, and the sample was centrifuged at 5,000 g at RT for 5 min.

**Digestion:** from each sample (isolated undigested, and pre-digested (with liquified chromatin) nuclei and lysed cells) the pellet was resuspended in 500 µL of ice-cold 1X NEBuffer 3.1, and pelleted for 5 min at 4,000 g. The pellet was washed twice using 500 µL of ice-cold 1X NEBuffer 3.1. After the last wash, the pellet was resuspended in 350 µL 1X NEBuffer 3.1, and 8 µL was taken and kept at 4°C to assess the DNA integrity later. 38 µL of 1% SDS was added to 342 µL (380 µL total volume), and the mixture was resuspended and incubated for 10 min at 65°C. The tube was placed on ice immediately afterward. Next 43 µL of



10% Triton X-100 was added and the sample was mixed gently by pipetting. The tubes were placed at room temperature and 12  $\mu$ L of 10X NEBuffer 3.1 was added. Then 400 U of DpnII (R0543L) was added and mixed gently before an overnight incubation at 37°C on a Thermomixer (with 900 rpm for 30 sec every 4 min).

**Biotin Fill-in:** After overnight digestion, the sample was incubated at 65°C for 20 min in order to inactivate the restriction enzyme. Then, 10  $\mu$ L of the digested sample was taken and kept at 4°C to assess the digestion efficiency later. DNA ends were marked with biotin-14-dATP by adding 60  $\mu$ L of biotin fill-in master mix [1XNEB 3.1, 0.25 mM dCTP, 0.25 mM dGTP, 0.25 mM dTTP, 0.25 mM biotin-dATP (ThermoFisher#19524016), 50U Klenow polymerase Polymerase I (NEB M0210L)]. Next, the sample was incubated for 4 h at 23°C on a thermocycler (with 900 rpm for 30 sec every 4 min). Finally, the sample was placed on ice immediately for 15 min before proceeding to the next step.

**Ligation:** After fill-in, the total sample volume was ~535  $\mu$ L. Ligation was performed by adding 665  $\mu$ L of ligation mix [240  $\mu$ L of 5x ligation buffer (1.8X) (Invitrogen), 120  $\mu$ L 10% Triton X-100, 12  $\mu$ L of 10 mg/mL BSA, 50  $\mu$ L T4 DNA ligase (Invitrogen 15224090), and 243  $\mu$ L ultrapure distilled water (Invitrogen)], to make a total volume of 1,200  $\mu$ L. The reaction was then incubated at 16°C for 4 hours in a Thermomixer with interval shake.

**Reverse Crosslinking:** 50  $\mu$ L of 10 mg/mL proteinase K (Fisher BP1750I-400) was added after ligation, the sample was incubated at 65°C for 4 hr followed

by a second addition of 50  $\mu$ L 10 mg/mL Proteinase K and overnight incubation 65°C

**DNA purification:** Reactions were cooled to room temperature and the 1.3 mL total volume was transferred to a 15 mL tube. The DNA was extracted by adding an equal volume of 1.3 mL of saturated phenol pH 8.0: chloroform (1:1) (Fisher BP1750I-400) and vortexing for 1 min. Then the total volume of 2.6 mL was transferred to a 15 ml phase-lock tube (Quiagen #129065) and tubes were centrifuged at 5,000 g for 10 min. The upper phase was transferred to a 15 mL tube to start the second extraction. An equal volume of 1.3 mL saturated phenol pH8.0: chloroform (1:1) was added and the sample was vortexed for 1 min. Then the mix was transferred to 15 ml phase-lock tube (Quiagen #129065) followed by spinning tubes at 5,000 g for 10 min. The upper phase of ~1.3 mL was transferred to a 15 mL tube (high speed) to precipitate the DNA. 1/10 volume (130  $\mu$ L) of 3 M sodium acetate pH 5.2 was added and the sample was briefly vortexed. Then, 2.5 volumes of ice-cold 100% ethanol 3.25 mL was added, the tube was inverted slowly several times and then incubated at -80° C for 1hr. Next, the DNA was pelleted at 16,000 g for 30 min at 4°C. The supernatant was discarded and the pellet was dissolved in 500  $\mu$ L 1X TLE and transferred to a 0.5 mL AMICON Ultra Centrifuge filter (UFC5030BK EMD Millipore). The column was spun for 5 min at 14,000 g and the flow-through was discarded. The column was washed 4 times using 450  $\mu$ L of 1X TLE for desalting of DNA. After the final wash the DNA remaining in the column (~50  $\mu$ L) was eluted in 52  $\mu$ L of 1XTLE.

The column flipped upside down into a new tube to collect DNA and spun for 3 min at 4,000 g, the volume was adjusted to 102  $\mu$ L. RNA was degraded by adding 1  $\mu$ L of 10 mg/mL RNAase A and incubation for 30 min at 37°C. To quantify the DNA concentration, 2  $\mu$ L of the final DNA sample along with the first 8  $\mu$ L sample taken before digestion, the 10  $\mu$ L sample taken after digestion, and various amounts of the 1 kb ladder (NEB#N3232s) were run on 1% Agarose gel.

**Removal of Biotin from unligated ends:** To remove biotinylated nucleotides at DNA ends that did not ligate, the Hi-C sample was treated with T4 DNA polymerase. For each Hi-C sample, we assembled the following reaction: [up to 5  $\mu$ g of Hi-C library, 5  $\mu$ L 10x NEBuffer 3.1, 0.025 mM dATP, 0.025 mM dGTP and 15 U T4 DNA polymerase (NEB # M0203L). The samples were brought up to 50  $\mu$ L total volume adding ultrapure distilled water. Reactions were incubated at 20°C for 4 hours, the enzyme was then inactivated by incubation of the reaction for 20 mins at 75°C and placed at 4°C. Next, the samples were pooled and the volume was brought up to 130  $\mu$ L 1XTLE in preparation for sonication.

**Sonication:** the DNA was sheared to a size of 100-300 bp using a Covaris instrument [Duty cycle 10%, Intensity 5, Cycles per Burst 200, set Mode Frequency sweeping, continuous degassing, process time 60 sec, Number of cycles] for 3 cycles. The volume was brought up to 500  $\mu$ L using TLE for Ampure fractionation.

**Size fractionation using AMPure XP:** 500  $\mu$ L AMPure beads (Beckman Coulter A63881) were added to a 1.5 mL tube labeled as 1.1X. Then the tube was placed

on the Magnetic Particle Separator (MPS) for 5 min, and the supernatant was removed. Beads were resuspended in 150  $\mu$ L AMPure mixture in order to make the 1.1X solution. 400  $\mu$ L of AMPure mixture was added to 500  $\mu$ L of sonicated DNA from the previous step and the tube was labeled 0.8X. The sample was vortexed and spun down briefly followed by incubation at RT for 10 min on a rotating platform. Then the tube was placed on the MPS for 5 min at RT. The supernatants were collected and added to the 1.1X tube, the tube was briefly vortexed and spun down followed by incubation at RT for 10 min on a rotating platform. Then the tube was placed on the MPS for 5 min at RT. The supernatant was discarded and the beads in 0.8X and 1.1X tubes were washed twice with 1 mL 70% ethanol. Beads were reclaimed by the MPS for 5 min. Beads were then air-dried on the MPS until ethanol had evaporated completely. Next, 51  $\mu$ L of 1XTLE was added to the 0.8X and 1.1X tubes to resuspend the DNA from the beads. Tubes were incubated at RT on a rotating platform for 10 min. Then the tubes with AMPure beads from both 0.8X and 1.1X tubes were placed on the MPS for 5 min. Finally, the supernatants were transferred to 1.7 mL tubes labeled 0.8X and 1.1X. Our sample with DNA that ranges from 100-300 bp is in the 1.1X sample, the 0.8X sample was kept in case more DNA was needed. DNA from both samples 0.8X and 1.1X were quantified by running 1  $\mu$ L on a 2% agarose gel along with different amounts of low molecular weight DNA ladder (100 ng, 200 ng, 400 ng).

**End Repair:** 50  $\mu$ L of Hi-C sample was transferred to a PCR tube, then 20  $\mu$ L of the end-repair mix [3.5X NEB ligation buffer (NEB B0202S), 17.5 mM dNTP mix, 7.5 U T4 DNA polymerase (NEBM0203L), 25 U T4 polynucleotide kinase (NEB M0201S), 2.5 U Klenow polymerase Polymerase I (NEB M0210L)] was added. The 70  $\mu$ L total volume reaction was then incubated at 37°C for 30 min, followed by incubation at 65°C for 20 min to inactivate Klenow polymerase, and then the sample was put at 4°C. The volume was brought up to 400  $\mu$ L using 1X TLE for the next step.

**Biotin pull-down:** All the following steps were performed with 1.5 mL loBind tubes (Eppendorf 22431021). 15  $\mu$ L of MyOne streptavidin C1 beads mix (Thermo Fisher 65001) was transferred to a 1.5 mL tube. The beads were washed twice by adding 400  $\mu$ L of TWB [5 mM Tris-HCl pH8.0, 0.5 mM EDTA, 1 M NaCl, 0.05% Tween20] followed by incubation for 3 min at RT. The tube was then placed on an MPS for 1 min and the supernatant was removed. After the washes, the beads were resuspended in 400  $\mu$ L of 2X Binding Buffer (BB) [10 mM Tris-HCl pH8, 1 mM EDTA, 2 M NaCl] and mixed with the 400  $\mu$ L DNA from the previous step in a new 1.5 mL tube. The mixture was incubated for 15 min at RT with rotation, the tube was then placed on the MPS for 1 min and the supernatant was removed. The DNA bound to the beads was washed by adding 400  $\mu$ L of 1X BB and transferred to a new tube. The beads were reclaimed against the MPS for 1 min, and the supernatant was discarded. The second wash used 100  $\mu$ L of 1X TLE, beads were reclaimed against MPS for 1 min, and

the supernatant was discarded. Finally, the DNA bound to the beads was eluted in 32  $\mu$ L of 1X TLE.

**A-tailing:** A dATP was added to the 3' ends by adding 18  $\mu$ L of A-tailing mix [5  $\mu$ L NEB buffer 3.1, 10  $\mu$ L of 1 mM dATP, 3 U Klenow exo (NEB M0212S)] to the 32  $\mu$ L of DNA sample from the previous step. The reaction was incubated in a PCR machine [at 37°C for 30 min, then at 65°C for 20 min, followed by cool down to 4°C]. Next, the tube was placed on ice immediately. The sample was transferred to a 1.5 mL loBind tube, the tube was placed on the MPS for 1 min and the supernatant was removed. The streptavidin beads bound to DNA were washed twice using 100  $\mu$ L 1X T4 DNA Ligase Buffer (Invitrogen). Finally, streptavidin beads bound to DNA were resuspended in 40  $\mu$ L 1X T4 DNA Ligase buffer (Invitrogen).

**Illumina adapter ligation and paired-end PCR:** For this step, the TruSeq DNA LT kit Set A (REF#15041757) was used. 10  $\mu$ L of ligation mix [5  $\mu$ L Illumina paired-end adapters, 3  $\mu$ L T4 DNA ligase Invitrogen, 2  $\mu$ L 5x T4 DNA ligase buffer (Invitrogen 5X)] was added to the 40  $\mu$ L Hi-C sample from the previous step. The ligation sample was then incubated at RT for 2 hours on a rotator. The sample was transferred to a 1.5 mL loBind tube, the tube was placed on the MPS for 1 min and the supernatant was removed. The streptavidin beads bound to DNA were washed twice with 400  $\mu$ L of TWB, then twice using 100  $\mu$ L 1X TLE. Finally, the sample was resuspended in 20  $\mu$ L of 1XTLE.

**Illumina Truseq Kit for PCR:** We performed three trial PCR reactions as follows [2.5  $\mu$ L DNA bound to beads, 2  $\mu$ L of Primers mix (TruSeq DNA LT kit Set A 15041757)), 10  $\mu$ L Master Mix (TruSeq DNA LT kit Set A 15041757), 10.5  $\mu$ L of ultrapure distilled water (Invitrogen)]. We split the 25  $\mu$ L over three PCR tubes (5  $\mu$ L, 5  $\mu$ L, 15  $\mu$ L per tube). Each of the three samples was then amplified with different numbers of PCR cycles (6, 8, 10 respectively) to assess the Hi-C library quality: [30 sec at 98°C, n cycles of (30 sec at 98°C, 30 sec at 65°C, 30 sec at 72°C), 5 min at 72°C, hold at 10°C]. 10  $\mu$ L was taken from the 15  $\mu$ L sample (with 10 PCR cycles), the 10  $\mu$ L sample was then digested with ClaI for 1 h by adding 10  $\mu$ L of digestion mix [1.5  $\mu$ L 10x NEB Cutsmart buffer, 1.5  $\mu$ L ClaI (NEB R0197S ), 7  $\mu$ L ultrapure distilled water]. The 5  $\mu$ L of each PCR cycle sample along with the 20  $\mu$ L digested sample, and titration of the low molecular ladder (100 ng, 200 ng, 400 ng) (NEB) were run on a 2% Agarose gel. After digestion with ClaI, a downward shift of the amplified DNA to smaller sizes is expected, which indicates DNA ends were correctly filled in and ligated (creating a ClaI site). The number of PCR cycles to generate the final Hi-C material for deep sequencing was chosen based the minimum number of PCR cycles in the PCR titration that was needed to obtain sufficient amounts of DNA for sequencing using the remaining 17.5  $\mu$ L Hi-C

## RESULTS

### CELL CULTURE & CROSSLINKING CELLS USING FORMALDEHYDE

The objective to increase the resolution of Hi-C requires a robust and efficient capturing of spatial DNA interactions, such as between enhancers and promoters. Digesting the genome into more and smaller pieces of DNA increases both the resolution and the complexity of a Hi-C library. To fully capture individual interactions within this complex library of pair-wise interactions, it is helpful to start with a large amount of cells. As such, even very infrequent interactions can still be captured, but in a statistically significant manner. In our Hi-C protocol, we start with 5 Million cells to ensure the generation of complex libraries. This improvement from 25 Million cells in our previous protocol, has successfully been implemented after adapting to *in situ* Hi-C ( Rao et al., 2014). Using a further adaptation to the protocol described here, we have successfully generated libraries with as little as 500,000 cells of starting material. However, the reduced amount of genome copies made these libraries less complex.

We use a final 1% concentration of formaldehyde to crosslink DNA-DNA interactions that are bridged by proteins (**Fig. 2.1A**). Serum can affect the cross-linking efficiency because it is very rich in proteins and it will compete for formaldehyde. Therefore we replace serum containing medium with serum free medium before fixation. Although formaldehyde-based cross-linking biases have been proposed (Gavrilov, Razin, & Cavalli, 2015), our current fixation protocol has been the standard for immunoprecipitation and has remained unaltered from previous Hi-C or 3C based protocols (Belton et al., 2012; J Dekker et al., 2002).



Further, any such biases can be removed using several normalization strategies (section 3.1.2).

We distinguish between adherent and suspension cells in order to fix them in their normal growth conditions. Adherent cells are washed once with the relevant serum-free medium before fixation. Fixation occurs by incubation in formaldehyde containing medium without detaching cells from their growth surface. For suspension cells we replace the wash medium with medium containing formaldehyde after centrifugation.

For both cell types, the formaldehyde is quenched with glycine to terminate the crosslinking. Cells are washed with PBS and pelleted cells can be snap-frozen with dry ice or liquid nitrogen. These cells can be stored at  $-80^{\circ}\text{C}$  for up to a year before continuing Hi-C.

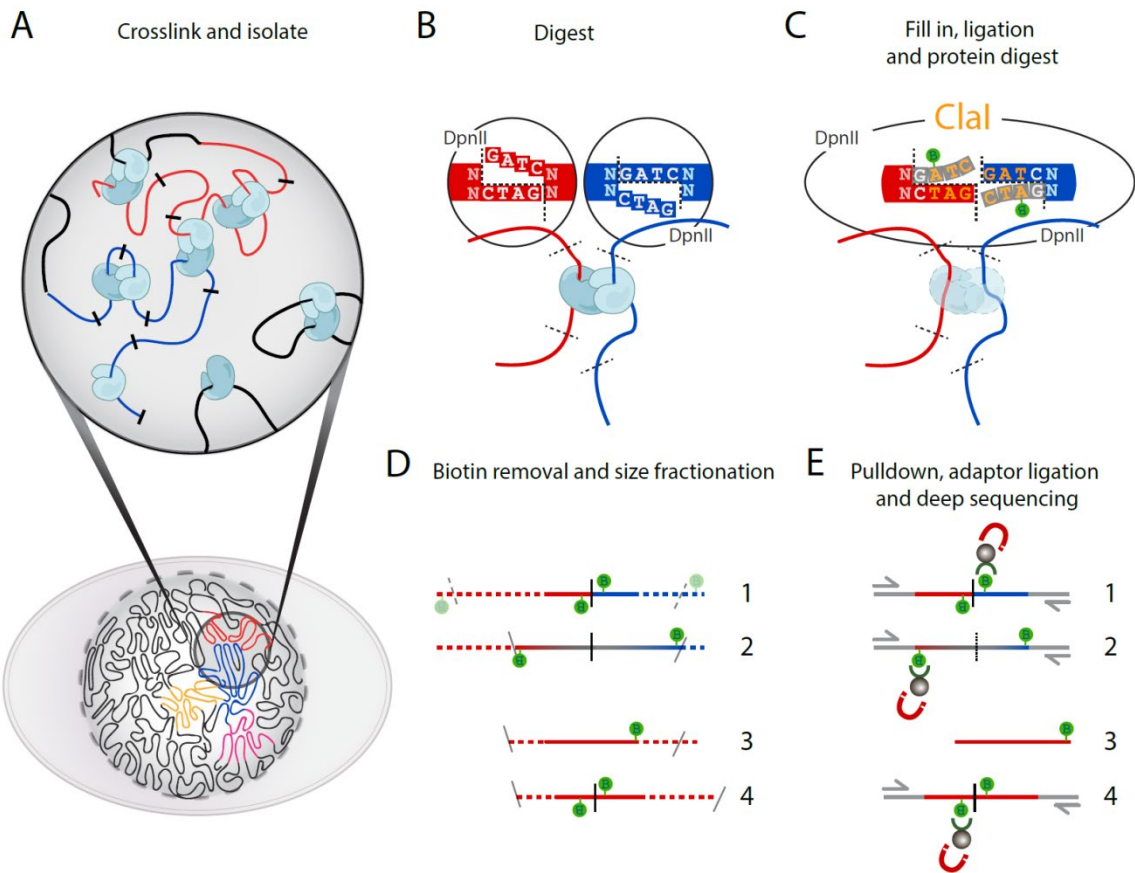


**Figure 0.1.1 : Overview of the Hi-C method**

**(A)** Cells fixed with formaldehyde contain protein-mediated DNA-DNA interactions. **(B)** DNA digestion with DpnII, recognizing GATC, generates a 5'-GATC overhang. **(C)** Filling in of the 5' overhang with dNTPs and biotin-14-dATP blunts the overhang. Ligation of the blunted ends creates a new restriction site (ClaI), which can be used to assess fill-in efficiency. After ligation, crosslinks are reversed to remove proteins from DNA. **(D)** Removal of Biotin (green lollipops) from un-ligated ends. DNA is fragmented to 200-300bp DNA fragments to enable paired-end sequencing. Numbers 1-4 indicate the different ligation products observed: 1: valid interaction; 2: partial digest; 3: dangling end; 4: self-circle. Size fractionation results in fragment size reduction, indicated by dotted lines **(E)** Enrichment of ligation junctions by using the high affinity of streptavidin-coated beads for the incorporated biotin allows for ligation product enrichment prior to adaptor ligation. Numbering of fragment types is as in **(D)**.

### **Cell lysis and chromatin digestion**

We perform Hi-C on lysed cross-linked cells. We use a douncer to lyse the cells in cold hypotonic buffer that is supplemented with protease inhibitors to maintain Protein-DNA complexes. After two rounds of douncing we pellet the material and wash twice with a cold buffer that we will use during digestion. At this point an aliquot of ~ 5% volume can be taken to check the integrity of DNA on an agarose gel.

Before digestion, we incubate the lysed cells in 0.1% of SDS to eliminate proteins that are not cross-linked to DNA, and open the chromatin for a better and more homogenous digestion. The reaction is terminated by addition of triton X-100 to a 1% final concentration. Now the DNA is accessible for digestion by an endonuclease of choice (**Fig. 2.1B**). The restriction fragment size poses a hard limit to the maximum resolution for 3C-based methods. We previously described the use of HindIII, which has an average fragment length of ~4kb. Previous high resolution Hi-C libraries have used Mbol or DpnII ( Rao et al., 2014) to fragment DNA with restriction endonucleases to an average length of ~500 bp. Alternative ways of digestion include alternative enzymes, the use of micrococcal nuclease, which digests in between nucleosomes (T. H. Hsieh et al., 2015), and random breakage by sonication. Here an endonuclease is used that leaves a 5'overhang, which allows marking the sites of digestion with a biotinylated deoxyribonucleotide during overhang fill-in.

Both DpnII and MboI recognize and digest GATC, and leave a 5'-GATC overhang. We prefer the use of DpnII for eukaryotes, because unlike MboI it is insensitive to CpG methylation. The GATC sequence is frequently found genome-wide and should theoretically result in a median digestion into ~256 base pairs fragments for the  $3 \times 10^9$  base pair (bp) human genome. To ensure maximal digestion, chromatin is incubated with DpnII overnight in a thermocycler with interval agitation. After digestion DNA forms a smear of 400-3000 bp on agarose gel (**Fig. 2.2A**). Digestion is terminated by heat inactivation of the restriction enzyme at 65°C for 20 minutes.

#### ***Marking of DNA ends with biotin***

DNA digestion generates a 5'overhang that is then filled in with deoxyribonucleotides. By strategically replacing one of the deoxyribonucleotides with a biotin-conjugated variant, we can mark the site of digestion and enable enrichment for those sites in a later step. It is this specific fill-in that separates Hi-C from other chromosome conformation capture based methods. For DpnII, we incorporate biotin-14-dATP (**Fig. 2.1C**). Although the incorporation of biotinylated dCTP is theoretically possible, we have found that this incorporation of a biotinylated nucleotide at the end the overhang leads to less efficient ligation (below).

Klenow fragment of DNA polymerase I is used to fill in the 5' overhang for 4 hours at 23°C. This low temperature is crucial for efficient incorporation of the

large biotinylated dATP and decreases 3'→ 5'exonuclease activity. Not all overhangs will be filled to completion; therefore, not all digested fragments can be properly ligated. In a later step, after DNA purification, unligated biotinylated ends are removed in a “dangling end removal” step to enrich for proper ligations.

### ***In situ Ligation of proximal ends***

Before starting ligation a 10 µl aliquot is taken that will be used to assess digestion efficiency on an agarose gel (**Fig. 2.2A**, middle lane panel2). The size of the digested DNA is then compared to DNA that was kept aside after lysis before digestion and the DNA that is to be isolated from our ligated Hi-C library. While previous protocols used SDS to inactivate the restriction enzyme prior to ligation, here we use an “*in situ*” ligation protocol (T Nagano et al., 2013; Takashi Nagano, Várnai, et al., 2015; Rao et al., 2014; Splinter et al., 2012), which leaves out this step and inactivates the restriction enzyme by heat. Leaving out this SDS step has previously been shown to better preserve nuclear structure and reduces random ligation (Takashi Nagano, Várnai, et al., 2015). Chromatin is then ligated for 4 hours at 16°C, which is efficient for most of Hi-C libraries. However, in some cases increasing the ligation time to improve the ligation efficiency may be needed. Note that prolonged ligation may increase random ligation. Ligation of the 2 blunted ends creates a new restriction site that can be used to assess the ligation efficacy (**Fig. 2.1C**).

This blunt end ligation can lead to specific chimeric ligation products between ends that were in close spatial proximity. However, this process can also generate circularized ligation products of single restriction fragments. These are not informative and are not considered valid pairs (**Fig. 2.3B-3**).

### ***Reversal of crosslinking and DNA purification***

Now that interacting loci are ligated into chimeric pieces of DNA, proteins that hold interacting fragments in close proximity can be removed. This is achieved by thermal reversion of cross-links and incubation with proteinase-K.

After proteinase K treatment DNA is isolated using 2 steps of phenol:chloroform (pH=7.9) and DNA is precipitated using a standard sodium acetate plus ethanol protocol. An Amicon column is used to wash pelleted DNA with low EDTA, tris-buffered water (TLE) to remove any excess of salt.

### ***Quality Control of Hi-C ligation products***

During the procedure described above, small aliquots were taken after three key steps in the protocol: lysis, digestion and ligation. DNA isolated from these aliquots can be run on an agarose gel to ascertain the intactness of the DNA prior to digestion, the extent of digestion and efficiency of subsequent ligation. The undigested genomic DNA typically runs as a tight band of over 20 Kb in size (**Fig. 2.2A-1**). After digestion, the DNA runs as a smear with a size range specific for the applied restriction enzyme (**Fig. 2.2A-2**). Both of these controls allow for a comparison with the actual library of DNA containing the

chimeric ligated ends. These ligated chimeras should have a higher molecular weight than the digestion control and are most likely smaller in size than the undigested control. For DpnII digestion we usually obtain sizes ranging between 3Kb and 10kb (**Fig. 2.2A-2**).

A second quality control involves quantification of the level of fill-in of overhangs prior to ligation. This is done by PCR amplification of a specific ligation product with primer pairs that were designed for 2 nearby digestion sites (e.g. adjacent restriction fragments) followed by digestion of the PCR product with a restriction enzyme that only cuts at the ligation junction when fill-in has occurred prior to ligation.

Specifically, PCR reactions are set up to detect head-to-head ligation products (**Fig. 2.2B-C**). Primers are designed near neighboring restriction sites that have a high likelihood of being in close spatial proximity, which can only generate PCR products when properly ligated chimeras are present (**Fig. 2.2B**). For some endonucleases, including HindIII and DpnII, ligation of the 2 blunt ends generates a new digestion site that can be used to quantify the ligation and fill-in efficiency (NheI for HindIII and ClaI in the case of DpnII) (**Fig. 2.1C, .2B**). After PCR amplification of a specific ligation product, the PCR product is digested with the enzyme that recognizes this newly generated ligation product. Typically the majority of the PCR product is cleaved indicating efficient fill-in (**Fig. 2.2B**).

### ***Removal of Biotin from un-ligated ends***

We have found that in most Hi-C experiments some digested sites will have remained unligated. For example, if the fill-in of some overhangs was incomplete, ligation to a proximal fragment will not occur and the overall ligation will not be 100% efficient. Such cases result in biotinylated but unligated ends. We prefer to remove these “dangling” ends from the Hi-C library, because they would make sequencing less efficient by generating uninformative reads (**Fig. 2.1D**). Some of these uninformative reads can be readily recognized computationally as both reads will map to a single restriction fragment, and can be easily removed from the dataset (**Fig. 2.3C**). However, given that digestion in Hi-C is not complete, sequencing of unligated but biotinylated partial digestion products can yield read pairs that map to different restriction fragments and appear as valid interactions. This can be a relatively large number of reads in a given library (below). These apparent valid interactions will be interactions between adjacent restriction fragments, and thus will contaminate very short-range interactions, and lead to over-estimation of the number of intra-chromosomal interactions in general. Experimentally removing these dangling ends of partial digestion products is therefore important.

Our biotin removal step uses T4 DNA polymerase and a low concentration of dNTPs to favor the 3' to 5' exonuclease activity over its 5' to 3' polymerase activity. By only providing dATP and dGTP, which are complementary to the inside of the 5' overhang, the polymerase will not be able to complete re-filling the overhang after removing filled in bases. Dangling end removal reduces the



level of unligated molecules (dangling ends at single, fully digested, fragments) in the Hi-C library to as low as 0.1-1.5% of read pairs. The in situ Hi-C protocol [13] also produces low amounts of such dangling ends (here 0.2-2.5%) (**Fig. 2.4A**), but we note that this frequency can be more variable between experiments (**Fig. 2.4A**).

### ***Sonication***

In order to sequence both ends of ligation products, DNA is sonicated to reduce their size to 200-300 bp in preparation for paired-end sequencing. We prefer to use a Covaris sonicator because its reproducibility in generating a tight range of DNA fragments. For sequenced reads to be mapped correctly, each end of a read pair should not pass the chimeric ligation junction, since this will result in a sequence that cannot be mapped to a reference genome. Fragments that are 200-300 bp are likely to contain enough mappable sequence at each end before reaching a ligation junction.

### ***Size selection***

Covaris sonication results in a relatively small size range of DNA fragments. Therefore, additional size selection could be omitted, but we prefer to use SPRI beads (AMPure) to create an even tighter distribution of fragments. Ampure is a mixture of magnetic beads and polyethylene glycol (PEG-8000). Adding AMPure to a DNA solution reduces the solubility of DNA, because PEG, a crowding agent, will effectively occupy the hydrogen bonds of aqueous solutions.

As a result of this crowding, DNA will come out of the solution and bind to the coated magnetic beads. Since larger DNA molecules will come out of solution first, the final concentration of PEG can be used to generate a size cut-off. After sonication 2 consecutive size selections with Ampure are performed. The first AMPure selection will precipitate DNA larger than 300 bp. Using a magnet, bead-bound DNA is separated from the PEG supernatant, which contains fragments smaller than 300 bp. This supernatant undergoes an additional AMPure selection that precipitates DNA larger than 150 bp. Here after, the bead-bound DNA will be narrowly sized to 150-300 base pairs.

### ***End repair***

The shearing of DNA by sonication will inevitably damage DNA ends. To repair all the ends after sonication a mix of T4 and Klenow DNA polymerase is used together with T4 polynucleotide kinase (PNK). The first 2 enzymes will repair nicked DNA and single stranded ends, while T4 PNK phosphorylates 5'-ends allowing subsequent A-tailing and adaptor ligation.

### ***Biotin pulldown***

To enrich for Hi-C ligation junctions, we use streptavidin-coated beads with a high affinity for the incorporated biotin. This effectively eliminates any DNA without biotin, i.e. DNA that wasn't properly digested, filled-in and ligated (**Fig. 2.1E**).

As mentioned above, the step to remove biotin at DNA ends (see 2.3.1) reduces the pulldown of a large fraction of unwanted unligated fragments (**Fig. 2.1D-E**). However, some unwanted fragments might still be captured. These include self-circled ligation products and other fragments that were insensitive to biotin removal (**Fig. 2.3B**). For instance, during biotin incorporation, internally nicked DNA could be repaired with biotinylated nucleotides and when too far away from the DNA ends, these incorporated biotinylated nucleotides will not be removed by T4 Polymerase in our biotin removal step. Some of these read pairs (e.g. self-circles) can be removed during bioinformatic analysis of the data.

### ***A-tailing and adaptor ligation***

For DNA sequencing Illumina PE adaptors are ligated to both ends of the size selected ligation products. The PE adaptors were generated from DNA oligos, which after duplexing have a 5'-dTTP overhang. This overhang increases ligation efficiency when presented with a free 3'Adenyl. The 3'end of the ligation products are adenylated using dATP and a Klenow fragment lacking 3' to 5' exonuclease activity, and then adaptors are ligated using T4 DNA ligase. Depending on whether the preferred sequencing protocol includes multiplexing, one can either use indexed or non-indexed paired-end adaptors. We have successfully used paired-end single index adaptors to sequence multiple libraries in a single lane. Strategically choosing the right combination of multiplex adaptors, as suggested by Illumina, at this step is essential when multiplexing is intended.

### ***PCR titration and production***

To obtain enough DNA for deep sequencing, the library of ligated fragments is amplified by PCR, using primers designed to anneal to the PE adaptors. Since over-amplification by PCR can result in reduced library complexity, a PCR titration is performed on an aliquot to find the optimal amount of PCR cycles. The smallest number of PCR cycles, producing enough DNA for sequencing will be chosen (**Fig. 2.2C**). After PCR, the PCR product is separated from the bead-bound DNA for a final AMPure cleanup. Generally, 6 to 10 PCR cycles will successfully produce enough DNA for sequencing.

As a final quality control an aliquot of the amplified library is digested with *Clal* (**Fig. 2.2C**). Ligation of blunted *DpnII* sites creates a new *Clal* site at the ligation junction. When fill-in and ligation was successful and efficient one expects the majority of the PCR products to be cleaved, resulting in a shift in size compared to undigested PCR product which can be observed by running an aliquot of DNA on an agarose gel (**Fig. 2.2C**).

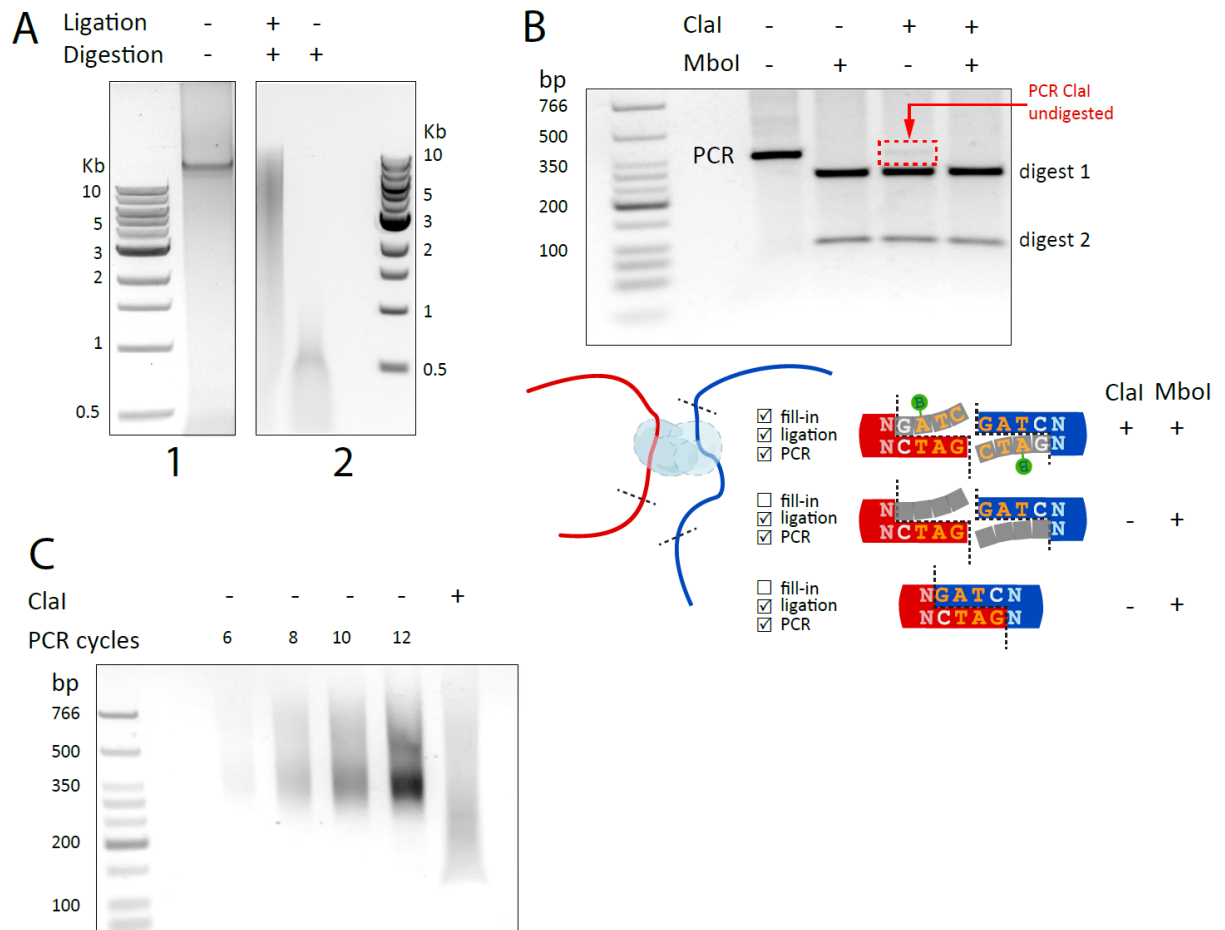


**Figure 2.2: Quality Control of Hi-C ligation products**

**(A.2)** Hi-C DNA after digestion and ligation (+,+) compared to unligated, digested control (-,+). Size is indicated by the 1Kb Molecular Weight Ladder from NEB (1 and 2). **(B)** PCR amplification of a specific ligation product to assess ligation efficiency. The PCR product (lane 1), PCR product digested with Mbol (lane2), Clal (lane3), or both Clal and Mbol (lane4). Only properly filled-in ligation products will be digested with Clal (see cartoon). This allows for a qualitative comparison to Mbol digestion, which cuts GATC sites that are present at the ligation junction of both properly filled-in and non-filled-in ligation products. Digestion of the PCR product using Clal indicates efficient fill-in and the Clal undigested fraction from the PCR can be used to estimate the fill-in efficiency (red arrow). The molecular weight ladder used is the Low Molecular Weight Ladder from NEB. **(C)** PCR titration of the final Hi-C library and quantification of the fill-in and ligation efficiency by Clal digestion. PCR amplification is performed

with primers that recognize the PE adaptors that were ligated to the Hi-C library before sequencing. With 6-cycles of PCR amplification enough DNA was produced for sequencing (lane #1). The last lane shows a downward shift of the amplified library after digestion with *Clal*, indicative of efficient fill-in.

### ***Sequencing***

We sequence Hi-C libraries using Illumina 50 bp or 100 paired-end sequencing. Using longer paired end reads (e.g. 100 bp instead of 50 bp) will increase the number of mappable reads. However, as a cautionary note we also found that longer reads will disproportionally increase the number of read pairs with inward read orientations leading to overestimation of very short-range interactions. As mentioned above, such partial digestion products can appear as valid interactions and cannot be filtered out computationally.

### **MAPPING AND BINNING PIPELINE**

The paired end sequencing information can be downloaded from the sequencing platform as standard fastq files. The reads are then mapped to a reference genome and valid interaction pairs are identified using read orientation (inward, outward, or same direction). Reads mapping to different fragments are used to assemble the Hi-C dataset. All 4 read strand combinations are possible and are expected to be observed in equal proportions (25% per combination). However, inward read pairs could be the result of undigested restriction sites (partial digests) (Lajoie, Dekker, & Kaplan, 2015). Reads mapping to a single

fragment are considered uninformative. There are several types of such uninformative single fragment read pairs (**Fig. 2.3C**): self-ligations (self-circles), unligated fragments (dangling ends) and error pairs. These can be identified by the read orientation, as shown in **Figure 2.3C**. Inward pointing reads are considered unligated fragments (dangling ends). Outward pointing reads are classified as self-ligated fragments (“self-circles”). Same-strand reads are classified as “error pairs” as these products are a result of either a mis-mapping, random break, or an incorrect genome assembly products (Lajoie et al., 2015) (**Fig. 2.3**). Improper ligations can be detected and filtered out by evaluating read orientation of the paired ends and whether the reads map to the same fragment (Lajoie et al., 2015). However, one particular type of improper interaction that is derived from dangling ends cannot be accounted for by computational analysis alone because the two reads map to two (adjacent) restriction fragments. Dangling ends flanking an undigested restriction fragment (partial digest) will computationally be indistinguishable from a valid pair interaction with an inward orientation (**Fig. 2.3C**). Such read pairs increase in frequency with decreasing restriction fragment size (i.e. when using more frequently cutting enzymes such as DpnII) (**Fig. 2.4A**). We find that such “inward” read pairs are overrepresented in most Hi-C datasets (i.e. they occur more frequently than the expected 25%), and they represent almost all valid interactions between adjacent restriction fragments. A dangling end removal step can remove a subset of such problematic read pairs by removing unligated partial digest products.

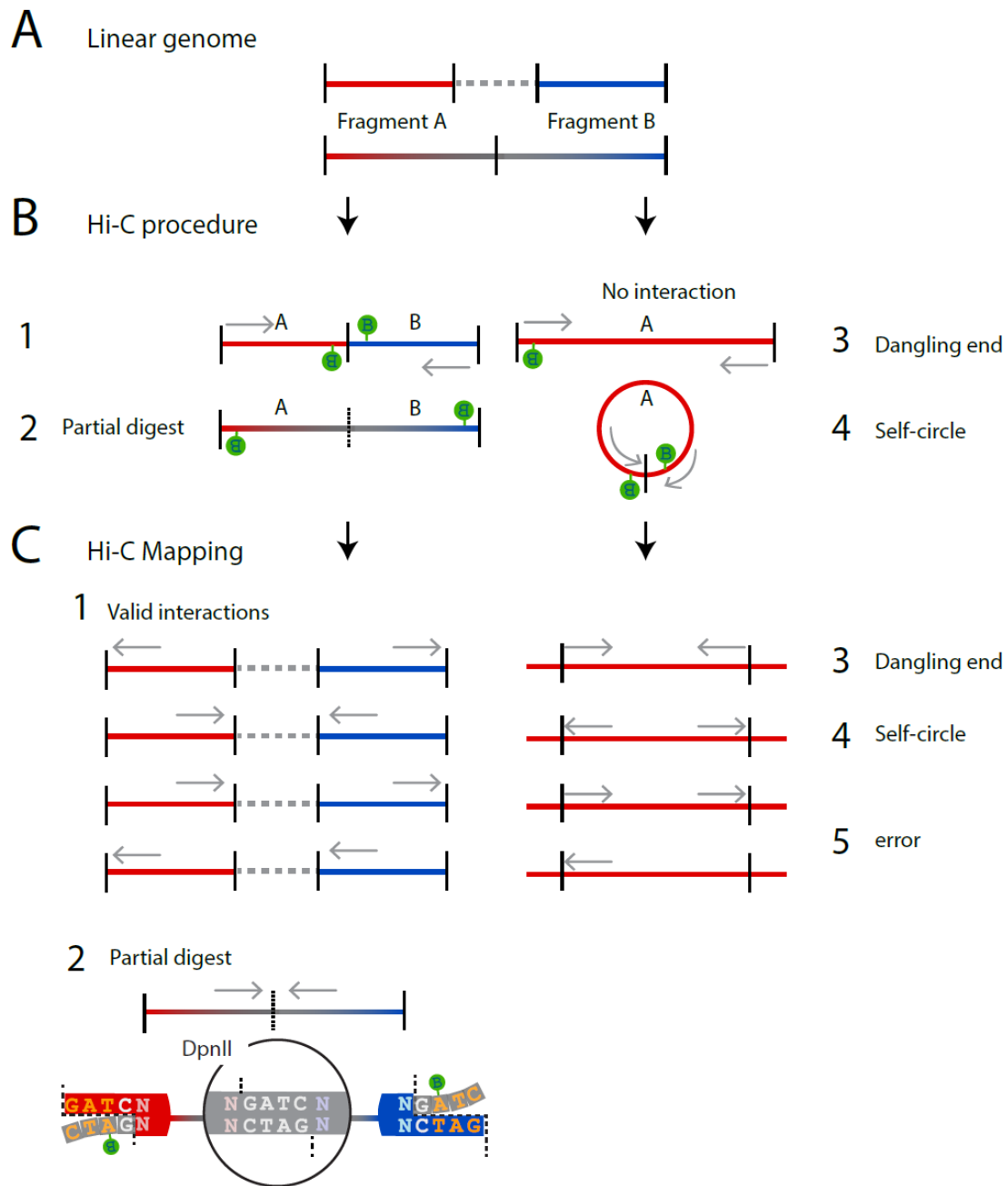


**Figure 2.3: Possible products generated by Hi-C**

**(A)** Two fragments: A (red) and B (blue), are spatially separated in the linear genome (gray dotted line) or neighboring (red and blue to gray fading). **(B)** If fragment A and B are in close spatial proximity they can become cross-linked and ligated during the Hi-C procedure (1). Partial digests result from undigested neighboring fragments that were biotinylated (2). Other possible, non-valid



products can be derived from non-ligated DNA (dangling-end; 3) or single fragments that have become circularized after ligation (self-circles; 4). The gray arrow indicate the orientation of the paired-end reads in the Hi-C library **(C)** Dangling ends can be removed from the Hi-C library prior to sequencing, as described in this protocol. Any remaining dangling-ends and self-circles can be filtered out from the sequenced library computationally after mapping and assessing the orientation of the DNA reads. After mapping, valid reads locate to different fragments in the reference genome and are either inward or outward oriented, or directed in the same direction (both pointing left or both pointing right) (1). Unligated partial digestion products cannot be distinguished from valid reads because the two reads will map to two (neighboring) restriction fragments. This category is characterized by an inward read orientation (2). Invalid reads have mapped to the same fragment in the reference genome and can be either inward (dangling ends; 3), outward (self-circles; 4) or same direction (error; 5). Gray arrows indicate the read orientation in the reference genome.

### **Bias in inward read orientation**

Unligated partial digestion products will always produce “inward” read pairs mapping to adjacent or very nearby restriction fragments (genomic distance <500 bp). We compared data we obtained with Hi-C 2.0 to the data published by Rao et al. ( Rao et al., 2014) obtained with in situ Hi-C without dangling end removal (**Fig. 2.4A**). We find that data obtained with both protocols display a bias in detection of interactions with inward read orientation (average 30-35% of all interactions). There can be quite a large experiment-to-experiment variation in the frequency of the inward read pairs. The number of inward reads between sites separated by less than 500 bp can represent up to 20% of all valid interactions in some datasets. Almost all such short-range interactions are in fact of the inward type, indicating that the general bias for inward read orientation is driven to a large extent by very short-range interactions. The experiment-to-

experiment variation in this bias appears to be lower with Hi-C 2.0. This indicates that at least a subset of these reads may represent dangling ends of partial digestion products and also suggests that dangling end formation can be quite variable between experiments. In summary, Hi-C 2.0 and in situ Hi-C produce on average similar levels of such potentially problematic molecules (dangling ends, and inward read pair interactions), but Hi-C 2.0 appears to display less experiment-to-experiment variation at least for the set of experiments analyzed here.

### **Analysis of valid interaction pairs**

Valid interaction pairs can be binned at a range of resolutions (e.g. 5-100 Kb bins) (Lajoie et al., 2015). At some point the digestion frequency becomes the limiting factor for obtaining higher resolution. With an average digestion every 4kb for HindIII, a 10kb resolution heatmap will start showing unfilled bins; i.e. bins that are smaller than the restriction fragment covered. These (**Fig. 2.4B**).

Binned reads are stored as a symmetric matrix with each row and column representing a genomic location (bin). Interacting regions are represented by the number of reads for every bin within this matrix. We use the percentage of bins filled with at least one valid pair read (non-zero) to estimate the resolution that can be obtained (**Fig. 2.4C**). Matrices are routinely displayed as heatmaps that display these interactions by coloring entries for the amount of reads they contains.

Binned interaction matrices are corrected for intrinsic biases in Hi-C such as read mappability, restriction site density and GC- content. Several approaches have been developed for bias removal. Yaffe and Tanay developed a computational approach to estimate each of these biases and then remove them (Yaffe & Tanay, 2011). We use an iterative correction approach, developed by Imakaev and co-workers to balance the matrix of interactions such that the sum of all interactions genome-wide for each bin adds up to the same number (Imakaev et al., 2012). This correction should remove both known and unknown biases, such as potential cross-linking differences. We note that such balancing methods often exclude very short-range interactions (i.e. the first diagonal of a Hi-C interaction map) from analysis because these are contaminated with a variety of problematic read pairs, as we have outlined above. This reduces the ability to detect short-range interactions.

There are several public pipelines for processing Hi-C data, e.g. HOMER (Heinz et al., 2010), HiCPro (Servant et al., 2015a), HiCUP (Wingett et al., 2015) and Juicer (Durand et al., 2016). For a more detailed description of mapping and binning of data using our pipeline, we refer to in Lajoie et al., *Methods* (2015) (Lajoie et al., 2015). A high quality Hi-C library for mammalian genomes typically has 50-70% of interactions mapping to intra-chromosomal interactions, less than 2 % dangling ends, less than 1% self-ligated circles, and less than 5% PCR redundant interactions per 400 million reads. We note that with the Illumina HiSeq 4000 platform additional apparently redundant reads on the flow cell can

be produced that are not due to PCR amplification but the result of sample loading. Additional washing of libraries (on AMPure beads) and optimization of loading has helped us reduce such artifacts. Finally, these numbers can depend on biological state and therefore are only general guidelines for assessment of library quality.

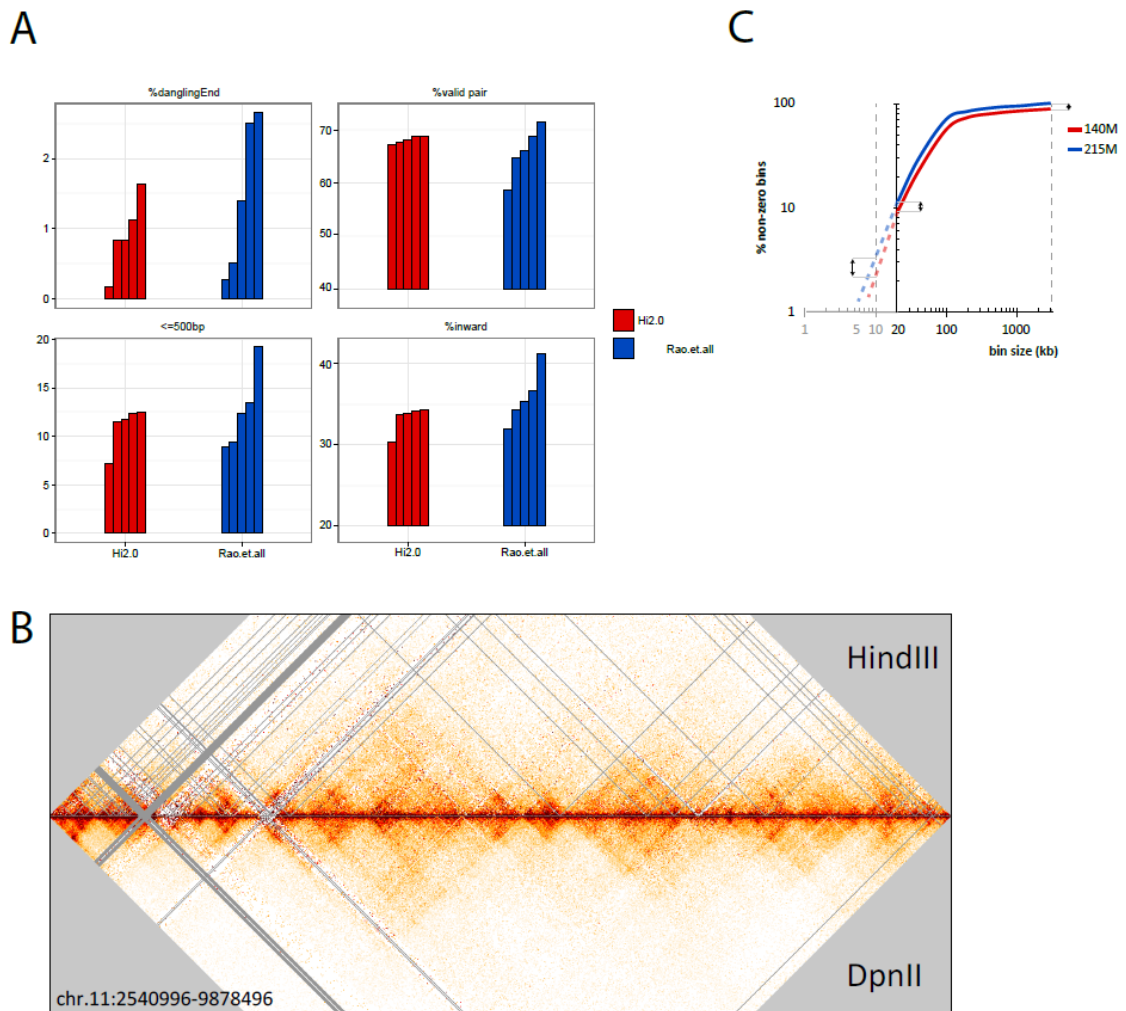


**Figure 2.4: Dangling end removal and to increase valid pair reads**

**(A)** Comparison of frequency of dangling ends, total valid pairs, valid pairs with inward read orientation for short range interactions between nearby fragments (separated by less than 500 bp), and frequency of total inward reads for datasets obtained with in situ Hi-C (SRR1658706, SRR1658593, SRR1658712, SRR1658671, SRR1658648) (Rao et al. ( Rao et al., 2014)) and for datasets obtained with Hi-C 2.0. All datasets were analyzed by 100 bp paired end reads. Datasets from Rao et al. were selected solely based on their read depth that was comparable to datasets obtained with Hi-C 2.0 (100-200 million reads). All data were analyzed through our Hi-C mapping pipeline (available in Github: <https://github.com/dekkerlab/cMapping>). Hi-C 2.0 and removal of dangling ends results in a more consistent percentage of valid reads. Within the set of valid pair

reads, we see a reduction in experiment-to-experiment variation of total amount of inward read pairs. The overrepresentation of inward reads appears due to a large extent to the fact that almost all read pairs between neighboring restriction fragments (separated by less than 500 bp) are inward and this category can be 10-20% of all valid pairs. Hi-C 2.0 reduces the experiment-to-experiment variation of interactions between fragments separated by less than 500 bp. This suggests that at least a subset of interactions between adjacent fragments (interactions separated by less than 500 bp) represent dangling ends. **(B)** A 10 kb resolution heatmap for chromosome 11 (hg19: 2,540,996-9,878,496 bp) derived from 2 libraries with 300M reads. Libraries were generated with HindIII (top triangle) or DpnII (bottom triangle). Color scales are normalized and bins without reads are visualized as gray lines. More unfilled bins (gray) in HindIII are caused by larger fragment sizes **(C)** An increase in valid pair reads, scored as bins containing at least 1 read (i.e. non-zero), allows for analyses at a higher resolution. The plot compares 2 libraries generated with the same protocol, but with different numbers of valid pair reads (blue: 215 million; red: 140 million). Double arrows indicate that at a higher resolution (smaller bins), adding more valid pair reads (by deeper sequencing) becomes important. These libraries were binned with 20kb as the highest resolution from where dotted lines (red, blue) start extrapolating the data to higher resolutions.

Recent research has shown that the genome is composed of several layers of structure, ranging from compartments to topologically associating domains (TADs) and loops (**Fig. 2.5**). We will briefly describe how those features can be measured. For more details we refer to Lajoie et al., *Methods* (2015) (Lajoie et al., 2015).

### ***Compartments***

Compartments are defined as groups of domains, located along the same chromosome or on different chromosomes that display increased interactions with each other. In heatmaps generated from 100Kb bins, this is visible as a specific plaid pattern. These alternating blocks of high and low interaction frequencies represent A and B compartments (Lieberman-Aiden et al., 2009). Principal component analysis (PCA) readily identifies these compartments that tend to be captured by the first component. The active “A” compartments are gene-dense euchromatic regions, whereas the inactive “B”-compartments are gene-poor heterochromatic regions (**Fig. 2.5**)

### ***Topologically associated domains (TADs)***

TADs are contiguous regions that display high levels of self-association and that are separated from adjacent regions by distinct boundaries (J R Dixon et al., 2012; Nora et al., 2012). The locations of TADs can be determined when interaction data is binned at 40 Kb or less. There are several computational

approaches to identify the locations of TAD boundaries including the directionality index (J R Dixon et al., 2012) or an insulation score algorithm (Crane et al., 2015) to determine the location of TADs (**Fig. 2.5**).

### ***Point to point interactions (loops)***

Many point-to-point interactions or loops appear as off-diagonal “dots” in a heatmap. Typically, a 10Kb resolution or higher is required for identifying looping interactions. Mapping to smaller bins will allow for more specific interactions, but this comes at the cost of a decreased number of reads per bin. Specific interactions between for instance pairs of CTCF sites are expected to show up as increased signal compared to their surrounding area ( Rao et al., 2014). Rao et al describe a useful approach to detect such dots using a local background model ( Rao et al., 2014). Other types of local interactions, e.g. lines in the heatmap can be detected using global background models (Jin et al., 2013; A Sanyal, Lajoie, Jain, & Dekker, 2012). Using HiCUP, we have observed loops at 10 kb resolution with a library containing 300M valid reads.



**Chromosome 14, 106Mb**

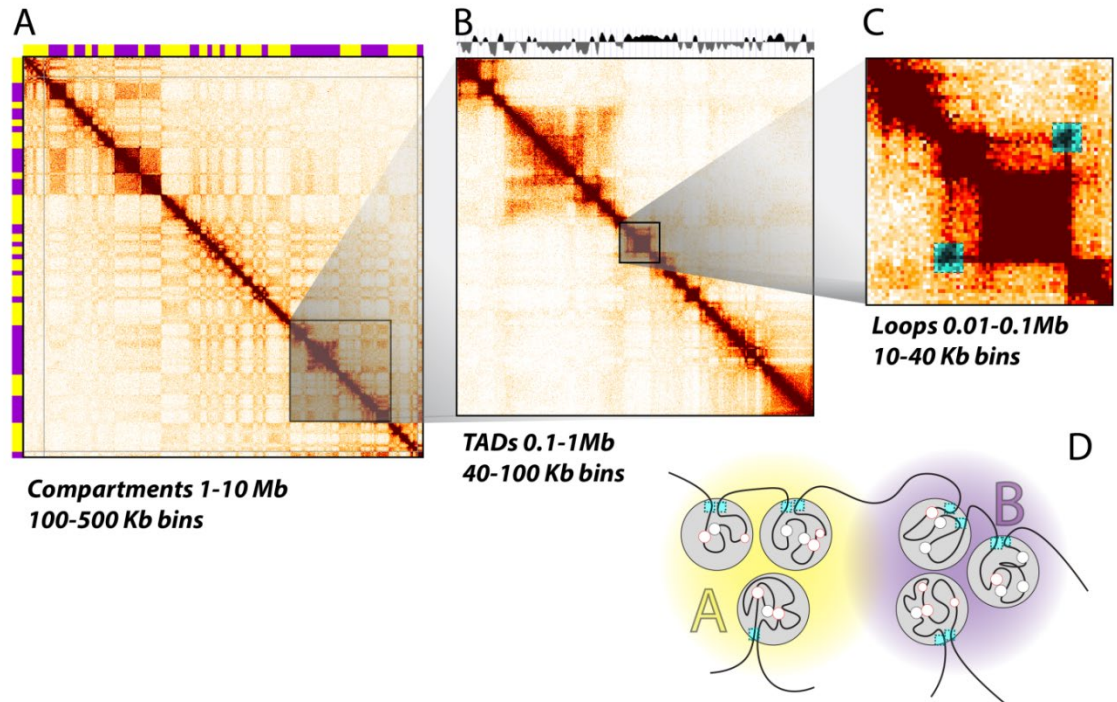


**Figure 2.5: Topological structures observed with Hi-C**

**(A)** Heatmaps generated from 100 kb binned Hi-C data for chromosome 14 show the alternating pattern of A and B compartments (yellow/purple) **(B)** On a sub-chromosomal level, heatmaps at 40 kb resolution show the location of TADs, as indicated by an insulation score on top (gray). **(C)** Within TADs, DNA loops can form that show up as “dots” of interactions in heatmaps of sufficient resolution (typically 10 Kb bins or less). **(D)** Interpretation of the topological hierarchy obtained from Hi-C. TADs (gray circles) within the same compartment (A or B) interact more frequently than those located in different compartments. TADs are bordered by insulating proteins (e.g. CTCF, cyan squares). DNA loops form between CTCF sites, enhancers and promoters (red/black circles).

## **CONCLUSION**

This Hi-C 2.0 protocol combines in situ ligation with dangling end removal to produce Hi-C libraries enriched in intra-chromosomal valid interaction pairs. This protocol can effectively be used to visualize chromosome conformation at Kb resolution genome-wide.

# CHAPTER III: CBF $\beta$ -SMMHC Inhibition Triggers Apoptosis by Disrupting MYC Chromatin Dynamics in Acute Myeloid Leukemia

## PREFACE

The content of this chapter is a part of the following publication:

John Anto Pulikkan,<sup>1</sup> Mahesh Hegde,<sup>1</sup> Hafiz Mohd Ahmad,<sup>1</sup> **Houda Belaghzal**,<sup>2</sup> Anuradha Illendula,<sup>3</sup> Jun Yu,<sup>1</sup> Kelsey O'Hagan,<sup>1</sup> Jianhong Ou,<sup>1</sup> Carsten Muller-Tidow,<sup>4</sup> Scot A. Wolfe,<sup>1</sup> Lihua Julie Zhu,<sup>1</sup> Job Dekker,<sup>2</sup> John Hackett Bushweller,<sup>3</sup> and Lucio Hernán Castilla<sup>1</sup>. Cell 174, 172–186, June 28, 2018

## SUMMARY

Some cancer cells form through oncogenes or mutations in tumor suppressor genes., and a subset of these alter transcription factors and chromatin-associated elements. In blood-associated cell types, these factors often drive leukemia initiation and maintenance. Specifically, in acute myeloid leukemia (AML) *MYC* is up-regulated after its repressor RUNX1 is inhibited by the fusion oncoprotein CBF $\beta$ -SMMHC. The treatment of AML cells with small molecule AI-10-49 blocks RUNX1 binding to CBF $\beta$ -SMMHC. As a result, RUNX1 availability at the *MYC* regulatory elements decreases *MYC* expression and AML cell viability. In this study, an assessment of overall epigenetic and genomic changes in 4Mb around *MYC* in AML cells before and after AI-10-49 treatment

was conducted. AI-10-49 treatment induces a 7-fold increase in RUNX1 occupancy in regulatory elements downstream of *MYC*, 10-fold decrease of *MYC* expression, and induction of apoptosis. To further investigate how RUNX1 binding to *MYC* regulatory elements ME1, ME2, and BDME after treatment induces a 10-fold decrease in *MYC* expression, we applied chromosome conformation capture carbon copy 5C for 4Mb around the *MYC* gene. This experiment provides a critical piece of evidence that the *MYC* promoter physically interacts with RUNX1-associated enhancers ME1, ME2, and E3 in AML cells before and after treatment with AI-10-49. These results demonstrate that, at an established loop, changes in transcription factor occupancy in regulatory elements are sufficient to replace the activating chromatin complexes for repressive complexes at the target gene in order to disrupt its expression.

## INTRODUCTION

The genome-wide association study, GWAS revealed that the majority of the variants fall in noncoding regions of the genome and lack a defined target gene (Variation et al., 2012). A lot of these disease-specific variants alter the association of transcription factors and repressor at regulatory elements (Variation et al., 2012). In acute lymphoblastic leukemia (ALL) of T-cell type “T-ALL cell lines”, the *MYC* promoter interacts with the Notch-dependent *MYC* enhancer element “NDME”, which is found 1.3 Mb (Yashiro-ohitani et al., 2014).

The NDME binds Notch transcription complexes to activates reporter genes in (ALL) of T-cell type. The survival and aberrant self-renewal potential of acute myeloid leukemia (AML) RN2 cells require the mammalian SWI/SNF chromatin remodeling complex, recruited to the *MYC* promoter by a cluster of enhancers located 1.7 Mb downstream (Shi et al., 2013). Similarly, in acute myeloid leukemia (AML) ME-1 cells *MYC* promoter is enriched by transcription activating SWI/SNF chromatin remodeling complex.

### ***MYC* expression is critical for the survival of leukemia cells**

*MYC* regulates the balance between self-renewal and differentiation of HSCs (Wilson et al., 2004), and is essential for lymphoid (Alboran et al., 2001) (Douglas, Jacobs, Bothwell, & Hayday, 2001) and megakaryocytic-erythroid development (Y. Guo et al., 2019). *MYC* expression however, needs to be downregulated during myeloid differentiation since *MYC* repression promotes granulopoiesis, while its ectopic expression blocks granulopoiesis (Gowda, Koler, & Jr, 1986) (Holt, Redner, & Nienhuis, 1988) (Johansen et al., 2001). The accumulation of polycomb-repressive complexes (PRC1 and PRC2) in *MYC* downstream target enhancers induces tri-methylation of lysine-27 in histone H3 (H3K27me3), thereby promoting local compaction of the chromatin structure around enhancers and silencing the expression of target genes (Croce & Helin, 2013). Emerging evidence indicates that the epigenetic regulation of enhancer activity plays a critical role in myeloid differentiation and leukemia. The SWI/SNF and BRD4 complexes regulate expression of the proto-oncogene *MYC* from the

distal super-enhancer *BDME* (BRD4-dependent *MYC* enhancer). *BDME* is located 1.7 megabases downstream from its transcription start site (TSS) (Shi et al., 2013). The regulation of *MYC* expression can be controlled by different distal enhancers in a cell type-specific manner. The *BDME* super-enhancer is composed of five enhancer elements and is occupied by a number of transcription factors with roles in myeloid differentiation. The SWI/SNF ATPase subunit Brahma related gene 1 (BRG1) is required for normal granulopoiesis and associates with *BDME* to maintain *MYC* levels in mixed-lineage leukemia cells (Shi et al., 2013) (Vradii et al., 2005). Finally, *MYC* is up-regulated after its repressor RUNX1 is inhibited by the fusion oncoprotein CBF $\beta$ -SMMHC in AML B cells (ME-1 cells).

### **RUNX1 recruits transcription factors at its target sites**

RUNX1 associates with chromatin-modifying proteins, including histone deacetylases (Vanden-eynden, Xie, & Lutterbach, 2006) (H. Guo & Friedman, 2011), acetyl-transferases (Kitabayashi, Yokoyama, Shimizu, Ohki, & Pebp, 1998)(Kitabayashi, Aikawa, Nguyen, & Yokoyama, 2001) and methyl-transferases (X. Zhao et al., 2008) (Vanden-eynden et al., 2006) (Vu et al., 2013) in hematopoiesis. These proteins interactions regulate RUNX1 affinity to DNA, transcriptional activity, and modulate its association with activating and repressing chromatin complexes (Lichtinger, Hoogenkamp, Krysinska, Ingram, &

Bonifer, 2010). RUNX1 is less accessible to its specific DNA target sites in inv(16)(p13;q22) acute myeloid leukemia (AML), as a consequence of its high binding affinity to the oncoprotein CBF $\beta$ -SMMHC. However, how depletion of chromatin-binding RUNX1 leads to survival of AML cells and what modulates leukemia maintenance is poorly understood.

### **The inhibitory role of CBF $\beta$ -SMMHC oncoprotein**

The transcription factor complex core-binding factor (CBF) is a heterodimer composed of the stabilizing subunit CBF $\beta$  and the DNA-binding subunit RUNX (encoded by three genes: *RUNX1*, *RUNX2*, and *RUNX3*). The RUNX1/CBF $\beta$  complex regulates pathways associated with proliferation, survival, and differentiation (Blyth, Cameron, & Neil, 2005). The genes encoding CBF $\beta$  and RUNX1 are frequent targets of mutations in hematologic malignancies. The chromosome inversion inv(16)(p13;q22), found in 8% of acute myeloid leukemia (AML), disrupts and fuses the *CBF $\beta$*  and *MYH11* genes to produce the leukemia oncoprotein CBF $\beta$ -SMMHC (**Fig. 3.1A**) (P. Liu et al., 1993). This fusion protein out-competes CBF $\beta$  from the WT allele *in vitro* since CBF $\beta$ -SMMHC has significantly higher affinity and altered stoichiometry for RUNX1 relative to the native CBF $\beta$  (**Fig. 3.1B**) (Cao et al., 1997) (Lukasik et al., 2002). During development, CBF $\beta$ -SMMHC expression blocks definitive hematopoiesis and embryos die at mid-gestation (Castilla 1996). A similar phenotype is seen when *Runx1* and *Cbf $\beta$*  are knocked out in embryos (Castilla et al., 1996). These

findings demonstrated that the CBF $\beta$ -SMMHC has a dominant negative role in CBF function.

### AI-10-49 restores RUNX1 binding

The inhibitor AI-10-49 is a selective inhibitor of CBF $\beta$ -SMMHC which disrupts its binding to RUNX1 and induces apoptosis of inv(16) AML cells (Illendula et al., 2015). Analysis of chromatin-immunoprecipitation (ChIP) experiments shows that treatment of ME-1 cells revealed that AI-10-49 restores RUNX1 transcriptional activity by increased RUNX1 binding to its target promoters (**Fig. 3.1B**) (Illendula et al., 2015).

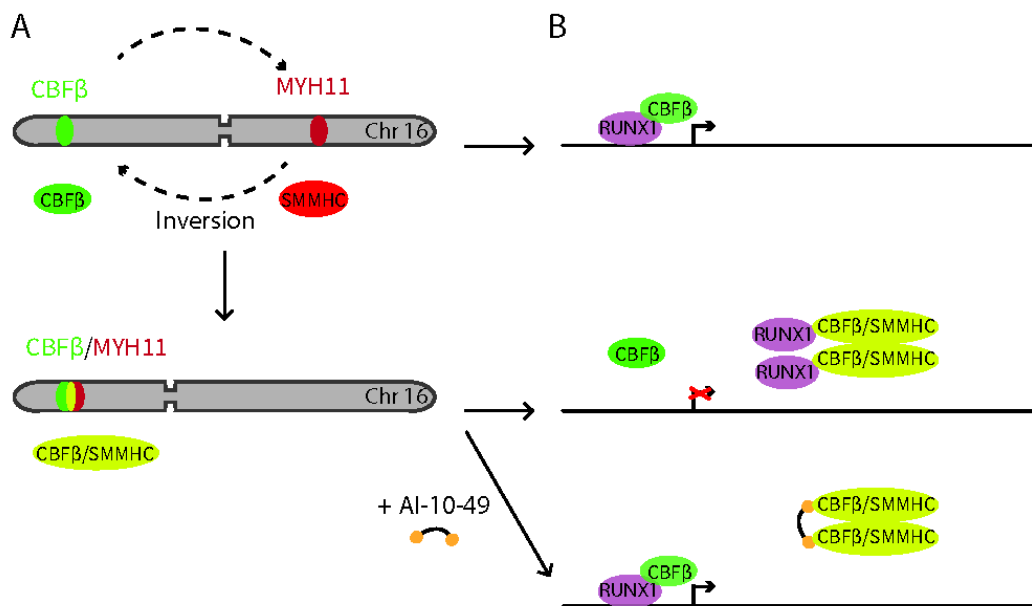


**Figure 3.1: Schematic of inv(16)(p13;q22), which fuse CBF $\beta$  and MYH11 genes.**

**(A)** inv(16)(p13;q22) fuse CBF $\beta$  and MYH11 genes (CBF $\beta$ -MYH11). **(B)** (top) RUNX1-CBF $\beta$  binding to one of its target genes before inv(16)(p13;q22), (middle) CBF $\beta$ -SMMHC altering RUNX1 binding to CBF $\beta$  because of its higher affinity to



RUNX1. (bottom) AI-10-49 binding to oncoprotein CBF $\beta$ -SMMHC, which restores RUNX1 transcriptional activity.

In this study, we combined pharmacologic, genomic, and genetic approaches to define the mechanism by which RUNX1 binding to CBF $\beta$ -SMMHC inhibition drives apoptosis in inv(16) AML cells. This effort uncovered a RUNX1-mediated mechanism of *MYC* regulation at distal enhancers by the replacement of activating chromatin complexes for repressive complexes.

## **MATERIALS AND METHODS**

### **Cell growth**

The inv(16) AML ME-1 cells (40 years old male) were cultured in RPMI 1640 with 20% fetal bovine serum, 25 mM HEPES, 100 U/mL Penicillin, 100 mg/mL Streptomycin and 1ml/mL Plasmocin

### **Assay for Transposase-Accessible Chromatin with sequencing (ATAC-seq)**

To profile for accessible chromatin regions, we used ATAC-seq as described elsewhere (Buenrostro et al., 2015) with the following modifications: ME-1 cells (50,000) were treated with DMSO or AI-10-49 (1 mM) for 6 hr followed by washing once with 1x PBS by centrifugation using 5 min at 500 g and 4°C with low acceleration and brake settings. Cell pellets were re-suspended in 50ml of cold lysis buffer (10 mM Tris-HCl pH 7.4, 10 mM NaCl, 3 mM MgCl<sub>2</sub>, 0.1% IGEPAL CA-630) and nuclei were pelleted by centrifugation for 10 min at

500 g, 4°C. Supernatant was discarded and nuclei were re-suspended in 25 ml reaction buffer containing 2.5 ml of Tn5 transposase and 12.5 ml of TD buffer (Nextera Sample preparation kit, Illumina). The reaction was incubated at 37°C for 45 min. Immediately following transposition, tagmented DNA was purified using a QIAGEN MiniElute PCR Purification Kit. For library amplification, two sequential PCRs were conducted with indexing primers included in the Nextera Index kit and NEBNext High-Fidelity 2x PCR Master Mix. After the first PCR, the libraries were enriched for fragments less than 600 by using Agencourt AMPure XP 5 mL Kit (Beckman Coulter). A second PCR was conducted with the similar settings followed by size enrichment by Agencourt AMPure XP 5 mL Kit. DNA was eluted and concentration was measured with a Qubit fluorometer (Life Technologies) and library quality evaluated using 2100 Bioanalyzer (Agilent Technologies). The libraries were sequenced in 100 bp paired-end on an Illumina HiSeq2000. ATAC-seq data analysis

The preprocessing of ATAC-seq data was followed as reported (Buenrostro et al., 2013). Briefly, the adaptors were removed using cutadapt program v 1.3, and reads were mapped onto the human genome hg19 assembly using Bowtie2 (Langmead and Salzberg, 2012). The standard default settings were modified to allow mapped paired-end fragments up to 2 kb. Only the reads with mapping quality greater than 20 were kept, and the duplicated reads were removed using Picard tools v1.96 (<https://broadinstitute.github.io/picard/>), the reads from mitochondria were also removed. To visualize the mapped reads, the bigwig files

were generated using deepTools2. Quality assessment of ATAC-seq data was performed using ATACseqQC (Ou et al., 2017). Reads enrichment were called by MACS2 v2.1.0 (Zhang et al., 2008) with default parameters using the reads with insert size less than 100 bp as nucleosome-free regions.

### **ATAC-qPCR**

For ATAC-qPCR, ME-1 cells were nucleofected with CRISPR/Cas9 plasmids with sgRNAs that delete a 275 bp segment including the RUNX1 binding site, sorted by flow cytometry 24 hr later and cultured overnight. ATAC libraries were prepared from three independent biological replicates as described above. 5% of non-transposed genomic DNA was taken as input. Enrichment of open chromatin in the ATAC samples over input was performed by qPCR using primers for each regulatory element, and a region centromeric from the deleted E3 segment.

### **CRISPR/Cas9 – mediated deletion of the enhancer regions**

The sgRNAs specific for 5' to the region of interest were cloned in pLentiCRISPRv2 (Addgene #52961). sgRNAs corresponding to 3' to the region of interest were cloned in pDecko-mCherry (Addgene #78534). The puromycin resistance cassette in pLentiCRISPRv2 was replaced by a GFP gene using standard cloning techniques. All sgRNA cloning was done in respective plasmids using standard guide RNA cloning method. Briefly, top and bottom strand guide RNA oligos were phosphorylated using T4 Polynucleotide Kinase, annealed and

inserted into the vectors at BsmB1 site. Guide RNA's cloned inside the pLentiCRISPRv2GFP were transfected into 293T/17 cells using the FuGENE 6 method according to the manufactures instructions. 48 hr after transfection, genomic DNA was isolated and PCR was carried out to amplify the region of interest. PCR product was re-annealed and treated with T7 endonuclease according to the manufactures instruction. The reaction was later resolved on 2% agarose gel and the product was analyzed. 2-3x10<sup>6</sup> ME-1 cells were nucleofected with CRISPR/Cas9 plasmids (2mg each) using Nucleofector Technology with the program X-01 and Amaxa Cell Line Nucleofector Kit V. Samples were sorted by flow cytometry 24 hr later. Cells were cultured overnight and dead cells were eliminated by dead cell removal kit.

### **5C experimental design**

3C libraries were generated as described before (Hnisz et al., 2016) (Ferrauiolo et al., 2012), with the following modifications: 1) After HindIII digestion no SDS was added for restriction enzyme inactivation. 2) The ligation volume as 1.2 mL for 5 million cells and a total of 20 -30 million cells were used per 5C library preparation. 5C was carried out as previously described (Dostie et al., 2006) (Dostie et al., 2006; (Ferrauiolo et al., 2012) (Lajoie, Berkum, Sanyal, & Dekker, 2009), with one modification: gel purification after adapter ligation was replaced by an Ampure step to remove unligated DNA. 5C primers were designed for a 3.98 Mb region (chr8: 127,753,661 – 131,737,521) around the *MYC* locus. 5C primers were designed at HindIII restriction sites using publicly

available 5C primer design tools published previously (Lajoie et al., 2009). Primers were designed according to a double alternating scheme exactly as described before (Hnisz et al., 2016). We designed two primers for each HindIII fragment: one primer designed on the 5' end of the fragment, and one on the 3' end. For a fragment, we either designed a right 5' forward (FOR) and a left 3' reverse (LREV) primer, or a right 5' reverse (REV) and a left 3' forward (LFOR) primer (**Fig. 3.2**). These two primer designs alternate along with consecutive fragments throughout the entire region of interest. This design allows interrogation of all pairwise interactions among all fragments, which is not possible with a more simple alternating design used previously (Lajoie et al., 2009).

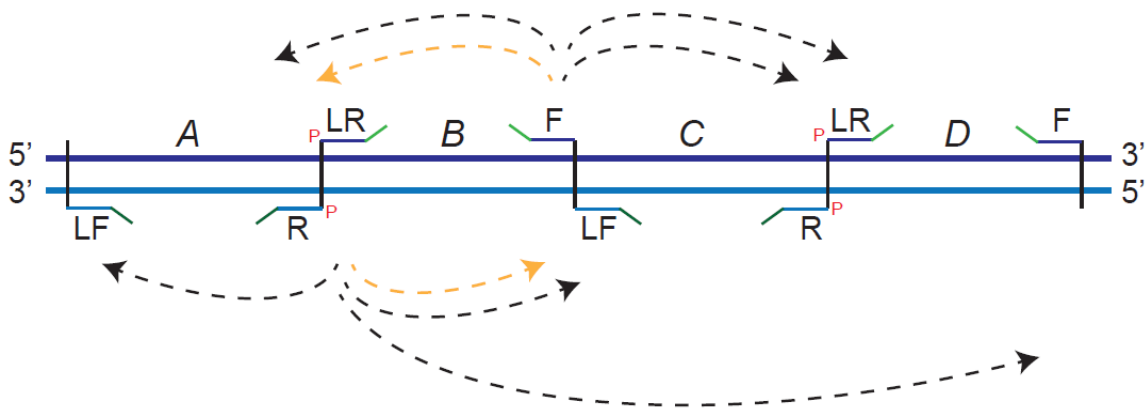


**Figure 3.2: Double alternating design for 5C probes.**

F: right 5' forward (FOR), LR: left 3' reverse (LREV), R: right 5' reverse (REV), LF: left 3' forward (LFOR).

### **Primer settings**

Primers settings were: U-BLAST, 3; S-BLAST, 50, 15-MER, 800, MIN\_FSIZE, 100; MAX\_FSIZE, 50,000; OPT\_TM, 65; OPT\_PSIZE, 40. The 5C primer tails were: FOR/LFOR: T7 sequence 5'-TAATACGACTCACTATAGCC-3'; REV/LREV: T3 sequence 5'-TCCCTTTAGTGAGGGTTAATA-3'. The full length of all FOR/LFOR primers was 60 bases; the length of all REV/LREV was 61 bases. In total we designed 359 forward (FOR), 367 left forward (LFOR), 367 reverse (REV) and 367 left reverse (LREV) primers that combined interrogate 532,158 long-range chromatin interactions. Primers sequences are listed in (GEO: GSE109764).

### **Generation of 5C libraries**

A 5C multiplex primer annealing reaction was performed overnight at 50°C. Pairs of annealed 5C primers were ligated at the same temperature using Taq DNA ligase for 1h. Seven ligation reactions were performed to generate 5C libraries, except for the second biological replicate for AI-10-49-treated cells, where 14 ligation reactions were performed. Each ligation contained 600,000 genome copies, except for the second biological replicate for AI-10-49-treated cells, which contained 400,000 genome copies. Each primer was added to a final amount of 0.325 fmoles. Ligated 5C primer pairs, which represent a specific ligation junction in the 3C library and thus a long-range interaction between the two corresponding loci, were then amplified using 20 cycles of PCR with T7 and

T3R universal tail primers that recognize the common tails of the 5C forward and reverse primers. Four separate amplification reactions were carried out for each annealing reaction described above and all the PCR products of each library were pooled together. This pool constitutes the 5C library. The libraries were concentrated using Amicon Ultra Centrifugal filters - 0.5ml 30K (Millipore) and purified with Qiaquick PCR purification kit.

### **5C read mapping**

5C libraries were sequenced on an Illumina HiSeq 4000 instrument, reads were mapped (with Novoalign mapping algorithm V3.02.00) and 5C interactions assembled exactly as described before (Lajoie et al., 2009) (Amartya Sanyal et al., 2012). Data from the two biological replicates were pooled, producing a single interaction map for DMSO treated, and AI-10-49 treated cells. Each library has approximately 90 million valid reads.

### **5C filtering and analysis**

5C matrices were processed using previously described methods (Lajoie et al., 2009) (Amartya Sanyal et al., 2012). And as describe [https://github.com/dekkerlab/5C-CBFβ-SMMHC-Inhib/blob/master/data\\_processing\\_steps.md](https://github.com/dekkerlab/5C-CBFβ-SMMHC-Inhib/blob/master/data_processing_steps.md).

Briefly, first, we removed 5C interactions that represent self-ligated restriction fragments. Second, in 5C PCR can lead to over amplification of individual pair-wise interactions (outliers). To remove these we first calculated

the average interaction frequency, and standard deviation, of all pair-wise interactions as a function of their genomic distance using LOWESS smoothing, as described in (Amartya Sanyal et al., 2012). This average value represents the expected interaction frequency for a pair of loci. We then calculated the observed/expected ratio for each interaction and expressed this as a z-score  $[(\text{observed}-\text{expected})/\text{standard deviation}]$  (Amartya Sanyal et al., 2012). Outliers were then defined as those interactions with a Z-score greater than 20 in each dataset. We then took the union of all outliers identified in the four 5C datasets and removed these interactions from all four datasets. Third, some primers strongly over or underperform leading to strongly enriched or depleted rows of interactions. To identify these primers we calculated to sum of all interactions detected with each of the 5C primers. We then defined over- and underperforming primers as those with a sum that is outside the 1.5 times the interquartile range (of the distribution of all row/col sums). We then took the union of all flagged primers across the four 5C matrices and removed these from all four datasets. Fourth, we scaled the four matrices to the same number of total reads (50,000,000). Fifth, the matrices were balanced according to the ICE method so that the sum of each row and each column is equal (Imakaev et al., 2012). Sixth, data were binned at 20kb (median) with a sliding window with 2.5 kb steps, or at 15 kb (median) with a sliding window with 2.5 kb steps when data was plotted as interaction profiles of single loci (4C-style plots). Seventh, matrices were balanced again after binning.



### 4C-style plots

To display the interaction profiles (4C-style plots) of selected loci we extract rows for corresponding bins that overlap the *MYC* Promoter, ME1- ME2- and E3 enhancers from the 15 Kb binned 5C interaction matrix. We also calculated and plotted the LOWESS smoothed average plus and minus 1 standard deviation of the 5C signal as a function of genomic distance (representing the expected 5C signal).

## RESULTS

### Inhibition of CBF $\beta$ -SMMHC Activity by AI-10-49 Represses *MYC* Expression

Gene expression analysis in the AI-10-49-treated inv(16) AML cell line ME-1, identified 591 up- and 696 downregulated genes (>2-fold change; false discovery rate [FDR] < 0.01). *MYC* was one of the most repressed genes, with over 10-fold repression compared to untreated (**Fig. 3.3A-B**). Next, we determined whether *MYC* levels regulate survival in inv(16) AML cells. We quantified the cells viability of ME-1 *MYC* knockdown cells using small hairpin RNAs (shRNAs). Compared to scrambled control *MYC* knockdown reduced the viability of ME-1 cells by 66% (**Fig. 3.3C**). This suggests that *MYC* is required for

the maintenance of inv(16) leukemic cells and that reduced MYC levels mediated by AI-10-49 treatment induced cell death.

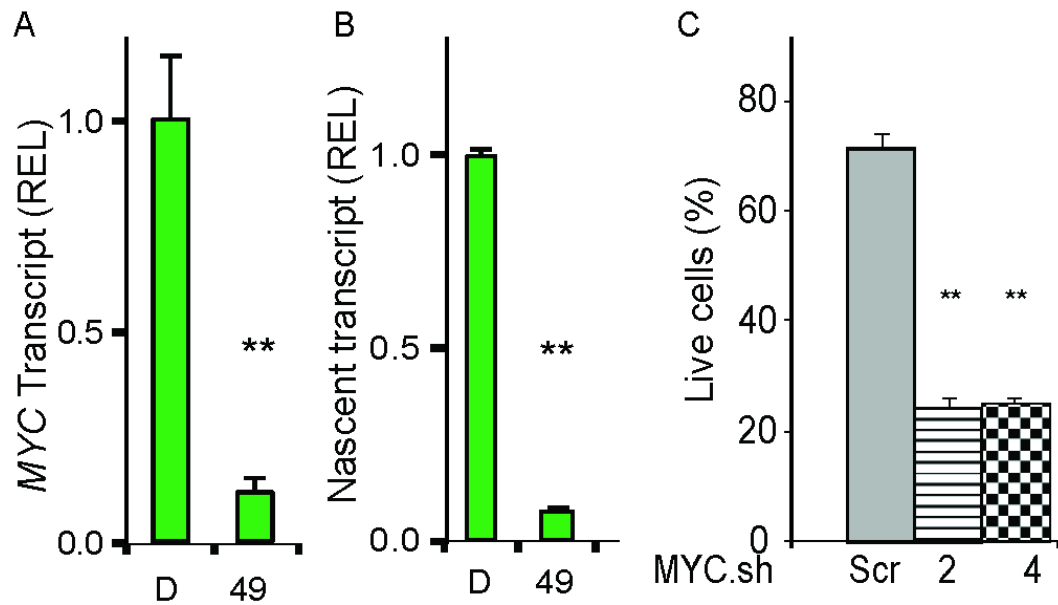


**Figure 3.3: MYC transcript level in response to AI-10-49 treatment.**

(A) MYC transcript levels in ME-1 cells treated with DMSO (D) or AI-10-49 (49), estimated by RT-PCR. (B) MYC nascent transcript levels in treated ME-1 cells, estimated by RT-PCR. (C) Viability analysis (annexin V/7AAD assay) in ME-1, cells transduced with control or MYC shRNAs. Each data point represents the mean of triplicate experiments.

#### AI-10-49 enhances genome-wide RUNX1 DNA binding

ChIP-seq analysis for RUNX1 revealed that AI-10-49 treatment induces a 7-fold increase in RUNX1 binding to its target regulatory elements (**Fig. 3.4A-B**). Analysis of peak distribution indicated a relative enrichment for promoter regions (**Fig. 3.4C**). Runx1 recruits polycomb-repressive complexes (PRC1 and PRC2) to its DNA target, which induces tri-methylation of lysine-27 in histone H3 (H3K27me3), thereby promoting local compaction of the chromatin structure. Therefore, we evaluated whether AI-10-49 can modulate chromatin accessibility in ME-1 cells by using an assay for transposase accessible chromatin with high-throughput sequencing (ATAC-seq) (Buenrostro, Giresi, Zaba, Chang, & Greenleaf, 2013). Analysis of ATAC-seq data in cells treated with DMSO or AI-10-49 revealed that AI-10-49 induced a general reduction in chromatin accessibility (**Fig. 3.4D**). These results suggest that AI-10-49 inhibits CBF $\beta$ -SMMHC / RUNX1 binding, and increases the occupancy of RUNX1 to its targets, especially the gene promoters. Once RUNX1 is bound, it triggers a global reduction in the activity of promoters and enhancers by decreasing DNA accessibility.

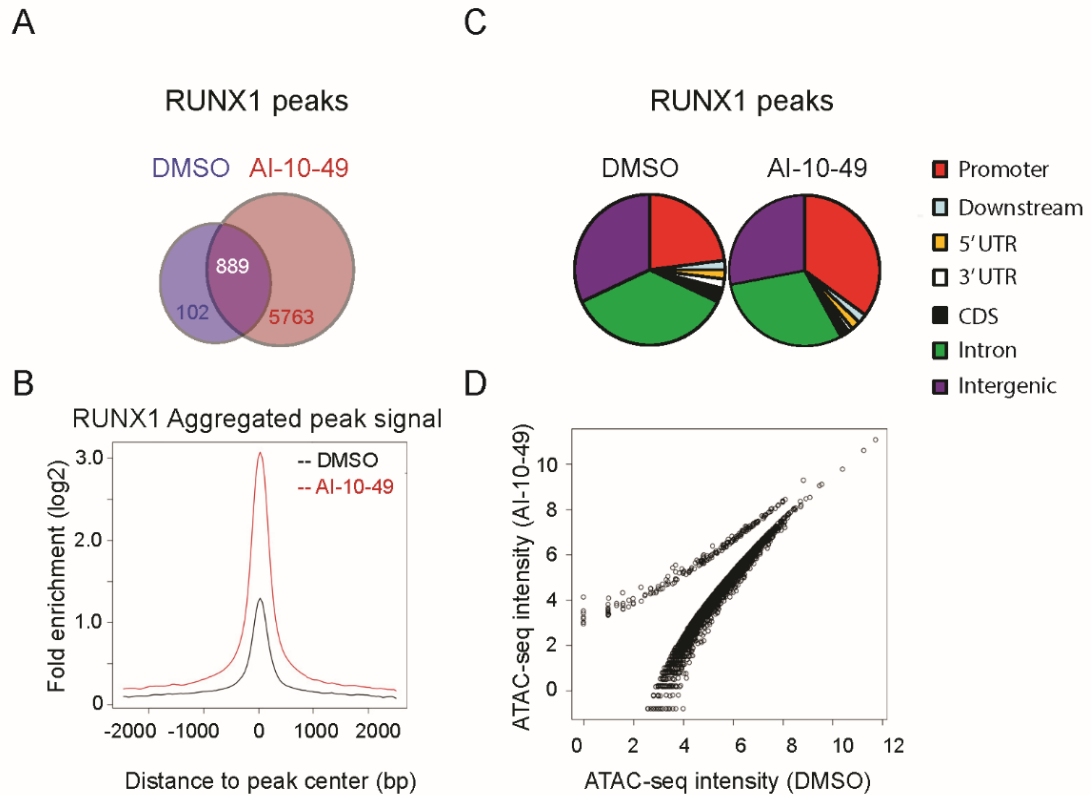


**Figure 3.4: RUNX1 binding in response to AI-10-49 treatment.**

(A, B, and C) RUNX1 ChIP-seq peaks in ME-1 cells. (A) Venn diagram of peak distribution for RUNX1. (B) Aggregated peak signal from peak center treated with DMSO (black) or AI-10-49 (red). (C) Gene distribution RUNX1 peaks in ME-1 cells treated with DMSO (left) or AI-10-49 (right). (D) Scatterplot representing open chromatin peaks by ATAC-seq analysis in DMSO- and AI-10-49-treated cells.

### **RUNX1 represses MYC expression through binding at downstream enhancers**

Active enhancers regulate elements associated with oncogene expression in cancer including tumor-type-specific distal enhancers that regulate oncogenic *MYC* expression in solid tumors (Sigova et al., 2013) (Croce & Helin, 2013)

(Hoke et al., 2013)(America et al., 2009). We hypothesized that AI-10-49 mediated RUNX1 function represses *MYC* expression by perturbing the active distal enhancers. To test this hypothesis, we analyzed a 4 Mb genomic region surrounding the *MYC*-TSS. Analysis of the 2 Mb downstream region revealed no significant changes to chromatin accessibility (by ATAC-seq) and a small reduction in H3K27ac mark in AI-10-49 treated cells (**Fig. 3.5A**). Moreover, analysis of RUNX1 ChIP-seq peaks identified three elements with an increase in AI-10-49 treated cells. The primary RUNX1 peak was within the BDME super-enhancer (BRD4-mediated *MYC* enhancer), located 1.7 Mb downstream of the *MYC*-TSS (**Fig. 3.5A-B**). The BDME associates with the SWI/SNF, BRG1, and BRD4 proteins to regulate *MYC* expression in myeloid cells and in mixed-lineage leukemia (Shi et al., 2013). After AI-10-49 treatment the primary RUNX1 peak was located at element 3 and 5 (E3, E5) of the 5 conserved elements of the BDME (**Fig. 3.5A-B**). The two other RUNX1 peaks at *MYC* enhancer 1 and 2 (ME1 and ME2) were located at 0.18 Mb and 0.5 Mb, respectively, which are downstream of the *MYC* TSS. Surprisingly, RUNX1 peaks were not increased at the *MYC* promoter (**Fig. 3.5A-B**). We evaluated if AI-10-49 treatment would alter binding of the transcription activator p300 in the *MYC* locus, using ChIP-PCR (**Fig. 3.5C**). And p300 was significantly reduced in ME1 and ME2 and in the 5 elements of BDME ( $p < 0.05$ ). These data suggest that the association of RUNX1 with *MYC* regulatory elements ME1, ME2, and E3 enhancers may induce the reduction in *MYC* expression in inv(16) AML cells treated with AI-10-49.

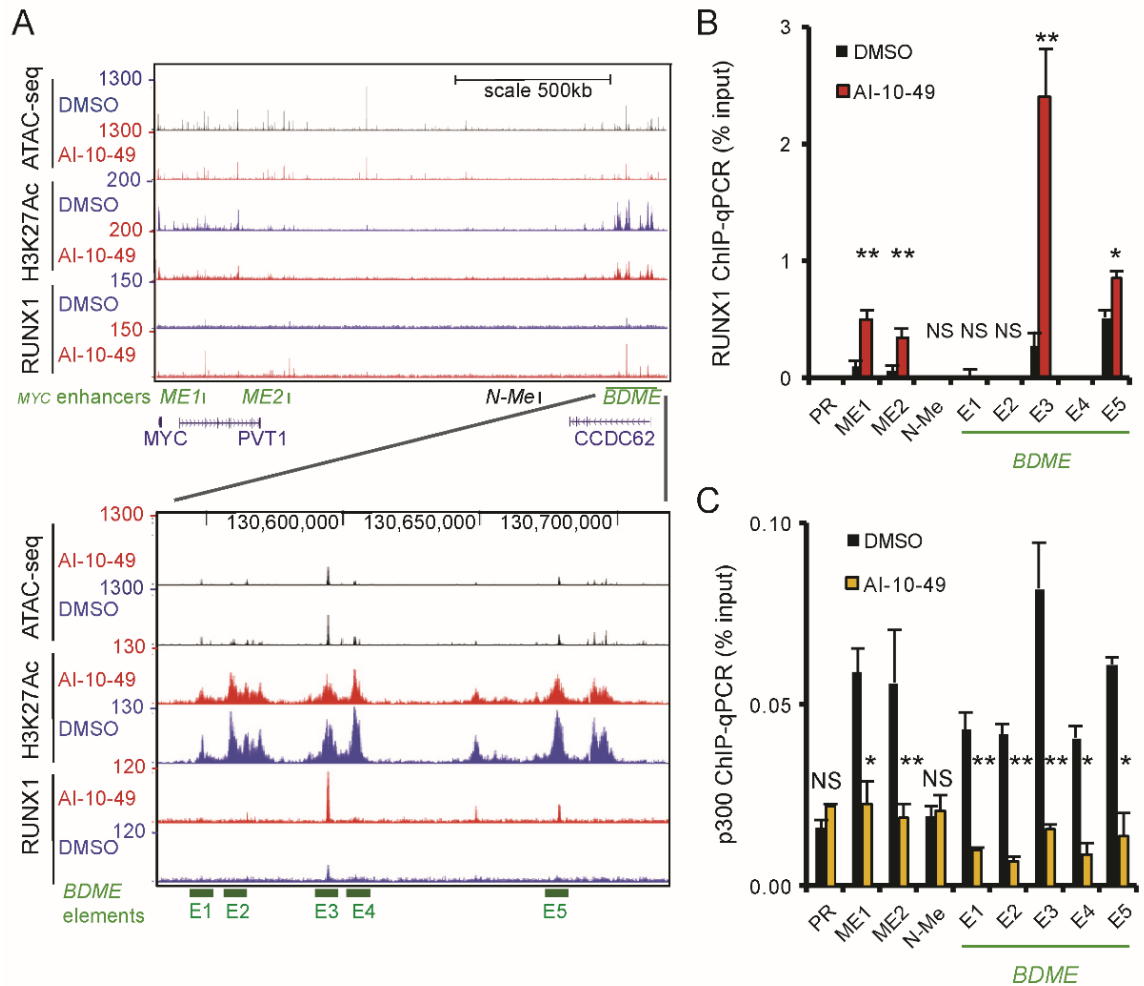


**Figure 3.5: RUNX1 binding to MYC downstream enhancers.**

(A) Analysis of ATAC-seq, H3K27ac, and RUNX1 ChIP-seq profiles, (top) in a 2-Mb genomic region downstream of MYC, the three enhancer regions (ME1, ME2, and BDME) are depicted in green, (bottom) zoom in at the +1.7 Mb BDME super-enhancer. Five previously reported enhancer regions (E1 to E5) are depicted below the profile. (B-C) ChIP-qPCR analysis in ME-1 cells for RUNX1 in DMSO- or AI-10-49-treated cells (B), and for p300 in DMSO or AI-10-49-treated (C).

### **ME1, ME2, and E3 enhancers physically interact with the *MYC* promoter**

Since genes are regulated in the context of topologically associating domains (TADs) ( Nora et al., 2012) (Jesse R Dixon et al., 2012), we were interested to determine whether AI-10-49 repressed *MYC* expression by modulating TAD and/or chromatin loop formation around the *MYC* locus.

A critical determinant of enhancer activity in the regulation of *MYC* expression is the identification of physical interaction between regulatory elements. Considering that distant *MYC* enhancers have been reported up and downstream of *MYC* in a variety of cancers (Yashiro-ohsaki et al., 2014), we analyzed the DNA interactions in a 4 Mb region around the *MYC* locus. This region includes 1 Mb upstream and 3 Mb downstream of the *MYC* TSS and was captured by utilizing chromosome conformation capture (5C) in ME-1 cells treated with DMSO or AI-10-49. We designed 727 forward probes and 733 reverse probes to investigate a total of 532,891 interactions along the 4 Mb region. The connectivity heatmap maps between treatment conditions identified three major TADs. Importantly the second TAD contained the *MYC* gene and downstream enhancers ME1, ME2 and E3 (**Fig. 3.6A**). The second TAD is comprised of three smaller TADs (**Fig. 3.6A**, arrows), wherein the first sub-TAD included *MYC*, ME1, and ME2, and the third sub-TAD included the BDME super-enhancer with E3. Notably, the TADs and CTCF binding were generally weakened by AI-10-49 treatment (**Fig. 3.6A**, right panel). Analysis of the

interaction between these elements using 4C plots anchored at the *MYC* promoter revealed its interaction with ME1, ME2 and E3/E5 enhancers (**Fig. 3.6B**, top). The *MYC* promoter also displays prominent interactions with other elements of the BDME super-enhancer containing CTCF (**Fig. 3.6B**, top, arrowhead). and these interactions become less prominent in AI-10-49 treated cells. Similar analysis with anchoring at ME1, ME2 or E3 confirmed the interactions between the four regulatory elements (**Fig. 3.6B**). Furthermore, analysis of DMSO and AI-10-49 4C plots determined that AI-10-49 treatment did not significantly alter these interactions (**Fig. 3.6B**). These experiments provide critical evidence that the *MYC* promoter physically interacts with the three RUNX1-associated enhancers ME1, ME2 or E3 in inv(16) AML cells before and after treatments with AI-10-49. Which strengthen the hypothesis that *MYC* expression and Viability of inv(16) AML cells depend on the Activity of ME1, ME2, and E3/E5 Enhancers, which recruits the active elements at *MYC* promoter. Furthermore, these results bridge the effect of RUNX1 on decreasing *MYC* expression by binding to its four regulatory elements of ME1, ME2, and E3/E5 after AI-10-49 treatment.



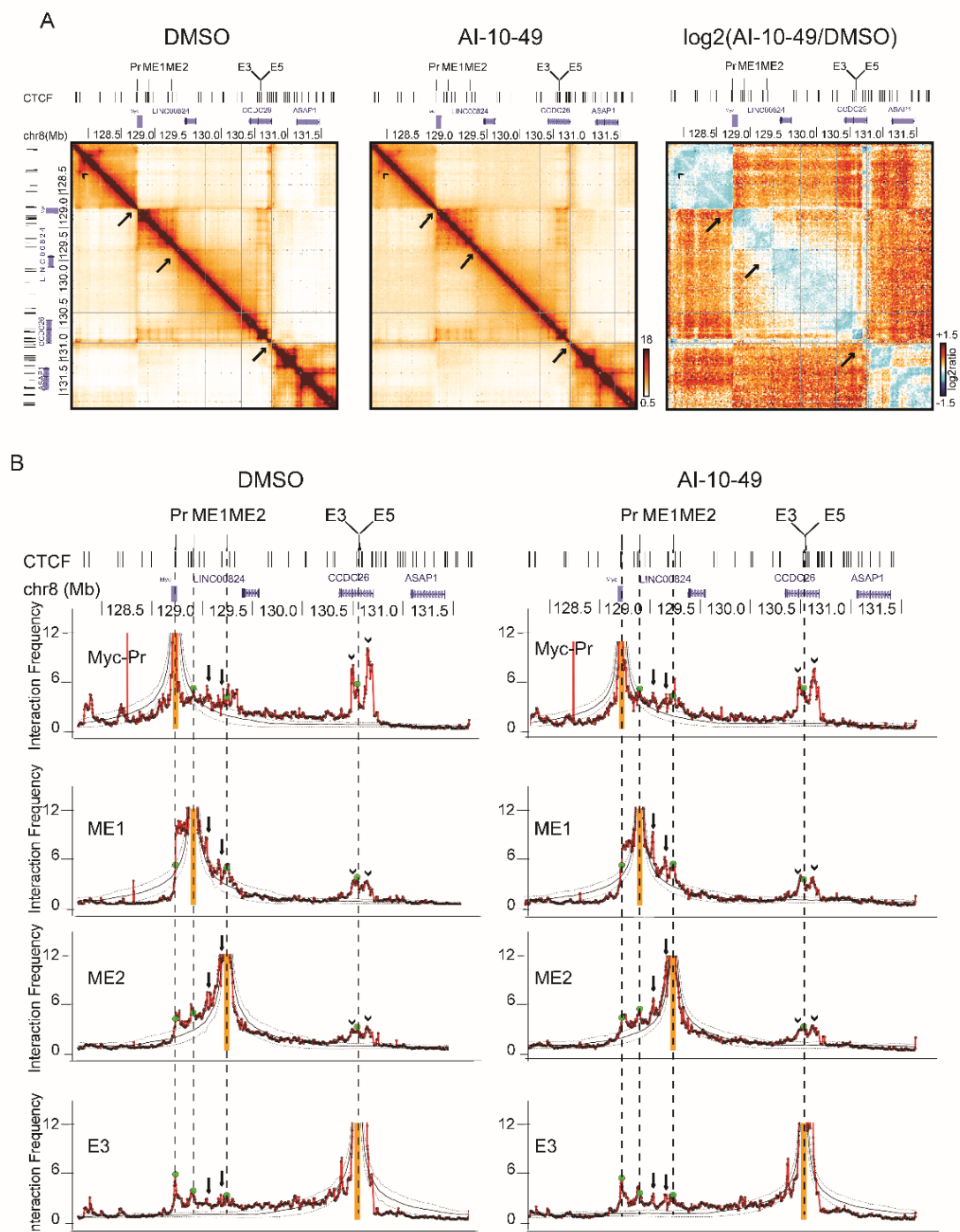


**Figure 3.6: Three enhancers downstream of MYC interact directly with MYC promoter.**

**(A)** 5C interaction matrices for the *MYC* locus for control ME1 cells (treated with DMSO, left panel) and for ME1 cells treated with AI-10-49 for 6 hours (middle panel). The right panel shows the  $\log_2(\text{AI-10-49/DMSO})$  ratio of the interaction matrices (blue color scheme: higher interaction frequencies in DMSO treated cells. Orange color scheme: higher interaction frequencies in AI-10-49 treated cells). Arrows point to TAD boundaries, arrowhead points to an example of a CTCF-CTCF looping interaction. **(B)** 4C-style plots for 15 Kb bins (anchor bins) containing the *MYC* promoter (*MYC*-Pr), ME1, ME2, and E3 enhancers for DMSO and AI-10-49 treated cells. Anchor bins are shown in orange, solid black lines represent the LOWESS mean (the expected interaction frequency as a function of genomic distance) and the dotted black lines are the LOWESS plus and minus 1 standard deviation. Redline is the observed 5C interaction frequencies. Green dots and vertical dotted lines highlight the positions and interactions between *MYC*-Pr, ME1, ME2, and E3. Arrowheads indicate interactions with CTCF sites around the BDME super-enhancer. Arrows indicate peaks of interactions pointing to loci interacting with *MYC*-Pr, ME1, ME2, and E3.

### ***MYC* expression and viability of inv(16) AML cells depend on ME1, ME2, and E3 enhancers**

After confirming the direct physical contact between *MYC* and the three regulatory elements ME1, ME2, and E3, we wanted to establish the functional significance of the three enhancers identified in inv(16) AML cells by single deletion of each enhancer utilizing CRISPR/Cas9 technology. We asked whether single deletions are sufficient to alter *MYC* expression. ME-1 cells were transfected with Cas9 and two guide RNAs for each enhancer, in order to produce deletions for each of the three enhancers. Analysis of sequencing results determined that sites within the enhancers showed frequent deletion of 41 bp (ME1), 67 bp (ME2), and 275 bp (within the approximately 2,800 bp of E3), with the overall frequency of deleted RUNX binding site alleles ranging from 77 to 99%. Furthermore, these single deletions resulted in 40% to 50% reduction in *MYC* expression (**Fig. 3.7B**) and a reduction of cell viability (60% to 70%) (**Fig. 3.7C**). Taken together, these data demonstrate that ME1, ME2, and E3 function as enhancers to maintain *MYC* expression levels and the viability of inv(16) AML. However, deletion of N-Me did not affect *MYC* expression, which interacts and regulate *MYC* In acute lymphoblastic leukemia (ALL) of T-cell type “T-ALL cell lines”. (Yashiro-ohitani et al., 2014)

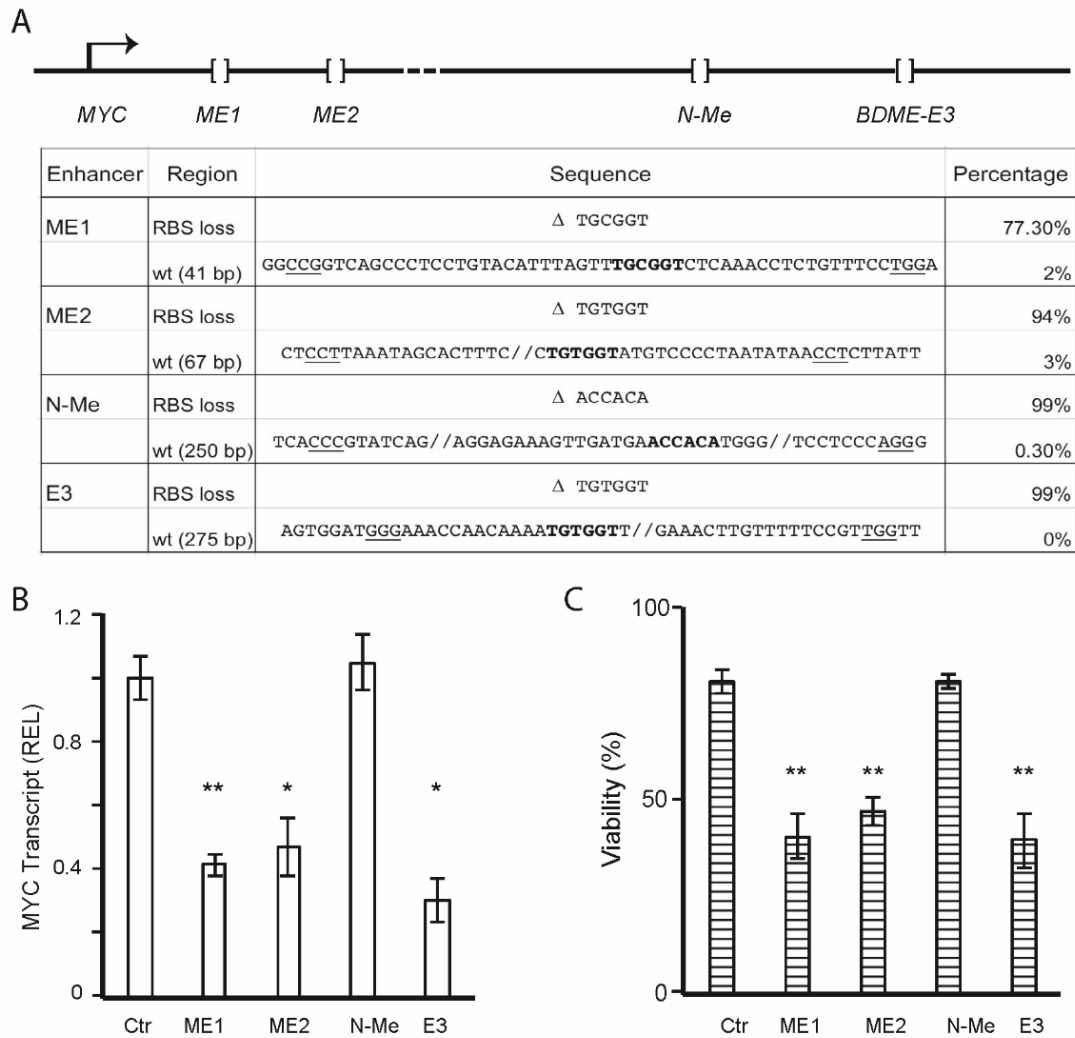


**Figure 3.7: Deletion of Three RUNX1-Associated MYC Enhancer Elements Impairs MYC Expression and Viability of *inv(16)* AML**

(A) Schematic of CRISPR/Cas9-mediated deletion of MYC enhancer elements (top) and frequency of deletions with RUNX1 binding site (RBS, bold) loss and of wild-type (WT) alleles at each element by sequencing analysis (bottom); PAM sequences are underlined. (B and C) MYC expression analysis by qRT-PCR (B) and viability (Annexin V-/7AAD-) analysis (C) of ME-1 cells edited for single MYC enhancers, using CRISPR/Cas9.

### **AI-10-49 induces a switch of SWI/SNF active to PRC-repressive complexes at the AML-associated *MYC* enhancers**

RUNX1 associates with chromatin-modifying proteins, including histone deacetylases to modulate its association with activating and repressing chromatin complexes active chromatin complexes. Therefore, we assessed AI-10-49-mediated changes in chromatin complex BRG1 occupancy a component of the SWI/SNF complex that participates in BDME-mediated *MYC* expression (Shi et al., 2013). ChIP-qPCR analysis in ME-1 cells revealed that BRG1 is displaced from the *MYC* promoter, ME1, ME2, and BDME elements after AI-10-49 treatment (**Fig. 3.8A**). In addition, the active enhancer-specific histone mark histone H3 Lys 4 mono-methylation (H3K4me1) was significantly reduced at ME1, ME2, and ME3, but not at the *MYC* promoter ( $p < 0.05$ ) after AI-10-49 treatments (**Fig. 3.8B**). Similarly, *SMARCA4* knockdown (the *BRG1* gene) reduced *MYC* levels ( $p < 0.005$ ) (**Fig. 3.8C**). These results suggest that inhibition of CBF $\beta$ -SMMHC binding to RUNX1 leads to an increase of RUNX1 binding at *MYC* distal enhancers, which causes the removal of SWI/SNF-activating complexes. On the other hand, after AI-10-49 treatment RING1B binding and H3K27me3 marks significantly increased at the *MYC* promoter and distal enhancers (**Fig. 3.8D-E**). Similarly, *MYC* expression was partially rescued by *RNF2* knockdown (the *RING1B* gene) in treated inv(16) AML cells (**Fig. 3.8F**). To define the dynamics of chromatin complex replacement associated with AI-10-49 treatment in inv(16) AML, we performed time-course ChIP-qPCR for RUNX1, RING1B, and BRG1 at E3 in ME-1 cells AI-10-49 treated for 6 hr (**Fig. 3.8G**).

RUNX1 and RING1B binding show a similar pattern, increasing at approximately 2.5 hr, and reaching 90% occupancy by 5 hr. Conversely, BRG1 binding was reduced between 4 and 6 hr of treatment (**Fig. 3.8G**). In addition, we evaluated the interaction between RUNX1 and BRG1 or RING1B at E3 utilizing ChIP-re-ChIP technique. This analysis revealed that RUNX1 specifically interacts with RING1B, but not with BRG1 at E3 and that this interaction is induced by AI-10-49 treatment (**Fig. 3.8H**).

These results indicate that AI-10-49 induces RUNX1 mediated repression of *MYC* expression by RUNX1 directing the recruitment of PRC-repressive complexes to the *MYC* enhancers, thereby evicting the SWI/SNF activating complexes.

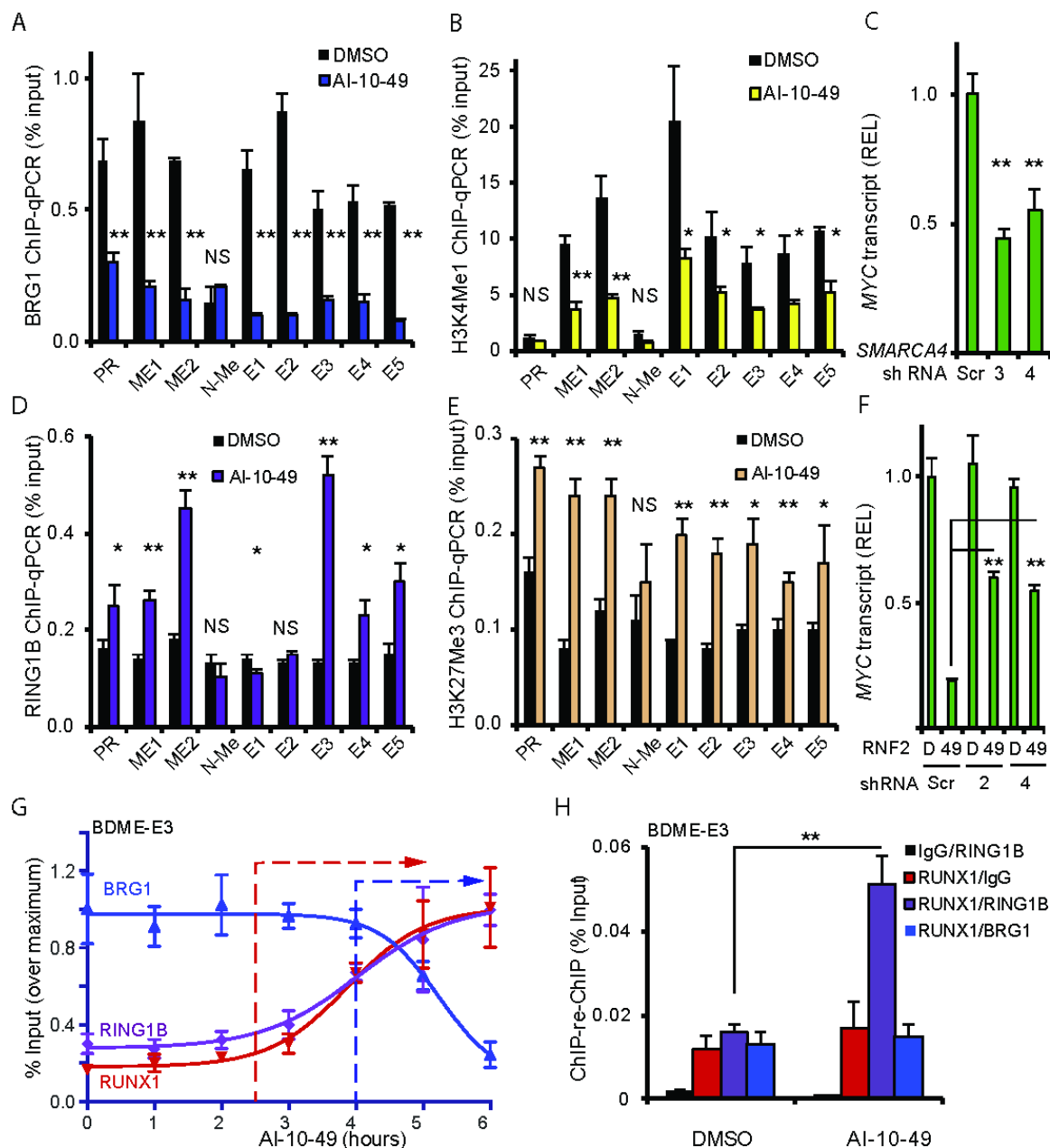


**Figure 3.8: AI-10-49 Induces a Switch of Activation for Repressive Marks at RUNX1-Associated MYC Enhancers.**

(A and B) ChIP-qPCR analysis of treated ME-1 cells at the promoter (PR) and eight MYC enhancers (ME1, ME2, N-Me, and BDME elements E1 to E5) for BRG1 (A) and H3K4me1 (B). (C) MYC transcript level analysis in ME-1 cells transduced with scramble (Scr) or SMARCA4 shRNAs (sh3 and sh4), estimated by qRT-PCR. (D and E) ChIP-qPCR analysis of treated ME-1 cells at MYC

promoter and MYC enhancers for RING1B (**D**) and H3K27Me3 mark (**E**). (**F**) MYC transcript level analysis in ME-1 cells transduced with scramble (Scr) or RNF2 shRNAs (sh2 and sh4) and treated with DMSO (D) or AI-10-49 (49), estimated by qRT-PCR. (**G**) Time-course ChIP-qPCR analysis of RUNX1, RING1B, and BRG1 binding at E3 in treated ME-1. (**H**) Quantitative ChIP-re-ChIP of treated ME-1 ChIPed for RUNX1 or immunoglobulin G (IgG) and re-ChIPed for IgG (red), RING1B (violet), or BRG1 (blue), at the E3 enhancer.

## CONCLUSION

### Transcription factor function can determine leukemia maintenance

In the present study, we have investigated the mechanism underlying the dependency of inv(16) AML cells on the function of the fusion protein CBF $\beta$ -SMMHC. We demonstrate that acute release of the RUNX1 transcription factor from CBF $\beta$ -SMMHC directs the replacement of chromatin remodeling complexes at three *MYC* distal enhancer elements, which decrease *MYC* expression and induces cell death in inv(16) AML cells. Our study provides new insights on how transcription factor function can determine leukemia maintenance. We demonstrate that one mechanism by which CBF $\beta$ -SMMHC maintains inv(16) AML cell viability is by blocking RUNX1 repression of *MYC* expression.

### The direct role of RUNX1 in *MYC* repression

The balance between SWI/SNF and PRC epigenetic complexes modulates enhancer activity. SWI/SNF has an oncogenic function in AML (Shi et al., 2013) and rapidly evicts PRC1 from chromatin in a BRG1 dependent manner (Stanton et al., 2016). Therefore, the competition between BRG1 and RING1B



activities seem to be critical for inv(16) AML survival. We found that inhibition of RUNX1 binding to CBF $\beta$ -SMMHC does not increase RUNX1 binding at *MYC* promoter, but does increase RUNX1 occupancy at three distal enhancers downstream of *MYC*. Therefore, RUNX1 binding at the distal enhancers promotes the disassociation of the BRG1 and association of RING1B, which provides a mechanistic explanation for the observed phenotype. Analysis of our results provide evidence to strengthen the direct role of RUNX1 in *MYC* repression. First, the results from 5C assays indicate that the three RUNX1-bound enhancers physically interact with each other and with the *MYC* promoter in inv(16) AML cells. Second, the deletion of discrete DNA regions that include the RUNX1 binding sites in each of these enhancers is sufficient to reduce *MYC* expression, alter chromatin marks in the region, and induce cell death. Third, ChIP-re-ChIP assays indicate that RUNX1 directly binds to RING1B at E3 after treatment. Therefore, acute RUNX1 activity, probably in consort with other cofactors, may direct the eviction of SWI/SNF complexes and binding of PRC repressive complexes at the distal enhancers.

### **Enhancers can modulate the expression of their targets gene in a pair-wise manner**

5C data indicate that RUNX1-mediated replacement of chromatin complexes and subsequent repression of *MYC* expression took place without altering the architecture of the locus. This suggests that disruption of enhancer-

promoter looping may not be required to repress target gene expression. Instead, changes in transcription factor availability and subsequent association with chromatin complexes at pre-established loops may be more efficient to disrupt target gene expression. Interestingly, RUNX1 has not been directly associated with *MYC* expression in hematopoiesis and may suggest that the looping interactions detected between *MYC* gene ME1, ME2, and E3/E5 distal enhancers in ME-1 are not established in hematopoietic stem cell, which delineates RUNX1 binding in the enhancers from *MYC* expression.

## **CHAPTER IV: Compartment-dependent chromatin interaction dynamics revealed by liquid chromatin Hi-C**

The content of this chapter is a manuscript in the process of submission.

**Houda Belaghzal**<sup>1\*</sup>, Tyler Borrman<sup>2\*</sup>, Andrew D. Stephens<sup>3</sup>, Denis L. Lafontaine<sup>1</sup>, Sergey Venev<sup>1</sup>, Zhiping Weng<sup>2</sup>, John F. Marko<sup>3,4</sup>, Job Dekker<sup>1</sup>

### **SUMMARY**

Chromosomes are folded so that active and inactive chromatin domains are spatially segregated to form a variety of sub-nuclear neighborhoods. Compartmentalization is thought to occur through polymer phase/microphase separation mediated by interactions between loci of similar type. The nature and dynamics of these interactions are not known. We developed liquid chromatin Hi-C to map the stability of associations between loci genome-wide. Before fixation and Hi-C, chromosomes are fragmented removing the strong polymeric constraint to enable detection of intrinsic locus-locus interaction stabilities and chromatin mobility. Nuclear compartmentalization is stable when fragments are over 10-25 kb in length. Fragmenting chromatin into pieces smaller than 6 kb led to a gradual loss of spatial genome organization. Dissolution kinetics of chromatin interactions vary widely for different chromatin domains, with lamin associated domains being most stable, and speckle-associated loci most dynamic. The polycomb-enriched B1 subcompartment also displayed highly

unstable interactions. Cohesin-mediated loops dissolve after fragmentation, possibly because cohesin rings can slide off nearby DNA ends. Liquid chromatin Hi-C provides a genome-wide view of chromosome interaction dynamics, revealing a remarkable diversity in conformational stability at different sub-nuclear structures

## INTRODUCTION

The spatial organization of chromosomes plays roles in many aspects of genome function, including gene regulation, DNA replication, DNA repair, and chromosome compaction and segregation. Genomic and imaging approaches are producing high-resolution descriptions of the conformation of chromosomes in cell populations, in single cells, across the cell cycle, and during development (Kind et al., 2013) (Bonev & Cavalli, 2016) (Job Dekker & Mirny, 2016)(Chen et al., 2018)(Lieberman-aiden et al., 2009)(Job Dekker & Misteli, 2015b) (Job Dekker, 2014)(Wang et al., 2016b)( Rao et al., 2014).

Major new questions revolve around the molecular and biophysical processes by which different aspects of chromosome conformation form. Significant progress has been made in developing and testing mechanistic models for TAD and loop formation. The model that currently has most experimental support proposes that TADs and loops form via loop extrusion performed by the cohesin complex (Alipour & Marko, 2012)(Fudenberg et al., 2015) (Sanborn et al., 2015) (Bouwman & Laat, 2015) (Nichols & Corces,

2015)(Schwarzer et al., 2017). Much less is known about the processes that determine nuclear compartmentalization. Mechanisms of compartmentalization are distinct from the formation of TADs and loops, as mutations in CTCF or cohesin disrupt TADs but not compartmentalization per se (Nora et al., 2017) (Nuebler et al., 2018) (Haarhuis et al., 2017) (Extension et al., 2017) (Glenn et al., 2017) (Schwarzer et al., 2017)(Wutz et al., 2017). Compartmentalization has been proposed to be the result of polymer phase separation driven by attractions between chromatin domains of the same or similar status (Lieberman-aiden et al., 2009) (Pieroo et al., 2016) (Falk et al., 2019) (Erdel & Rippe, 2018) (Jost et al., 2014) (Micheletto et al., 2016) (Nuebler et al., 2018) (L. Liu et al., 2018)(Shin et al., 2018). Polymer models simulating such attractions can reproduce the plaid pattern characteristic of Hi-C interaction maps (Jost et al., 2014) (Micheletto et al., 2016) (Pieroo et al., 2016) (Falk et al., 2019). However, the molecular and biophysical basis of these attractions is unknown. Possibly these attractions result from co-association of domains with sub-nuclear bodies that themselves appear to form by a process of liquid-liquid phase separation (Feric et al., 2016) (Larson et al., 2017) (Marzahn et al., 2016) (Strom & Alexander, 2017). An example is the interaction between heterochromatic loci driven by multivalent interactions among HP1 proteins and between HP1 proteins and H3K9me3-modified chromatin domains (Larson et al., 2017) (Strom & Alexander, 2017).

Hi-C contact maps readily reveal global spatial separation of active and inactive chromatin domains, and Hi-C sub-compartments suggest the presence of a

number of different types of sub-nuclear neighborhoods. However, Hi-C interaction maps are population-averaged, steady-state datasets and do not reveal the biophysical nature of the interactions that lead to this diverse set of nuclear neighborhoods or the dynamic mobility of loci within these compartments. For instance, A and B compartments appear equally prominent in Hi-C datasets, but whether the forces that lead to their formation are equally strong, frequent, or dynamic is not known.

Live-cell imaging studies have shown that loci are constrained in their motion and that there are substantial variations in the dynamics and mobility of different loci, e.g. euchromatic vs. heterochromatic loci and loci tethered to the nuclear periphery vs. loci located in the nuclear interior (Foisner & Garini, 2015) (Hediger et al., 2002) (Marshall et al., 1997) (Nagashima et al., 2019) (Shinkai, Nozaki, Maeshima, & Togashi, 2016) (Thakar, Gordon, & Csink, 2006). Such differences can be reproduced in coarse-grained simulations of chromatin (L. Liu et al., 2018). Imaging-based studies have been instrumental in uncovering aspects of chromatin interactions and dynamics, but are limited in scale, i.e. only one or a few specific loci can be studied at one time. In addition, when whole genome dynamics is analyzed microscopically (Zidovska, Weitz, & Mitchison, 2013), positions of specific sequences have not as yet been determined.

New approaches are required to identify and quantify the molecular processes and biophysical forces that drive chromosome and nuclear compartmentalization

and to characterize the dynamics and mobility of loci within these compartments. Here we describe liquid chromatin Hi-C, a Hi-C variant that quantifies the stability of chromosome conformation and chromatin interactions between loci genome-wide. We find that different types of nuclear sub-compartments differ in stability of chromatin interactions. The results suggest that compartmentalization is mainly due to strong and stable heterochromatic interactions, while associations between open regions at and around nuclear speckles, and between loci in the B1 sub-compartment enriched in polycomb binding, are more dynamic.

## **MATERIALS AND METHODS**

### **Digestion, cross-linking and copolymer architecture and hetero/euchromatin phase separation**

We have found that moderate digestion leads to formation of stronger inter-compartment interactions in Hi-C. While this may seem somewhat paradoxical at first glance, this effect is rather straightforward to explain if we remember two basic physical facts about chromatin in the G1 nucleus. First, individual chromosomes have a "blocky" structure, with hundreds of kilobase-scale stretches of alternately heterochromatin-like and euchromatin-like character along their length. Second, the chromatin is in a state of quite extensive "crosslinking" (i.e., noncovalent chromatin-chromatin interactions mediated by

proteins including gene regulatory factors such as cohesin, and heterochromatin linkers such as HP1 $\alpha$ .

Therefore, chromatin in the G1 nucleus can be considered as a set of blocks of euchromatin and heterochromatin (the A and B compartments consisting of regions of predominantly euchromatin vs heterochromatin, respectively), which are constrained to be near each other by being part of the same linear chromosomes, i.e., effectively being long many-block copolymers. We suppose that the A and B heterochromatin/euchromatin monomers have a weak tendency to repel one another (or equivalently that A-A or B-B attract one another, for example via protein-mediated nucleosome-nucleosome interactions acting preferentially on euchromatin or heterochromatin, or even via physio-chemical effects such as relative hydrophobicity of more methylated nucleosomes).

If we suppose the A and B blocks to be on average  $N$  monomers long (roughly nucleosomes for the sake of this discussion), then under melt-like conditions the standard Flory theory of polymer phase separation predicts that if we were to cut the polymers into pure A and B blocks at the block boundaries (i.e., at a spacing of  $N$  monomers commensurate with the block sizes), they would phase separate for a segment-segment interaction strength stronger than  $\chi^* = 2/N$ . Note that this level of interaction (given approximately in  $k_B T$  units) is proportional to  $1/N$  where  $N$  is crudely in nucleosome units; for 200 kilobase blocks, we have approximately  $N=1000$ , indicating that small fractions of a  $k_B T$



in effective A/B repulsion or A-A or B-B attraction is sufficient to drive strong euchromatin/heterochromatin phase separation (Marshall et al., 1997)

Now if we were to instead cut less frequently than this, say at every second block boundary, so as to arrive at a system of AB linear diblock copolymers each of length  $2N$  ( $N$  monomers of A followed by  $N$  monomers of B), the constraint that the A and B blocks be connected suppresses phase separation, increasing the critical interaction (all other factors held constant) to  $\chi^* = 5.3/N$  (Leiblerf, 1980). In this case bulk phase separation cannot occur, but instead local, or "microphase separation" occurs, with formation of micelle-like or layered phase-separated structures. Nevertheless, for  $\chi \gg \chi^*$ , strong segregation of the A and B monomers can still occur.

If we were to not cut at all, but rather to suppose that the chromosomes are very long multiblock copolymers, with many blocks each of  $N$  monomers alternating between A and B ("ABABABAB... multiblock copolymers"), the critical interaction strength will rise with increasing number of blocks, approaching the limit  $\chi^* = 7.5/N$  for many blocks {Matsen, 1994 #1534}. Therefore, starting from this limit, the tendency for chromosome domains to phase separate will be enhanced by cutting the chromosomes up into successively smaller pieces: as chromatin cutting increases from no cutting, we expect to see intensification of A/B compartment contrast in the Hi-C map.

Now, if we cut too frequently, when the cuts become spaced smaller than the block size (cut spacing  $M < N$  monomers), we will have the situation that the critical interaction strength will become  $\chi^* = 2/M > 2/N$ , i.e., the cuts are frequent enough to suppress phase separation by decreasing the amount of interaction enthalpy per polymer "molecule". Therefore we expect that overly frequent cutting will cause a reduction in A/B compartment Hi-C map contrast, i.e., for some intermediate level of cutting similar to the sizes of the A and B blocks, one will see a maximum level of A/B compartment contrast.

There is also likely an effect of "crosslinking" ("chromatin cross-bridging"), which provides an additional level of constraint suppressing phase separation, above the linear-multiblock architecture of chromosomes. For example, taking linear diblock copolymers ( $N$  A monomers followed by  $N$  B monomers) and circularizing them raises the critical interaction for microphase separation from  $5.3/N$  to  $8.9/N$ , nearly a factor of 2 (Separation & Rings, 1993)

Similarly, if we start with A and B homopolymers each of length  $N$ , constraining them to have their ends at a flat surface, thus forcing them to mix at the surface, increases the critical interaction for phase separation from  $2/N$  up to  $4.5/N$  {Marko, 1991 #1536}, with microphase separation again occurring in the constrained case. Releasing chromatin crosslinking/cross-bridging constraints (which also will occur for chromatin cutting) will in general also reduce the interaction strength needed to drive phase separation, increasing A/B compartment contrast in Hi-C maps.

In conclusion, basic polymer phase separation theory predicts that gradually increasing the cleavage of chromatin will gradually increase the intensity of A/B compartment contrast in Hi-C maps until the cuts are spaced by approximately one A or B block; further cutting will reduce the intensity of phase separation and A/B compartment contrast. Notably, the nature of the segregation can be expected to be "microphase segregation" rather than bulk phase separation, until the number of cuts is sufficient to liberate A or B "homopolymer" segments.

### **K562 nuclei purification**

Three sucrose cushions were made before starting nuclei purification. 30 mL of 30% sucrose [10 mM PIPES pH 7.4, 10 mM KCl, 2 mM MgCl<sub>2</sub>, pH adjusted to 7.4 using 1 N KOH, 30% sucrose, 1 mM DTT (added prior to use), 1:100 protease inhibitor (Thermo Fisher 78438) (added prior to use)] was transferred to a 50 mL tube, then 5 mL of 10% sucrose [10 mM PIPES pH 7.4, 10 mM KCl, 2 mM MgCl<sub>2</sub>, 10% Sucrose, 1 mM DTT (added prior to use), 1:100 protease inhibitor (added prior to use)] was slowly loaded in top of 30% sucrose, and the tubes were incubated at 4°C until needed. K562 cell pellets (100 million cells) were lysed using the following nuclear isolation procedure. After the cells were spun, the pellets were washed twice with 10 mL HBSS, then pelleted after each wash at 300 rpm for 10 min at 4°C. Cell pellets were dissolved in 15 mL nuclear isolation buffer [10 mM PIPES PH 7.4, 10 mM KCl, 2 mM MgCl<sub>2</sub>, 1 mM DTT (added prior to use), 1:100 protease inhibitor (added prior to use)], pH

adjusted to 7.4 using 1 M KOH]. Then, cells were lysed on ice in a 15 mL Dounce homogenizer with pestle A (KIMBLE Kontes 885002-0015) by moving the pestle slowly up and down 20 times, followed by incubation on ice for 20 min and another 20 strokes. Next, each 5 mL of lysed extract was loaded slowly on top of a sucrose cushion prepared earlier. Then the tubes were spun for 15 min at 800 g at 4°C. The supernatant was removed carefully for a good recovery of the nuclei pellet in the bottom of the tube. Nuclei pellets were resuspended in 1 mL of HBSS, then spun for 5 min at 5,000 g at 4°C using a benchtop refrigerated centrifuge. Then, the nuclei pellet was resuspended in 3 mL HBSS, and 1 µL was taken to quantify the nuclei before the 3 mL was split over two microfuge tubes and spun for 5 min at 5,000 g at 4°C using a benchtop refrigerated centrifuge. Finally, the nuclei pellet was dissolved into an adequate total volume to obtain 1 million nuclei per 0.1 mL of Nuclei storage buffer (NSB) [10 mM PIPES pH 7.4, 10 mM KCl, 2 mM MgCl<sub>2</sub>, 50% glycerol, 8.5% sucrose, 1 mM DTT (added prior to use), 1:100 protease inhibitor (added prior to use)]. Each 0.5 mL of NSB containing 5 million nuclei was transferred to a microfuge tube and stored at -80°C.

### **3C (Chromosome Conformation Capture)**

3C was performed as described in “From cells to chromatin: Capturing snapshots of genome organization with 5C technology” (Dostie et al., 2006).

Crosslinking: 1.25 mL of 37% formaldehyde was added to 40 mL of HBSS. 50 million cells or nuclei were washed twice using 20 mL of HBSS and

then pelleted at 500 g for 10 min. The pellet was resuspended in 5 mL HBSS and then added to 41.25 mL of HBSS and formaldehyde (final formaldehyde concentration was 1% ). The sample was incubated at RT for 10 min on a rocking platform. Afterward, to stop cross-linking 2.5 mL of 2.5 M glycine was added and samples were incubated at RT for 5 min on a rotating platform. To pellet the crosslinked cells or nuclei the sample was centrifuged at 800 g for 10 min at 4°C. After discarding the supernatant the pellet was washed twice using HBSS. Next, the pellet was either processed immediately as described below or was stored at -80 °C after flash freezing using liquid nitrogen.

Cell lysis: (This step was included when cells are used, but was skipped for 3C with purified nuclei). Cells were lysed by adding 2 mL of cold lysis buffer [10 mM Tris-HCl (pH=8.0), 10 mM NaCl, 0.2% Igepal CA-630 (NP40)] and 20 µL of 100x Protease inhibitors. The sample was incubated on ice for 15 min to let the cells swell. The cells were lysed on ice using the homogenizer with pestle A (KIMBLE Kontes 885300-0002) by moving the pestle slowly up and down 30 times and incubating on ice for 1 min followed by another 30 strokes. The sample was transferred to two 1.5 mL microcentrifuge tubes, spun at 5,000 g at RT for 5 min using a benchtop centrifuge.

Digestion: each pellet was washed using 1 mL cold 1X NEBuffer 2.1, then spun at 5,000 g for 5 min at RT using a benchtop centrifuge, afterward each pellet was resuspended in 250 µL of 1X NEB2.1 buffer, and the two pellets were pooled (~ 500 µL). 50 µL aliquots of the suspension were transferred to 10 new

1.5 mL microfuge tube and 292  $\mu$ L of 1x NEBuffer 2.1 was added to each tube. Next, 38  $\mu$ L of 1% SDS was added per tube and mixed well, the samples were incubated at 65°C for 10 min, then placed on ice. 44  $\mu$ L of 10% Triton X-100 was added to each tube to quench SDS. Finally, 400 U of EcoRI (NEB R0101L) was added per tube and incubated at 37°C overnight on a thermocycler (with 900 rpm for 30 sec every 4 min).

Ligation: 86  $\mu$ L of 10% SDS was added to the digested samples and the samples were then incubated at 65°C for 30 min for EcoRI inactivation after which the tubes were placed on ice. Each sample was then transferred to a 15 mL conical tube and 7.69 mL of ligation mix was added [820  $\mu$ L 10% Triton X-100, 820  $\mu$ L 10x ligation buffer (500 mM Tris-HCl pH7.5, 100 mM MgCl<sub>2</sub>, 100mM DTT), 82  $\mu$ L 10 mg/mL BSA, 82  $\mu$ L 100 mM ATP and 5.886  $\mu$ L ultrapure distilled water]. Finally, 10 U of T4 ligase (Invitrogen 15224090) was added per tube before incubation at 16°C for 2 hr on a thermocycler (with 900 rpm for 30 sec every 4 min).

Reverse Crosslinking: 50  $\mu$ L of 10 mg/mL proteinase K (Fisher BP1750I-400) was added per tube, the sample was incubated at 65°C for 4 hr followed by a second addition of 50  $\mu$ L 10 mg/mL Proteinase K and overnight incubation at 65°C on a thermocycler (with 900 rpm for 30 sec every 4 min).

DNA purification: Tubes were cooled at room temperature, at this stage each tube contains ~ 8.21 mL final volume. The samples from every two tubes were combined to a 50 mL conical tube (~16,42 mL) to have five tubes in total.

DNA was extracted by adding an equal volume of 17 mL of saturated phenol pH8.0: chloroform (1:1) (Fisher BP1750I-400) and vortexing for 3 min. Then the mix was transferred to a 15 mL phase-lock tube (Quiagen 129073) followed by spinning tubes at 5,000 g for 10 min. The upper phase was taken to a 50 mL tube to start the second extraction. We added an equal volume of 17 mL saturated phenol pH 8.0: chloroform (1:1), vortexing for 1 min. Then the upper phase was transferred to a 15 mL phase-lock tube, and tubes were centrifuged at 5,000 g for 10 min. We pooled all the upper phases from all 5 tubes ~ 85 mL into a single 300 mL high-speed centrifuge tube to precipitate the DNA. 8.5 mL (1/10 volume) of 3M sodium acetate pH 5.2 was added and brief vortexing was performed, then 212 mL (2.5 volumes) of ice-cold 100% ethanol was added, and the tube was inverted slowly several times and incubated at -80° C for 1 hr. Afterward, the DNA was pelleted at 16,000 g for 30 min at 4°C. The supernatant was discarded and the pellet was dissolved in 500 µL 1X TLE and transferred to a 0.5 mL AMICON Ultra Centrifuge filter (UFC5030BK EMD Millipore). The column was centrifuged for 5 min at 14,000 g and the flow-through was discarded. The column was washed 4 times using 450 µL of 1X TLE for desalting DNA. After the final wash, the library remaining in the column (~50 µL) was eluted in 30 µL of 1XTLE, the column was flipped upside down into a new tube to collect DNA by centrifugation for 3 min at 4,000 g. RNA was degraded by adding 1 µL of 10 mg/mL RNAase A and incubation for 30 min at 37°C.

Quality control assessment: to test the quality of the 3C library we used PCR to amplify a specific ligation product formed by two nearby restriction fragments, using the following primers:

GPF33: GACCTCTGCACTAGGAATGGAAGGTTAGCC

GPF23: GACTAATTCCTGACACTACTTGAGGGATAC

The amplicon was digested with EcoRI to assess the efficiency of 3C ligation.

### **BAC library for 3C-PCR**

BAC DNA was generated as described (Dostie et al., 2006). A control ligation library covering the Beta-globin locus (ENCODE region ENm009) was generated using BACs overlapping the region. Starting with a mixture of DNA of seven BACs (CTC-775N13, RP11-715G8, CTD-3048C22, CTD3055E11, CTD-2643I7, CTD-3234J1, and RP11-589G14) (Invitrogen), mixed in equimolar ratios, we used the same steps described in the 3C protocol above starting from the digestion step. BAC clones were digested with EcoRI, then randomly ligated, and the DNA was purified. The BAC ligation library reflects random ligation of EcoRI fragments throughout the beta-globin locus, so any difference in PCR signal for 3C primer pairs along the beta-globin locus due to differences in primer efficiency can be corrected by normalizing the amount of PCR product obtained with the 3C library to the amount obtained with the BAC ligation library.

### **Chromosome Conformation Capture Carbon Copy (5C)**



Experimental design : Probes were designed as described (Dostie et al., 2006). 213 5C probes were designed for a ~1 Mb region (chr11:4730996 - 5729937; hg18) around the Beta-globin locus at EcoRI restriction sites using publicly available 5C primer design tools (Lajoie et al., 2009). Probes were designed according to a single alternating scheme exactly as described before (Lajoie et al., 2009) and the genomic uniqueness of all primers was verified with the SSAHA algorithm. For each EcoRI fragment at the 1 Mb target region a primer was designed. 104 5' forward (FOR) and 109 5' reverse (REV) primers were designed.

Generation of 5C libraries : 5C libraries were generated as described before (Ferraiuolo et al., 2012) with three modifications. First, we skipped the gel purification after the adaptor ligation and replaced this with a 1:1 Ampure step to remove unligated DNA and adaptors. Second, barcoded Illumina adaptors were used. Third, we performed the final PCR using TruSeq DNA LT kit Set A (REF 15041757).

Annealing: The 5C probes were pooled and combined with the 3C template each reaction contained 800,000 genome copies of 3C template and 0.2 fmol per 5C probe [800,000 genome copies of 3C template, 2  $\mu$ L of 10X NEB4 (NEB B7004S), 2.75  $\mu$ L of Salmon Sperm DNA (250 ng; (Invitrogen™ 15632011), 0.25  $\mu$ L of 1 fmol/ $\mu$ L probes , up to 20  $\mu$ L ultrapure distilled water]. We set up 8 annealing reactions for each library in a 96-well PCR plate. We then

incubated the samples in a PCR machine and ran the following program [95°C for 9 min, Ramp 0.1°C/sec to 55°C, then keep at 55°C for 12 hr].

Ligation: We ligated 5C probe pairs, which represent a specific ligation junction in the 3C library, by adding 20 µL of ligation mix [2 µL of [10X *Taq* DNA ligase buffer (NEB B0208S), 0.25 µL *Taq* DNA ligase (NEB M0208S), 17.75 µL ultrapure distilled water] while the samples are kept in the PCR block at 55°C. We then incubated the reactions for 1 hr at 55°C followed by a 10 min incubation at 65°C; samples were then cooled to 4°C. Negative controls (no ligase, no template, no 5C oligonucleotide) were included to ensure the absence of any contamination.

PCR amplification: Universal emulsion primers were used for amplification of the ligated product by using 5C forward and reverse emulsion primers [Forward\_primer: CCTCTCTATGGGCAGTCGGTGAT. Reverse\_primer : CTGCCCCGGGTTCTCATTCTCT] for 25 PCR cycles [6 µL of ligation product, 2.5 µL of 10XPCR (600 mM Tris-SO<sub>4</sub>, pH 8.9, 180 mM (NH<sub>4</sub>)<sub>2</sub>SO<sub>4</sub>), 1.8 mM MgCl<sub>2</sub>, 0.2 mM dNTP, 0.5 µL F-emulsion primer (80 µM), 0.5 µL R-emulsion primer (80 µM), 0.225 µL *AmpliTaq* Gold DNA polymerase, ultrapure distilled water to bring volume up to 25 µL]. We then amplified DNA using this PCR program: [95° 9 min, 25 cycles (95°C 30 s, 65°C 30 s, 72° 30 s), 95°C 30 s, 65°C 30 s, 72°C 8 min, 4°C].

We pooled all the PCR reactions for the same library together and concentrated the DNA to 50 µL using 0.5 mL AMICON Ultra Centrifuge filter (UFC5030BK

EMD Millipore). DNA was then loaded on a 2% agarose gel, along with a low molecular weight ladder, and the gel was run in a 4°C room at 200 volts for 90 min. The 150 bp DNA that corresponded to the ligated 5C probes was isolated from the gel using the QIAquick Gel Extraction Kit Protocol (QIAGEN 28115). DNA was finally eluted in 32 µL of 1XTLE.

A-tailing: A dATP was added to the 3' ends of the 5C library by adding 18 µL of A-tailing mix [5 µL NEB buffer 2.1, 10 µL of 1 mM dATP, 3 µL Klenow exo (NEB M0212S)] to the 32 µL of DNA sample from the previous step. The reaction was then incubated in a PCR machine [at 37°C for 30 min, then at 65°C for 20 min, and finally cooled down to 4°C]. Next, the tube was placed on ice immediately. 1:1 Ampure was used to remove unligated adaptors. The DNA was finally eluted in 40 µL 1X T4 DNA Ligase buffer (Invitrogen).

Illumina adapter ligation and paired-end PCR: For this step, we used the TruSeq DNA LT kit Set A (REF 15041757). 10 µL of ligation mix [5 µL Illumina paired-end adapters, 3 µL T4 DNA ligase Invitrogen, 2 µL 5x T4 DNA ligase buffer (Invitrogen 5X)] was added to the 40 µL sample from the previous step. The ligation sample was then incubated at RT for 2 hours on a tube rotator. Afterward, the sample was run on a 2% agarose gel in a cold room 4°C at 150 volts for 120 min along with a low molecular weight ladder. The 270 bp band that corresponds to 5C products (150 bp) ligated to the two adaptors (64 bp) was extracted from the gel and isolated using the QIAquick Gel Extraction Kit (QIAGEN 28115). DNA was finally eluted in 30 µL 1XTLE.

### **Pre-digestion of nuclei (liquify chromatin)**

Purified nuclei as described above (**K562 nuclei purification**) were placed on ice and 1 mL of HBSS was added to each 0.5 mL of 5 million frozen nuclei. After thawing, nuclei were centrifuged 5 min at 5,000 g. The nuclei pellet was washed twice with 1XNEB3.1 for nuclei that would be digested with DpnII or 1XNEB2.1 for nuclei that would be digested with HindIII. The nuclei were pelleted for 5 min at 5,000 g after each wash.

Isolated nuclei: a sample of 5 million nuclei was resuspended in 1,250  $\mu$ L of 1X NEB3.1 as control, and then processed immediately for Hi-C starting at the crosslinking step (see below Hi-C 2.0 protocol).

Undigested nuclei: Each sample of two million nuclei was resuspended in 500  $\mu$ L of 1X NEB3.1 on ice, as and control for the pre-digestion and then treated as described immediately below.

DpnII pre-digestion: Each sample of two million nuclei was resuspended in 500  $\mu$ L of 1X NEB3.1 on ice. Next, 120 U of DpnII (NEB R0543S) was added to the sample in order to obtain 10 U DpnII/ $\mu$ g DNA and then treated as described immediately below.

HindIII pre-digestion: Each sample of two million nuclei was resuspended in 500  $\mu$ L of 1X NEB2.1 on ice. Next, 600 U of HindIII (NEB R0104T) was added to the sample in order to obtain 50 U HindIII/ $\mu$ g of DNA and then treated as described immediately below.

Next, control and pre-digestion samples were incubated at 37°C on a thermocycler (900 rpm for 30 sec every 4 min) for 5 min up to 16 h. Afterward, samples were placed on ice for 10 min. For DpnII-seq and assessment of fragmentation level, a final volume of 10 mM of EDTA was added to inactivate the endonuclease, followed immediately by the DpnII-seq protocol (details of protocols below. DpnII-Seq) or DNA purification for fragment analyzer analysis. For Hi-C, we proceeded immediately to the first step of the protocol (crosslinking as described below). For microscopy, nuclei samples were cross-linked with a 4% final concentration of paraformaldehyde.

## **Hi-C 2.0**

Hi-C was performed as described (Belaghzal, Dekker, & Gibcus, 2017) and in Method of chapter II with some modifications in the crosslinking and lysis step as described below.

Crosslinking: isolated, undigested, and pre-digested (with liquified chromatin) nuclei were not pelleted after the pre-digestion step above but were crosslinked immediately as follows: for each sample 1,250 µL volume of nuclei in the digestion buffer was transferred to a 21.875 mL mix [625 µL of 37% formaldehyde + 21.25 mL of HBSS]. For intact cells: 5 million K562 cells or nuclei were washed twice with 15 mL of HBSS and pelleted at 300 g for 10 min, then

resuspended in 2.5 mL of HBSS. The sample was transferred to 20.625 mL crosslinking mix [625  $\mu$ L of 37% formaldehyde + 20 mL of HBSS]. All samples were incubated at RT for 10 min on a rocking platform. Next, to stop cross-linking 1.25 mL of 2.5 M glycine was added to each sample and the mix was incubated at RT for 5 min on a rocking platform. To pellet the crosslinked cells/nuclei, the sample was centrifuged at 1,000 g for 10 min at 4°C. The supernatant was discarded and the pellet was washed twice with HBSS before going to the next step or storing samples at -80°C.

Cells lysis: This step is not needed for isolated, undigested, and pre-digested (with liquified chromatin) nuclei. For Hi-C with intact cells: the 5 million crosslinked cells were lysed by adding 1 mL cold lysis buffer [10 mM Tris-HCl (pH=8.0), 10 mM NaCl, 0.2% Igepal CA-630 (NP40)] and 10  $\mu$ L of 100X Protease inhibitors. The sample was incubated on ice for 15 min to let the cells swell. The cells were lysed on ice using a dounce homogenizer with pestle A (KIMBLE Kontes 885300-0002) by moving the pestle slowly up and down 30 times and incubating on ice for 1 min followed by another 30 strokes. The sample was transferred to a new 1.5 mL microcentrifuge tube, and the sample was centrifuged at 5,000 g at RT for 5 min.

### **DpnII-Seq**

For each DpnII-Seq library, 10 million nuclei were used right after the pre-digestion procedure described above (Pre-digestion of nuclei). The pre-digested nuclei were then treated as follows:

Proteinase K: 50  $\mu$ L of 10 mg/mL proteinase K (ThermoFisher # 25530) was added to each 500  $\mu$ L pre-digested nuclei sample (2 million nuclei) (See Methods: Pre-digestion) and the 5 tubes were incubated at 65°C for 3 hours.

DNA purification: Tubes were cooled to room temperature and all 5 samples were pooled in a single 15 mL tube (2.75 mL total volume). The DNA was extracted by adding an equal volume of 2.75 mL of saturated phenol pH8.0: chloroform (1:1) (Fisher BP1750I-400), followed by vortexing for 1 min. The sample (5.5 mL) was transferred to a 15 mL phase-lock tube (Quiagen #129065) followed by centrifugation at 5,000 g for 10 min. The upper phase was transferred to a 15 mL tube to start the second extraction. An equal volume of 2.75 mL saturated phenol pH8.0: chloroform (1:1) was added, followed by vortexing for 1 min. Then the mix was transferred to a 15 mL phase-lock tube (Quiagen #129065) followed by centrifugation at 5,000 g for 10 min. The upper phase of ~ 2.75 mL was transferred to a 15 mL tube (high speed), 1/10 volume (275  $\mu$ L) 3M sodium acetate pH 5.2 was added followed by brief vortexing and then 2.5 volumes of ice-cold 100% ethanol (6.875 mL) were added. The tube was inverted slowly several times, incubated at -80°C for 1 hr and then DNA was pelleted by centrifugation at 16,000 g for 30 min at 4°C. The supernatant was discarded and the pellet was dissolved in 500  $\mu$ L 1X NEB3.1 and transferred to a 0.5 mL AMICON Ultra Centrifuge filter (UFC5030BK EMD Millipore). The column was centrifuged for 5 min at 14,000 g and the flow-through was discarded. The column was washed 4 times using 450  $\mu$ L of 1X NEB3.1 for desalting of DNA.

After the final wash, the library remaining in the column (~50  $\mu$ L) was eluted in 450  $\mu$ L of 1XNEB3.1; the column was flipped upside down into a new tube to collect DNA and centrifuged for 3 min at 4,000 g. ~500  $\mu$ L of DNA was recovered. RNA was degraded by adding 1  $\mu$ L of 10 mg/mL RNAase A and incubation for 30 min at 37°C. The amount of DNA was estimated by running an aliquot on a 1% Agarose gel along with a 1kb ladder (NEB#N3232s).

Biotin Fill-in: 1XNEB3.1 was added the reaction to a final volume of 680  $\mu$ L, and then the 680  $\mu$ L was split over 2 1.5 mL tubes. DNA ends were filled in and marked with biotin-14-dATP. To each tube 60  $\mu$ L of biotin fill-in master mix was added: [1xNEB2.1, 0.25 mM dCTP, 0.25 mM dGTP, 0.25 mM dTTP, 0.25 mM biotin-dATP (ThermoFisher#19524016), 50 U Klenow polymerase Polymerase I (NEB M0210L)]. Samples were incubated at 37°C in a Thermocycler for 75 mins. Next, the tubes were placed on ice immediately for 15 mins, and samples from the 2 tubes were combined to obtain a final volume ~800  $\mu$ L. Amicon filters were used to reduce the volume of the final sample from 801  $\mu$ L to 130  $\mu$ L.

Sonication: DNA was sonicated to a size of 100 – 300 bp using a Covaris instrument (Duty Cycle 10%, Intensity 5, Cycles per Burst 200, set Mode Frequency sweeping, continuous degassing, process time 60 sec, Number of cycles) for 4 cycles. The 130  $\mu$ L of sonicated DNA was transferred to a 1.5 mL tube and 1XTLE was added to a total volume of 500  $\mu$ L. DNA fragment size was



determined by running 2  $\mu$ L of DNA along with low molecular ladder (NEB) on a 2% agarose gel.

Size fractionation using AMPure XP: 500  $\mu$ L AMPure beads (Beckman Coulter A63881) were added to a 1.5 mL tube labeled as 1.1X. The tube was placed on the MPS for 5 min, and the supernatant was removed. Beads were resuspended in 150  $\mu$ L AMPure mixture in order to make 1.1X. 400  $\mu$ L of AMPure mixture was added to 500  $\mu$ L of sonicated DNA from the previous step and the tube was labeled 0.8X. The sample was vortexed and centrifuged briefly using a tabletop small centrifuge followed by incubation at RT for 10 min on a rocking platform. Then the tube was placed on the MPS for 5 min at RT. The 0.8X supernatants were collected and added to the 1.1X tube, the tube was briefly vortexed and centrifuged followed by incubation at RT for 10 min on a rocking platform. The tube was placed on the MPS for 5 min at RT, and the supernatant discarded. Beads in the 0.8X and 1.1X tubes were washed twice with 1 mL 70% ethanol, reclaiming beads against the MPS for 5 min. Beads on the MPS were then dried until ethanol had evaporated completely. Next, 51  $\mu$ L of 1XTLE was added to the 0.8X and 1.1X tubes to elute DNA from the beads. Tubes were incubated at RT on a rocking platform for 10 min. The 0.8X and 1.1X tubes were placed on the MPS for 5 min. Finally, the supernatants were transferred to 1.7 mL tubes labeled 0.8X and 1.1X. The 1.1X sample contains DNA that ranges in size from 100-300 bp. The DNA in the 0.8X sample was kept in case more DNA was required, in which case the DNA would be sonicated using 2 cycles followed

by a similar round of size fractionation as described above. The amount of DNA from both samples 0.8X and 1.1X was quantified by running 1  $\mu$ L on a 2% agarose gel along with a titration of low molecular weight DNA ladder (100 ng, 200 ng, 400 ng).

End Repair: 50  $\mu$ L from the 1.1X sample was transferred to a PCR tube, and 20  $\mu$ L of end repair mix was added: [3.5X NEB ligation buffer (NEB B0202S), 0.875 mM dNTP mix, 0.375 U/ $\mu$ L T4 DNA polymerase, 1.25 U/ $\mu$ L T4 polynucleotide kinase, 0.125 U/ $\mu$ L Klenow DNA polymerase]. The 70  $\mu$ L total volume reaction was incubated for 30 min at 20°C in a PCR machine and then placed on ice. The DNA was purified by 1:2 Ampure, by adding 140  $\mu$ L 2X Ampure solution to the 70  $\mu$ L DNA sample followed by incubation for 5 min at RT. The tube was placed on the MPS for 4 min to reclaim the beads and the supernatant was discarded. The beads were washed twice with 1 mL of 70% ethanol while on the MPS. After beads were dried DNA was eluted in 32  $\mu$ L TLE (pH 8.0) and incubation for 10 min at RT. The supernatant was transferred to a 1.5 mL tube.

A-tailing: A dATP was added to the 3' ends by adding 18  $\mu$ L of A-tailing mix [5  $\mu$ L NEB buffer 3.1, 10  $\mu$ L of 1 mM dATP, 3 U Klenow exo (NEB M0212S)] to the 32  $\mu$ L of DNA sample from the previous step. The reaction was then incubated in a PCR machine at 37°C for 30 min followed by incubation 65°C for 20 min and cooling down to 4°C. The tube was placed on ice. The volume was brought to 100  $\mu$ L by adding 1X NEB2.1. The DNA was then purified by adding

1:2 Ampure mix ( 200  $\mu$ L of Ampure was added to the 100  $\mu$ L final DNA volume). Finally, the DNA was eluted in 40  $\mu$ L of 1X T4 DNA ligase buffer (Invitrogen 5X).

Illumina adapter ligation and paired-end PCR: For this step we used the TruSeq DNA LT kit Set A (REF#15041757). 50  $\mu$ L of ligation mix [25  $\mu$ L Illumina paired-end adapters, 15  $\mu$ L T4 DNA ligase Invitrogen, 10  $\mu$ L 5X T4 DNA ligase buffer (Invitrogen 5X)] was added to the 40  $\mu$ L sample from the previous step. The ligation sample was then incubated at RT for 2 hours on a rotator. Next, the DNA was purified by adding 1:1 Ampure solution (180  $\mu$ L of Ampure mix was added to the 90  $\mu$ L sample), the supernatant was discarded and beads were washed twice with 1 mL of 70% ethanol. After the last wash step, the beads were resuspended in 400  $\mu$ L of 1X TLE and incubated at RT on a rocking platform for 10 mins. The tube was placed on the MPS for 4 mins. Finally, the 400  $\mu$ L supernatant was transferred to a new tube.

Biotin pull-down: All the following steps are done using 1.5 mL loBind tube (Eppendorf 22431021). 15  $\mu$ L of MyOne streptavidin C1 beads mix (Thermo Fisher 65001) was transferred to a 1.5 mL tube. The beads were washed twice with 400  $\mu$ L of TWB [5 mM Tris-HCl pH8.0, 0.5 mM EDTA, 1 M NaCl, 0.05% Tween20] by incubation for 3 min at RT. After each wash, the tube was placed on the MPS for 1 min and the supernatant was removed. After the washes, the beads were resuspended in 400  $\mu$ L of 2X Binding Buffer (BB) [10 mM Tris-HCl pH8.0, 1 mM EDTA, 2 M NaCl] and mixed with the 400  $\mu$ L DNA from the previous step in a new 1.5 mL. The mixture was incubated for 15 min at RT with

rotation. The tube was then placed on the MPS for 1 min and the supernatant was removed. The DNA bound to the beads was washed first by adding 400  $\mu$ L of 1X BB and transferring to a new tube. The beads were reclaimed against the MPS for 1 min, and the supernatant discarded. 100  $\mu$ L of 1X TLE was added and the beads were reclaimed against the MPS for 1 min, then the supernatant was discarded. Finally, the DNA bound to the beads was eluted in 32.5  $\mu$ L of 1X TLE.

PCR optimization: The Illumina Truseq Kit (DNA LT kit Set A (REF#15041757)) was used for PCR amplification of DNA for DpnII-Seq. The trial PCR reaction was set up as follows: [2.5  $\mu$ L DNA bound to beads, 2  $\mu$ L of Primers mix (Truseq kit), 10  $\mu$ L Master Mix (Truseq kit), 10.5  $\mu$ L of ultrapure distilled water (Invitrogen)]. The 25  $\mu$ L was split over four PCR tubes (5  $\mu$ L/per tube). Each of the four samples was incubated for different PCR cycles (6, 8, 10, or 12 cycles): [30 sec at 98°C, n cycles of (30 sec at 98°C, 30 sec at 65°C, 30 sec at 72°C), 7 min at 72°C, hold at 10°C]. The optimal PCR cycle number needed to get enough DNA for sequencing was determined by running the 4 PCR reactions on a 2% agarose gel along with low molecular ladder titration (100 ng, 200 ng, 400 ng). Three PCR reactions of 50  $\mu$ L volume were then performed: [5  $\mu$ L DNA bound to beads, 4  $\mu$ L of Primers mix (Truseq kit), 20  $\mu$ L Master Mix (Truseq kit), 21  $\mu$ L of ultrapure distilled water (Invitrogen)]. The 3 PCR reactions were pooled together to obtain 150  $\mu$ L total volume. The samples were reclaimed against the MPS for 1 min, then the PCR products (supernatant) were taken to new 1.5 mL tubes. 1:1 Ampure was performed for removal of primer dimers (150

μL of Ampure and 150 μL DNA sample). Finally, beads were resuspended in 35 μL of TLE to elute the DNA. DNA that remained bound to beads was saved after a first wash using TBW followed by two washes with 1X TLE and then resuspended in 30 μL of 1X TLE.

### **Lamin A Immunofluorescence and DAPI**

For nuclei immunofluorescence, we prepared a coverslip by adding 1 mL of 0.1% Poly-L-lysine solution (Sigma SLBQ5716V) for 10 min, then coverslips were dried using Whatman papers. Each coverslip was transferred to a single well of an eight wells plate. The coverslips were washed twice using PBS. Next 500 μL of 30% sucrose with 1 mM DTT was added on top of the coverslips to protect nuclei from an abrupt contact with coverslip during spinning. 1 million control nuclei or nuclei after chromatin digestion were crosslinked for 20 min using a 4% final concentration of Paraformaldehyde immediately after pre-digestion. Next, nuclei were added slowly on top of the sucrose solutions on the coverslips and spun for 15 mins at 2,500 g at 4°C. Next, nuclei were assumed to be attached to the coverslips which were then transferred to a new 8 well plate. The coverslips were washed five times with 1% PBS. Next, non-specific binding of the primary antibody was blocked by adding 500 μL of the blocking buffer [3% BSA, 1X PBS, 0.1% Triton X-100 (Sigma [9002-93-1](#))] and incubating for 60 min at RT. Afterward, lamin A antibody (ab 26300) was diluted 1:1000 in blocking buffer, and the coverslip was incubated face-down on top of a 250 μL of lamin A antibody droplet that was placed on parafilm for 120 min at RT. Then, the

coverslip was placed back in the well of a new plate face-up and washed five times with washing buffer (1X PBS, 0.1% Triton X-100). The secondary antibody Goat Anti-Rabbit (ab150077) was diluted 1:1000 in blocking buffer, and the coverslip was incubated face-down on top of a 250  $\mu$ L droplet of the secondary antibody (Goat Anti-Rabbit (ab150077) that was placed on parafilm for 60 min at RT. Next, the coverslip was placed back in the well of a new plate face-up and washed five times with washing buffer (1X PBS, 0.1% Triton X-100) and twice with 1X PBS. The slide was mounted and sealed using 10  $\mu$ L antifade mountant with DAPI (Invitrogen P36931).

For image acquisition, we used a Nikon Eclipse Ti microscope. Imaging was performed using an Apo TIRF, N.A. 1.49, 60X oil immersion objective (Nikon), and a Zyla sCMOS camera (Andor). Z-series of 0.2  $\mu$ m slices were acquired using Nikon Elements software (Version 4.4).

### **Chromatin fractionation assay**

Chromatin-bound proteins were isolated and separated from free proteins. A sample of 2 million control nuclei or pre-digested nuclei (obtained as described above “Pre-digestion of nuclei”) was centrifuged at 5,000 g for 5 min at 4°C. The supernatant was transferred to an Amicon column to reduce the volume from 500  $\mu$ L to 100  $\mu$ L by centrifugation for 4 min at 14,000 g. This sample contains the free protein fraction. Next, 26  $\mu$ L of glycerol and 1.3  $\mu$ L of 100X protease inhibitor cocktail were added to the 100  $\mu$ L free proteins sample. The pellet containing the nuclei was resuspended in 100  $\mu$ L of nuclei purification buffer with Triton (10 mM

PIPES pH 7.4, 10 mM KCl, 2 mM MgCl<sub>2</sub>, 0.25% Triton, 1% Protease inhibitor, 1mM DTT) and incubated for 10 min on ice. Then, in order to protect protein structure during sonication, 25 µL of glycerol was added to the 100 µL pellet sample to have 20% final glycerol concentration. The sample was sonicated using a Covaris instrument at 4°C as follows: (Duty Cycle 10%, Intensity 5, Cycles per Burst 200, set Mode Frequency sweeping, continuous degassing, process time 60 sec, 4 cycles). The pellet sample contains chromatin-bound proteins, was transferred to a 1.5 mL tube. All samples were stored at -20. These samples contain the protein bound CTCF and cohesin. Note: when these samples were centrifuged after the triton solubilization, we found that no SMC3 or CTCF could be detected in the supernatant. These results indicate that non-chromatin-bound proteins exit the nuclei and were recovered in the supernatant prior to triton solubilization step.

For analysis of CTCF and SMC1 chromatin binding: 15 µL from each protein sample (supernatant or pellet) was mixed with 5 µL of 5X Lane Marker Reducing Sample Buffer (Thermo Fisher 39000), then the mix was boiled for 10 min. The samples were cooled down to RT before loading them on a 3-8% Tris-Acetate Protein Gels (Invitrogen EA0375PK2). Next, the gel was run in 1X Tris-Acetate SDS Running Buffer (Invitrogen LA0041) for 75 min at 150V. For Histone H3: 1 µL of protein sample was mixed with 14 µL of PBS containing 1% Protease inhibitor, 5 µL of 5X Lane Marker Reducing Sample Buffer was added to the mix and boiled for 10 min. The samples were cooled down to RT before loading them

in Tris-Base 4-12% (Invitrogen NP0322BOX), then the gel was run in 1X MES-SDS running buffer (Invitrogen B0002) for 60 min at 150V. The proteins were transferred from the gel to nitrocellulose membrane using 1X western blot transfer buffer (Thermo science 35040). The transfer was 120 min for SMC1 and CTCF and 75 min for H3. The nitrocellulose membranes were washed using 1X TBST [50 mM Tris-Cl, pH 7.6; 150 mM NaCl, 0.1 mL of Tween 20], then Blocked for 120 min using 5% milk (1 g milk in 20 mL 1X TBST). The membrane was then incubated overnight at 4°C with primary antibody diluted in 5% milk [1:1000 CTCF antibody cell signaling (activeMotif 61311), 1:2000 SMC1 (Bethyl Antibody, A300-055A), 1:4000 H3 Abcam (ab1791)] . Next, the membranes were washed 6 times for 10 min per wash using 1X TBST. The secondary antibody anti-rabbit IgG HRP from cell signaling was diluted using 5% milk for CTCF and SMC1 [1:1000 for CTCF, 1:2000 SMC1] and in 1% milk for H3 1:5000 dilution. Membranes were incubated for 120 min at RT. Finally, membranes were washed 6 times for 10 min using 1X TBST. Finally, the membranes were developed using luminol-based enhanced chemiluminescence(Thermo science 34076).

### **Micromanipulation force measurement and treatments of an isolated nuclei**

Micromanipulation force measurements were conducted as described previously (Stephens, Banigan, Adam, Goldman, & Dunn, 2017). K562 cells were grown in microscope slide wells and treated with 1 µg/mL latrunculin A (Enzo Life Sciences) for ~45 min before single nucleus isolation. The nucleus was isolated by using small amounts of detergent (0.05% Triton X-100 in PBS) locally sprayed



onto a living cell via an “isolation” micropipette. This gentle lysis allows the use of a second micropipette to retrieve the nucleus from the cell, using slight aspiration and non-specific adherence to the inside of the micropipette. A third micropipette was then attached to the opposite end of the nucleus in a similar fashion. This last “force” micropipette was pre-calibrated for its deflection spring constant, which is on the order of 2 nN/ $\mu$ m. A custom computer program written in LabView was then run to move the “pull” micropipette and track the position of both the “pull” and “force” pipettes. The “pull” pipette was instructed to move 5  $\mu$ m at 45 nm/sec. The program then tracked the distance between the pipettes to provide a measure of nucleus extension  $\sim$ 3  $\mu$ m. Tracking the distance that the “force” pipette moved/deflected multiplied by the pre-measured spring constant provides a calculation of force exerted. Calculations were done in Excel (Microsoft) to produce a force-extension plot from which the best-fit slope of the line would provide a spring constant of the nucleus (nN/ $\mu$ m). Isolated nuclei were measured twice initially to establish the native spring constant prior to treatment. After 50  $\mu$ L of buffer only (control), 100 units DpnII (|GATC) with NEB buffer 3.1, or 100 units HindIII (A|AGCTT) with NEB buffer 2.1 was added to the 1.5 mL imaging well and mixed gently. Force measurements were performed 5 min, 30 min, and 60 min post-treatment

### **3C-PCR**

The human  $\beta$ -globin locus is an ideal region to examine looping interactions between enhancers and genes because of the strong looping interactions

between the LCR and HBG globin gene in the erythroleukemia cell line K562, which highly expresses the globin genes (Dostie et al., 2006). 3C libraries were generated from: (1) K562 cells that have an LCR-HBG interaction, (2) GM12878 cells in which the LCR-HBG looping interaction is absent, and (3) beta-globin BAC (ENm009) control to normalize for primer bias. To investigate the interaction between the LCR and HBG gene, 3C primers from {Dostie, 2006 #593} were used. 16 forward primers of 28-33 bp length were designed 40-60 bp upstream of each EcoRI site throughout a 110 kb region around the Beta Globin locus (chr11: 5221788- 5337325). The EcoRI fragment overlapping with the LCR (HS3,4,5) was used as an anchor to detect the interaction frequencies between the LCR and EcoRI fragments throughout the  $\beta$ -globin locus. For each primer pair, triplicate PCR reactions were set up, and the mean of the three was normalized to the BAC signal for the same primer pair before plotting normalized interaction frequency in the y-axis, the distance from EcoRI fragment overlapping with LCR to neighboring EcoRI fragments is plotted in the x-axis. Error bars are the standard error of the mean (SEM).

### **5C data processing**

The fastq files for 5C sequencing data were processed as described in [https://github.com/dekkerlab/5C-CBFb-SMMHC-Inhib/blob/master/data\\_processing\\_steps.md](https://github.com/dekkerlab/5C-CBFb-SMMHC-Inhib/blob/master/data_processing_steps.md)

The Fastq files were mapped using novoalign to a reference genome built from the pool of all 277 probes. After mapping, we combined the read-pairs. The

results were then transferred to a matrix format, and interactions were filtered as previously described (Lajoie et al., 2009) (Amartya Sanyal et al., 2012). First, interactions that belong to the same EcoRI fragment were removed. Second, outliers that are overrepresented as a result of overamplification were also removed. Outliers were defined as the interactions with a Z-score greater than 20 in all datasets. Third, probes that strongly over or underperform which leads to strongly enriched or depleted interactions in a whole row of interactions, were also removed. The four matrices were then scaled to the same number of total reads. Finally, data were binned at 20 Kb (median) with a sliding window with 2.5 Kb steps.

### **Hi-C data processing**

Hi-C read mapping, filtering, binning and matrix normalization were performed using the cMapping pipeline available at <https://github.com/dekkerlab/cMapping> (Lajoie et al., 2015). In brief, Hi-C reads were mapped to reference human genome assembly hg19 using an iterative mapping strategy and Bowtie 2. Successfully mapped reads were then filtered to remove reads mapping to the same restriction fragment and to remove PCR duplicates. Interaction frequency versus distance plots displayed high variance for interactions below 1 kb for all samples. Hence, after mapping of valid pair, we removed all pairs with a genomic distance less than 1 kb. The remaining valid read pairs were then binned to 500 kb, 40 kb, and 10 kb resolution matrices. Outlier bins of these matrices with low signal were assigned values of NA. Then as a bias correction step, matrices

were normalized such that the sum of interactions in each row/column are approximately equivalent via an iterative correction procedure (ICE) (Imakaev et al., 2012). Lastly, for comparison between samples, matrices were scaled such that the total interactions for a genome-wide matrix equals one billion for each sample. These ICEd scaled matrices were used for subsequent analyses.

### **A/B compartments**

All reads from Hi-C in control K562 samples were pooled to identify A (active) and B (inactive) compartments in K562 cells. A/B compartments were identified at 40 kb resolution following the procedure described in {Lieberman-Aiden, 2009 #771} using `matrix2compartment.pl` in <https://github.com/dekkerlab/cworld-dekker>. Briefly, each *cis* interaction matrix was first transformed into a z-score matrix followed by transformation into a correlation matrix. PCA was performed on the correlation matrix and the first eigenvector (PC1) of the PCA analysis was used to identify compartments for each chromosome. A/B compartments were assigned based on gene density such that the A-compartment was more gene-dense than the B-compartment. Positive PC1 values indicate gene-rich A compartments and negative PC1 values indicate gene-poor B compartments. For chromosome 9 the compartments were called for each chromosome arm separately as PC1 captured preferences for interactions within the same arm as opposed to canonical compartment preferences.

### **LOS and half-life calculation**

To measure the 3D structure changes resulting from DpnII or HindIII pre-digestion we quantified the amount of cis interactions lost or gained in a 6 Mb window centered at every 40 kb bin genome wide. For each 40 kb bin, the percent of interactions occurring within its 6 Mb window (corresponding to interactions less than or equal to 3 Mb in distance either upstream or downstream from 40 kb bin) out of total interactions for the 40 kb bin (cis and trans) was calculated. These 6 Mb cis percentages were calculated for control, DpnII pre-digested, and HindIII-pre-digested nuclei. The change in 3D structure relative to control using these cis percentages was given by the following loss of structure (LOS) metric:

$$LOS = \frac{Control_{cis\%} - Predigest_{cis\%}}{Control_{cis\%}}$$

Hence, LOS values in the range (0, 1) represent a loss in short range contacts after pre-digestion; LOS values < 0 represent an increase in short range contacts after pre-digest, and an LOS equal to zero would indicate no change in structure after pre-digestion. A window of 6 Mb was chosen as we sought here to quantify interactions disrupted by pre-digestion. Many longer range interactions increased after pre-digestion, potentially due to random ligations of cut fragments that start to mix. Differences noted in A and B stability was preserved when LOS was calculated using cis percents for entire chromosomes as opposed to a 6 Mb

window, however, the size of chromosomes did bias results by giving 40 kb bins in small chromosomes greater LOS.

To quantify the timing of disrupted interactions we generated a half-life track utilizing the Hi-C matrices from the DpnII timecourses. For each 40 kb bin we fit a curve to the LOS of each timepoint following an exponential decay of the form (**Fig. 4.8C**):

$$LOS = a - (b \times e^{-c \times minutes})$$

such that  $a$ ,  $b$  and  $c$  are parameters to fit. The half-life,  $t_{1/2}$ , was defined as the time required to reach half saturation, saturation being the 16 hour timepoint where maximal cis interactions have been lost. Half-life values were then computed for every 40 kb bin genome wide. To remove noisy and less reliable  $t_{1/2}$  data, we first removed all extreme outliers bins where the sum of squared residuals (SSR) for the exponential fit was greater than 0.1. Then all bins with an SSR greater than two standard deviations from the mean was deemed an outlier and also removed from analyses.

As LOS and  $t_{1/2}$  are both dependent on digestion efficiency we also generated residual LOS and  $t_{1/2}$  tracks to account for bin to bin variation in digestion

efficiency. We used a moving average approach to calculate residuals for LOS as a function of DpnII-seq signal and also  $t_{1/2}$  as a function of DpnII-seq signal since the relationships between these variables were non-linear (**Fig. 4.5F** left, **Fig. 4.5C**). For both stability metrics LOS and  $t_{1/2}$ , a sliding window of 200 DpnII-seq signal with a step size of one was used to calculate mean LOS or  $t_{1/2}$  signal for each DpnII-seq signal increment (**Fig. 4.5F** left). Window and step size were selected by manual inspection of moving averages and compromising between over and underfitting. These moving averages were used to calculate residuals such that a positive LOS residual indicates more structure loss than expected by given digestion efficiency and a negative LOS residual indicates less structure loss than expected. As  $t_{1/2}$  is inversely related to LOS, positive  $t_{1/2}$  residuals indicate less structure loss than expected and negative  $t_{1/2}$  residuals indicate more structure loss than expected. Moving averages were also used to generate residuals for DpnII-seq as a function of PC1 and LOS as a function of PC1 (**Fig. 4.5G**, right)

### DpnII-seq data analysis

Sequenced reads were mapped to the genome using the Bowtie read aligner <https://doi.org/10.1186/gb-2009-10-3-r25>] and reads mapping to multiple sites of the genome were removed. As expected, a high percentage of reads mapped precisely to their associated restriction cut site (**Fig. 4.6C**). To remove potential artificial biases, we filtered out paired-end reads from fragments whose start or

end coordinate was more than three nucleotides from an appropriate restriction cut site. Filtered reads were then binned to 500 kb or 40 kb resolutions. The K562 cell line has a primarily triploid karyotype with regions of the genome in diploid and tetraploid states. Copy number state assignments for each 500 kb or 40 kb bin were assigned using publicly available K562 copy number data from the Catalogue of Somatic Mutations In Cancer (COSMIC) database ([https://cancer.sanger.ac.uk/cell\\_lines/download](https://cancer.sanger.ac.uk/cell_lines/download)). Copy number segments in the COSMIC dataset were identified by PICNIC analysis of Affymetrix SNP6.0 array data (PMID:19837654). Read coverage files at 500 kb and 40 kb were corrected to a genome wide diploid state using the copy number state assignments and dividing coverage by appropriate correction value (diploid = 1, triploid =1.5, tetraploid = 2, etc.) per bin. (**Fig. 4.6D, Fig. 4.6E**). Final copy number corrected coverage files were used for all downstream analysis and are available . DpnII-seq computational workflow is maintained at <https://github.com/tborrman/DpnII-seq>

### **Subcompartments**

Rao et al. ( Rao et al., 2014) divided the canonical A/B compartments into five primary subcompartments A1, A2, B1, B2, B3 based on each subcompartment's preferential Hi-C interactions in GM12878 cells. Subcompartments were annotated using high resolution (~1 kb) Hi-C data and were shown to display unique genomic and epigenomic profiles. K562 subcompartments were annotated in (Xiong & Ma, 2018) via the method SNIPER using lower resolution



Hi-C data. In short, SNIPER infers subcompartments via a neural network approach to accurately annotate subcompartments using Hi-C datasets with moderate coverage (~500 million mapped read pairs). Xiong et al.'s K562 SNIPER subcompartments showed a substantial conservation with GM12878 annotations from Rao et al. (Rao et al., 2014) and were also enriched in similar epigenetic features, hence we utilized these SNIPER annotations to compare subcompartment status with chromatin stability. K562 SNIPER subcompartments were annotated at 100 kb resolution. To compare with our 40 kb resolution liquid chromatin Hi-C data, we binned the 100 kb subcompartment annotations to 40kb such that any 40 kb bin overlapping a boundary of two separate subcompartments was assigned a value of NA. Upon piling up K562 subcompartment boundaries, we also found enrichment and depletion of various chromatin features consistent with those described in (Rao et al., 2014) and (Xiong & Ma, 2018)

### **Sub-nuclear structures**

To assess the effect of sub-nuclear structures on chromatin stability we utilized the extensive genetic and epigenetic data publicly available for K562 cells.

Fold change over control ChIP-seq tracks for histone modifications, chromatin remodellers, and other various proteins were downloaded from the ENCODE Portal. To compare ChIP-seq data with  $t_{1/2}$ , or residuals of  $t_{1/2}$  after correction for DpnII-signal, we binned the ChIP-seq signal tracks into 40 kb such that each 40

kb bin represented the mean signal found across the bin. Bins with no overlapping signal were designated a value of NA.

To examine the association between methylation state and  $t_{1/2}$  or residuals of  $t_{1/2}$  after correction for DpnII-signal, we downloaded methylation state at CpG Whole-Genome Bisulfite Sequencing (WGBS) tracks from ENCODE. As the methylation data was mapped to hg38, we used the UCSC LiftOver program to convert coordinates to hg19. Then percentage methylation at CpG sites was binned to 40 kb resolution using the mean.

As there is currently no nucleolus associated domains (NADs) data available for K562, we analyzed a binary NADs state track for the human embryonic fibroblast IMR90 cell line . Dillinger et al. annotated NADs via a two-state hidden Markov model of aCGH data from DNA of isolated nucleoli. Using these annotated NADs, coverage of each 40 kb bin for NADs was assessed and used for all our downstream analyses.

Mapping of nuclear speckle, nuclear lamina and PolIII associated loci for K562 cells was accomplished recently via the TSA-seq protocol (Chen et al., 2018). Signal tracks of  $\log_2(\text{pull-down/input})$  were downloaded from GEO and binned to 40 kb as previously described for ChIP-seq files. Microarray data for LaminB1 associated domains identified through the DamID protocol was also available from that study. We used the UCSC LiftOver program to convert coordinates from hg18 to hg19. We then binned the  $\log_2(\text{Dam-LaminB1/Dam})$  signal to 40 kb bins as previously described for ChIP-seq files.

To analyze cell cycle relationship with chromatin stability we downloaded Repli-seq data for K562 cells from ENCODE. Actively replicating regions are quantified as a percentage normalized signal for FACS sorted cells in G1 phase, four stages of S phase (S1-S4) and G2 phase. Signal tracks for Repli-seq data were binned to 40 kb as previously described for ChIP-seq files.

Binning of data was performed using the bedtools/v2.26.0 software. To assess the quality of the publicly downloaded data we generated the spearman correlation matrix of all binned signal tracks (**Fig. 4.10A**). Hierarchical clustering of rows of the correlation matrix position heterochromatic marks (H3K9me3, HP1 $\alpha$ , HP1 $\beta$ , NADs, and LADs) near one another as expected. The majority active marks form a larger cluster, with the markers for polycomb regions (H3K27me3, CBX8, BMI1, RNF2, and SUZ12) representing facultative heterochromatin clustered together segregating active from inactive marks.

### **Gene Expression**

To assess the effect of gene expression on chromatin stability we utilized processed gene expression quantifications of total RNA-seq for K562 cells available from ENCODE (Accession ID: ENCFF782PCD). Gene locations were mapped using the hg19 ensGene table from UCSC Table Browser. To compare expression values with 40 kb resolution  $t_{1/2}$  or residuals of  $t_{1/2}$  after correction for DpnII-signal tracks, fragments per kilobase million (FPKM) values for each gene were binned to 40 kb such that each 40 kb bin represented the mean FPKM for all genes overlapping that bin. Bins without any genes were assigned a value of

NA. Binned FPKM  $\geq 1$  was determined to be a reasonable cutoff for expression by inspection of the full distribution of FPKM values.

### **Compartmentalization saddle plots**

Saddle plot was adapted from cool tools ([https://github.com/hms-dbmi/hic-data-analysis-bootcamp/tree/master/notebooks/04\\_analysis\\_cooltools-eigenvector-saddle.ipynb](https://github.com/hms-dbmi/hic-data-analysis-bootcamp/tree/master/notebooks/04_analysis_cooltools-eigenvector-saddle.ipynb)).

To measure the strength of compartments the average intra-chromosomal interactions frequencies between 40 kb bins were normalized by genomic distance (observed/expected Hi-C maps). Then, in a 50 by 50 bin matrix, the distance corrected interaction bins were sorted based on their PC1 value in increasing order. Finally, all intra-chromosomal interactions with similar PC1 values were aggregated to obtain compartmentalization saddle plots. In these plots, preferential B-B interactions are in the upper left corner, and preferential A-A interactions are in the lower right corner.

### **Homotypic interaction saddle plots**

The average intra-chromosomal interactions frequencies between 40 kb bins were normalized by genomic distance (observed/expected Hi-C maps). Then, in a 50 by 50 bin matrix, the distance corrected interaction bins were sorted based on their signal value (TSA-seq, DamID) for a given factor (SON, Lamin). Finally, all intra-chromosomal interactions with similar signal values were aggregated to obtain homotypic interaction saddle plots. In these plots, pair-wise

interactions between loci enriched in factor binding are shown in the lower right corner, and pair-wise interactions between loci not bound by the factor are shown in the upper left corner.

### **Scaling plot**

The script to generate scaling plots was adapted from cooltools Genome-wide curves of normalized contact frequency  $P(s)$  is plotted as a function of genomic distance for all intra-chromosomal interactions. Each library was normalized by total valid interactions

### **Mean z-score heatmap**

Each genome wide 40kb signal vector for a sub-nuclear structure was cleaned for outliers above three standard deviations of the vector's mean. Each cleaned vector was z-score transformed and then partitioned based on the different  $t_{1/2}$  residual intervals for associated bins. The mean z-score for all bins within a given  $t_{1/2}$  residual interval is plotted as a square in the heatmap.

### **Code availability**

All code for data processing and analysis, described in detail in the Methods, is available through the following GitHub accounts:

<https://github.com/dekkerlab/5C-CBFb-SMMHC-Inhib>

<https://github.com/dekkerlab/cMapping>

<https://github.com/dekkerlab/cworld-dekker>

<https://github.com/tborrman/DpnII-seq>

<https://github.com/tborrman/digest-Hi-C>

<https://github.com/hms-dbmi/hic-data-analysis-bootcamp>

## RESULTS

### Measuring the stability of chromatin interactions that maintain nuclear compartmentalization

As we discuss in chapter I, Flory-Huggins polymer theory predicts that spatial segregation will occur when the product of the length of the blocks ( $N$ , the number of monomers that make up blocks) and their effective preferential homotypic interaction strength ( $\chi$ , a parameter that represents the difference in the strength of homotypic interactions as compared to heterotypic (A-B) interactions) is larger than a critical value  $C$  ( **Fig. 1.2**) (Leiblerf, 1980) (Matsen & Schick, 1994). The dependence of microdomain formation on the product of block size and interaction strength suggests an experimental approach to quantify the strengths and dynamics of interactions between individual loci that drive chromosome compartmentalization. One can start with a compartmentalized state of the genome and fragment the chromosomes, e.g., by *in situ* restriction digestion, and then identify conditions where chromatin fragments become so short that the chromatin interaction strength between the segments is not sufficient to maintain a phase- or microphase-separated state.

As a result, chromosomal domains and compartments will disassemble over time and the chromosomal fragments of different type (e.g., As and Bs) will become mixed, i.e. chromatin becomes liquid-like as opposed to a glassy state for intact chromosomes (L. Liu et al., 2018). The kinetics of this dissolution and mixing process can then be assessed genome-wide by Hi-C at different times after chromatin fragmentation. Domains formed by strong, stable, and abundant interactions will dissociate more slowly than domains formed by weak, unstable, or infrequent interactions (**Fig. 4.1**). Such approach will identify the minimum length of the blocks of monomers required for phase separation, the strength and stability of chromatin interactions, the dissolution kinetics of initially phase-separated sub-nuclear domains upon fragmentation, and how these parameters vary along the genome. Here we describe such strategy that we call liquid chromatin Hi-C.

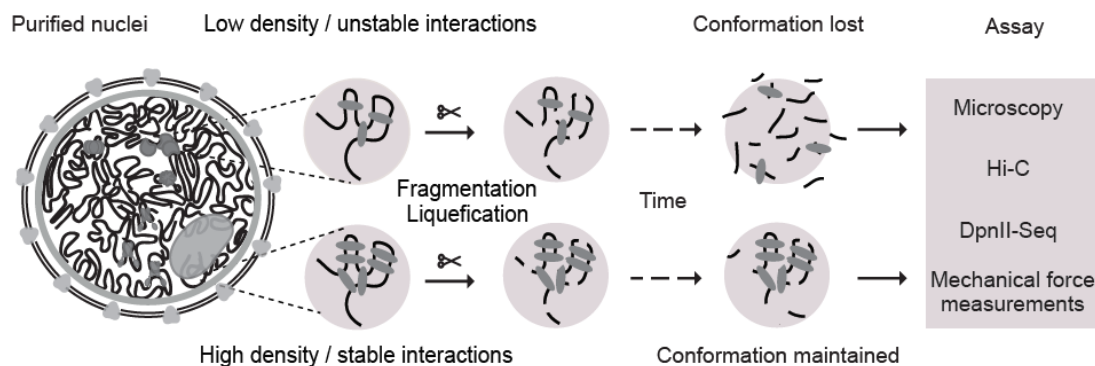


**Figure 4.1: Approach for measuring chromatin interaction stability**

Workflow to determine the stability of chromatin interactions genome-wide, DNA (black), varying chromatin features or proteins maintaining DNA conformation (grey ovals).

## Chromosome conformation in isolated nuclei

To facilitate enzymatic fragmentation of chromosomes, we isolated nuclei from K562 cells, a cell line with extensive public data on chromosome conformation and chromatin state through efforts of the ENCODE project (Consortium, 2012). We performed four analyses to demonstrate that chromosome conformation in isolated K562 nuclei was the same as that in intact cells. First, DAPI staining and imaging showed that nuclei were intact with Lamin A as a ring at the nuclear periphery (**Fig. 4.3A**). Second, we performed 3C (Job Dekker et al., 2002) to assess known looping interactions between the beta-globin locus control region and the expressed gamma-globin genes (Chien et al., 2011) (Dostie et al., 2006). These interactions were readily detected in purified nuclei, as they were in intact cells (**Fig. 4.2**). Third, 5C analysis (Dostie et al., 2006) of a 1 Mb region surrounding the beta-globin locus showed that known CTCF-mediated interactions were also preserved (**Fig. 4.2**). Fourth, genome-wide Hi-C analysis (Belaghzal et al., 2017) (Lieberman-aiden et al., 2009) confirmed that chromosome territories, compartments (determined by principle component analysis, with compartments captured by the first principle component (PC1) (Belaghzal et al., 2017) (Lieberman-aiden et al., 2009). TADs, and CTCF-CTCF loops were intact in isolated nuclei and quantitatively similar to those in intact cells (**Fig. 4.2**). We conclude that chromosome conformation and nuclear compartmentalization as detected by 3C-based assays are intact in purified nuclei.



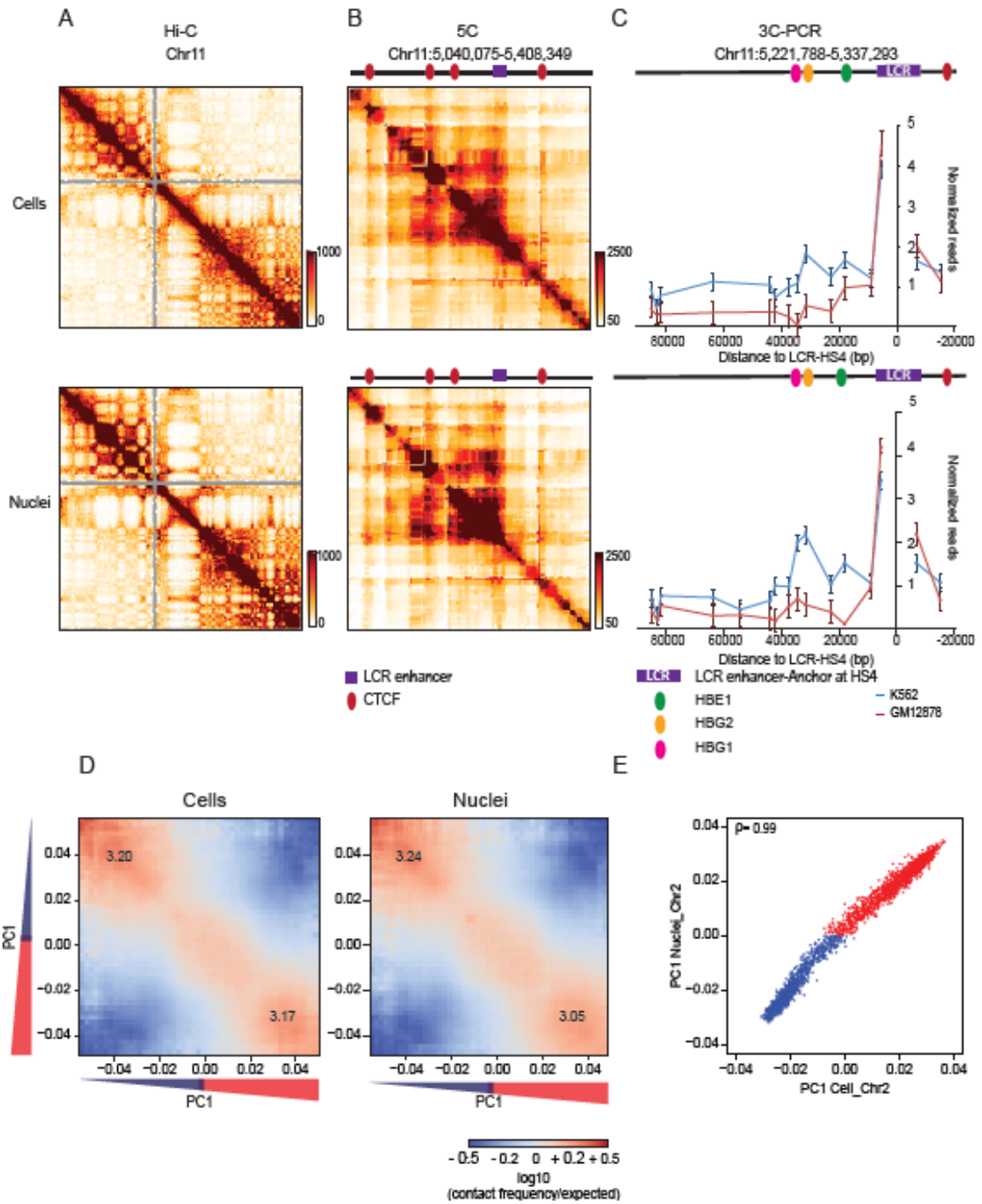


Figure 4.2: Chromosome conformation in isolated nuclei

**(A)** Hi-C 2.0 intra-chromosomal interaction maps for K562 cells display chromosomal compartments and TADs. Top: cells. Bottom: purified nuclei. **(B)** 5C interaction map of 1 Mb region surrounding the beta-globin locus in K562 cells. Top: cells. Bottom: purified nuclei. CTCF-mediated interactions are preserved in purified nuclei. Red circles: positions of CTCF sites, purple square Beta-globin locus control region (LCR). **(C)** 3C-PCR for a 44120 kb region surrounding the beta-globin LCR on chromosome 11, detects at high resolution the known looping interactions between the LCR and the expressed gamma-globin genes (HBE1, HBG2) in K562 cells. Looping interactions are not detected in GM12878 cells that do not express these genes. Top: cells. Bottom: purified nuclei. **(D)** Compartmentalization saddle plots: average intra-chromosomal interaction frequencies between 100 kb bins, normalized by genomic distance. Bins are sorted by their PC1 value derived from Hi-C data obtained with K562 cells. In these plots preferential B-B interactions are in the upper left corner, and preferential A-A interactions are in the lower right corner. Numbers in the corners represent the strength of AA interactions as compared to AB interactions and BB interactions over BA interactions. Left: cells. Right: purified nuclei. **(E)** Spearman correlation ( $\rho$ ) of PC1 in cells vs PC1 in nuclei for chromosome 2 at 100kb resolution ( $\rho = 0.99$ ).

### **Extensive chromatin fragmentation leads to the formation of liquid chromatin**

Next, we determined the effect of different levels of chromatin fragmentation on overall nuclear organization. We incubated purified nuclei for four hours with restriction enzymes that digest chromatin with different frequencies. To quantify the extent of digestion, DNA was purified, and the size distribution of DNA fragments was determined using an Agilent Fragment Analyzer. Digestion with HindIII resulted in fragments that ranged in size from ~10-25 kb (**Fig. 4.3B**). A minority of molecules was over 25 kb (<15%), indicating that most of the genome was fragmented to a similar extent. Digestion with DpnII resulted in fragments that ranged in size between ~1 and ~6 kb, with less than 6% of fragments >6 kb (**Fig. 4.3B**). Microscopic inspection of nuclear morphology by DAPI and Lamin A immunofluorescence staining showed that fragmentation of chromatin with HindIII had only minor effects on nuclear morphology (**Fig. 4.3A**). We did occasionally notice some small amounts of DNA emerging as tiny droplets from the nuclear periphery, suggesting that HindIII digestion led to some solubilization of chromatin. In contrast, fragmentation of chromatin with DpnII led to large-scale alteration of nuclear morphology as detected by DAPI staining, and large droplets of apparently liquid chromatin (not surrounded by Lamin A) emerged from the nuclear periphery (**Fig. 4.3A**, arrow).

We next tested whether different chromatin fragmentation levels had an effect on nuclear stiffness, which reflects the integrity of chromosome conformation and chromatin interactions inside the nucleus. We previously showed that single-nucleus isolation and whole-nucleus extension via micromanipulation with micropipettes provides a reliable and robust way to measure the stiffness of the nucleus (Stephens et al., 2017). K562 cells were pre-treated with the actin depolymerizing drug latrunculin A to allow isolation of the nucleus. Isolated nuclei were attached to two micropipettes at opposite ends, and the whole nucleus was extended by moving an extension micropipette. The deflection of a force micropipette multiplied by its premeasured spring constant provides a measure of the force (**Fig. 4.3C**). This data provides a force vs. extension plot (**Fig. 4.3D**, plots on the left), in which the slope of the line fitted to the data is the nuclear spring constant in nN/um (**Fig. 4.3D**, bar plots on the right). Extension between 0 – 30% strain measures the chromatin-dominated regime of nuclear force response (Stephens et al., 2017) (Stephens, Liu, Banigan, Almassalha, & Misteli, 2018), and simulations of nuclear mechanics suggest chromosomal interactions contribute to this regime (Banigan, Stephens, & Marko, 2017). Isolated single nuclei were measured for their native spring constant before treatment with a restriction endonuclease and then re-measured 60 minutes post-treatment. Nuclei treated with control conditions (only restriction buffer added to the media) showed a slight stiffening of the nucleus (**Fig. 4.3D**). Treatment of nuclei with

HindIII did not significantly decrease the stiffness compared to controls. In sharp contrast, DpnII-treated nuclei displayed a significant decrease (~75%) in stiffness, consistent with previous experiments treating nuclei isolated from mouse embryonic fibroblasts with AluI (Stephens et al., 2017). We conclude that global chromosome and nuclear organization can tolerate genome-wide fragmentation to 10-25 kb segments, indicating that sufficient numbers of relatively stable chromatin interactions are maintained between these large fragments throughout the genome to maintain nuclear stiffness. In contrast, fragmenting the genome to smaller than 6 kb segments results in extensive loss of chromatin morphology, loss of chromatin-mediated stiffness, and the appearance of a liquid-like state of chromatin.

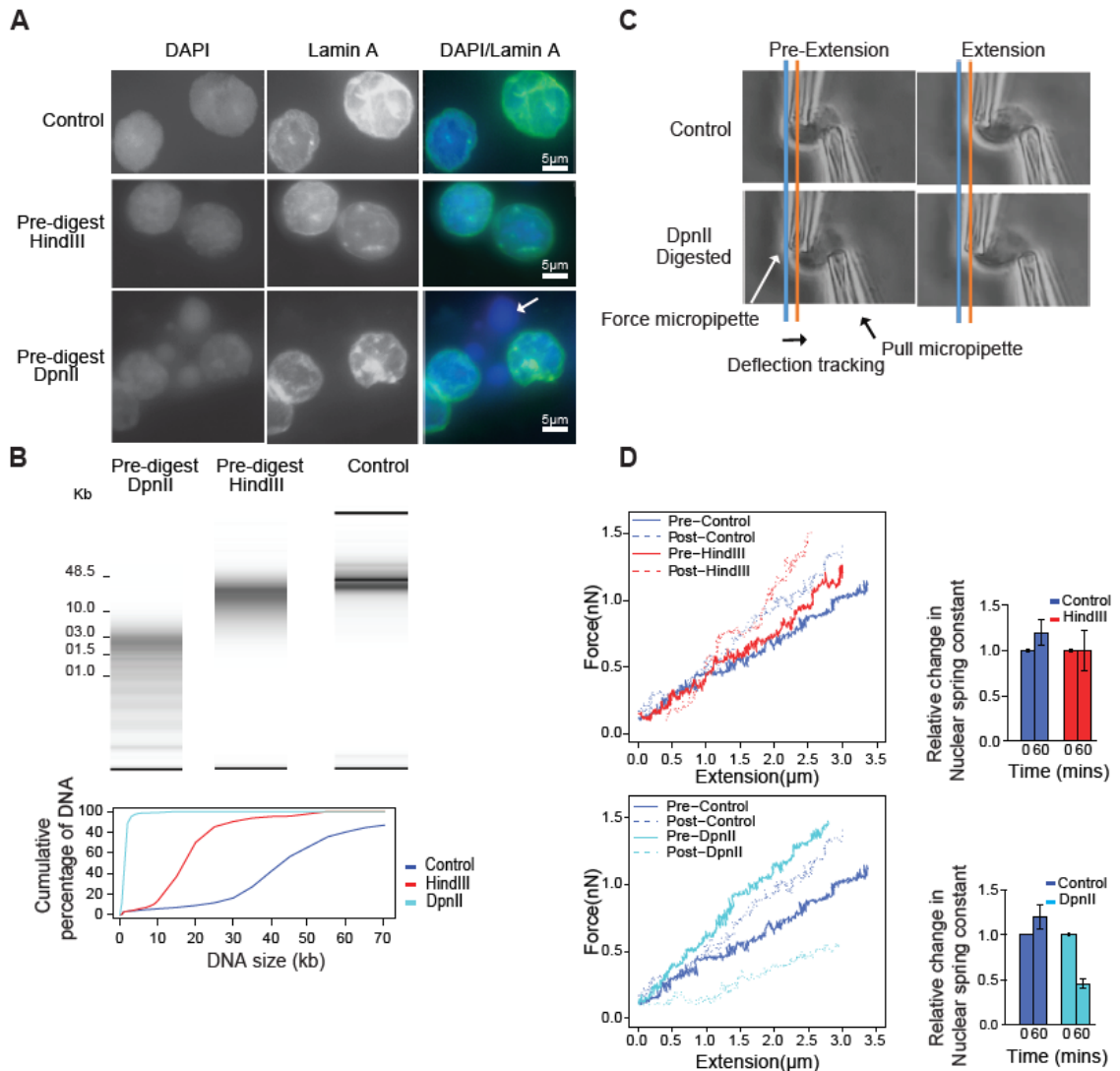


**Figure 4.3: Extensive fragmentation of chromatin leads to liquefied chromatin**

**(A)** Nuclear and chromatin morphology before and after chromatin fragmentation. Top row: control nuclei in restriction buffer, middle row nuclei digested for 4 hours with HindIII. Bottom row: nuclei digested for 4 hours with DpnII. Nuclei were stained with DAPI (left column), with antibodies against Lamin A (middle column). The right column shows the overlay of the DAPI and Lamin A stained images. HindIII digestion did not lead to major alteration in nuclear morphology and chromatin appearance, while DpnII digestion led to the appearance of DAPI stained droplets (arrow) exiting the nuclei. **(B)** Top: DNA purified from

undigested nuclei, and nuclei pre-digested with DpnII and HindIII was run on a Fragment Analyzer. Bottom: cumulative DNA length distributions calculated from the Fragment Analyzer data. **(C)** Micromanipulation of single nuclei. Isolated nuclei were attached to two micropipettes at opposite ends. Nuclei were extended by moving the right micropipette (Extension micropipette) and the force required was calculated from the deflection of the calibrated “force” (left) pipette. Blue and orange lines indicate the position of the force pipette before and after extension for control nuclei. After digestion of nuclei with DpnII (bottom) extension required less force as indicated by the much smaller deflection of the force pipette as compared to control nuclei (see also Supplemental Movies 1 and 2). **(D)** Force-extension plots (left) for control nuclei before and 60 minutes after incubation in restriction buffer (pre- and post control), for nuclei before and after digestion with DpnII, and for nuclei before and after HindIII digestion. Right panel: relative change in nuclear spring constants, calculated from the slopes of the force-extension plots shown on the left. Bars indicate standard error of the mean (n = 5 DpnII pre-digested nuclei, and n = 4 HindIII pre-digested nuclei).

### **Liquid chromatin Hi-C analysis reveals that compartmental segregation requires chromatin fragments larger than 6 kb**

To determine how chromosome folding and nuclear compartmentalization across the genome is altered as a function of chromatin fragmentation level, we applied Hi-C before (conventional Hi-C) and after chromatin liquefaction (liquid chromatin Hi-C). Nuclei were incubated with only restriction buffer (control) for 4 hours or were digested with either HindIII or DpnII for 4 hours followed by formaldehyde fixation and Hi-C analysis (**Fig. 4.4A**). Liquid chromatin Hi-C interaction maps obtained from nuclei that were pre-digested with HindIII were remarkably similar to those obtained with nuclei that were not pre-digested (**Fig. 4.5A**). The relationship between interaction frequency and genomic distance was largely unaffected, with only a slight redistribution to longer-range interactions

(**Fig. 4.5B**). The ratio of intra- vs. inter-chromosomal interactions was also highly similar to that in untreated nuclei (**Fig. 4.5B**). Compartments (**Fig. 4.5D**) were readily detectable as a plaid pattern in Hi-C interaction maps. This pattern is captured by the first principle component (PC1). Compartment positions were unaffected (Spearman  $R=0.99$ ).

Chromosome compartment strength can be visualized and quantified by plotting interaction frequencies between pairs of 40 kb loci arranged by their values along the first eigenvector (PC1) to obtain compartmentalization saddle plots (**Fig. 4.5C**). In these plots the upper left quadrant represents B-B interactions and the lower right corner represents A-A interactions. Interestingly, in nuclei pre-digested with HindIII, the strength of preferential A-A and B-B interactions (**Fig. 4.5C**; **Fig. 4.4C**) was somewhat increased, indicating stronger segregation of A and B compartments. This observation, puzzling at first, is in fact readily understood when chromosomes fold as block co-polymers. Polymer theory predicts that very mild fragmentation of a copolymer can enhance phase (or microphase) separation by removing covalent linkages between A and B blocks as long as the fragments are still large enough to sufficiently attract each other. Our results show that chromatin fragments of 10-25 kb are long enough to allow stable segregation of A and B compartments genome-wide.

Much more extensive changes in chromosome conformation were observed when nuclei were pre-digested for 4 hours with the frequent cutting



enzyme DpnII (**Fig. 4.5A**) followed by formaldehyde fixation and Hi-C analysis. We observed a considerable loss in shorter range (<10 Mb) intra-chromosomal interactions, with a gain of longer range (>10 Mb) interactions and inter-chromosomal interactions (**Fig. 4.5B**). The gain in inter-chromosomal interactions appeared to be the result of random mixing of As and Bs as the preference for interchromosomal A-A and B-B interactions decreased. Moreover, compartment strength *in cis* was greatly reduced with a greater relative reduction evident in the A compartment (**Fig. 4.5C**). This more prominent loss of A-A interactions compared to B-B interactions is also apparent from direct visual inspection of the Hi-C interaction maps: while in Hi-C maps from undigested nuclei a plaid interaction pattern is clearly visible with two alternating patterns of chromatin interactions (representing A and B compartments), in liquid chromatin Hi-C maps from DpnII-pre-digested nuclei one of these two patterns is weakened more or lost (corresponding to the A compartment). Combined, these observations show that fragmentation in <6 kb fragments leads to loss of spatial segregation of A and B compartments and dissolution of chromosome conformation genome-wide but with more extensive loss of the A compartment.

### **Quantification of chromosome conformation dissolution upon chromatin fragmentation**

Loss of chromosome conformation and dissolution of chromosomal compartments will result in randomly mixing of previously spatially separated loci both *in cis* and *in trans*. In Hi-C this will be apparent by loss of short-range

interactions and gain in longer range and inter-chromosomal interactions. We used this phenomenon to quantify for each locus along the genome the extent of loss of chromosome conformation upon chromatin fragmentation. Specifically, using Hi-C data binned at 40 kb resolution we developed a metric which represents the percentage change in short range intra-chromosomal interactions (up to 6 Mb) for each fragmentation condition relative to control nuclei, which we call loss of structure (LOS) (**Fig. 4.4B**).

We first calculated LOS after 4 hours for chromatin fragmented with HindIII. We observe that in general short-range interactions are only somewhat reduced, consistent with the above observation that interactions are somewhat redistributed to longer-range interactions (**Fig. 4.5B**). When LOS is plotted along chromosomes (**Fig. 4.5D**), we observed that LOS is not uniform: some regions display more loss of short-range interactions than others. To determine how the loss of interactions is related to A and B compartments, we compared LOS to the PC1 value that captures compartmentalization (Lieberman-aiden et al., 2009) and observed that LOS was positively correlated with PC1 (**Fig. 4.5D**; **Fig. 4.5E** left panel): ~3 - 12% loss for loci in A and <5% loss for loci in B (**Fig. 4.5E**). We note that this effect is very small and close to technical variation between replicates. Thus, chromosome conformation and compartmentalization are intact in nuclei pre-digested with HindIII (**Fig. 4.4C** for a replicate).

We performed the same analysis for nuclei pre-digested with DpnII for 4 hours followed by formaldehyde fixation and Hi-C. Consistent with the micromechanical measurements described above, we find an extensive loss of chromosome conformation, with LOS generally >80%. LOS varies along chromosomes and is strongly positively correlated with PC1 with loci in the A compartment displaying the largest loss (**Fig. 4.5D**; **Fig. 4.5E** right panel). These results again show that chromatin fragmentation to <6 kb fragments leads to extensive genome-wide dissolution of chromosome conformation, random mixing of loci, and loss of spatial segregation of A and B compartments, with the A compartment affected to the largest extent.

#### **Independent contributions of compartment status and fragmentation level to chromatin dissolution**

As outlined above, phase segregation of polymers is predicted to depend on both the length of fragments and the attractive forces between them. Therefore, one explanation for the greater effect of fragmentation on chromatin interactions and chromosome conformation in the A compartment could be solely that DpnII cuts more frequently in the open and potentially more accessible A compartment. To assess this, we determined the cutting frequency of DpnII in isolated nuclei across the genome (DpnII-seq; **Fig. 4.6**). Nuclei were digested with DpnII for 4 hours, and free ends were filled in with biotinylated nucleotides. After shearing, biotin-containing fragments were isolated, DNA was sequenced and reads were mapped to the genome. The frequency of fragments mapping

with one end at a DpnII restriction site was calculated along chromosomes at 40 kb resolution and compared to PC1. We find that digestion frequency is positively correlated with PC1 and with LOS (**Fig. 4.5D**; **Fig. 4.5F** left panel; **Fig. 4.4D**).

To determine whether the correlation between LOS and PC1 is only due to the fact that DpnII digestion is correlated with PC1 we calculated the partial correlation between LOS and PC1 after correcting for the correlations of PC1 and LOS with DpnII digestion frequency. We find that the residuals of PC1 and LOS are still highly correlated (Spearman  $R = 0.46$  for chromosome 2; **Fig. 4.5G**). To illustrate the correlation between LOS and PC1 independent of fragmentation level directly we selected a set of loci along chromosome 2 that are all cut to the same extent (1000-1100 reads in the DpnII-seq dataset). When we plot LOS vs. PC1 for this set we find a strong correlation (**Fig. 4.5F** right panel, Spearman  $R = 0.55$ ). We also determined the partial correlation between LOS and DpnII-seq signal after correcting for their correlations with PC1. We find that after this correction LOS and DpnII-seq signal show remain correlated (Spearman  $R = 0.17$ , **Fig. 4.5G** right panel). We conclude that when generally digested to <6 kb fragments both compartment status (PC1) and fragment size independently contribute to LOS. Importantly, this implies that the interaction strength between chromatin segments is related to their compartment status.

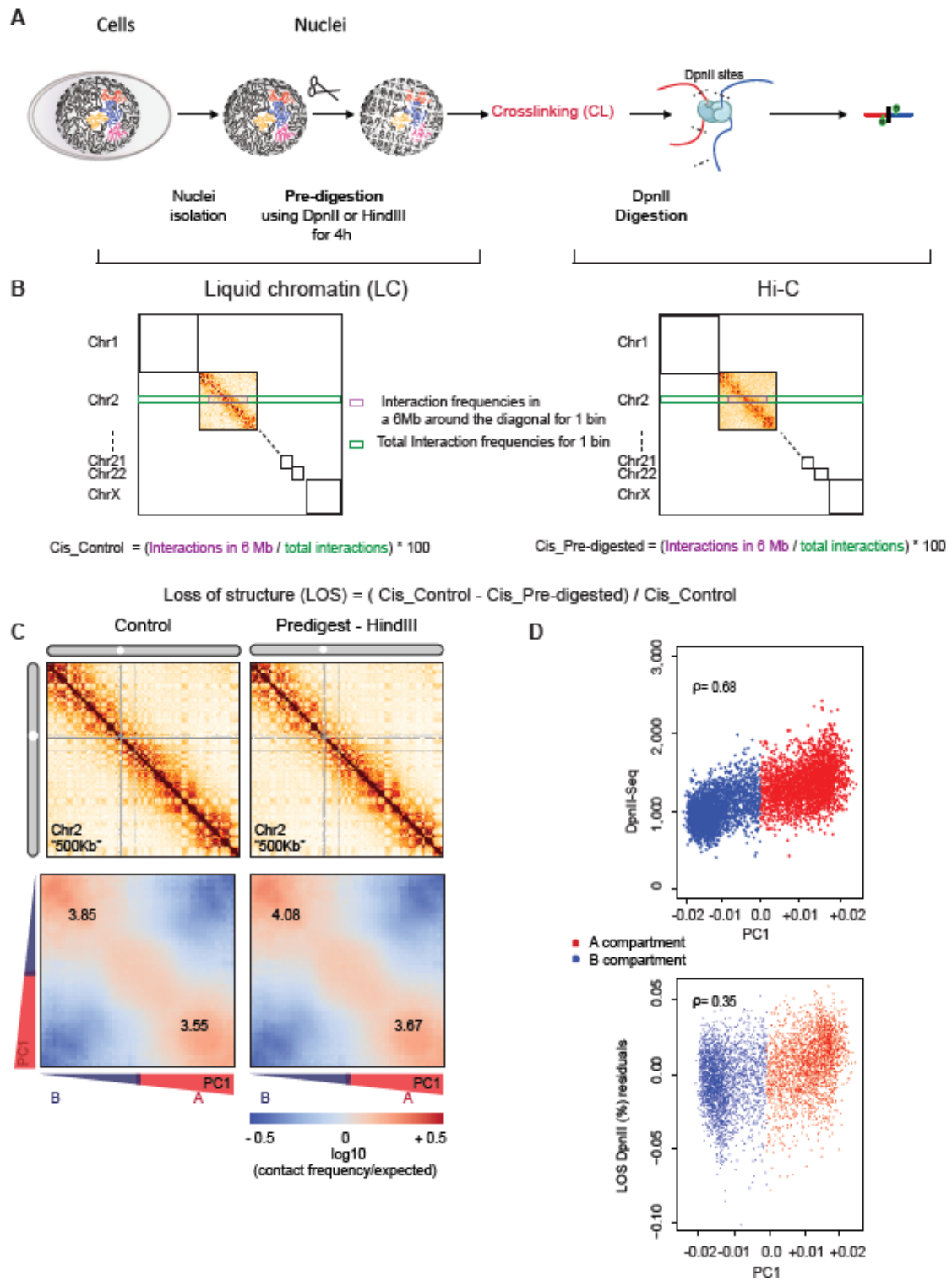
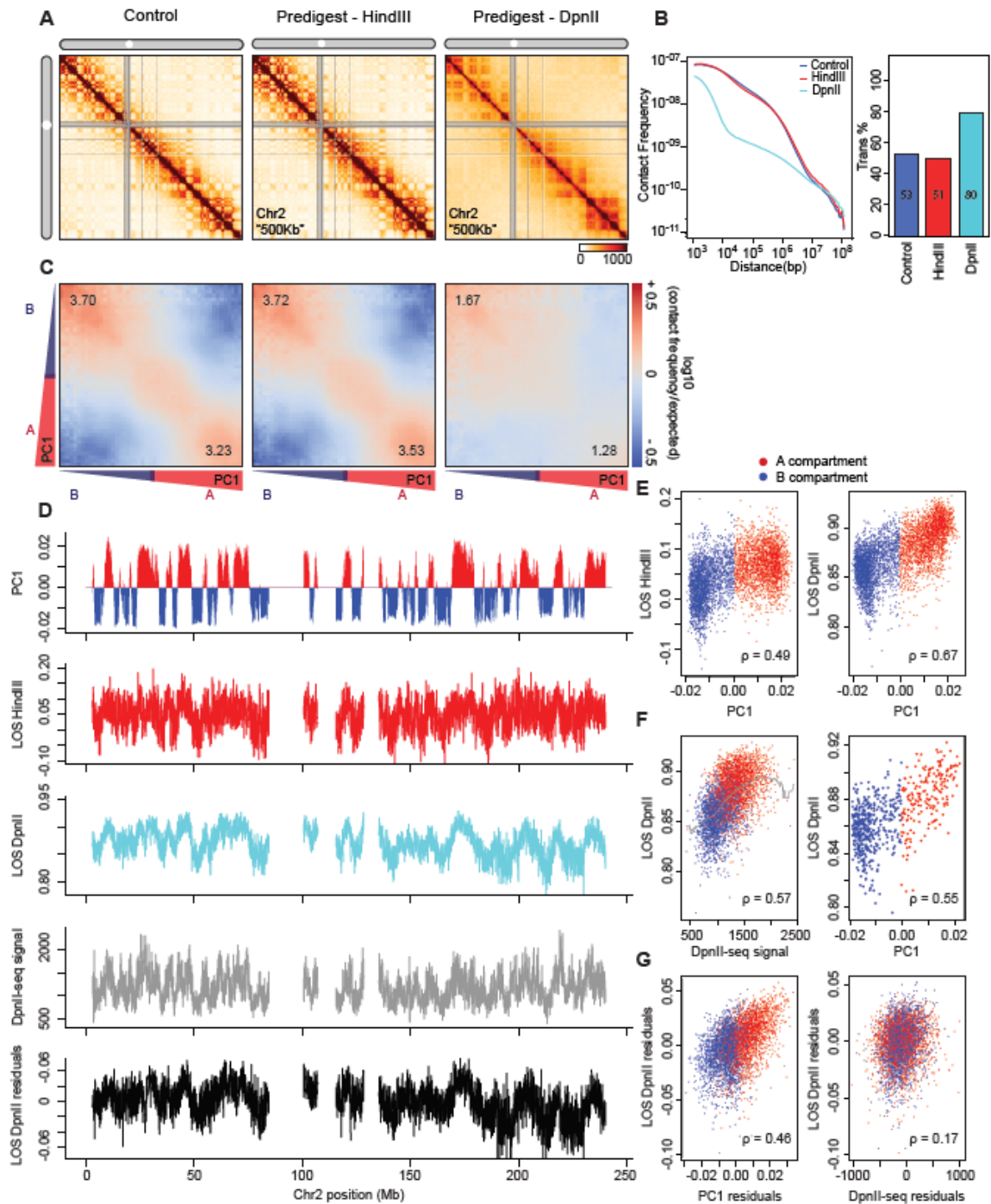


Figure 4.4: Chromosome conformation dissolution upon chromatin fragmentation

**(A)** Workflow for Liquid chromatin Hi-C. **(B)** Illustration of loss of structure metric using a pre-digested sample and a control. **(C)** Hi-C interaction maps and compartmentalization saddle plots for a second replicate of control nuclei (incubated for 4 hours in restriction buffer) and nuclei pre-digested with HindIII for 4 hours. **(D)** Top: Spearman correlation of DpnII restriction digestion efficiency (DpnII-seq) and PC1 for chromosome 2 at 40 kb resolution. Bottom: Partial correlation of LOS (LOS residuals) with PC1 after controlling for restriction efficiency (DpnII-seq), for chromosome 2 at 40kb resolution. Spearman correlation is indicated.



**Figure 4.5: Hi-C analysis reveals chromosome disassembly upon chromatin liquefaction**

**(A)** Hi-C interaction maps of chromosome 2 binned at 500 kb. Left: interaction map for control nuclei in restriction buffer prior to pre-digestion. Middle: nuclei pre-digested for 4 hours with HindIII prior to Hi-C. Right: nuclei digested for 4 hours with DpnII prior to Hi-C (see Figure 4.4A). **(B)** Left: genome-wide interaction frequency as function of genomic distance for control nuclei (dark blue), nuclei pre-digested with HindIII (red), and nuclei pre-digested with DpnII (cyan). Right: percentage of inter-chromosomal (trans) interaction frequencies. **(C)** Compartmentalization saddle plots: average intra-chromosomal interaction frequencies between 40 kb bins, normalized by expected interaction frequency based on genomic distance. Bins are sorted by their PC1 value derived from Hi-C data obtained with control nuclei. In these plots preferential B-B interactions are in the upper left corner, and preferential A-A interactions are in the lower right corner. Numbers in corners represent the strength of AA interactions as compared to AB interaction and BB interactions over BA interactions (Figure 4.8B). **(D)** Top plot: Eigenvector 1 values (PC1, 40 kb resolution) across a section of chromosome 2, representing A (red) and B (blue) compartments. Second plot: Loss of pair-wise interactions “LOS” (Methods and Figure 4.4B) along chromosome 2 at 40 kb resolution for nuclei pre-digested with HindIII. Third plot: LOS for nuclei pre-digested with DpnII. Fourth plot: DpnII-seq signal along chromosome 2 at 40 kb resolution. Bottom plot: LOS-residuals for nuclei pre-digested with DpnII after correction for DpnII signal. **(E)** Correlation between LOS for nuclei pre-digested with DpnII (left) or HindIII (right) and PC1 (for chromosome 2, Spearman correlation values are indicated). **(F)** Left: correlation between LOS for nuclei pre-digested with DpnII and DpnII-seq signal (for chromosome 2). Grey line indicates moving average used for residual calculation. Right: correlation between LOS for nuclei pre-digested with DpnII and PC1 for loci cut to the same extent by DpnII (1000-1100 DpnII-seq reads/ 40 kb bin; for chromosome 2). Spearman correlation values are indicated. **(G)** Left: partial correlation between residuals of LOS for nuclei pre-digested with DpnII and residuals of PC1 after correcting for correlations between LOS and DpnII-seq and PC1 and DpnII-seq signal. Right: partial correlation between residuals of LOS for nuclei pre-digested with DpnII and residuals of DpnII-seq signal after correcting for correlations between LOS and PC1 and DpnII-seq signal and PC1. Spearman correlation values are indicated.



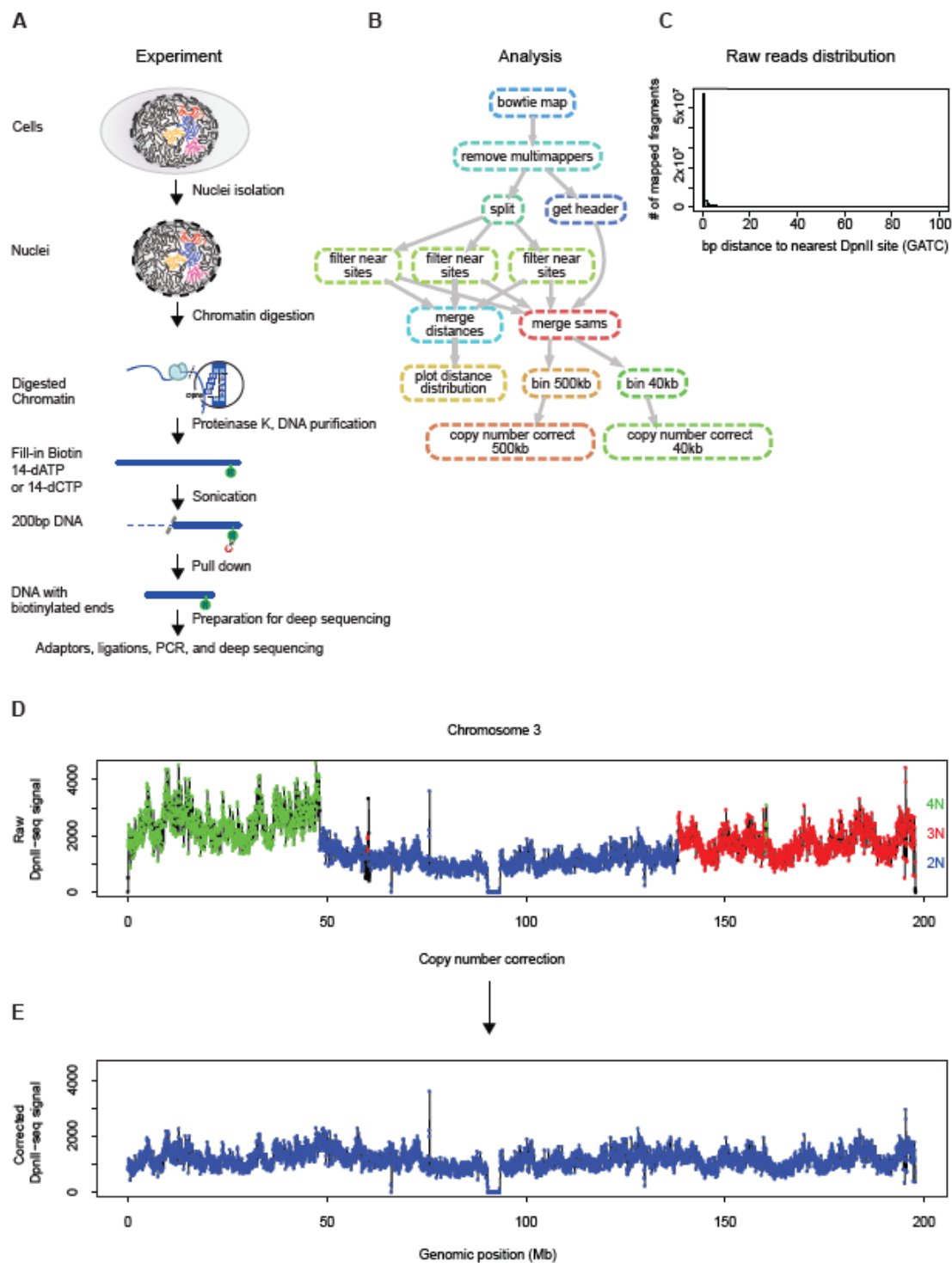


Figure 4.6: Experimental protocol and computational workflow for DpnII-seq

**(A)** Schematic of DpnII-seq experimental protocol for recovering DNA fragments digested by the restriction enzyme DpnII. **(B)** Directed graph of DpnII-seq computational pipeline. **(C)** Histogram of distance to nearest DpnII recognition site for each recovered DpnII digested fragment. **(D)** Raw DpnII-seq signal displaying multiple copy number states (2N, 3N, 4N) within chromosome 3 (data binned at 40 kb). **(E)** Copy number corrected DpnII-seq signal displaying single copy number state (2N) across chromosome 3.

### **Dissociation kinetics of chromatin interactions and compartments**

The observation that pre-digestion of chromatin with DpnII produces chromatin fragments that are too small to maintain segregation of chromatin in A and B compartments allowed us to measure the dissociation kinetics of compartments and stability of chromatin interactions as loci become mobile and start to mix. We first determined the kinetics of chromatin fragmentation (**Fig. 4.8A**). We digested nuclei with DpnII for different amounts of time, ranging from 5 minutes to 16 hours. At each time point, we isolated DNA to determine the extent of digestion (**Fig. 4.7A**). After 5 minutes the size range of fragments was between 3 and 15 kb (80% of fragments). After one hour 80% of DNA fragments were smaller than 7 kb and during the subsequent hours of digestion the fragments became gradually shorter. After 16 hours of digestion 85% of fragments were smaller than 3.5 kb. We again sequenced DNA ends to determine the distribution of DpnII cuts across the genome (**Fig. 4.7B**). We find that at all timepoints the number of DpnII cuts per 40 kb bins was correlated with

PC1 (**Fig. 4.7B**), but that the pattern did not change much over time (**Fig. 4.7B**, correlation matrix; **Fig. 4.9**). We conclude that digestion is more frequent in the A compartment at all timepoints, but that the relative pattern of fragmentation along chromosomes is relatively stable over the timecourse.

Micromanipulation was again used to measure the nuclear spring constant corresponding to nuclear stiffness. Nuclei displayed a significant loss in stiffness within 5 minutes, reaching background levels after 1 hour ((Stephens et al., 2017), **Fig. 4.7C**) when chromatin fragments are smaller than 7 kb. Combined these analyses show that the bulk of DNA fragmentation and chromatin liquefaction occurs within the first hour, after which the nuclei have completely lost their nuclear stiffness.

Next, we used liquid chromatin Hi-C to determine the kinetics with which chromosome conformation and compartmentalization are lost after chromatin fragmentation. Nuclei were pre-digested with DpnII for 5 minutes up to 16 hours, followed by formaldehyde fixation and Hi-C analysis (**Fig. 4.8A**). Interestingly, after 5 minutes of pre-digestion chromosome conformation and compartmentalization are intact, even though chromatin was fragmented to 3-15 kb segments before fixation and nuclear stiffness was significantly reduced (**Fig. 4.7C**, **Fig. 4.7D**). Further, the percentage of intra-chromosomal interactions especially for loci separated by <1 Mb was increased (**Fig. 4.7E**). Compartmentalization is somewhat increased for the A compartment (**Fig.**

**4.7D**). These increases may be due to the fact that fragments are on average around 10 kb long, only somewhat shorter than after HindIII digestion, but longer than after 4 hours of DpnII digestion (**Fig. 4.3, Fig. 4.5**). As discussed above mild fragmentation of a block copolymer is predicted to enhance both microphase or phase separation, depending on the cut frequency (see Methods at the first section).

At subsequent time points, when most chromatin fragments are <7 kb long and nuclear stiffness is completely lost, we observe increased loss of intra-chromosomal interactions and concomitant increased inter-chromosomal interactions genome-wide (**Fig. 4.7D, Fig. 4.7E**). Compartmentalization, as quantified by the preference of A-A and B-B interactions over A-B interactions, is progressively lost (**Fig. 4.7D**, lower row of heatmaps, **Fig. 4.8B**). A-A interactions disappear faster than B-B interactions. After 16 hours, only a low level of preferential B-B interaction remains. This analysis shows that chromatin fragmentation transiently leads to more frequent intra-chromosomal interactions and stronger compartmentalization due to partial digestion which is then followed by progressive genome-wide dissolution of chromosome conformation as fragments become too short, and interactions between these fragments too weak to maintain compartmentalization.

#### **Quantification of the half-life of chromosome conformation across the genome**

To quantify the kinetics of loss of chromosome conformation and compartmentalization, we calculated LOS genome-wide for each time point (**Fig. 4.7F**). At  $t = 5$  minutes, LOS is generally negative indicating a gain in chromatin interactions: on average ~25% gain of intra-chromosomal interactions between loci separated by <6 Mb, consistent with the initial increase in overall intra-chromosomal interactions described above (**Fig. 4.7E**). LOS is inversely correlated with PC1, indicating that loci located within A compartments gain more intra-chromosomal interactions than loci located within B compartments (Spearman  $R = -0.53$  for chromosome 2, Spearman  $R = -0.49$  genome-wide). At subsequent time points, LOS is increasingly positive as intra-chromosomal interactions are progressively lost and non-specific inter-chromosomal interactions are gained. LOS is the highest for loci located in the A compartment. At  $t = 16$  hours, LOS is generally as high as 90%, intra-chromosomal interactions are low (<20% of total), and only preferential B-B interactions are still observed in the Hi-C interaction map (**Fig. 4.7D**). Very similar results were obtained with an independent replicate of this time course experiment (see below). In that experiment, we again observed an initial transient gain in intra-chromosomal interactions after 5 minutes of pre-digestion, followed by a progressive loss of chromosome conformation genome-wide, but especially in the A compartment.

Now that we measured LOS as a function of time after chromatin fragmentation, we could calculate the dissociation rates of chromatin interactions genome-wide. LOS as a function of time for each 40 kb locus was fitted to an

exponential curve, which was then used to calculate the time at which each locus lost 50% of its intra-chromosomal (<6 Mb) interactions (**Fig. 4.8C**). We refer to this time as the half-life  $t_{1/2}$  (minutes) of chromatin interactions at each locus (Fig. 4F). A short  $t_{1/2}$  represents unstable interactions, while more stably interacting loci will have longer  $t_{1/2}$  values. Examining  $t_{1/2}$  along chromosomes, we observe a strong inverse correlation with PC1 (Spearman  $R = -0.87$ ; **Fig. 4.8F**): interactions in the A compartment dissolve relatively fast ( $t_{1/2} = 40$ -80 minutes) while interactions in the B compartment dissolve slower ( $t_{1/2} = 60$ -120 minutes; **Fig. 4.8D**). We also calculated  $t_{1/2}$  genome-wide for the second independent time course experiment and find a strong correlation between  $t_{1/2}$  calculated from the two datasets (Spearman  $R = 0.78$  for chromosome 2; Spearman  $R = 0.76$  genome-wide; **Fig. 4.8E**). The value of  $t_{1/2}$  is proportional to the dissociation rate constant and thus independent of the initial level of intra-chromosomal interactions for a given locus. Indeed,  $t_{1/2}$  remains highly correlated with PC1 even after correcting for correlations between the initial level of intra-chromosomal (<6 Mb) interactions and  $t_{1/2}$  and between the level of intra-chromosomal interactions and PC1 (Spearman  $R = -0.82$ , **Fig. 4.8F**, **Fig. 4.8G**).

We can also estimate the half-life of compartmentalization directly by calculating the rate of loss of preferential A-A and B-B interactions specifically from the compartmentalization saddle plots shown in **Figure 4.7D**. Using this metric, similar values of  $t_{1/2}$  were observed: 50% loss of preferential A-A

interactions was observed after ~60 minutes, while a 50% loss of preferential B-B interactions occurred after ~115 minutes.

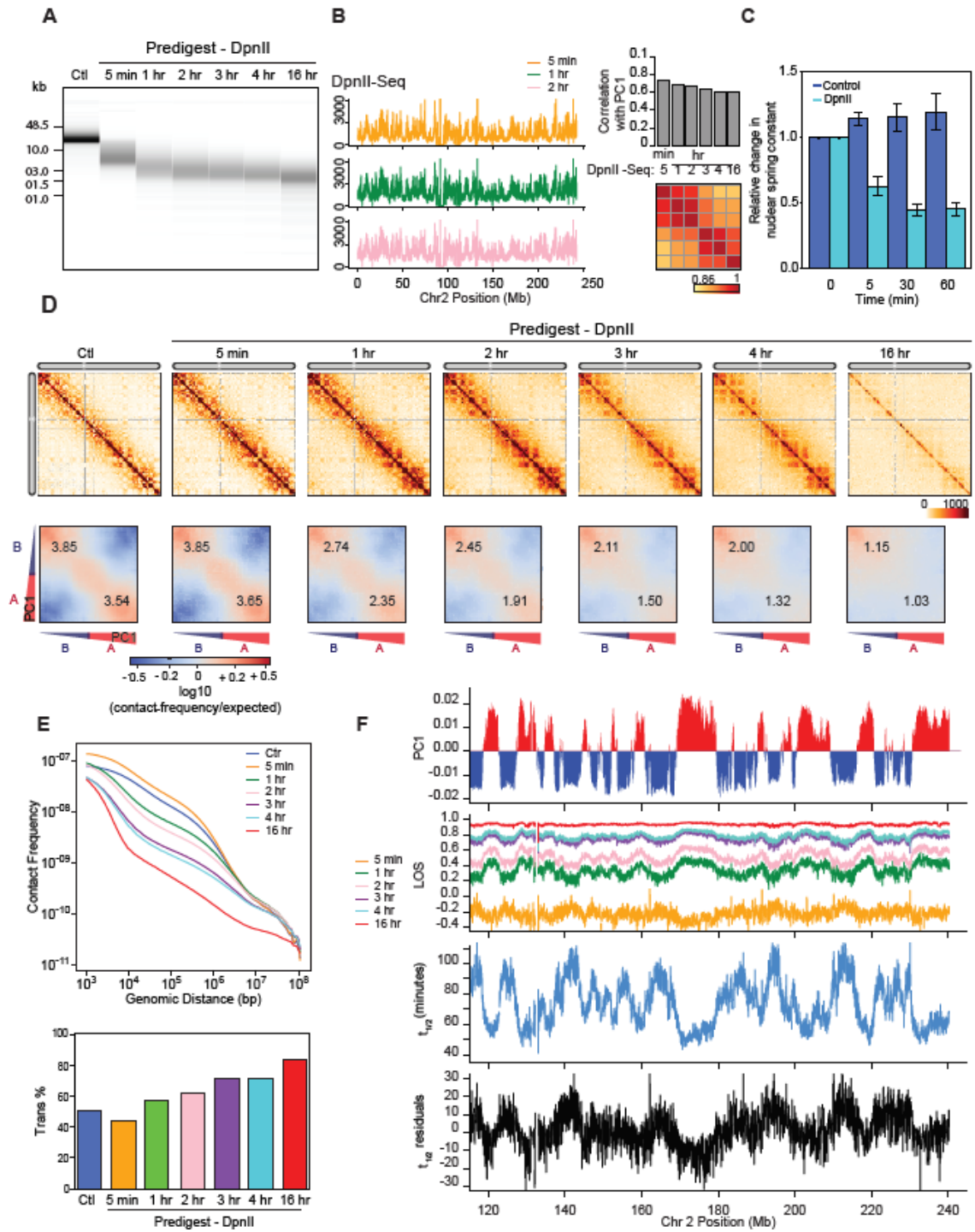


**Figure 4.7: Kinetics of chromatin fragmentation and chromatin dissolution**



**(A)** DNA purified from undigested nuclei, and nuclei pre-digested with DpnII for different time points were run on a Fragment Analyzer. **(B)** Left: DpnII-seq signals along chromosome 2 binned at 40 kb resolution after digestion for 5 minutes, 1 hour and 2 hours. Right: correlation between DpnII-seq signals and PC1 and between DpnII-seq signals at different time points. **(C)** Relative change in nuclear spring constant ( $\text{nN}/\mu\text{m}$ ) after DpnII fragmentation at different time points. Spring constant is significantly decreased after 5 minutes and at background level by 1 hour ( $p = 0.002$ , two-tailed t-test). **(D)** Top row: Hi-C interaction maps of chromosome 2 binned at 500 kb. Control: nuclei in restriction buffer for 4 hours. Pre-digest DpnII: nuclei were pre-digested with DpnII for 5 minutes up to 16 hours. (Figure 4.8A). Bottom row: compartmentalization saddle plots for the corresponding conditions. Numbers indicate strength of A-A and B-B interactions. **(E)** Top: genome-wide interaction frequency as function of genomic distance for Hi-C data shown in panel (C). Bottom: percentage of inter-chromosomal (trans) interactions genome-wide for control nuclei and for nuclei pre-digested with DpnII for up to 16 hours. **(F)** Top: PC1 along a section of 120 Mb of chromosome 2. Second plot: LOS along chromosome 2 at 40 kb resolution for all time points (Figure 4.4B). Third plot: half-life ( $t_{1/2}$ ) values derived from the exponential fit of the six time-points for every 40 kb bin (Figure 4.8C). Bottom plot: residuals of  $t_{1/2}$  after correcting for correlations between  $t_{1/2}$  and DpnII-seq (DpnII-seq data for  $t = 1$  hour).

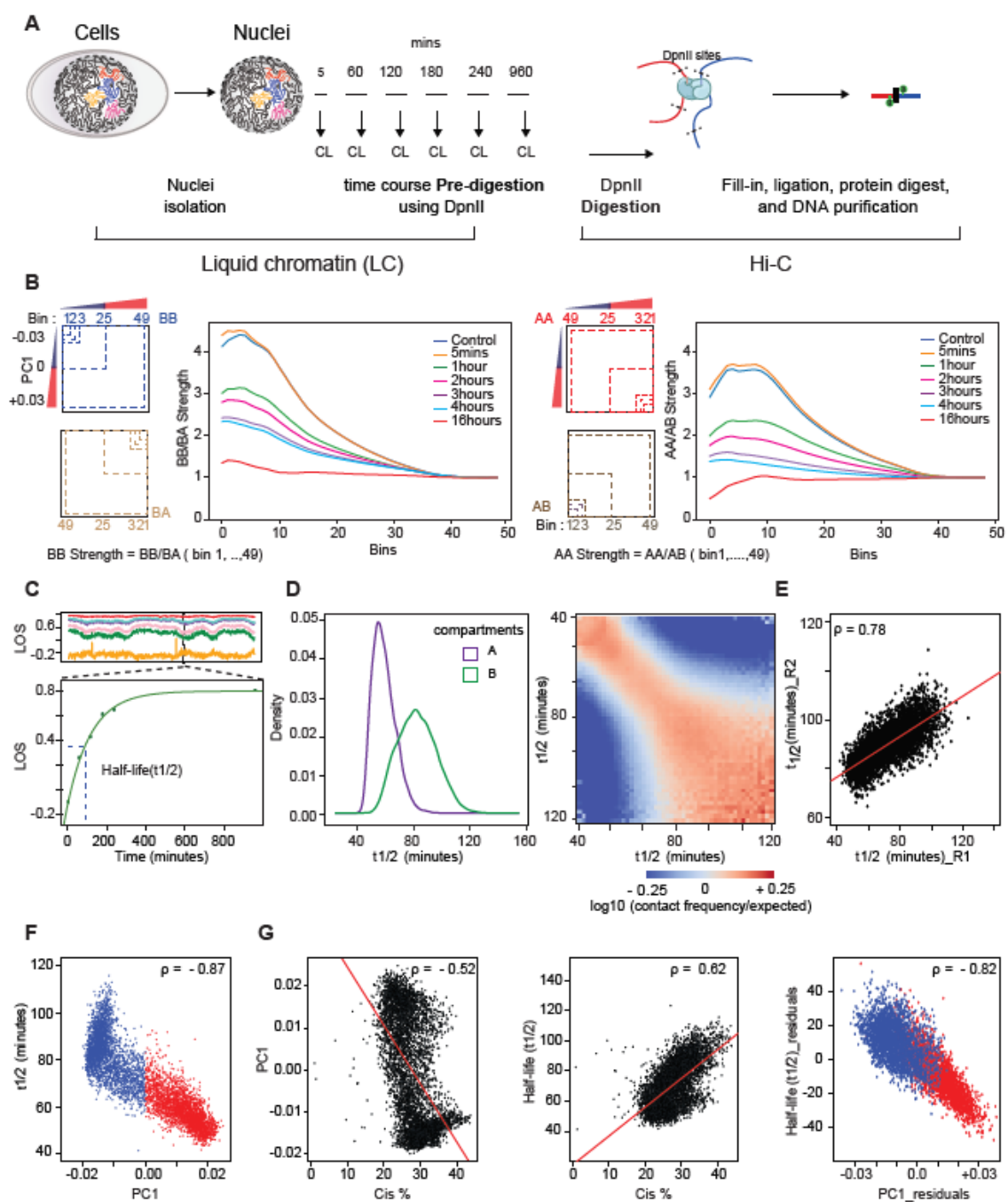


**Figure 4.8: Liquid chromatin-Hi-C protocol and quantification of loss of structure after chromatin pre-digestion**

**(A)** Workflow for Liquid chromatin Hi-C timecourse. CL = cross-linking step. **(B)** Compartment strength derived from compartment saddle plots (See Methods). Left: Diagram depicting compartment strength calculation for B-B interactions. Plot to the right of diagram: B-B interaction strength as a function of bin number for all timepoints of the time course. Right: Diagram depicting compartment strength calculation for A-A interactions. Plot to the right of diagram: A-A interaction strength as a function of bin number for all time points of the time course. **(C)** Top: LOS signal across a 40 Mb region on chromosome 2 calculated for indicated timepoints in the digestion timecourse. Line colors as in Figure 4.8 E. Bottom: Exponential curve fit to LOS timepoints for a single 40kb bin.  $t_{1/2}$  (dashed vertical blue line) representing time elapsed to reach half saturation of LOS signal. **(D)** Left: Density distributions of  $t_{1/2}$  for A and B compartments. Right:  $t_{1/2}$  saddle plots: average intra-chromosomal interaction frequencies between 40 kb bins, normalized by genomic distance. Bins are sorted by their  $t_{1/2}$  value derived from digestion timecourse. Bins with high  $t_{1/2}$  preferentially interact (bottom right of heatmap) and bins with low  $t_{1/2}$  preferentially interact (top left of heatmap). **(E)** Scatterplot of  $t_{1/2}$  vs  $t_{1/2}$  for two timecourse replicates (R1 and R2) on chromosome 2. Regression line (red). Spearman correlation is indicated. **(F)** Scatterplot of PC1 vs  $t_{1/2}$  for chromosome 2. A compartment (red); B compartment (blue). **(G)** Left: Scatterplot of percent interactions occurring *in cis* within a 6 Mb distance out of total genome wide interactions for each 40 kb bin in control Hi-C map (Cis %) vs PC1. Middle: Cis% vs  $t_{1/2}$ . Right: Scatterplot of partial correlation between PC1 and  $t_{1/2}$  controlled by Cis %. A compartment (red); B compartment (blue). Solid red lines are regression lines. Spearman correlations are indicated.

### **Independent contributions of compartment status and fragmentation level to the half-life of chromatin interactions**

Similar to LOS,  $t_{1/2}$  is correlated with DpnII digestion frequency at all timepoints (**Fig. 4.9A**). We again determined the individual contributions of compartment status and fragmentation level to  $t_{1/2}$ . We calculated the partial correlation between  $t_{1/2}$  and PC1 after correcting for correlations between PC1 and  $t_{1/2}$  with DpnII cutting frequency. We find that  $t_{1/2}$  and PC1 remain strongly correlated (**Fig. 4.7F**), regardless of which DpnII fragmentation dataset ( $t = 5$  min up to  $t = 16$  hours) was used for the calculation of the partial correlation (**Fig. 4.9A, Fig. 4.9B**). We also calculated the partial correlation between  $t_{1/2}$  and fragmentation level after correcting for their correlations with PC1 and find that fragmentation level also contributes to  $t_{1/2}$  but to a smaller extent (genome wide Spearman  $R = -0.48$ , chromosome 2 Spearman  $R = -0.31$ ). We conclude that after digestion with DpnII dissolution kinetics are determined by both the compartment status of loci and their fragmentation level.

Finally, we considered whether we could have overestimated the  $t_{1/2}$  for loci in the B compartment because fragmentation of these loci could be slower than for loci in the A compartment. We reasoned that because after 1 hour incubation with DpnII digestion is largely complete, calculation of LOS using the Hi-C data at  $t = 1$  hour as starting condition would provide an estimate of dissolution kinetics starting at a timepoint when A and B compartments are both extensively fragmented. We find that LOS, and  $t_{1/2}$  calculated this way are still

strongly correlated with PC1, and this correlation remains strong after correcting for fragmentation level (**Fig. 4.9D, Fig. 4.9E, Fig. 4.9F**).

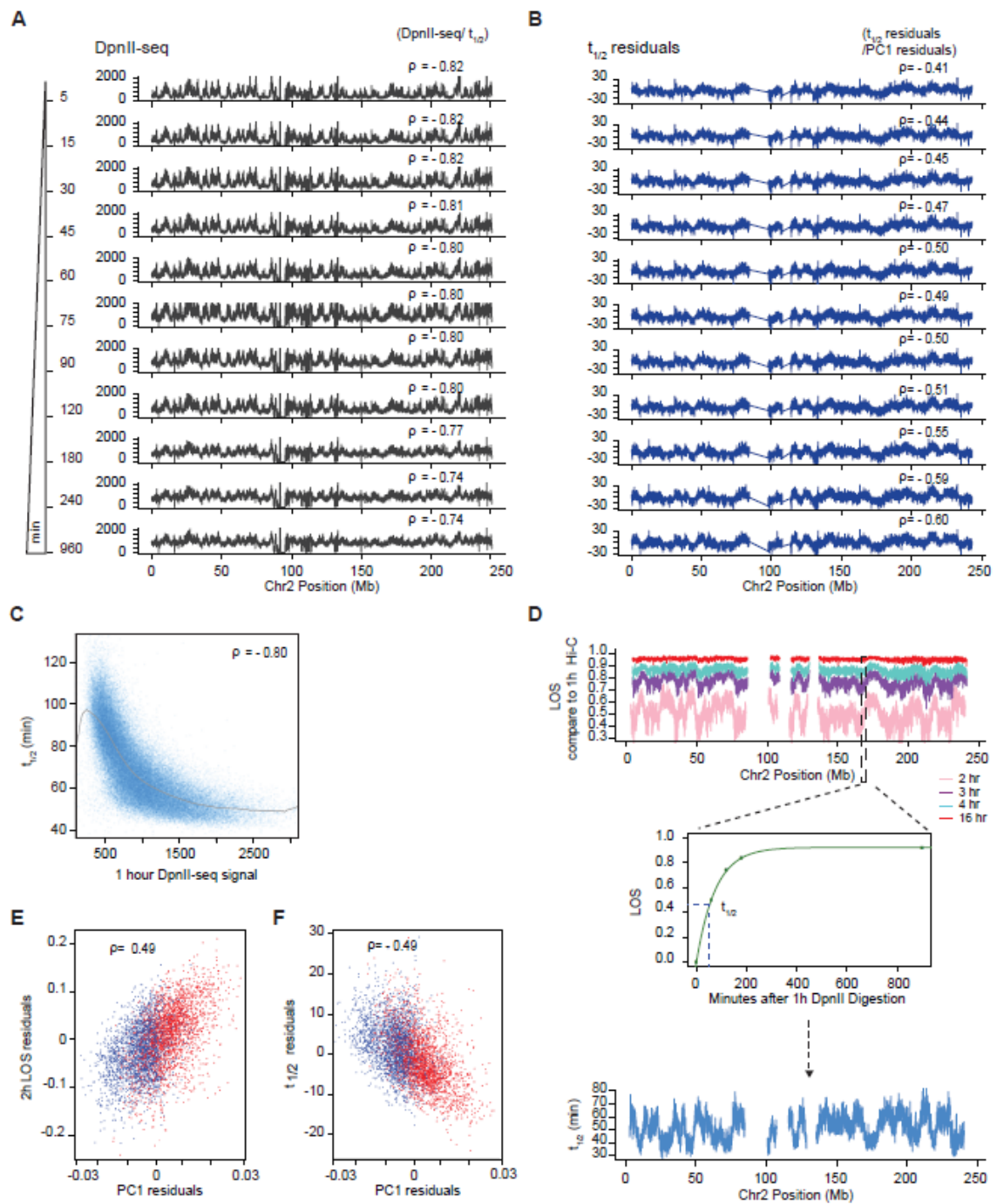


**Figure 4.9: Variations in Half-life and LOS are not explained by DpnII digestion kinetics.**

**(A)** DpnII-seq signals along chromosome 2 after indicated times of digestion. Spearman correlations between DpnII-seq and  $t_{1/2}$  at each timepoint is indicated. **(B)**  $t_{1/2}$  residuals along chromosome 2 after correcting  $t_{1/2}$  values by the correlation between  $t_{1/2}$  and DpnII-seq signals shown on the left obtained after the indicated times of digestion. Spearman correlation between  $t_{1/2}$  residuals and PC1 residuals are indicated. **(C)** Genome wide scatterplot of  $t_{1/2}$  versus 1 hour DpnII-seq signal. Gray line: moving average. **(D)** Top: LOS along chromosome 2 at the indicated timepoints of digestion and calculated by comparison to Hi-C data obtained after 1 hour of digestion. Middle: calculation of  $t_{1/2}$  from LOS at different timepoints. Bottom:  $t_{1/2}$  along chromosome 2. This  $t_{1/2}$  is calculated using the Hi-C data obtained after 1 hour of pre-digestion as starting point. **(E)** Partial correlation between LOS and PC1 after correcting for their correlations with DpnII-seq. LOS (at 2 hours) is calculated as in panel D using the Hi-C data obtained after 1 hour of pre-digestion as starting point. **(F)** Partial correlation between  $t_{1/2}$  and PC1 after correcting for their correlations with DpnII seq.  $t_{1/2}$  is calculated as in panel D using the Hi-C data obtained after 1 hour of pre-digestion as starting point. Spearman correlations are indicated.

### **Compartment size and boundaries influence chromatin interaction stability**

We next explored the correlation between PC1 and  $t_{1/2}$  in more detail. Although these two parameters are highly correlated, visual inspection of the data suggested that the largest A compartments appeared to have the smallest  $t_{1/2}$  while the largest B compartments had the largest  $t_{1/2}$ . To quantify this, we plotted  $t_{1/2}$  for each 40 kb bin as a function of the size of the compartment that the bin was located in (**Fig. 4.10D**). We find that loci within small A compartments had larger  $t_{1/2}$  values than loci in larger A compartments. Analogously, loci within small B compartments had smaller  $t_{1/2}$  values than loci in larger B compartments.

One explanation for this effect is that proximity to a compartment boundary modulates the stability of loci. To analyze this, we aggregated PC1 and  $t_{1/2}$  around A-B compartment boundaries (**Fig. 4.10C**). We find that while PC1 switches sharply at boundaries,  $t_{1/2}$  changes less rapidly. As a result, loci in A compartments but near a boundary have larger  $t_{1/2}$  values than expected for their PC1 value, while loci in B compartments but near a boundary have smaller  $t_{1/2}$  values than expected for their PC1 value. This boundary effect can contribute to bins in smaller compartments having larger (A compartment) or smaller (B-compartment)  $t_{1/2}$  values than loci in larger compartments.



## Dissociation kinetics of chromatin interactions at different sub-nuclear structures

A compartments can be split into A1 and A2 sub-compartments that are both characterized by open and active chromatin, with the A1 sub-compartment the most enriched in active histone modifications. The A1 sub-compartment is found in close proximity to nuclear speckles (Chen et al., 2018). Inactive chromatin can be classified into B1, B2 and B3 sub-compartments. B2 and B3 are generally inactive domains and are located near the nuclear lamina (B2 and B3) and the nucleolus (B2) (Chen et al., 2018) (Quinodoz et al., 2018) (Rao et al., 2014). B1 is enriched in the repressive H3K27me3 mark, which is often associated with polycomb binding. To relate sub-compartment status to chromatin dissociation rates, we compared the residuals of  $t_{1/2}$  (after correcting for fragmentation level) for loci located in the 5 sub-compartments defined for K562 cells (Xiong & Ma, 2018); **Fig. 4.11A**). We find that  $t_{1/2}$  varies greatly between sub-compartments:  $t_{1/2}$  (A1)  $\sim$   $t_{1/2}$  (B1)  $<$   $t_{1/2}$  (A2)  $<$   $t_{1/2}$  (B2)  $\sim$   $t_{1/2}$  (B3).

It is noteworthy that interaction dissociation rates for loci in the B1 sub-compartment are as high or higher (residuals of  $t_{1/2}$  as or more negative) than those for loci in the active and open A2 sub-compartment. Many B1 sub-compartments are indeed embedded within A compartments (**Fig. 4.10C**, **Fig. 4.10E**) and a subset is found close to nuclear speckles (Chen et al., 2018). Within the B compartment, interactions between Lamin-associated loci in the B3

sub-compartments dissociate the slowest while interactions between loci in the B2 sub-compartment dissociate somewhat faster. These observations indicate that loci associated with different sub-nuclear structures display a range of interaction stabilities. We also noted that A2 sub-compartments are frequently found near A-B boundaries (**Fig. 4.10C**) and that A2 and B2 sub-compartments tend to be located in smaller A and B compartments respectively (**Fig. 4.10E**), providing an additional explanation for the compartment size effect on  $t_{1/2}$  described above.

Consistent with the relation between chromatin state, sub-compartment status, and DNA replication timing ( Rao et al., 2014), we find a strong correlation between  $t_{1/2}$  residuals and replication timing. We split the genome into 10 bins, where each bin corresponds to sets of loci that share the same  $t_{1/2}$  residual interval. We then explored the enrichment for varying chromatin features for each  $t_{1/2}$  residual interval (**Fig. 4.11B**, **Fig. 4.11D**). Chromatin interactions for early replicating domains had short half-lives, while interactions for loci in later replicating domains were more stable (**Fig. 4.11B**). Interestingly, loci with the shortest  $t_{1/2}$  replicate in the middle of S-phase, which correlate with enrichment of polycomb bound chromatin.

The strong correlation between active chromatin and relatively unstable chromatin interactions led us to examine the role of transcription in more detail

(**Fig. 4.11C**). For each sub-compartment, we split loci into expressed (FPKM $\geq$ 1) or not expressed (FPKM $<$ 1) categories. We find that sub-compartment status is the major determinant of chromatin interaction stability, irrespective of transcriptional status. However, transcriptional status modulates  $t_{1/2}$  to some extent: in general, loci located in B2 and B3 sub-compartments are engaged in relatively stable chromatin interactions, but interactions that involve loci that are expressed have shorter half-lives. Conversely, the expression status of loci located in the A1, A2 sub-compartments had only very minor effect of  $t_{1/2}$ . Expressed loci in A1 or A2 sub-compartments had slightly longer and shorter residual  $t_{1/2}$  values. Although statistically significant, the average fold difference was small (A1: fold change = 0.84; A2: fold change = 1.72).

To explore the relationship between chromatin interaction stability, chromatin state, and association at and around sub-nuclear structures in more detail, we leveraged the wealth of chromatin state data available for K562 cells (**Fig. 4.11D**, **Fig. 4.10A**, **Fig. 4.10B**). Chen et al. mapped loci in K562 cells that are localized near nuclear speckles using the recently developed TSA-seq method (Chen et al., 2018). We find that loci near the speckle-associated protein pSC35 are engaged in the most unstable interactions in the genome. A similar result was obtained for an independent TSA-seq dataset for the speckle associated protein SON. Similarly, transcriptionally active loci, identified by ChIP-

seq for a range of histone modifications and factors associated with open chromatin such as H3K4me3 and RNA PolII, were also involved in relatively unstable chromatin interactions, though for some marks  $t_{1/2}$  varied widely.

Interestingly, interactions for loci bound by polycomb complexes (a subset of which are in the B1 sub-compartment) were as unstable as active and speckle associated loci (**Fig. 4.11D**, **Fig. 4.11B**). This suggests that polycomb-bound domains, are held together by highly dynamic interactions. Interestingly, half-lives differed for loci bound by different polycomb subunits. Loci with the shortest  $t_{1/2}$  values are enriched specifically for binding the CBX8 subunit. An example of a large polycomb-bound domain in K562 cells is the HoxD cluster. The cluster is around 100 kb in size and covered by the polycomb subunits Suz12, RNF2, CBX8 and BMI1 and the histone modification H3K27me3 (**Fig. 4.10G**). The half-life of chromatin interactions for loci in the HoxD cluster is relatively short.

Silent and closed chromatin loci around the nucleolus or at the nuclear lamina were generally engaged in the most stable interactions (**Fig. 4.11D**). Chromatin interaction stabilities for loci associated with the three distinct heterochromatin proteins 1 (HP1) differed: chromatin interactions for loci associated with HP1  $\gamma$  (CBX3) were relatively unstable while interactions for loci associated with HP1 $\beta$  (CBX1) or HP1 $\alpha$ (CBX5) were more stable. This variation is in agreement with the chromosomal locations and dynamics of these three HP1 proteins. HP1  $\gamma$  is associated with active chromatin and mobile, while HP1 $\beta$  and

HP1 $\alpha$  are typically found in constitutive heterochromatin near (peri) centromeres and much less mobile (Dialynas et al., 2007). Further indications that heterochromatic loci can display a range of chromatin interaction stabilities dependent upon their precise chromatin composition comes from the observation that stability is modulated by the ratio of HP1 $\alpha$  binding and lamin association: interactions for loci that display high levels of HP1 $\alpha$  binding but low levels of lamin association are not as stable as those for loci with lower levels of HP1 $\alpha$  binding and higher lamin association (**Fig. 4.10H**).

The differential stability of pair-wise chromatin interactions at different sub-nuclear structures can be directly visualized and quantified by plotting interaction frequencies between pairs of 40 kb loci arranged by their level of factor binding to obtain homotypic interaction saddle plots (**Fig. 4.11F**). In these plots, pair-wise interactions between loci enriched in factor binding are shown in the lower right corner, and pair-wise interactions between loci not bound by the factor are shown in the upper left corner. For instance, we observe preferential interactions between pairs of loci near speckles, as determined by SON TSA-Seq (Chen et al., 2018). After chromatin fragmentation with DpnII, we observe a progressive loss of preferential interactions between speckle associated loci, while preferential interactions between non-speckle associated loci can be observed even after 16 hours. Conversely, after chromatin fragmentation, we find that preferential interactions between lamin-associated loci remain detectable even at

late time points, while preferential interactions between loci not at the lamina disappear relatively fast.

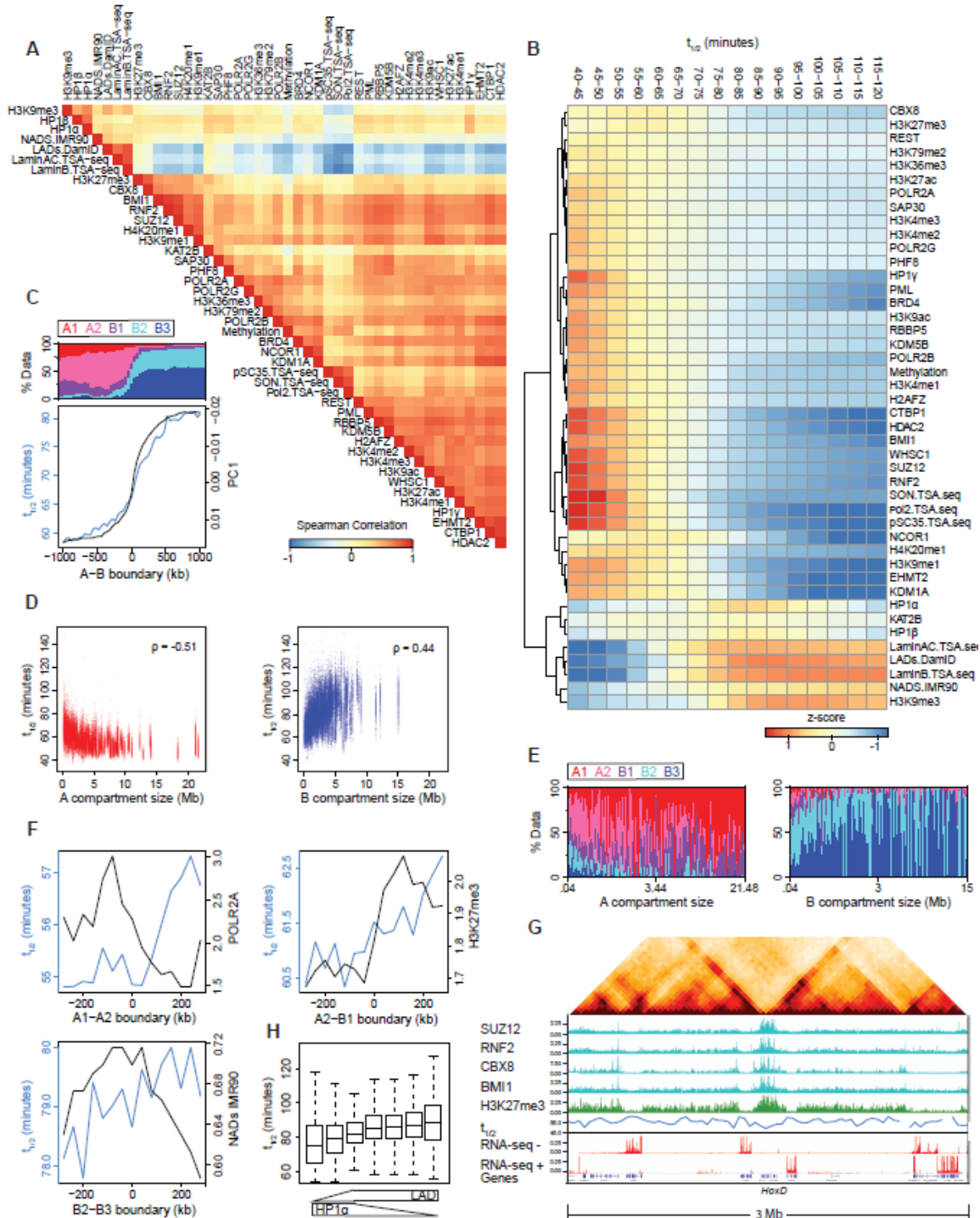


**Figure 4.10: Associations between sub-nuclear structures, compartment characteristics and chromatin interaction stability**

**(A)** Spearman correlation matrix between signals for various chromatin state markers of various sub-nuclear structures, chromatin remodellers and histone modifications with row order determined by hierarchical clustering. **(B)** The genome was split into 16 bins, where each bin corresponds to sets of loci that share the same  $t_{1/2}$  interval. For each  $t_{1/2}$  interval the mean z-score signal enrichment for various markers of sub-nuclear structures, chromatin remodellers and histone modifications was calculated and shown as a heatmap. Row order determined by hierarchical clustering. **(C)** Top: Stacked barplot displaying percentages for each of five sub-compartments within 1 Mb of A to B boundary switches with flanking A/B compartments larger than 1 Mb. Bottom: Transitions of mean  $t_{1/2}$  (blue) and mean PC1 (black) at same A to B boundary switches. **(D)** Left: Scatterplot of  $t_{1/2}$  vs size of A compartment containing  $t_{1/2}$  bin. Right:  $t_{1/2}$  vs size of B compartment containing  $t_{1/2}$  bin. **(E)** Left: Stacked barplot displaying percentages for each of five sub-compartments across and within A compartments of a specific size. Right: Stacked barplot displaying percentages for each of five sub-compartments across and within B compartments of a specific size. **(F)** Transitions of mean  $t_{1/2}$  (blue) and mean chromatin feature (black) across various sub-compartment boundary switches. **(G)** 3 Mb region surrounding *HoxD* locus. Top: Hi-C contact map for K562 control nuclei showing the position of the *HoxD* locus. Tracks: ChIP-seq tracks for polycomb subunits (cyan) and the polycomb associated histone modification H3K27me3 (green).  $t_{1/2}$  (blue). Minus strand and plus-strand signal of total RNA-seq (red). Refseq Genes (blue/black). The polycomb-bound domain displays shorter half-life compared to expressed genes in flanking regions. **(H)** Boxplots of  $t_{1/2}$  stratified by bins enriched in HP1 $\alpha$  and depleted in LADs (left) and bins depleted in HP1 $\alpha$  and enriched in LADs (right). The more LAD signal compared to HP1 $\alpha$  signal a bin has the longer it's  $t_{1/2}$ .



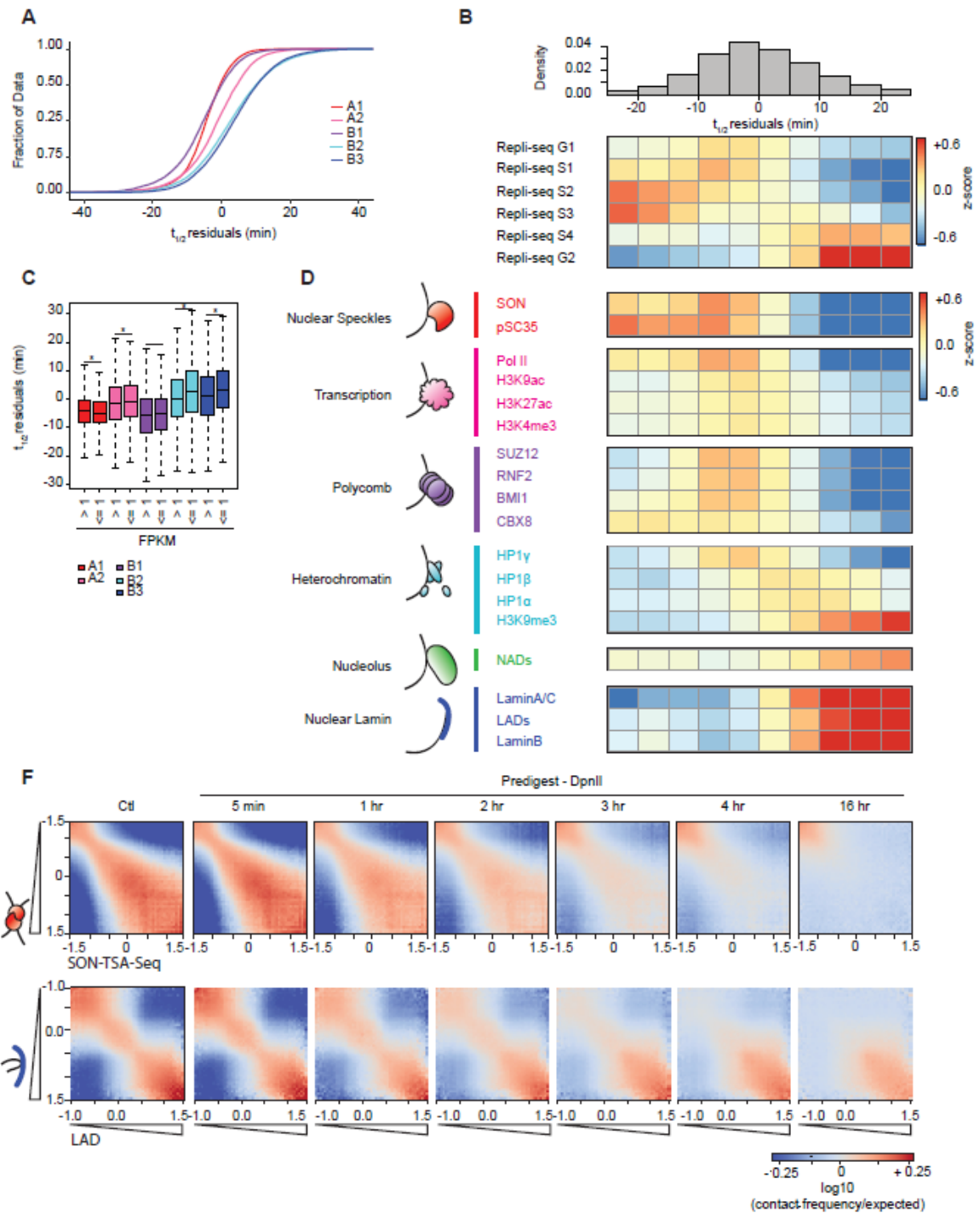


**Figure 4.11: Dissociation kinetics of chromatin interactions at different sub-nuclear structures**

**(A)** Cumulative distributions of residuals of  $t_{1/2}$  (in minutes) for each of the five annotated sub-compartments. **(B)** Heatmap of mean z-score signal enrichment for Repli-Seq data in different phases of the cell cycle G1, S1-4, G2 and stratified by  $t_{1/2}$  residual intervals (bottom). Histogram of  $t_{1/2}$  residual distribution (top). Top: the genome was split into 10 bins, where each bin corresponds to sets of loci that share the same  $t_{1/2}$  residual interval. Bottom: For each  $t_{1/2}$  residual interval the mean z-score signal of Repli-Seq data in different phases of the cell cycle G1, S1-4, G2. **(C)** Boxplot of  $t_{1/2}$  residuals for bins with expressed genes (mean FPKM > 1) and bins with low or no expression (mean FPKM ≤ 1) stratified by sub-compartment. Significance determined by two-sample two tailed  $t$ -test \* ( $p < 3.0 \times 10^{-12}$ ). **(D)** Heatmap of mean z-score signal enrichment for various markers of sub-nuclear structures (See Methods) stratified by  $t_{1/2}$  residual intervals (top of panel B). For loci in each  $t_{1/2}$  residual interval the mean z-score was quantified for different chromatin features. **(E)** Homotypic interaction saddle plots for loci ranked by their association with speckles (as detected by SON-TSA-seq, top (Chen et al., 2018) and by their association with the nuclear lamina. Preferential pair-wise interactions between loci associated with the lamina can still be observed after several hours, whereas preferential pair-wise interactions between loci associated with speckles are lost more quickly.

### **Chromatin loops dissociate upon chromatin fragmentation**

Enriched point-to-point looping interactions are detected as “dots” in Hi-C interaction maps. The majority of these represent interactions between pairs of convergent CTCF sites ( Rao et al., 2014). We were interested in determining the fate of such loops after chromatin fragmentation. We aggregated Hi-C data for purified nuclei at pairs of sites that had previously been shown to engage in looping interactions in K562 cells ( Rao et al., 2014b). We readily detected these loops in intact purified nuclei (**Fig. 4.12A**). After fragmentation with HindIII for 4 hours, loops remained present and appeared to become slightly stronger. However, fragmenting chromatin with DpnII resulted in loss of loops over time. Although loops appeared somewhat increased at  $t = 5$  minutes after DpnII digestion, they were greatly reduced at  $t = 1$  hour and at later timepoints.

Chromatin loops are thought to be formed by loop extrusion mediated by cohesin that is blocked at convergent CTCF sites. Therefore, we assessed whether CTCF and cohesin binding to chromatin is affected by chromatin fragmentation. We fractionated proteins in chromatin-bound and soluble fractions using the previously described chromatin binding assay ((Liang & Stillman, 1997), Materials and Methods). In intact nuclei, most of the CTCF and cohesin is associated with chromatin (**Fig. 4.12B, Fig. 4.12 C**). Digesting chromatin with HindIII did not lead to dissociation of CTCF or cohesin. However, fragmenting chromatin with DpnII led to dissociation of cohesin after 1 hour, while CTCF

binding was only weakly affected. We conclude that DNA fragmentation to <6 kb fragments, but not to 10-25 kb fragments, leads to loss of cohesin binding and loss of looping interactions. These results are consistent with earlier observations that showed that in yeast stable chromatin binding by cohesin requires intact DNA (Ciosk et al., 2000). These data can be interpreted in the context of the model where cohesin rings encircle DNA (pseudo-) topologically (Srinivasan et al., 2018). This model of binding predicts that when DNA is fragmented, the cohesin ring can slide off nearby free ends. Our observation that cohesin binding and loops are disrupted when chromatin is fragmented to <6 kb fragments suggest that loops are maintained by the encirclement of cohesin rings around the loop bases bound by CTCF.

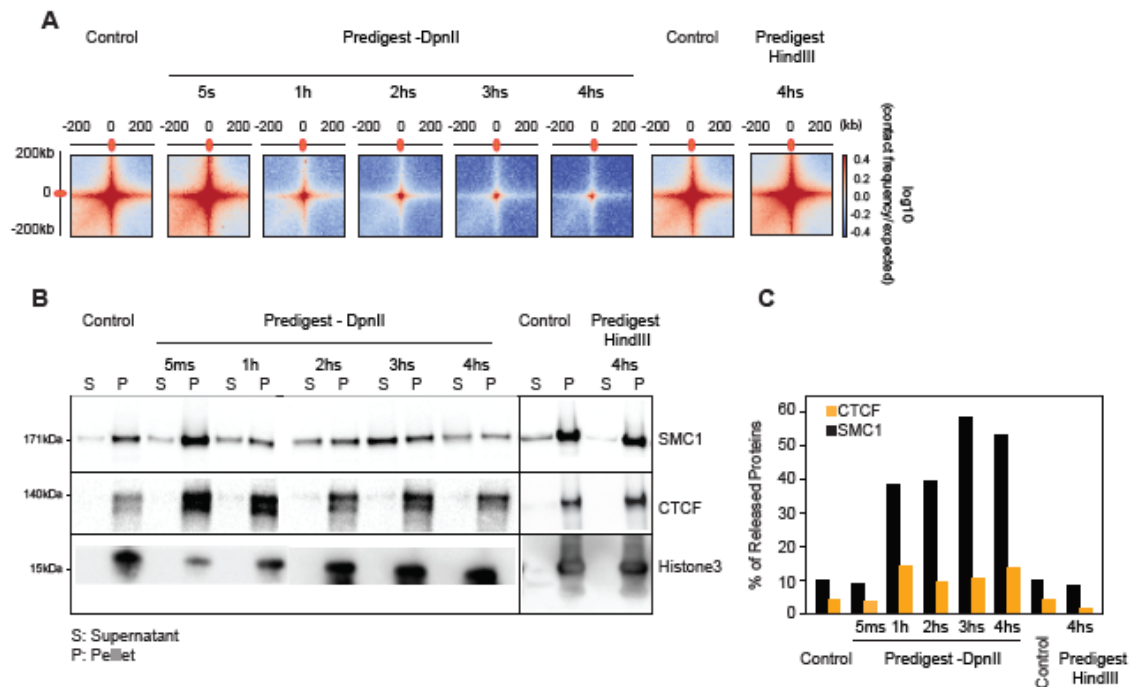


**Figure 4.12: Chromatin loop dissociation upon fragmentation**

**(A)** Aggregated distance-normalized Hi-C interactions around 6,057 loops detected in K562 cells by HiCCUPS (Rao et al., 2014) at 10 kb resolution, for control nuclei and nuclei digested with DpnII up to 16 hours, and for nuclei digested with HindIII for 4 hours. **(B)** Western blot analysis of CTCF, cohesin and Histone H3 abundance in soluble and chromatin-bound fractions obtained from control nuclei and from nuclei pre-digested with DpnII up to 16 hours and HindIII for 4 hours. **(C)** Quantification of the data shown in panel B. Percentage of released protein is the ratio of protein level in the soluble fraction divided by the sum of the levels in the soluble and chromatin-bound fractions.

## DISCUSSION

Hi-C interaction maps represent population-averaged folding of chromosomes but do not reveal whether individual pair-wise contacts are dynamic or stable. Liquid chromatin Hi-C reveals chromatin interaction stabilities genome-wide. In liquid chromatin Hi-C chromatin is fragmented prior to fixation. After fragmentation, Hi-C is then used at different time points to determine the extent to which the initially compartmentalized conformation of chromosomes is lost and the formerly spatially separated loci become mixed.

We observe an initial strengthening of A/B compartmentalization following partial digestion. This result supports a “block copolymer” model of chromatin in the interphase nucleus, where B regions of chromosomes tend to cluster together, and A regions cluster together. Partial DNA digestion leads to a strengthening of compartmentalization by removing covalent linkages between A and B blocks, as long as the fragments are still large enough so that attractive forces between them are sufficient for phase segregation.

Further fragmentation of chromatin into pieces that are too short to maintain the phase-separated state leads to the progressive dissolution of chromatin conformation. The kinetics of this dissolution process provides insights into the attractive forces between chromatin segments, the intrinsic mobility of loci, the dynamics of nuclear organization, and the protein factors that can mediate chromatin interaction stability.

## CHAPTER V: Discussion

### 3C-based technologies

3C-based technologies allow the conversion of information based on the linear genome into 3D regulatory DNA networks. Within the last decade, we have witnessed an unprecedented number of studies addressing genome folding, that have advanced our understanding on how the genome folds and how variants in DNA sequence translate to a rewiring of genome folding that leads to gene misregulation (Visel & Mundlos, 2015) (Hnisz et al., 2016) (P. Nora et al., 2017). It is likely that studies within the next decade will give us an insight into the molecular mechanisms governing the establishment of the genome folding.

A substantial reduction in sequencing costs and an increase in sequencing throughput has tremendously contributed to improving Hi-C resolution. Indeed, recent *in-situ* Hi-C studies have increased the resolution of Hi-C to 1 kb, which made it possible to detect CTCF-CTCF looping interactions between TAD boundaries as well as some promoter-enhancer interactions in very high coverage Hi-C maps. Our Hi-C 2.0 protocol discussed in chapter II is an adaptation of *in-situ* Hi-C with extra steps that eliminate uninformative outputs of Hi-C like unligated ends. In addition to technical and experimental innovations, many Hi-C data analysis and visualization platforms have been developed, including the 3dgenome browser (<http://www.3dgenome.org>) from

Feng Yue, the Juicebox tool (<http://www.aidenlab.org/juicebox/>) from the Aiden lab, Hi-C-Pro (<https://github.com/nservant/HiC-Pro>) (Servant et al., 2015b), and HiGlass, (<https://higlass.io/>) from Nils Gehlenborg lab (Kerpedjiev et al., 2018).

Hi-C 2.0 can still be improved. In particular, a better signal to noise ratio in Hi-C contact probability matrices could be obtained by modifying some of the key steps such as cross-linking, digestion, and ligation, which would produce sharper structures in Hi-C heatmaps. The improvement of signal to noise will enable detection of very infrequent interactions, such as the long-range interactions between promoters and enhancers. Another important effort will be to successfully scale down the number of cells needed for informative Hi-C experiments in order to enable the use of Hi-C to investigate genome structure from pure cell populations sorted by FACS, as well as in normal and disease-related patient tissues,

The optimization of Hi-C also relies on robust bioinformatics pipelines to validate the quality and assess the different optimization protocols. For example, the development of an analysis pipeline enabling the detection of Hi-C noise, and a pipeline to improve the resolution for a low cells input Hi-C. In a similar vein, new data standards are needed for assessing the quality of chromatin-interaction maps. One proposition for quality control would entail comparison a subset of robust pair-wise interactions that have been rigorously assessed in different cell types.



## Promoter-enhancer interactions

The genomic community used to consider that coding DNA and active genes are the most important for study because their perturbation leads to disease (Misteli, 2007). However, the genome-wide association study, GWAS, aimed at identifying disease-related SNPs, revealed that the majority of the variants fall in noncoding regions of the genome and lack a defined target gene (Variation et al., 2012). Most of these disease-specific variants systematically alter the association of transcription factors at the altered target, suggesting that they are regulatory elements (Variation et al., 2012). Regulatory elements often interact with genes that are not nearest them in the linear genome (Amartya Sanyal et al., 2012) (Sahlén et al., 2015), which makes it harder to delineate the gene target for each variant. Chromosome conformation-based method is necessary to connect each variant to its target gene, in order to explain the phenotype. For example, a SNP in an intron leading to aberrant enhancer-promoter contacts, as detected by 5C has recently linked a new target gene to obesity (Norton & Cremins, 2017) (Aneas et al., 2014). Additionally investigations of chromosome conformation using Capture Hi-C around 14

colorectal cancer risk loci in cancer cell lines (Migliorini et al., 2015), and around variants linked to four autoimmune disorders in human B and T cell lines (Martin et al., 2015) (Jäger et al., 2015; Martin et al., 2015) were each able to connect numerous disease variants to their target genes.

In the last decade, an unprecedented number of studies have investigated the functionality and mechanistic establishment of TADs. Topologically associating domains (TADs) were found to be functional blocks of the chromatin because alteration of a TAD boundary rewires the proximal gene-enhancer interactions leading to alterations in gene expression (Hnisz et al., 2016) (P. Nora et al., 2017) (Visel & Mundlos, 2015) (Wutz et al., 2017)(Gassler et al., 2017) (Sanborn et al., 2015) (Fudenberg et al., 2015). On the other hand, not much is known about the establishment and maintenance of promoter-enhancer interactions.

The majority of gene-enhancer interactions are intra-TAD, though some of these interactions resist the insulation at TAD boundaries. In acute lymphoblastic leukemia (ALL) of T-cell type “T-ALL cell lines”, the *MYC* promoter interacts with the Notch-dependent *MYC* enhancer element “NDME”, which is found 1.3 Mb downstream (Yashiro-ohsaki et al., 2014). In AML (ME-1) cells, the *MYC* gene is involved in a hub of interactions with three enhancers; ME1, ME2 (found within the same TAD with *MYC* gene), and E3 (1.7 Mb away from the promoter in a different neighboring Sub-TAD with *MYC* gene). One very important result in

chapter III is the fact that promoter-enhancer interactions remain after *MYC* inactivation, which contradicts the concept that active genes interact with their enhancers to ensure efficient recruitment of transcription factors. For example, looping between the LCR enhancer and  $\beta$ -globin locus only occurs when the gene is active in fetal liver and this loop is not established in the brain where the  $\beta$ -globin gene is inactive (Tolhuis, Palstra, Splinter, Grosveld, & Laat, 2002). A similar result for the same regulatory element LCR was shown in K562 cells when it is active, and in GM12879 when it is inactive (Dostie et al., 2006). However, interactions between super-enhancers and genes have been found to occur in small domains within TADs enriched for CTCF, cohesin, and mediator. Importantly, these super-enhancer domains remain even when the constituent genes are silenced, although mediator is switched with polycomb (Mifsud, Tavares-cadete, et al., 2015). Similarly, we have shown that the binding of the transcription factor RUNX1 to the ME1, ME2, E3 enhancers but not to the promoter, efficiently induced a switch from the transcription activator complex BRG1 to the transcription repressor RING1B at *MYC* promoter and at the ME1, ME2, E3 enhancers. The hub of interactions that is maintained between these elements independently of gene activation status facilitates the efficient recruitment of the transcription repressor RING1B upon AI-10-49 treatment, and it is possible that this hub facilitates the recruitment of transcription activator complex BRG1 when *MYC* is still active before AI-10-49 treatment. These results further validate the concept that promoter-enhancer interactions are important for

the recruitment of regulatory elements to the appropriate promoters. Importantly, the depletion of any of the three enhancers ME1, ME2, E3 altered MYC expression up to 70%, which indicates the direct role of each of the enhancers for expression of the target gene ( Figure 3.7). One experiment that was not explored in chapter III is performing 5C experiments after depletion of each single enhancer to check whether the interaction hub is maintained between the two remaining enhancers and the MYC promoter, in order to determine whether loss of the hub interactions is causing the alteration of *MYC* expression in ME-1 cancer cells. These data will also determine whether all three regulatory elements are involved in establishing this hub of interactions.

Based on this study in chapter III, extending the detection of enhancer-promoter interactions in different disease states, will enable a better understanding of the mechanism underlying a particular disease phenotype. Additionally, this information will help to identify more promising candidates for targeted therapeutics that could, for example, employ endonuclease-deficient Cas9 to recruit silencing regulatory elements to the enhancer in order to deactivate a gene and *vice versa*. There are still many unanswered questions regarding the establishment of promoter-enhancer interactions, including how an enhancer recognizes its specific target gene.

For intra-TAD gene-enhancer interactions, I and others have speculated that the TAD blocks are fundamental and are built first and that there is a hierarchical structure between TAD and gene-enhancer interactions. In such a

model, the TAD blocks bring genes and promoters in very close proximity in 3D space, then looping interaction is driven by attractions of promoters and enhancers with similar epigenetic status

Enhancers are embedded between CTCF factors, as we have seen for the E3 enhancer ( Figure 3.6) and promoters interact strongly with CTCF clusters as they tend to fall near TAD boundaries. I hypothesize that for long-range interactions  $> 1$  Mb this hub of CTCF enrichment brings the enhancer in close 3D proximity to its target promoter where they attract one another based on their epigenetic compatibility. This hypothesis can be tested using genome editing to translocate the enhancer, that is surrounded by CTCF and engaged in a long-range interaction, distantly 100~ 200 kb downstream of the surrounding CTCF hubs present in the non-diseased state. If the specific CTCF hub is important, the change in the enhancer position will alter the promoter interactions. Endonuclease-deficient Cas9 could also be used to change the epigenetic marks of an enhancer that engaged in long-range interaction during the exit from mitosis before the establishment of the loop (Huangfu & Raya, 2017), in order to determine whether the enhancer still recognizes its target promoter after the CTCF hub brings them in a close 3D proximity.

A combination of genomic, epigenetic, chromosome conformation and genome engineering approaches are necessary to connect the SNPs defined by GWAS studies with the phenotype for each associated disease. I propose that

we first need to map all interactions between promoters and enhancers for different tissue-appropriate control and diseased cells, by investigating chromosome conformation at high-resolution 3-4 Mb (using 5C or capture Hi-C) around all SNP non-coding DNA found by GWAS. Once candidate gene-targets have been defined based on 3D interactions for each regulatory element containing a variant, the DNA condensation status can be more routinely verified in a large number of individuals using ATAC-Seq, which can be done in 500 hundreds of cells (Buenrostro et al., 2013). As we have seen in chapter III, the switch from active regulatory elements to inactive elements binding the *MYC* promoter and the three enhancers ME1, ME2, and E3 lead to a condensed chromatin state at the promoter and enhancers that can be detected by ATAC seq (Figure 3.5). Finally, ChIP of activator and repressor elements could be performed for a couple of cases in order to validate the ATAC-Seq data.

### **liquid chromatin Hi-C**

Hi-C interaction maps represent population-averaged folding of chromosomes but do not reveal whether individual pair-wise contacts are dynamic or stable. Liquid chromatin Hi-C reveals chromatin interaction stabilities genome-wide. In liquid chromatin Hi-C chromatin is fragmented prior to fixation. After fragmentation, Hi-C is then used at different time points to determine the

extent to which the initially compartmentalized conformation of chromosomes is lost and the formerly spatially separated loci become mixed.

We observe an initial strengthening of A/B compartmentalization following partial digestion. This result supports a “block copolymer” model of chromatin in the interphase nucleus, where B regions of chromosomes tend to cluster together, and A regions cluster together. Partial DNA digestion leads to a strengthening of compartmentalization by removing covalent linkages between A and B blocks, as long as the fragments are still large enough so that attractive forces between them are sufficient for phase segregation.

Further fragmentation of chromatin into pieces that are too short to maintain the phase-separated state leads to the progressive dissolution of chromatin conformation. The kinetics of this dissolution process provides insights into the attractive forces between chromatin segments, the intrinsic mobility of loci, the dynamics of nuclear organization, and the protein factors that can mediate chromatin interaction stability. Using liquid chromatin Hi-C we obtain a view of the dynamics of chromatin interactions throughout the nucleus and the genome (**Fig. 5.1A**). We find that chromatin dissolution is dependent on both chromatin state and fragmentation level. After correcting for fragmentation level we observe that chromatin interactions at different sub-nuclear structures differ in their stability, with lamin-associated loci engaged in the most stable interactions and speckle and polycomb associated loci being most dynamic. Further, we find

support for the model that CTCF-CTCF loops are stabilized by cohesin rings that encircle loop bases (**Fig. 5.1B**).

Loci that are part of longer intact chromosomes display sub-diffusive dynamics, and their mobility is strongly constrained by the polymeric nature of chromatin and its folded state. In addition, their mobility is modulated by attractive interactions with other loci by factors that themselves are dynamic, and by local chromatin density. Live-cell imaging experiments have examined locus motion extensively and found differences in mobility and constrained diffusion dependent on sub-nuclear position and chromatin state and activity (Foisner & Garini, 2015) (Hediger et al., 2002) (Marshall et al., 1997) (Nagashima et al., 2019) (Shinkai et al., 2016) (Thakar et al., 2006). In such experiments, the movement detected is strongly constrained by the fact that loci are part of very long chromosomes. A previous key study, which inspired the current work, aimed to determine the factors that determine intrinsic locus-locus interactions and locus mobility by explicitly removing the strong polymeric constraint due to linkage (Gartenberg et al., 2004). In that work, the mobility of an individual locus and its preference for association with sub-nuclear structures was measured by imaging after excising the locus from its normal genomic location so that it was freed from the polymeric constraint (Gartenberg et al., 2004). Specifically, a silent locus was excised from a yeast chromosome and its intrinsic preference for association with other silent loci and the nuclear periphery was assessed and found to depend on specific protein complexes bound to these loci that are



involved in gene silencing. In our liquid chromatin Hi-C experiments, we digest DNA *in situ* and the polymeric constraint on movement is removed for all loci simultaneously, in effect performing a genome-wide variant of the experiments performed by (Gartenberg et al., 2004) After fragmentation, dynamics of locus mixing is mostly determined by interactions of individual chromatin fragments with each other and with sub-nuclear structures mediated by local chromatin-associated factors, histone modifications, and chromatin density.

We show that chromosomal compartmentalization can tolerate genome-wide fragmentation with HindIII in >10-25 kb fragments. Our micro-mechanical elasticity measurements also show that chromosomes remain mechanically fully connected in those conditions. These results indicate that interactions between 10-25 kb fragments are stable enough to maintain the initially phase- or microphase- separated state of the nucleus, at least for several hours. This is in agreement with recent independent locus-specific experiments. First, previous studies had suggested that regions of several hundred kb were long enough to correctly position themselves *in vivo* according to their chromatin state in the corresponding compartment (Werken et al., 2017) . Second, super-enhancers that typically range in size between 10 and 25 kb were found to associate both *in cis* and *in trans*, especially in the absence of cohesin (Glenn et al., 2017), indicating that interactions between these 10-25 kb elements are stable enough to facilitate their clustering. Third, high-resolution Hi-C analysis in *Drosophila* indicates that domains ~25 kb in size can phase separate according to their

chromatin status (Bonev & Cavalli, 2016). Similarly, in *Drosophila*, polycomb-bound loci can cluster together at polycomb bodies when these loci are at least tens of kilobases long (Organization et al., 2017) (Rowley et al., 2019) . Combining all these data with our liquid chromatin Hi-C results, we conclude that chromatin phase segregation can occur when domains of a particular chromatin state are at least 10 kb. Notably, digestion studies indicate that mitotic chromosomes are also constrained by stable chromatin interactions spaced by approximately 15 kb (Poirier & Marko, 2002)

Our results obtained with DpnII digestion where the genome is fragmented in <6 kb fragments show that these fragments are too short to maintain stable phase-segregated domains. We find that the stability of interactions between <6 kb fragments, and the rate of mixing of initially segregated loci depends on their chromatin state and association with sub-nuclear structures: interactions at the nuclear lamina are relatively stable, those near nuclear speckles and polycomb complexes are highly unstable, while interactions for loci associated with different heterochromatin proteins and the nucleolus displayed a range intermediate stabilities. The dynamics of associations between loci are therefore determined by chromatin-associated factors, and may also be determined directly by the biochemical properties of histone tail modifications. For instance, in recent studies, the Rosen lab found that chromatin fragments can form droplets in vitro and that the dynamics of chromatin fragments within these droplets are dependent upon both H1 binding and histone acetylation (Francisco & Francisco,

2019): acetylation of histones resulted in more mobility of fragments and reduced droplet formation, while binding of H1 led to stable droplet with strongly reduced mobility of chromatin fragments. These results are consistent with the dynamics we observe here for active and inactive chromatin fragments within liquid chromatin.

Generally, heterochromatic loci are engaged in the most stable interactions. This implies that these associations play a dominant role in spatial compartmentalization of the nucleus, consistent with predictions made by simulations (Falk et al., 2019). However, there is a range of stabilities correlating with different types of heterochromatin. Interactions between loci at the nuclear lamina are the most stable, suggesting that these loci are firmly tethered to the lamina meshwork. Imaging experiments showed that loci near the lamina can become embedded within the lamina meshwork, and that lamin proteins themselves are also stably localized within the lamina (Broers et al., 1999) .

Loci associated with the three different HP1 proteins display different dissociation kinetics. Interestingly, these differences correlate with different dynamics and sub-nuclear locations of the HP1 proteins in the nucleus. HP1  $\gamma$  (CBX3) binds relatively transiently to euchromatin, which may explain the dynamic nature of chromatin interactions between loci bound by this protein (Dialynas et al., 2007). On the other hand, interactions between loci enriched in HP $\alpha$  (CBX5) are more stable, which likely is the result of more stable HP1 $\alpha$

binding to heterochromatin (Strom & Alexander, 2017). Further, the clustering of heterochromatic loci bound by HP1 $\alpha$  may be related to condensate formation by HP1 $\alpha$  proteins at and around heterochromatic loci (Strom & Alexander, 2017).

Polycomb bound regions of DNA are domains of facultative heterochromatin critical to proper vertebrate and invertebrate development. These regions spatially cluster together to form polycomb bodies visible in cell nuclei (Saurin et al., 1998). Polycomb bodies are shown to compact their associated chromatin as a potential mechanism for gene repression (Boettiger et al., 2016) (Francis, Kingston, & Woodcock, 2004) (Grau et al., 2011). Interestingly, liquid chromatin Hi-C showed differences in chromatin interaction stability between facultative heterochromatic domains marked by polycomb and constitutive heterochromatin domains marked by lamina association or binding of HP1 $\alpha$ /HP1 $\alpha$  proteins. While many chromatin contacts in constitutive heterochromatin were maintained even after 16 hours of digestion, the half-life for chromatin contacts at polycomb-bound regions was short, on a scale similar to more open and active regions of the genome. The compacted states of polycomb and HP1 $\alpha$  bound chromatin appear to form via a similar phase-separation mechanism mediated by multivalent interactions between specific CBX homologs. *In vitro and in vivo*, both CBX2 (polycomb subunit) and CBX5 (HP1 $\alpha$ ) are capable of forming condensates of polycomb bodies and constitutive heterochromatin, respectively (Larson et al., 2017). Our data indicate that these different structures associated chromatin have very different properties. Both are

dynamic with regards to the exchange of proteins and both have a fraction of stably bound proteins (Strom & Alexander, 2017) (Youmans, Schmidt, & Cech, 2018), but the stability of interactions between loci mediated by these factors is distinct, possibly related to differences in affinity between CBX proteins and chromatin: the binding affinity of CBX5 (Hp1 $\alpha$ ) for its preferential histone modification H3K9me3 is much stronger than the affinity of CBX2 for its preferential mark H3K27me3 . Highly dynamic interactions occurred between loci associated with speckles. This is interesting because previous work had identified speckles to be one of two structural anchors, the other one being the lamina, that determine the organization of the nucleus (Chen et al., 2018) (Quinodoz et al., 2018) Our data indicate that these structures differ greatly in how they anchor chromosome conformation: associations at the lamina involve stable interactions while anchoring at speckles is driven by more dynamic interactions.

The dynamics we observe for loci after chromatin fragmentation is likely related to the intrinsic dynamics of those loci while being part of full-length chromosomes. This is confirmed by the fact that active and inactive chromatin are both dynamic and mobile as assessed by both live cell imaging and liquid chromatin Hi-C. However, it is important to point out that during the liquid chromatin Hi-C procedure, some chromatin factors may dissociate from the nucleus, and this could affect the locus mixing behavior we observe. This will likely be the case for proteins that rapidly dissociate. As we discussed above,

protein binding dynamics, e.g., of HP1 proteins, may determine the stability of chromatin interactions as well. An example of proteins that dissociate from chromatin upon fragmentation is the cohesin complex, possibly due to the way it binds chromatin by encircling chromatin fiber(s). However, the cohesin complex is not involved in compartment formation (P. Nora et al., 2017) (Nuebler et al., 2018) (Haarhuis et al., 2017) (Extension et al., 2017) (Glenn et al., 2017) (Schwarzer et al., 2017)(Wutz et al., 2017) , and thus its dissociation may not influence the stability of phase separation-driven chromatin interactions detected by liquid chromatin Hi-C.

Our current work suggests that the status of chromatin condensation (e.g. DNA bound by polycomb or bound by HP1 $\alpha$ ) and status of chromatin anchoring (e.g. anchoring at speckles or anchoring at nuclear lamina) are not strong predictors of chromatin conformation stability. Furthermore, we have shown that the stability of a locus correlates with its histone marks and enrichment for bound proteins. For example, enrichment for the H3K9me3 histone mark and for binding of the protein HP1 $\alpha$  is indicative of highly stable interactions. However, it is not clear whether binding of HP1 $\alpha$  to DNA is dictating chromatin conformation stability. To answer this question, an appropriate experiment would be to perform liquid chromatin Hi-C on HP1 $\alpha$  knockout cells. If HP1 $\alpha$  knockout alone destabilizes the genomic loci that were bound by HP1 $\alpha$  in wildtype, we could assume that indeed chromatin conformation stability is controlled by the bound proteins

The current work analyzed the intrinsic chromatin interaction strengths and dissolution kinetics of chromosome conformation within otherwise inactive nuclei and how these measurements along chromosomes relate to chromatin state and chromosomal compartmentalization. Future work can focus on how these kinetic properties change in cells or nuclei, where active processes such as transcription, replication, chromatin compaction and condensation, and loop extrusion are also acting, and on determining the roles of RNAs, protein complexes, and histone modifications in modulating the attractive forces between loci and the dynamics of genome folding in general.

Performing liquid chromatin Hi-C demands 35 million nuclei for the seven-time points: control, 5mins, 1h, 2hs, 3hs, 4hs, and 16hs (since 5 million nuclei are needed for each time point). Additionally, to correct for the digestion bias we performed DpnII-Seq using 10 million nuclei for each time point. In order to optimize liquid chromatin Hi-C, we can perform fewer Hi-C library controls (1h, 3hs, 16hs) as a single control timepoint is used to extract the half-life genome-wide. For the current work, we corrected for biases in our half-life metric using different time point of DpnII-Seq (**Fig. 4.9B**). Results were only modestly altered after bias correction via DpnII-seq with the greatest differences occurring before 1h pre-digestion. It follows, performing a single DpnII-seq library using 1h pre-digest appears reasonable to correct half-life for the digestion bias.

The fractal globule is a polymer module that describes the static chromosome conformation capture we detected using conventional Hi-C (Lieberman-aiden et al., 2009). Development of a simulated fragmented fractal globule would allow testing of whether this polymer model can mimic the dissociation kinetics we observe in liquid chromatin Hi-C. Aggregating results from simulated polymer models and liquid chromatin Hi-C will prove essential for further understanding of the heterogeneous biophysical properties that maintain genome organization.

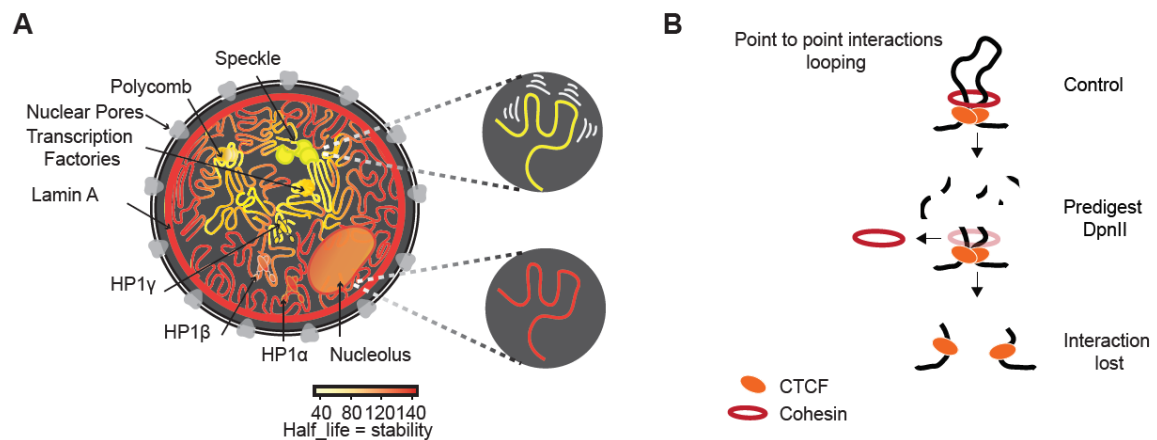


**Figure 5.1: Illustration of chromatin interaction dynamics in the nucleus and model for cohesin loss after chromatin digestion**

**(A)** Left: Schematic representation of varying chromatin interactions dynamics at different sub-nuclear domains. Shortest half-life reflects the least stable interactions (yellow), while the longest half-life reflects the most stable interactions (dark orange). Nuclear subdomains differ greatly in their stability.



Top right: Chromatin anchored at speckles is driven by the most dynamic interactions. Bottom right: Chromatin anchored at the nuclear lamina involves the most stable interactions. **(B)** Model for how cohesin rings stabilize CTCF-CTCF loops by encircling loop bases. Top: Cohesin ring encircles loop bases at convergent CTCF sites. Middle: Pre-digestion with DpnII cuts loop into chromatin fragments <6 kb, and the cohesin ring can slide off nearby ends. Bottom: CTCF remains bound to digested chromatin fragments but interactions between CTCF-bound sites are lost.

## BIBLIOGRAPHY

- Alboran, I. M. De, Malynn, B., Davidson, L., Rickert, R., Rajewsky, K., Depinho, R. A., & Alt, F. W. (2001). Analysis of C-MYC Function in Normal Cells via Conditional Gene-Targeted Mutation *Immunity*, 14, 45–55.
- Alexander, J. M., Guan, J., Li, B., Maliskova, L., Song, M., Shen, Y., ... Lomvardas, S. (2019). Live-cell imaging reveals enhancer- dependent Sox2 transcription in the absence of enhancer proximity. *ELife*, 1–42.  
<https://doi.org/https://doi.org/10.7554/eLife.41769>
- Alipour, E., & Marko, J. F. (2012). Self-organization of domain structures by DNA-loop-extruding enzymes. *Nucleic Acids Research*, 40(22), 11202–11212. <https://doi.org/10.1093/nar/gks925>
- Allahyar, A., Vermeulen, C., Bouwman, B. A. M., Krijger, P. H. L., Verstegen, M. J. A. M., Geeven, G., ... Laat, W. De. (2018). Enhancer hubs and loop collisions identified from single-allele topologies. *Nature Genetics*, 50(August). <https://doi.org/10.1038/s41588-018-0161-5>
- America, N., Pomerantz, M. M., Ahmadiyeh, N., Jia, L., Herman, P., Verzi, M. P., ... Freedman, M. L. (2009). The 8q24 cancer risk variant interaction with MYC in colorectal cancer. *Nature Genetics*, 41(8), 882–884.  
<https://doi.org/10.1038/ng.403>
- Andrey, G., Montavon, T., Mascres, B., Gonzalez, F., Noordermeer, D., Leleu, M., ... Duboule, D. (2013). RESEARCH ARTICLE SUMMARY Domains Underlies HoxD Genes Collinearity in Mouse Limbs. *Science*, 340(June). <https://doi.org/10.1038/nrg3207>
- Aneas, I., Sobreira, R., Wasserman, N. F., Lee, J. H., Puvion-Randall, V., Tam, D., & Shen, M. (2014). Obesity-associated variants within FTO form long-range functional connections with IRX3. *Nature*.  
<https://doi.org/10.1038/nature13138>
- Banigan, E. J., Stephens, A. D., & Marko, J. F. (2017). Article Mechanics and Buckling of Biopolymeric Shells and Cell Nuclei. *Biophysj*, 113(8), 1654–1663. <https://doi.org/10.1016/j.bpj.2017.08.034>
- Barbieri, M., Chotalia, M., Fraser, J., Lavitas, L., Dostie, J., & Pombo, A. (2012). Complexity of chromatin folding is captured by the strings and binders switch model. *PNAS*, 109(40), 16173–16178. <https://doi.org/10.1073/pnas.1204799109>
- Beagrie, R. A., Scialdone, A., Schueler, M., Kraemer, D. C., Chotalia, M., Xie, S. Q., ... Pombo, A. (2017). Complex multi-enhancer contacts captured by Genome Architecture Mapping (GAM). *Nature*, 543(7646), 519–524.

<https://doi.org/10.1038/nature21411>.Complex

- Belaghzal, H., Dekker, J., & Gibcus, J. H. (2017). Hi-C 2.0: An optimized Hi-C procedure for high-resolution genome-wide mapping of chromosome conformation. *Methods*, 123. <https://doi.org/10.1016/j.ymeth.2017.04.004>
- Belton, J. M., McCord, R. P., Gibcus, J. H., Naumova, N., Zhan, Y., & Dekker, J. (2012). Hi-C: A comprehensive technique to capture the conformation of genomes. *Methods*, 58(3), 268–276. <https://doi.org/10.1016/j.ymeth.2012.05.001>
- Benedetti, F., Dorier, J., Burnier, Y., & Stasiak, A. (2014). Models that include supercoiling of topological domains reproduce several known features of interphase chromosomes. *Nucleic Acids Research*, 42(5), 2848–2855. <https://doi.org/10.1093/nar/gkt1353>
- Bernardi, G. (2015). Chromosome Architecture and Genome Organization. *PloS One*, 10(11), e0143739. <https://doi.org/10.1371/journal.pone.0143739>
- Bintu, B., Mateo, L. J., Su, J., Sinnott-armstrong, N. A., Parker, M., Kinrot, S., ... Zhuang, X. (2018). Super-resolution chromatin tracing reveals domains and cooperative interactions in single cells. *Science*, 1783. <https://doi.org/10.1126/science.aau1783>
- Blyth, K., Cameron, E. R., & Neil, J. C. (2005). THE RUNX GENES : GAIN OR LOSS OF FUNCTION IN CANCER. *Nature Reviews Cancer*, 5(May), 376–387. <https://doi.org/10.1038/nrc1607>
- Boettiger, A. N., Bintu, B., Moffitt, J. R., Wang, S., Beliveau, B. J., Fudenberg, G., ... Zhuang, X. (2016). chromatin folding for different epigenetic states. *Nature*, 529(7586), 418–422. <https://doi.org/10.1038/nature16496>
- Bonev, B., & Cavalli, G. (2016). genome. *Nature Genetics*, 17, 661–678. <https://doi.org/10.1038/nrg.2016.112>
- Bouwman, B. A. M., & Laat, W. De. (2015). Getting the genome in shape : the formation of loops , domains and compartments. *Genome Biology*, 1–9. <https://doi.org/10.1186/s13059-015-0730-1>
- Branco, M. R., & Pombo, A. (2006). Intermingling of Chromosome Territories in Interphase Suggests Role in Translocations and Transcription-Dependent Associations. *PLOS Biology*, 4(5). <https://doi.org/10.1371/journal.pbio.0040138>
- Broers, J. L. V, Machiels, B. M., Eys, G. J. J. M. Van, Kuijpers, H. J. H., Manders, E. M. M., Driel, R. Van, & Ramaekers, F. C. S. (1999). Dynamics of the nuclear lamina as monitored by GFP-tagged A-type lamins. *Journal of Cell*

*Science*, 3475, 3463–3475.

- Buck, L., & Axel, R. (1991). A Novel Multigene Family May Encode Odorant Receptors : A Molecular Basis for Odor Recognition. *Cell*, 65, 175–187.
- Buenrostro, J. D., Giresi, P. G., Zaba, L. C., Chang, H. Y., & Greenleaf, W. J. (2013). Transposition of native chromatin for fast and sensitive epigenomic profiling of open chromatin , DNA-binding proteins and nucleosome position. *Nature Methods*, 10(12). <https://doi.org/10.1038/nmeth.2688>
- Cao, W., Britos-bray, M., Claxton, D. F., Kelley, C. A., Speck, N. A., Liu, P. P., & Friedman, A. D. (1997). CBF b -SMMHC , expressed in M4Eo AML , reduced CBF DNA-binding and inhibited the G1 to S cell cycle transition at the restriction point in myeloid and lymphoid cells. *Oncogene*, 15, 1315–1327.
- Castilla, L. H., Wijmenga, C., Wang, Q., Stacy, T., Speck, N. A., Eckhaus, M., ... Liu, P. P. (1996). Failure of Embryonic Hematopoiesis and Lethal Hemorrhages in Mouse Embryos Heterozygous for a Knocked-In Leukemia Gene CBFB – MYH11. *Cell*, 87, 687–696.
- Chambeyron, S., & Bickmore, W. A. (2004). Chromatin decondensation and nuclear reorganization of the HoxB locus upon induction of transcription. *GENES & DEVELOPMENT*, 18, 1119–1130. <https://doi.org/10.1101/gad.292104.tional>
- Chen, Y., Zhang, Y., Wang, Y., Zhang, L., Brinkman, E. K., Adam, S. A., ... Ma, J. (2018). Mapping 3D genome organization relative to nuclear compartments using TSA-Seq as a cytological ruler. *JCB*, 1–32. <https://doi.org/10.1083/jcb.201807108> 1
- Chien, R., Zeng, W., Kawauchi, S., Bender, M. A., Santos, R., Gregson, H. C., ... Yokomori, K. (2011). Cohesin Mediates Chromatin Interactions That Regulate Mammalian Beta globin Expression. *Journal of Biological Chemistry*, 286(20), 17870–17878. <https://doi.org/10.1074/jbc.M110.207365>
- Ciosk, R., Shirayama, M., Shevchenko, A., Tanaka, T., Toth, A., Shevchenko, A., & Nasmyth, K. (2000). Cohesin ' s Binding to Chromosomes Depends on a Separate Complex Consisting of Scc2 and Scc4 Proteins. *Molecular Cell*, 5, 243–254.
- Consortium, T. E. P. (2012). An integrated encyclopedia of DNA elements in the human genome. *Nature*, 489(57–74). <https://doi.org/10.1038/nature11247>
- Cook, P. R. (2002). Predicting three-dimensional genome structure from transcriptional activity. *Nature Genetics*, 32(november), 347–352.

- Crane, E., Bian, Q., McCord, R. P., Lajoie, B. R., Wheeler, B. S., Ralston, E. J., ... Meyer, B. J. (2015). Condensin-driven remodelling of X chromosome topology during dosage compensation. *Nature*, 523(7559), 240–244. <https://doi.org/10.1038/nature14450>
- Cremer, T, & Cremer, C. (2001). CHROMOSOME TERRITORIES , NUCLEAR ARCHITECTURE AND GENE REGULATION IN MAMMALIAN CELLS. *Nature Reviews Genetics*, 2(April), 292–301.
- Cremer, T, Cremer, C., Baumann, H. I., Luedtke, E., Sperling, K., Teuber, V., & Zorn, C. (1982). Rabl ' s Model of the Interphase Chromosome Arrangement Tested in Chinese Hamster Cells by Premature Chromosome Condensation and Laser-UV-Microbeam Experiments. *Human Genetics*, 60, 46–56.
- Cremer, Thomas, & Cremer, M. (2010). Chromosome Territories. *Cold Spring Harbor Perspectives in Biology*, 1–22. <https://doi.org/10.1101/cshperspect.a003889>
- Croce, L. Di, & Helin, K. (2013). RE V IE W Transcriptional regulation by Polycomb group proteins. *Nature Publishing Group*, 20(10), 1147–1155. <https://doi.org/10.1038/nsmb.2669>
- Dekker, J, Rippe, K., Dekker, M., & Kleckner, N. (2002). Capturing chromosome conformation. *Science*, 295(5558), 1306–1311. <https://doi.org/10.1126/science.1067799>
- Dekker, Job. (2014). Two ways to fold the genome during the cell cycle : insights obtained with chromosome conformation capture. *Epigenetics and Chromatin*, 1–12.
- Dekker, Job, & Heard, E. (2015). Structural and functional diversity of Topologically Associating Domains. *Federation of European Biochemical Societies.*, 589, 2877–2884.
- Dekker, Job, & Mirny, L. (2016). Perspective The 3D Genome as Moderator of Chromosomal Communication. *Cell*, 164(6), 1110–1121. <https://doi.org/10.1016/j.cell.2016.02.007>
- Dekker, Job, & Misteli, T. (2015a). Long-Range Chromatin Interactions. *Cold Spring Harbor Perspectives in Biology*. <https://doi.org/10.1101/cshperspect.a019356>
- Dekker, Job, & Misteli, T. (2015b). Long-Range Chromatin Interactions. *Cold Spring Harbor Perspectives in Biology*.
- Dekker, Job, Rippe, K., Dekker, M., & Kleckner, N. (2002). Capturing Chromosome Conformation. *Science*, 295(February), 1306–1312.

<https://doi.org/10.1126/science.1067799>

- Dialynas, G. K., Terjung, S., Brown, J. P., Aucott, R. L., Baron-luhr, B., Singh, P. B., & Georgatos, S. D. (2007). Plasticity of HP1 proteins in mammalian cells. *Journal of Cell Science*, 120, 3415–3424. <https://doi.org/10.1242/jcs.012914>
- Dixon, J R, Selvaraj, S., Yue, F., Kim, A., Li, Y., Shen, Y., ... Ren, B. (2012). Topological domains in mammalian genomes identified by analysis of chromatin interactions. *Nature*, 485(7398), 376–380. <https://doi.org/10.1038/nature11082>
- Dixon, Jesse R, Selvaraj, S., Yue, F., Kim, A., Li, Y., Shen, Y., ... Ren, B. (2012). identified by analysis of chromatin interactions. *Nature*, 485(7398), 376–380. <https://doi.org/10.1038/nature11082>
- Dostie, J., Richmond, T. A., Arnaout, R. A., Selzer, R. R., Lee, W. L., Honan, T. A., ... Dekker, J. (2006). Chromosome Conformation Capture Carbon Copy ( 5C ): A massively parallel solution for mapping interactions between genomic elements. *Genome Research*, 16, 1299–1309. <https://doi.org/10.1101/gr.5571506.1>
- Douglas, N. C., Jacobs, H., Bothwell, A. L. M., & Hayday, A. C. (2001). Defining the specific physiological requirements for c-Myc in T cell development. *Nature Immunology*, 2(4), 307–315.
- Dowen, J. M., Fan, Z. P., Hnisz, D., Ren, G., Abraham, B. J., Zhang, L. N., ... Young, R. A. (2014). Control of Cell Identity Genes Occurs in Insulated Neighborhoods in Mammalian Chromosomes. *Cell*, 159(2), 374–387. <https://doi.org/10.1016/j.cell.2014.09.030>
- Dryden, N. H., Broome, L. R., Dudbridge, F., Johnson, N., Orr, N., Schoenfelder, S., ... Fletcher, O. (2014). Unbiased analysis of potential targets of breast cancer susceptibility loci by Capture Hi-C. *Genome Research*, 24, 1854–1868. <https://doi.org/10.1101/gr.175034.114>.
- Durand, N. C., Shamim, M. S., Machol, I., *Iterative correction of Hi-C data reveals hallmarks of chromosome organization*, S. S. P., Huntley, M. H., Lander, E. S., & Aiden, E. L. (2016). Juicer Provides a One-Click System for Analyzing Loop-Resolution Hi-C Experiments. *Cell Systems*, 3(1), 95–98. <https://doi.org/10.1016/j.cels.2016.07.002>
- Erdel, F., & Rippe, K. (2018). Biophysical Perspective Formation of Chromatin Subcompartments by Phase Separation. *Biophysical Journal*, 114, 2262–2270. <https://doi.org/10.1016/j.bpj.2018.03.011>
- Extension, C. L., Weide, R. H. Van Der, Blomen, V. A., Brummelkamp, T. R., Wit, E. De, & Rowland, B. D. (2017). The Cohesin Release Factor WAPL

- Restricts Chromatin Loop Extension. *Cell*, 169, 693–707.  
<https://doi.org/10.1016/j.cell.2017.04.013>
- Falk, M., Feodorova, Y., Naumova, N., Imakaev, M., Lajoie, B. R., Leonhardt, H., ... Mirny, L. A. (2019). Heterochromatin drives compartmentalization of inverted and conventional nuclei. *Nature*, 570, 395–399.  
<https://doi.org/10.1038/s41586-019-1275-3>
- Feric, M., Vaidya, N., Harmon, T. S., Kriwacki, R. W., Pappu, R. V., Brangwynne, C. P., ... Brangwynne, C. P. (2016). Coexisting Liquid Phases Underlie Nucleolar Coexisting Liquid Phases Underlie Nucleolar Subcompartments. *Cell*, 165(7), 1686–1697. <https://doi.org/10.1016/j.cell.2016.04.047>
- Ferraiuolo, M. A., Sanyal, A., Naumova, N., Dekker, J., & Dostie, J. (2012). From cells to chromatin : Capturing snapshots of genome organization with 5C technology. *Methods*, 58(3), 255–267.  
<https://doi.org/10.1016/j.ymeth.2012.10.011>
- Finn, E. H., Pegoraro, G., Dekker, J., Mirny, L., Misteli, T., Valton, A., ... Misteli, T. (2019). Extensive Heterogeneity and Intrinsic Variation in Spatial Genome Organization. *Cell*, 176, 1502–1515.  
<https://doi.org/10.1016/j.cell.2019.01.020>
- Foisner, R., & Garini, Y. (2015). dynamics in the nuclear interior. *Nature Communications*, 6, 1–9. <https://doi.org/10.1038/ncomms9044>
- Francis, N. J., Kingston, R. E., & Woodcock, C. L. (2004). Chromatin Compaction by a Polycomb Group Protein Complex. *Science*, 306(November), 1574–1578.
- Francisco, S., & Francisco, S. (2019). *Organization and Regulation of Chromatin by Liquid-Liquid Phase Separation*.
- Fudenberg, G., Imakaev, M., Lu, C., Goloborodko, A., Abdennur, N., & Mirny, L. A. (2015). *Formation of Chromosomal Domains in Interphase by Loop Extrusion*.
- Fullwood, M J, Han, Y., Wei, C. L., Ruan, X., & Ruan, Y. (2010). Chromatin interaction analysis using paired-end tag sequencing. *Curr Protoc Mol Biol*, Chapter 21, Unit 21 15 1-25.  
<https://doi.org/10.1002/0471142727.mb2115s89>
- Fullwood, M J, Liu, M. H., Pan, Y. F., Liu, J., Xu, H., Mohamed, Y. B., ... Ruan, Y. (2009). An oestrogen-receptor-alpha-bound human chromatin interactome. *Nature*, 462(7269), 58–64. <https://doi.org/10.1038/nature08497>
- Fullwood, Melissa J, Han, Y., Wei, C., Ruan, X., & Ruan, Y. (2010). Chromatin

- Interaction Analysis Using Paired-End Tag Sequencing. *Molecular Biology*, 1–25. <https://doi.org/10.1002/0471142727.mb2115s89>
- Gartenberg, M. R., Neumann, F. R., Laroche, T., Blaszczyk, M., Gasser, S. M., Ansermet, Q. E., & Geneva, C.-. (2004). Sir-Mediated Repression Can Occur Independently of Chromosomal and Subnuclear Contexts. *Cell*, 119, 955–967.
- Gassler, J., Brandão, H. B., Imakaev, M., Flyamer, I. M., Ladstätter, S., Bickmore, W. A., ... Tachibana, K. (2017). A mechanism of cohesin-dependent loop extrusion organizes zygotic genome architecture. *EMBO Journal*, 36(24). <https://doi.org/10.15252/embj.201798083>
- Gavrilov, A., Razin, S. V., & Cavalli, G. (2015). In vivo formaldehyde cross-linking: it is time for black box analysis. *Briefings in Functional Genomics*, 14(2), 163–165. <https://doi.org/10.1093/bfpg/elu037>
- Gibcus, J. H., & Dekker, J. (2013). Review The Hierarchy of the 3D Genome. *Molecular Cell*, 49(5), 773–782. <https://doi.org/10.1016/j.molcel.2013.02.011>
- Glenn, B., Hilaire, S., Casellas, R., Lander, E. S., & Aiden, E. L. (2017). Cohesin Loss Eliminates All Loop Domains. *Cell*, 171(2), 305-309.e24. <https://doi.org/10.1016/j.cell.2017.09.026>
- Gorski, S., & Misteli, T. (2005). Systems biology in the cell nucleus. *Journal of Cell Science*, 118. <https://doi.org/10.1242/jcs.02596>
- Gowda, S. D., Koler, R. D., & Jr, G. C. B. (1986). Regulation of C-myc expression during growth and differentiation of normal and leukemic human myeloid progenitor cells . Find the latest version : *The Journal of Clinical Investigation*, 77(1), 271–278.
- Grau, D. J., Chapman, B. A., Garlick, J. D., Borowsky, M., Francis, N. J., & Kingston, R. E. (2011). Compaction of chromatin by diverse Polycomb group proteins requires localized regions of high charge. *Gene and Development*, 25, 2210–2221. <https://doi.org/10.1101/gad.17288211.Lys>
- Guo, H., & Friedman, A. D. (2011). Phosphorylation of RUNX1 by Cyclin-dependent Kinase Reduces Direct Interaction with HDAC1 and HDAC3 \*. *Journal of Biological Chemistry*, 286(1), 208–215. <https://doi.org/10.1074/jbc.M110.149013>
- Guo, Y., Niu, C., Breslin, P., Tang, M., Zhang, S., Wei, W., ... Zhang, J. (2019). c-Myc – mediated control of cell fate in megakaryocyte-erythrocyte progenitors. *HEMATOPOIESIS AND STEM CELLS*, 114(10), 2097–2107. <https://doi.org/10.1182/blood-2009-01-197947>.



- Haarhuis, J. H. I., Der, W. R. H. Van, Blomen, V. A., Yanez-Cuna, J. O., Amendola, M., Ruiten, M. S. van, ... Rowland, B. D. (2017). Article The Cohesin Release Factor WAPL Restricts Chromatin Loop Extension. *Cell*, 169, 693–707. <https://doi.org/10.1016/j.cell.2017.04.013>
- Hediger, F., Neumann, F. R., Houwe, G. Van, Dubrana, K., Gasser, S. M., & Geneva, C.-. (2002). Live Imaging of Telomeres : yKu and Sir Proteins Define Redundant Telomere-Anchoring Pathways in Yeast. *Current Biology*, 12(02), 2076–2089.
- Heinz, S., Benner, C., Spann, N., Bertolino, E., Lin, Y. C., Laslo, P., ... Glass, C. K. (2010). Simple combinations of lineage-determining transcription factors prime cis-regulatory elements required for macrophage and B cell identities. *Molecular Cell*, 38(4), 576–589. <https://doi.org/10.1016/j.molcel.2010.05.004>
- Hnisz, D., Weintraub, A. S., Day, D. S., Valton, A., Bak, R. O., Li, C. H., ... Young, R. A. (2016). Activation of proto-oncogenes by disruption of chromosome neighborhoods. *Science*, 351(6280), 3812–3814.
- Hoke, H. A., Lin, C. Y., Lau, A., Orlando, D. A., Vakoc, C. R., Bradner, J. E., ... Young, R. A. (2013). Selective Inhibition of Tumor Oncogenes by Disruption of Super-Enhancers. *Cell*, 153, 320–334. <https://doi.org/10.1016/j.cell.2013.03.036>
- Holt, J. T., Redner, R. L., & Nienhuis, A. W. (1988). An Oligomer Complementary to c-myc mRNA Inhibits Proliferation of HL-60 Promyelocytic Cells and Induces Differentiation. *Molecular and Cellular Biology*, 8(2), 963–973.
- Hsieh, T.-H. S., Fudenberg, G., Goloborodko, A., & Rando, O. J. (2016). Micro-C XL: assaying chromosome conformation from the nucleosome to the entire genome. *Nature Methods*. <https://doi.org/10.1038/nmeth.4025>
- Hsieh, T. H., Weiner, A., Lajoie, B., Dekker, J., Friedman, N., & Rando, O. J. (2015). Mapping Nucleosome Resolution Chromosome Folding in Yeast by Micro-C. *Cell*, 162(1), 108–119. <https://doi.org/10.1016/j.cell.2015.05.048>
- Huangfu, D., & Raya, A. (2017). Protocol Review CRISPR / Cas9-Based Engineering of the Epigenome. *Cell Stem Cell*, 21, 431–447. <https://doi.org/10.1016/j.stem.2017.09.006>
- Hughes, J. R., Roberts, N., McGowan, S., Hay, D., Giannoulatou, E., Lynch, M., ... Higgs, D. R. (2014). Analysis of hundreds of cis-regulatory landscapes at high resolution in a single, high-throughput experiment. *Nat Genet*, 46(2), 205–212. <https://doi.org/10.1038/ng.2871>
- Illendula, A., Pulikkan, J. A., Zong, H., Grembecka, J., Xue, L., Sen, S., ... Bushweller, J. H. (2015). A small-molecule inhibitor of the aberrant

- transcription factor CBF  $\beta$  -SMMHC delays leukemia in mice. *Science*, 347(6223), 779–785.
- Imakaev, M., Fudenberg, G., Mccord, R. P., Naumova, N., Goloborodko, A., Lajoie, B. R., ... Mirny, L. A. (2012). Iterative correction of Hi-C data reveals hallmarks of chromosome organization. *Nature Methods*, 9(10). <https://doi.org/10.1038/NMETH.2148>
- Ivanov, D., & Nasmyth, K. (2005). A Topological Interaction between Cohesin Rings and a Circular Minichromosome. *Cell*, 122, 849–860. <https://doi.org/10.1016/j.cell.2005.07.018>
- Jin, F., Li, Y., Dixon, J. R., Selvaraj, S., Ye, Z., Lee, A. Y., ... Ren, B. (2013). A high-resolution map of the three-dimensional chromatin interactome in human cells. *Nature*. <https://doi.org/10.1038/nature12644>
- Johansen, L. M., Iwama, A., Lodie, T. A., Sasaki, K., Felsher, D. W., Golub, T. R., & Tenen, D. G. (2001). c-Myc Is a Critical Target for C / EBP  $\alpha$  in Granulopoiesis. *Molecular and Cellular Biology*, 21(11), 3789–3806. <https://doi.org/10.1128/MCB.21.11.3789>
- Jost, D., Carrivain, P., Cavalli, G., & Vaillant, C. (2014). Modeling epigenome folding : formation and dynamics of topologically associated chromatin domains. *Nucleic Acids Research*, 42(15), 9553–9561. <https://doi.org/10.1093/nar/gku698>
- Kagey, M. H., Newman, J. J., Bilodeau, S., Zhan, Y., Orlando, D. A., Berkum, N. L. Van, ... Young, R. A. (2010). Mediator and cohesin connect gene expression and chromatin architecture. *Nature*, 467(7314), 430–435. <https://doi.org/10.1038/nature09380>
- Kerpedjiev, P., Abdennur, N., Lekschas, F., Mccallum, C., Dinkla, K., Strobelt, H., ... Gehlenborg, N. (2018). HiGlass : web-based visual exploration and analysis of genome interaction maps. *Genome Biology*, 1–12.
- Kind, J., Pagie, L., Ortazokoyun, H., Boyle, S., Vries, S. S. De, Janssen, H., ... Steensel, B. Van. (2013). Single-Cell Dynamics of Genome-Nuclear Lamina Interactions. *Cell*, 153(1), 178–192. <https://doi.org/10.1016/j.cell.2013.02.028>
- Kitabayashi, I., Aikawa, Y., Nguyen, L. A., & Yokoyama, A. (2001). Activation of AML1-mediated transcription by MOZ and inhibition by the MOZ  $\pm$  CBP fusion protein. *EMBO Journal*, 20(24).
- Kitabayashi, I., Yokoyama, A., Shimizu, K., Ohki, M., & Pebp, C. (1998). Interaction and functional cooperation of the leukemia-associated factors AML1 and p300 in myeloid cell differentiation. *EMBO Journal*, 17(11), 2994–

3004.

- Lajoie, B. R., Berkum, N. L. Van, Sanyal, A., & Dekker, J. (2009). My5C : web tools for chromosome conformation capture studies. *Nature Methods*, 6(10), 690–691. <https://doi.org/10.1038/nmeth1009-690>
- Lajoie, B. R., Dekker, J., & Kaplan, N. (2015). The Hitchhiker's guide to Hi-C analysis: Practical guidelines. *Methods*, 72(C), 65–75. <https://doi.org/10.1016/j.ymeth.2014.10.031>
- Larson, A. G., Elnatan, D., Keenen, M. M., Trnka, M. J., Johnston, J. B., Burlingame, A. L., ... Narlikar, G. J. (2017). phase separation in heterochromatin. *Nature Publishing Group*, 547(7662), 236–240. <https://doi.org/10.1038/nature22822>
- Leiblerf, L. (1980). Theory of Microphase Separation in Block Copolymers. *Macromolecules*, 1602–1617. <https://doi.org/10.1021/ma60078a047>
- Liang, C., & Stillman, B. (1997). Persistent initiation of DNA replication and chromatin-bound MCM proteins during the cell cycle in cdc6 mutants. *GENES & DEVELOPMENT*, 11, 3375–3386.
- Lichtinger, M., Hoogenkamp, M., Krysinska, H., Ingram, R., & Bonifer, C. (2010). Blood Cells , Molecules , and Diseases Chromatin regulation by RUNX1. *Blood Cells, Molecules, and Diseases*, 44(4), 287–290. <https://doi.org/10.1016/j.bcmed.2010.02.009>
- Lieberman-aiden, E., Berkum, N. L. Van, Williams, L., Imakaev, M., Ragoczy, T., Telling, A., ... Dekker, J. (2009). Comprehensive Mapping of Long-Range Interactions Reveals Folding Principles of the Human Genome. *Science*, 33292(October), 289–294. <https://doi.org/10.1126/science.1178746>
- Lieberman-Aiden, E., van Berkum, N. L., Williams, L., Imakaev, M., Ragoczy, T., Telling, A., ... Dekker, J. (2009). Comprehensive mapping of long-range interactions reveals folding principles of the human genome. *Science*, 326(5950), 289–293. <https://doi.org/10.1126/science.1181369>
- Liu, L., Shi, G., Thirumalai, D., & Changbong Hyeon. (2018). Chain organization of human interphase chromosome determines the spatiotemporal dynamics of chromatin loci. *PLOS Computational Biology*, 1–20. <https://doi.org/10.1371/journal.pcbi.1006617> December
- Liu, P., Tarle, S. A., Hajra, A., Claxton, D. F., Mariton, P., Freedman, M., ... Collins, F. S. (1993). Fusion Between Transcription Factor CBFP / PEBP2I3 and a Myosin Heavy Chain in Acute Myeloid Leukemia. *Science*, 261, 1041–1044.

- Lomvardas, S., Barnea, G., Pisapia, D. J., Mendelsohn, M., Kirkland, J., & Axel, R. (2006). Interchromosomal Interactions and Olfactory Receptor Choice. *Cell*, 126, 403–413. <https://doi.org/10.1016/j.cell.2006.06.035>
- Lukasik, S. M., Zhang, L., Corpora, T., Tomanicek, S., Li, Y., Kundu, M., ... Bushweller, J. H. (2002). letters Altered affinity of CBF<sub>NL</sub>-SMMHC for Runx1 explains its role in leukemogenesis. *Nature Structural Biology*, 9(9). <https://doi.org/10.1038/nsb831>
- Ma, W., Ay, F., Lee, C., Gulsoy, G., Deng, X., Cook, S., ... Duan, Z. (2014). Fine-scale chromatin interaction maps reveal the cis-regulatory landscape of human lincRNA genes. *Nature Methods*, 12(1), 71–78. <https://doi.org/10.1038/nmeth.3205>
- Markenscoff-papadimitriou, E., Allen, W. E., Colquitt, B. M., Goh, T., Murphy, K. K., Monahan, K., ... Lomvardas, S. (2014). Article Enhancer Interaction Networks as a Means for Singular Olfactory Receptor Expression. *Cell*, 159(3), 543–557. <https://doi.org/10.1016/j.cell.2014.09.033>
- Marshall, W. F., Straight, A., Marko, J. F., Swedlow, J., Dernburg, A., Belmont, A., ... Sedat, J. W. (1997). Interphase chromosomes undergo constrained diffusional motion in living cells. *Current Biology*, 7(12), 930–939.
- Martin, P., McGovern, A., Orozco, G., Duffus, K., Yarwood, A., Schoenfelder, S., ... Eyre, S. (2015). Capture Hi-C reveals novel candidate genes and complex long-range interactions with related autoimmune risk loci. *Nature Communications*, 6, 1–7. <https://doi.org/10.1038/ncomms10069>
- Marzahn, M. R., Marada, S., Lee, J., Nourse, A., Kenrick, S., Zhao, H., ... Mittag, T. (2016). Higher-order oligomerization promotes localization of SPOP to liquid nuclear speckles. *The EMBO Journal*, 35(12), 1254–1275.
- Matsen, M. W., & Schick, M. (1994). Melt. *Macromolecules*, 27, 7157–7163. <https://doi.org/10.1021/ma00102a025>
- Michael Rubinstein, & Colby-standand, R. H. (n.d.). Polymer Physics. In *Oxford University Press*.
- Michieletto, D., Orlandini, E., & Marenduzzo, D. (2016). Polymer model with Epigenetic Recoloring Reveals a Pathway for the de novo Establishment and 3D Organization of Chromatin Domains. *American Physical Society*, 041047(16), 1–15. <https://doi.org/10.1103/PhysRevX.6.041047>
- Mifsud, B., Tavares-cadete, F., Young, A. N., Sugar, R., Schoenfelder, S., Ferreira, L., ... Osborne, C. S. (2015). Mapping long-range promoter contacts in human cells with high-resolution capture Hi-C. *Nature Publishing Group*, 47(6), 598–606. <https://doi.org/10.1038/ng.3286>

- Mifsud, B., Tavares-Cadete, F., Young, A. N., Sugar, R., Schoenfelder, S., Ferreira, L., ... Osborne, C. S. (2015). Mapping long-range promoter contacts in human cells with high-resolution capture Hi-C. *Nature Genetics*, 47(6), 598–606. <https://doi.org/10.1038/ng.3286>
- Migliorini, G., Henrion, M., Kandaswamy, R., Speedy, H. E., Heindl, A., Whiffin, N., ... Houlston, R. S. (2015). Capture Hi-C identifies the chromatin interactome of colorectal cancer risk loci. *Nature Communications*, 1–9. <https://doi.org/10.1038/ncomms7178>
- Misteli, T. (2007). Review Beyond the Sequence : Cellular Organization of Genome Function. *Cell*, 128, 787–800. <https://doi.org/10.1016/j.cell.2007.01.028>
- Nagano, T, Lubling, Y., Stevens, T. J., Schoenfelder, S., Yaffe, E., Dean, W., ... Fraser, P. (2013). Single-cell Hi-C reveals cell-to-cell variability in chromosome structure. *Nature*, 502(7469), 59–64. <https://doi.org/10.1038/nature12593>
- Nagano, Takashi, Lubling, Y., Stevens, T. J., Schoenfelder, S., Yaffe, E., Dean, W., ... Fraser, P. (2013). variability in chromosome structure. *Nature*, 502(7469), 59–64. <https://doi.org/10.1038/nature12593>
- Nagano, Takashi, Lubling, Y., Yaffe, E., Wingett, S. W., Dean, W., Tanay, A., & Fraser, P. (2015). Single-cell Hi-C for genome-wide detection of chromatin interactions that occur simultaneously in a single cell. *Nature Protocols*, 10(12), 1986–2003. <https://doi.org/10.1038/nprot.2015.127>
- Nagano, Takashi, Várnai, C., Schoenfelder, S., Javierre, B.-M., Wingett, S. W., & Fraser, P. (2015). Comparison of Hi-C results using in-solution versus in-nucleus ligation. *Genome Biology*, 16(1), 175. <https://doi.org/10.1186/s13059-015-0753-7>
- Nagashima, R., Hibino, K., Ashwin, S. S., Babokhov, M., Fujishiro, S., Imai, R., ... Tamura, S. (2019). Single nucleosome imaging reveals loose genome chromatin networks via active RNA polymerase II. *JCB*.
- Nichols, M. H., & Corces, V. G. (2015). A CTCF Code for 3D Genome Architecture. *Cell*, 162(4), 703–705. <https://doi.org/10.1016/j.cell.2015.07.053>
- Noordermeer, D., Wit, E. De, Klous, P., Werken, H. Van De, Simonis, M., Lopez-jones, M., ... Laat, W. De. (2011). Variegated gene expression caused by cell-specific long-range DNA interactions. *Nature Cell Biology*, 13(8), 944–951. <https://doi.org/10.1038/ncb2278>
- Nora, E., Lajoie, B. R., Schulz, E. G., Giorgetti, L., Okamoto, I., Servant, N., ...

- Heard, E. (2012). Spatial partitioning of the regulatory landscape of the X-inactivation centre. *Nature*, 485, 381–385.  
<https://doi.org/10.1038/nature11049>
- Nora, E. P., Lajoie, B. R., Schulz, E. G., Giorgetti, L., Okamoto, I., Servant, N., ... Heard, E. (2012). Spatial partitioning of the regulatory landscape of the X-inactivation centre. *Nature*, 485(7398), 381–385.  
<https://doi.org/10.1038/nature11049>
- Nora, P., Goloborodko, A., Valton, A., Dekker, J., Mirny, L. A., Bruneau, B. G., ... Abdennur, N. (2017). Targeted Degradation of CTCF Decouples Local Insulation of Chromosome Domains from Genomic Compartmentalization. *Cell*, 169, 930–944. <https://doi.org/10.1016/j.cell.2017.05.004>
- Norton, H. K., & Cremins, J. E. P. (2017). Crossed wires : 3D genome misfolding in human disease. *JCB*, 216(11), 3441–3452.
- Nuebler et al. (2018). Chromatin organization by an interplay of loop extrusion and compartmental segregation. *PNAS*, 115.  
<https://doi.org/10.1073/pnas.1717730115>
- Nuebler, J., Fudenberg, G., Imakaev, M., Abdennur, N., & Mirny, L. A. (2018). Chromatin organization by an interplay of loop extrusion and compartmental segregation. *PNAS*, 115(9), E6697–E6706.  
<https://doi.org/10.1073/pnas.1717730115>
- Organization, C., Rowley, M. J., Nichols, M. H., Lyu, X., Wang, P., Ruan, Y., ... Hermetz, K. (2017). Evolutionarily Conserved Principles Predict 3D Chromatin Organization. *Molecular Cell*, 67(5), 837-852.e7.  
<https://doi.org/10.1016/j.molcel.2017.07.022>
- Parada, L. A., Mcqueen, P. G., & Misteli, T. (2004). Tissue-specific spatial organization of genomes. *Genome Biology*, 1–9. <https://doi.org/10.1186/gb-2004-5-7-r44>
- Parada, L. A., Mcqueen, P. G., Munson, P. J., & Misteli, T. (2002). Conservation of Relative Chromosome Positioning in Normal and Cancer Cells. *Current Biology*, 12(02), 1692–1697. [https://doi.org/S0960-9822\(02\)01166-1](https://doi.org/S0960-9822(02)01166-1)
- Phair, R. D., Scaffidi, P., Elbi, C., Vecerova, J., Dey, A., Ozato, K., ... Misteli, T. (2004). Global Nature of Dynamic Protein-Chromatin Interactions In Vivo : Three-Dimensional Genome Scanning and Dynamic Interaction Networks of Chromatin Proteins. *Molecular and Cellular Biology*, 24(14), 6393–6402.  
<https://doi.org/10.1128/MCB.24.14.6393>
- Phillips-cremins, J. E., Sauria, M. E. G., Sanyal, A., Gerasimova, T. I., Lajoie, B.

- R., Bell, J. S. K., ... Corces, V. G. (2013). Architectural Protein Subclasses Shape 3D Organization of Genomes during Lineage Commitment. *Cell*, 153(6), 1281–1295. <https://doi.org/10.1016/j.cell.2013.04.053>
- Pieroo, M. Di, Zhang, B., Lieberman, E., Wolynes, P. G., & Onuchic, J. N. (2016). Transferable model for chromosome architecture. *PNAS*, 113(43). <https://doi.org/10.1073/pnas.1613607113>
- Poirier, M. G., & Marko, J. F. (2002). Mitotic chromosomes are chromatin networks without a mechanically contiguous protein scaffold. *PNAS*, 99(24), 15393–15397.
- Politi, A., Moné, M. J., Houtsmuller, A. B., Hoogstraten, D., Vermeulen, W., Heinrich, R., & Driel, R. Van. (2005). Mathematical Modeling of Nucleotide Excision Repair Reveals Efficiency of Sequential Assembly Strategies. *Molecular Cell*, 19, 679–690. <https://doi.org/10.1016/j.molcel.2005.06.036>
- Quinodoz, S. A., Ollikainen, N., Tabak, B., McDonel, P., Garber, M., Guttman, M., ... Cheng, C. (2018). Higher-Order Inter-chromosomal Hubs Shape 3D Genome Organization in the Nucleus. *Cell*, 744–757. <https://doi.org/10.1016/j.cell.2018.05.024>
- Rao, S. S., Huntley, M. H., Durand, N. C., Stamenova, E. K., Bochkov, I. D., Robinson, J. T., ... Aiden, E. L. (2014). A 3D map of the human genome at kilobase resolution reveals principles of chromatin looping. *Cell*, 159(7), 1665–1680. <https://doi.org/10.1016/j.cell.2014.11.021>
- Rao, S. S. P., Huntley, M. H., Durand, N. C., Stamenova, E. K., Bochkov, I. D., Robinson, J. T., ... Aiden, E. L. (2014a). 3D Map of the Human Genome at Kilobase Resolution Reveals Principles of Chromatin Looping. *Cell*, 159(7), 1665–1680. <https://doi.org/10.1016/j.cell.2014.11.021>
- Rao, S. S. P., Huntley, M. H., Durand, N. C., Stamenova, E. K., Bochkov, I. D., Robinson, J. T., ... Aiden, E. L. (2014b). 3DMap of the Human Genome at Kilobase Resolution Reveals Principles of Chromatin Looping. *Cell*, 156(7), 1–16. <https://doi.org/10.1016/j.cell.2014.11.021>
- Rowley, M. J., Lyu, X., Rana, V., Ando-kuri, M., Karns, R., Bosco, G., ... Bosco, G. (2019). Condensin II Counteracts Cohesin and RNA Polymerase II in the Establishment of 3D Chromatin Condensin II Counteracts Cohesin and RNA Polymerase II in the Establishment of 3D. *CellReports*, 26(11), 2890–2903.e3. <https://doi.org/10.1016/j.celrep.2019.01.116>
- Sahlén, P., Abdullayev, I., Ramsköld, D., Matskova, L., Rilakovic, N., Lötstedt, B., ... Sandberg, R. (2015). Genome-wide mapping of promoter-anchored interactions with close to single-enhancer resolution. *Genome Biology*, 1–13.

<https://doi.org/10.1186/s13059-015-0727-9>

- Sanborn, A. L., Rao, S. S. P., Huang, S., Durand, N. C., & Huntley, M. H. (2015). Chromatin extrusion explains key features of loop and domain formation in wild-type and engineered genomes. *PNAS*.  
<https://doi.org/10.1073/pnas.1518552112>
- Sanders, M. A., Hoogenboezem, R., Wit, E. De, Bouwman, B. A. M., Erpelinck, C., Velden, V. H. J. Van Der, ... Delwel, R. (2014). A Single Oncogenic Enhancer Rearrangement Causes Concomitant EVI1 and GATA2 Deregulation in Leukemia. *Cell*, 369–381.  
<https://doi.org/10.1016/j.cell.2014.02.019>
- Sanyal, A, Lajoie, B. R., Jain, G., & Dekker, J. (2012). The long-range interaction landscape of gene promoters. *Nature*, 489(7414), 109–113.  
<https://doi.org/10.1038/nature11279>
- Sanyal, Amartya, Lajoie, B. R., Jain, G., & Dekker, J. (2012). The long-range interaction landscape of gene promoters. *Nature*, 489, 109–113.  
<https://doi.org/10.1038/nature11279>
- Saurin, A. J., Shiels, C., Williamson, J., Satijn, D. P. E., Otte, A. P., Sheer, D., & Freemont, P. S. (1998). The Human Polycomb Group Complex Associates with Pericentromeric Heterochromatin to Form a Novel Nuclear Domain. *The Journal of Cell Biology*, 142(4), 887–898.
- Schoenfelder, S., Furlan-magaril, M., Mifsud, B., Tavares-cadete, F., Sugar, R., Javierre, B., ... Fraser, P. (2015). The pluripotent regulatory circuitry connecting promoters to their long-range interacting elements. *Genome Research*, 25, 1–16. <https://doi.org/10.1101/gr.185272.114>. Freely
- Schwarzer, W., Abdennur, N., Goloborodko, A., Pekowska, A., Fudenberg, G., & Loe-mie, Y. (2017). Two independent modes of chromatin organization revealed by cohesin removal. *Nature Publishing Group*, 551(7678), 51–56.  
<https://doi.org/10.1038/nature24281>
- Separation, M., & Rings, C. (1993). Microphase Separation of Block Copolymer Rings. *American Chemical Society*, 93(5), 1442–1444.  
<https://doi.org/10.1021/ma00058a038>
- Servant, N., Varoquaux, N., Lajoie, B. R., Viara, E., Chen, C.-J., Vert, J.-P., ... Barillot, E. (2015a). HiC-Pro: an optimized and flexible pipeline for Hi-C data processing. *Genome Biology*, 16, 259. <https://doi.org/10.1186/s13059-015-0831-x>
- Servant, N., Varoquaux, N., Lajoie, B. R., Viara, E., Chen, C., Vert, J., ... Barillot, E. (2015b). HiC-Pro : an optimized and flexible pipeline for Hi-C data



- processing. *Genome Biology*, 1–11. <https://doi.org/10.1186/s13059-015-0831-x>
- Shi, J., Whyte, W. A., Zepeda-mendoza, C. J., Milazzo, J. P., Shen, C., Roe, J., ... Vakoc, C. R. (2013). Role of SWI / SNF in acute leukemia maintenance and enhancer-mediated Myc regulation. *Gene and Development*, 27, 2648–2662. <https://doi.org/10.1101/gad.232710.113>.
- Shin, Y., Chang, Y., Lee, D. S. W., Berry, J., Sanders, D. W., Ronceray, P., ... Brangwynne, C. P. (2018). Liquid Nuclear Condensates Mechanically Sense and Restructure the Genome. *Cell*, 175(6), 1481-1491.e13. <https://doi.org/10.1016/j.cell.2018.10.057>
- Shinkai, S., Nozaki, T., Maeshima, K., & Togashi, Y. (2016). Dynamic Nucleosome Movement Provides Structural Information of Topological Chromatin Domains in Living Human Cells. *PLOS Computational Biology*, 1–16. <https://doi.org/10.1371/journal.pcbi.1005136>
- Sigova, A. A., Hnisz, D., Abraham, B. J., Lee, T. I., Lau, A., Saint-andre, V., ... Young, R. A. (2013). Resource Super-Enhancers in the Control of Cell Identity and Disease. *Cell*, 155. <https://doi.org/10.1016/j.cell.2013.09.053>
- Simonis, M., Klous, P., Splinter, E., Moshkin, Y., Willemsen, R., de Wit, E., ... de Laat, W. (2006). Nuclear organization of active and inactive chromatin domains uncovered by chromosome conformation capture-on-chip (4C). *Nat Genet*, 38(11), 1348–1354. <https://doi.org/10.1038/ng1896>
- Smith, E. M., Lajoie, B. R., Jain, G., & Dekker, J. (2016). Invariant TAD Boundaries Constrain Cell-Type-Specific Looping Interactions between Promoters and Distal Elements around the CFTR Locus. *American Journal of Human Genetics*, 98(1), 185–201. <https://doi.org/10.1016/j.ajhg.2015.12.002>
- Spilianakis, C. G., Lalioti, M. D., Town, T., Lee, G. R., & Flavell, R. A. (2005). Interchromosomal associations between alternatively expressed loci. *Nature*, 435(June), 637–645. <https://doi.org/10.1038/nature03574>
- Splinter, E., de Wit, E., van de Werken, H. J., Klous, P., & de Laat, W. (2012). Determining long-range chromatin interactions for selected genomic sites using 4C-seq technology: From fixation to computation. *Methods*. <https://doi.org/10.1016/j.ymeth.2012.04.009>
- Srinivasan, M., Scheinost, J. C., Petela, N. J., Hu, B., Costanzo, V., Nasmyth, K. A., ... Nasmyth, K. A. (2018). The Cohesin Ring Uses Its Hinge to Organize DNA Using Non-topological as well as Topological Article The Cohesin Ring Uses Its Hinge to Organize DNA Using Non-topological as well as

- Topological Mechanisms. *Cell*, 173(6), 1508-1510.e18.  
<https://doi.org/10.1016/j.cell.2018.04.015>
- Stanton, B. Z., Hodges, C., Calarco, J. P., Braun, S. M. G., Ku, W. L., Kadoch, C., ... Crabtree, G. R. (2016). Smarca4 ATPase mutations disrupt direct eviction of PRC1 from chromatin. *Nature Publishing Group*, 49(2), 282–288.  
<https://doi.org/10.1038/ng.3735>
- Stephens, A. D., Banigan, E. J., Adam, S. A., Goldman, R. D., & Dunn, A. R. (2017). Chromatin and lamin A determine two different mechanical response regimes of the cell nucleus. *Molecular Biology of the Cell*.  
<https://doi.org/10.1091/mbc.E16-09-0653>
- Stephens, A. D., Liu, P. Z., Banigan, E. J., Almassalha, L. M., & Misteli, T. (2018). Chromatin histone modifications and rigidity affect nuclear morphology independent of lamins. *Molecular Biology of the Cell*, 29, 220–223. <https://doi.org/10.1091/mbc.E17-06-0410>
- Strom, A. R., & Alexander, V. (2017). formation. *Nature Publishing Group*, 547(7662), 241–245. <https://doi.org/10.1038/nature22989>
- Symmons, O., Uslu, V. V., Tsujimura, T., Ruf, S., Nassari, S., Schwarzer, W., & Ettwiller, L. (2014). Functional and topological characteristics of mammalian regulatory domains. *Genome Research*, 24, 390–400.  
<https://doi.org/10.1101/gr.163519.113>
- Terakawa, T., Bisht, S., Eeftens, J. M., Dekker, C., & Haering, C. H. (2017). The condensin complex is a mechanochemical motor that translocates along DNA. *Science*, 358(November), 672–676.
- Thakar, R., Gordon, G., & Csink, A. K. (2006). Dynamics and anchoring of heterochromatic loci during development. *Journal of Cell Science*, 119(20), 4165–4175. <https://doi.org/10.1242/jcs.03183>
- Tolhuis, B., Palstra, R., Splinter, E., Grosveld, F., & Laat, W. De. (2002). Looping and Interaction between Hypersensitive Sites in the Active  $\gamma$ -globin Locus. *Molecular Cell*, 10, 1453–1465.
- Valton, A.-L., & Dekker, J. (2016). TAD disruption as oncogenic driver. *Current Opinion in Genetics & Development*, 36, 34–40.  
<https://doi.org/10.1016/j.gde.2016.03.008>
- Vanden-eynden, S. K., Xie, J., & Lutterbach, B. (2006). RUNX1 associates with histone deacetylases and SUV39H1 to repress transcription. *Npg*, (May), 5777–5786. <https://doi.org/10.1038/sj.onc.1209591>
- Variation, D., Maurano, M. T., Humbert, R., Rynes, E., Thurman, R. E., Haugen,

- E., ... Sunyaev, S. R. (2012). Systematic Localization of Common Disease-Associated Variation in Regulatory DNA Matthew. *Science*, 337(September), 1190–1196.
- Visel, A., & Mundlos, S. (2015). Disruptions of Topological Chromatin Domains Cause Pathogenic Rewiring of Gene-Enhancer Interactions. *Cell*, 1012–1025. <https://doi.org/10.1016/j.cell.2015.04.004>
- Vradii, D., Zaidi, S. K., Lian, J. B., Wijnen, A. J. Van, Stein, J. L., & Stein, G. S. (2005). Point mutation in AML1 disrupts subnuclear targeting , prevents myeloid differentiation , and effects a transformation-like phenotype. *PNAS*, 102(20).
- Vu, L. P., Perna, F., Wang, L., Voza, F., Figueroa, M. E., Tempst, P., ... Liu, Y. (2013). Article PRMT4 Blocks Myeloid Differentiation by Assembling a Methyl-RUNX1-Dependent Repressor Complex. *Cell Reports*, 5, 1625–1638. <https://doi.org/10.1016/j.celrep.2013.11.025>
- Wang, S., Su, J., Beliveau, B. J., Bintu, B., Moffitt, J. R., Wu, C., & Zhuang, X. (2016a). single chromosomes. *Science*, 353(6299). <https://doi.org/10.1126/science.aaf8084>
- Wang, S., Su, J., Beliveau, B. J., Bintu, B., Moffitt, J. R., Wu, C., & Zhuang, X. (2016b). Spatial organization ofchromatin domains and compartments in single chromosomes. *Science*, 353(6299). <https://doi.org/10.1126/science.aaf8993>
- Werken, H. J. G. Van De, Haan, J. C., Feodorova, Y., Bijos, D., Weuts, A., Theunis, K., ... Joffe, B. (2017). Small chromosomal regions position themselves autonomously according to their chromatin class. *Genome Research*, 27, 922–933. <https://doi.org/10.1101/gr.213751.116>.
- Wilson, A., Murphy, M. J., Oskarsson, T., Kaloulis, K., Bettess, M. D., Oser, G. M., ... Trumpp, A. (2004). c-Myc controls the balance between hematopoietic stem cell self-renewal and differentiation. *GENES & DEVELOPMENT*, 2747–2763. <https://doi.org/10.1101/gad.313104.and>
- Wingett, S., Ewels, P., Furlan-Magaril, M., Nagano, T., Schoenfelder, S., Fraser, P., & Andrews, S. (2015). HiCUP: pipeline for mapping and processing Hi-C data. *F1000Research*, 4, 1310. <https://doi.org/10.12688/f1000research.7334.1>
- Wu, C., Bassett, A., & Travers, A. (2007). A variable topology for the 30-nm chromatin fibre. *EMBO Reports*, 8(12), 8–13. <https://doi.org/10.1038/sj.embor.7401115>
- Wutz, G., Várnai, C., Nagasaka, K., Cisneros, D. A., Stocsits, R. R., Tang, W., ...

- Peters, J. (2017). Topologically associating domains and chromatin loops depend on cohesin and are regulated by CTCF , WAPL , and PDS 5 proteins. *The EMBO Journal*, 36(24), 3573–3599. <https://doi.org/10.15252/emboj.201798004>
- Xiong, K., & Ma, J. (2018). *Revealing Hi-C subcompartments by imputing high-resolution inter-chromosomal chromatin interactions*.
- Yaffe, E., & Tanay, A. (2011). Probabilistic modeling of Hi-C contact maps eliminates systematic biases to characterize global chromosomal architecture. *Nat Genet*, 43(11), 1059–1065. <https://doi.org/10.1038/ng.947>
- Yashiro-ohtani, Y., Wang, H., Zang, C., Arnett, K. L., Bailis, W., & Ho, Y. (2014). Long-range enhancer activity determines Myc sensitivity to Notch inhibitors in T cell leukemia. *PNAS*. <https://doi.org/10.1073/pnas.1407079111>
- Youmans, D. T., Schmidt, J. C., & Cech, T. R. (2018). Live-cell imaging reveals the dynamics of PRC2 and recruitment to chromatin by SUZ12-associated subunits. *Gene and Development*, 32, 794–805. <https://doi.org/10.1101/gad.311936.118.the>
- Zhao, X., Jankovic, V., Gural, A., Huang, G., Pardanani, A., Menendez, S., ... Nimer, S. D. (2008). Methylation of RUNX1 by PRMT1 abrogates SIN3A binding and potentiates its transcriptional activity. *GENES & DEVELOPMENT*, 640–653. <https://doi.org/10.1101/gad.1632608.RUNX1c>
- Zhao, Z., Tavoosidana, G., Sjolinder, M., Gondor, A., Mariano, P., Wang, S., ... Ohlsson, R. (2006). Circular chromosome conformation capture (4C) uncovers extensive networks of epigenetically regulated intra- and interchromosomal interactions. *Nat Genet*, 38(11), 1341–1347. <https://doi.org/10.1038/ng1891>
- Zidovska, A., Weitz, D. A., & Mitchison, T. J. (2013). Micron-scale coherence in interphase chromatin dynamics. *PNAS*, (16). <https://doi.org/10.1073/pnas.1220313110>